

UNIVERSITY OF BIRMINGHAM

INVESTIGATION OF CRYOGENIC ENERGY ON CONDENSATION AND FROSTING FOR WATER GENERATION

by

MEIXI LIU

A thesis submitted to the University of Birmingham for the degree of
DOCTOR OF PHILOSOPHY

Department of Mechanical Engineering
School of Engineering
College of Engineering and Physical Sciences
University of Birmingham
August 2022

UNIVERSITY OF
BIRMINGHAM

University of Birmingham Research Archive

e-theses repository

This unpublished thesis/dissertation is copyright of the author and/or third parties. The intellectual property rights of the author or third parties in respect of this work are as defined by The Copyright Designs and Patents Act 1988 or as modified by any successor legislation.

Any use made of information contained in this thesis/dissertation must be in accordance with that legislation and must be properly acknowledged. Further distribution or reproduction in any format is prohibited without the permission of the copyright holder.

ABSTRACT

Due to the increasing demand of freshwater in the shipping industry, desalination is seen as an important solution to overcome shortage of freshwater storage on board ships. On LNG powered vessels, the released cooling energy through LNG regasification process is identified as an effective cooling source for various applications, which could maximize utilization of the energy content within the marine fuel, in turn, to further decrease the carbon intensity of LNG powered vessels. One potential usage is freshwater generation assisted with the cryogenic energy recovery from LNG or other emerging liquid marine fuels in a cryogenic state. This thesis focuses on the evaluation of the freshwater generator assisted by cryogenic energy for marine applications. The following objectives are achieved, including obtaining a comprehensive understanding of the effects of the surface treatment and surface temperature on condensation enhancement and anti-frosting phenomena, developing numerical models of the main components of the freshwater generator for system optimisation, and assessing the integration system and its performance on a real-world LNG powered case ship.

To meet these objectives, a test facility to explore the surface characteristics with varying cryogenic temperature is developed. The results and phenomena account for the mechanisms of condensation and frosting, the frost formation and condensation characteristics, and frosting delay with different surface treatment. The hydrophobic coatings have significant effects on the condensation intensification with an enhancement factor of 2.1 times that of untreated. And for the frosting conditions, the tubes with surface treatments help delay droplet freezing for up to 45 seconds

compared to plain tubes. A semi-empirical correlation to predict the frost porosity and the frost properties on cold surface is proposed from the experimental data with an error within ±15%.

A verified theoretical model in Siemens Simcenter Amesim software was developed to predict the performance of the evaporator and condenser in the freshwater generator system in terms of the water production and frost characteristics. The impacts of the operation parameters of the evaporator and condenser are evaluated, showing that the heating capacity, pressure, superheat degree, and flow rate have significant effects on the system efficiency. Therefore, the system employs the superheated seawater and operates in the vacuum condition. Then, the parametric analysis was explored on the geometry of the condenser, where the production increases with the contact area and the heat exchanger material. It is seen that the Aluminium alloy 3003-H14 is the best material to use with a greater heat and mass transfer rate.

Finally, regarding the use of the LNG cryogenic energy, the thermodynamics performance of freshwater generator is evaluated systematically in real-world conditions to satisfy the water demand on board. The feasibility of the integrated system of recovering LNG cryogenic energy on the LNG powered case ship with the surface treatment was investigated and optimised by maximize the freshwater production, exergy efficiency and the economic. The comparison between the bare tube, Fluorinated Ethylene Propylene tube, Polytetrafluoroethylene and Fluorine based tube, shows that the Polytetrafluoroethylene is preferred on the heat exchanger surface with a total water production of 14461 kg and water recovery rate of 67.7%.

Compared to the published literature, the proposed technology showed a significant increase in the freshwater recovery rate by 3 times.

ACKNOWLEDGMENTS

I would like to express my sincere thanks to my supervisor Dr Dawei Wu for his advice and guidance in the research. Throughout our meetings and discussions, his insights and intuitions have shaped my understanding of many topics. He has given me the flexibility to explore many research avenues, has confidence in my ability and capability, and encourage me to carry out further studies in PhD. I would also like to thank Prof. Athanasios Tsolakis as my second supervisor to support me with great new ideas and knowledge to successfully carry out the experimental rigs and publish research papers.

My sincere thanks also go to Prof. Wenzhong Gao at Shanghai Maritime University who supported me greatly in experimental work and for always being there to help with his great knowledge. I would like to express my sincere acknowledgement to my technician Sonny Mao, who kindly supports, provides the advice, and shares insightful ideas on my laboratory setting up and experiment operations.

I am grateful to our research group members: Emmanouil-Loizos Tsougranis, Dr. Attar, Yi Li, Fangyu Zhang, Mingqiang Li, Yifei Zhang, Salman Farrukh, Yuqi Zhang and Peihao Chen for their assistance during the research. And many thanks to my friends and colleagues Ilias Konstantinou, David Sedlak, Mingjian Liu, Mai Yang and Jitao Zhang who have helped me and motivated me during my PhD. Also, I would like to express thank you to my boyfriend, Fanggang Zhang for his encouragement.

Last but not the least, I wish to thank my parents and friends for the supports and encouragements in every way possible throughout my life.

CONTENTS

ABSTRACT ..... ***i***

ACKNOWLEDGMENTS ..... ***iv***

CONTENTS ..... ***v***

LIST OF FIGURES ..... ***xi***

LIST OF TABLES ..... ***xvii***

NOMENCLATURE ..... ***xix***

Roman symbols xix

Subscripts xxii

Greek symbols xxiv

Abbreviations xxv

LIST OF PUBLICATIONS ..... ***xxvii***

CHAPTER 1 INTRODUCTION ***1***

1.1 Background 1

1.1.1 Freshwater generator 1

1.2 Research objectives 3

1.3 Thesis layout 4

CHAPTER 2 LITERATURE REVIEW ***7***

2.1 Fresh water generation 7

2.1.1 Desalination techniques 7
2.1.2 Freshwater generator on board 8
2.1.3 Single-stage conventional distillation 9
2.1.4 Improvements on SCD 12
2.2 LNG cryogenic energy 14
2.2.1 Liquefied natural gas 14
2.2.2 LNG cryogenic energy recovery for desalination 17
2.3 Condensation enhancement – Surface modification 21
2.3.1 Condensation 21
2.3.2 Surface characteristic 25
2.3.3 Effect of the surface characteristic 27
2.4 Frosting 28
2.4.1 Frosting introduction 28
2.4.2 Frosting on LNG vaporizers 32
2.4.3 Solutions 33
2.5 Research motivation 38
2.6 Summary 40
CHAPTER 3 EXPERIMENTAL METHODOLOGY 42
3.1 Experiment description 42
3.1.1 Experimental apparatus 42
3.1.2 Preparation of the surfaces 47

3.1.3 Experimental procedure 48
3.2 Mechanism introduction 50
3.3 Performance analysis – Condensation 54
3.4 Performance analysis - Frosting 56
3.4.1 Frost properties 56
3.4.2 Heat transfer analysis 59
3.5 Summary 60
CHAPTER 4 EXPERIMENTAL RESULTS AND DISCUSSION 61
4.1 Introduction 61
4.2 Mechanism analysis 61
4.2.1 Condensation mechanism analysis 63
4.2.2 Condensation frosting mechanism 66
4.2.3 Nucleation on ice 74
4.3 Parametric study 75
4.3.1 Effect of air property 76
4.3.2 Effect of surface temperature 79
4.3.3 Effect of surface characteristics on condensation 81
4.3.4 Condensation frosting mechanism case 85
4.3.5 Direct frosting 89
4.3.6 Hybrid case 101
4.4 Summary 103

CHAPTER 5 NUMERICAL ANALYSIS 106

5.1 Introduction 106

5.2 System description 106

5.3 Methodology 108

5.3.1 Air property 110

5.3.2 Coolant property calculations 111

5.3.3 Coolant flow boiling in the tube 112

5.3.4 Evaporator modelled in Siemens Simcenter Amesim software 115

5.3.5 Condenser modelled in Siemens Simcenter Amesim software 117

5.3.6 Frosting phenomena modelled in Siemens Simcenter Amesim software 121

5.4 Validation 126

5.4.1 Evaporator 127

5.4.2 Condenser 129

5.5 Parametric study – Evaporator 138

5.6 Parametric study – condenser geometry parameters 141

5.6.1 Condensation 143

5.6.2 Frosting 147

5.7 Parametric study - condensation 152

5.8 Parametric study – frosting 158

5.8.1 Effect of air properties – air temperature 158

5.8.2 Effect of air properties – air velocity 162

5.8.3 Effect of coolant temperature 163

5.9 Summary 166

CHAPTER 6 CASE STUDY 167

6.1 Introduction 167

6.2 Case-study ship introduction 168

6.3 System description 169

6.4 Methodology 172

6.4.1 Energy and exergy analysis 172

6.4.2 Economic analysis 175

6.4.3 Optimisation process 176

6.5 Results and discussion 182

6.5.1 Single-objective optimisation 183

6.5.2 Multi objective optimisation 188

6.5.3 Optimisation analysis on surface treatments 192

6.5.3 System evaluation 195

6.5.4 Economic analysis 197

6.6 Summary 198

CHAPTER 7 Conclusions 200

7.1 Conclusions 200

7.2 Future work recommendations 203

Appendix A – Desalination technologies comparison 205

Appendix B – MATLAB code for frost layer thickness detection 206

Reference 207

LIST OF FIGURES

Fig. 1-1: Schematic of the system on the LNG powered ship. 3

Fig. 2-1: The freshwater generator on board. 10

Fig. 2-2: Schematic of four different kinds of vaporizers [42]. 17

Fig. 2-3: Phase diagram of water in P-T [62]. 22

Fig. 2-4: Phase change mechanism between solid, liquid and vapour. 23

Fig. 2-5: Psychrometric chart for nucleation process [65]. 24

Fig. 3-1: (a) Experiment setup diagram. (b) Photo of the test rig. 45

Fig. 3-2: Contact angle measurement shortcut. (a) static CA (b) advancing CA (c) receding CA 48

Fig. 3-3: Schematic of the experiment process. 50

Fig. 3-4: Illustration of the image processing. 58

Fig. 4-1: The comparison of theoretical critical supersaturation pressure for condensation and desublimation on each tube (a) bare tube, (b) FEP tube, (c) Fluorine based tube and (d) PTFE tube. 63

Fig. 4-2: Comparison of water vapour partial pressure and critical supersaturation pressure with the coolant temperature at 6 ºC in Case 4 (a) Bare tube, (b) FEP tube, (c) Fluorine based tube and (d) PTFE tube. 65

Fig. 4-3: Morphology photos of condensation on the bare tube with a coolant temperature of 6ºC. 66

Fig. 4-4: Comparison of water vapour partial pressure and critical supersaturation pressure with a coolant temperature of -8ºC in Case 3 (a) Bare tube, (b) FEP tube, (c) Fluorine based tube and (d) PTFE tube. 67

Fig. 4-5: Morphology photos of condensation frosting process on FEP tube with a coolant temperature of -8 ºC. 69
Fig. 4-6: Comparison of water vapour partial pressure and critical supersaturation pressure with a coolant temperature of -22 ºC in Case 2 (a) Bare tube, (b) FEP tube, (c) Fluorine based tube and (d) PTFE tube. 70
Fig. 4-7: Morphology photos of condensation frosting on Fluorine based tube with a coolant temperature of -22ºC. 71
Fig. 4-8: Comparison of water vapour partial pressure and critical supersaturation pressure with a coolant temperature of -36ºC in Case 1 (a) Bare tube, (b) FEP tube, (c) Fluorine based tube and (d) PTFE tube. 72
Fig. 4-9: Process of frost formation on the sample section with a coolant temperature of -36ºC. 74
Fig. 4-10: Comparison of theoretical critical supersaturation pressure on the ice surface. 75
Fig. 4-11: Variation of mass growth rate and thickness of frost on the bare tube with the moist air temperature. 78
Fig. 4-12: Experimental data of heat transfer comparison with different air temperatures. 78
Fig. 4-13: Experimental data of production with different coolant temperature on bare tube. 80
Fig. 4-14: Experimental data of total heat transfer performance in different cases on the bare tube. 81
Fig. 4-15: Experimental data of water accumulation and wall temperature with different sample tube. 83

Fig. 4-16: Experimental data of heat transfer performance comparison. 84
Fig. 4-17: Averaged condensation heat transfer coefficient on different tubes. 84
Fig. 4-18: Experimental data of production and heat transfer performance with a coolant temperature of -22ºC. 88
Fig. 4-19: Frost covered area percentage of the surface with a coolant temperature of -22ºC. 88
Fig. 4-20: The temperature profile with time on four surfaces with a coolant temperature of -22ºC. 89
Fig. 4-21: Experimental data of frost accumulation comparison with different coatings with a coolant temperature of -36ºC. 91
Fig. 4-22: Experimental data of frost thickness comparison with different coatings with a coolant temperature of -36ºC. 92
Fig. 4-23: Experimental data of frost density comparison with different coatings with a coolant temperature of -36ºC. 93
Fig. 4-24: Experimental data of heat transfer rate comparison on different coatings with a coolant temperature of -36ºC. 94
Fig. 4-25: Schematic of the frost column growth. 95
Fig. 4-26: Fitting of experimental data with the porosity and coefficient C. 98
Fig. 4-27: Comparison analysis on frost porosity and density between the experimental and the correlation. 100
Fig. 4-28: Experimental data of transition point of the sample tubes with a coolant temperature of -8ºC. 102
Fig. 4-29: Experimental data of production on four tubes with a coolant temperature of -8ºC. 103

Fig. 5-1: Schematic diagram of the FWG system. 107
Fig. 5-2: Flow chart of the modelling in the evaporator. 117
Fig. 5-3: Flow chart of the condenser model. 118
Fig. 5-4: Heat and mass transfer during frosting. 122
Fig. 5-5: Thermal resistance schematic of the vaporiser. 124
Fig. 5-6: Flowchart of calculation program for the frost formation. 126
Fig. 5-7: The evaporator diagram in Rahman, et al. [148]. 127
Fig. 5-8: Comparison between the measured and predicted in the evaporator model. 128
Fig. 5-9: Schematic of the test facility. [149] 130
Fig. 5-10 Comparison between the measured and predicted in the condenser model. 131
Fig. 5-11 Schematic of the polymer compact heat exchanger [150]. 132
Fig. 5-12 Comparison between the measured and predicted in the condenser model. 134
Fig. 5-13: Comparison between the measured and predicted for condensation cases. 135
Fig. 5-14: Validation result by the Nusselt theory of frosting conditions. 135
Fig. 5-15: Schematic of the experimental apparatus [152]. 136
Fig. 5-16: Variation of water vapour mass with different feed-in seawater temperature. 140
Fig. 5-17: Variation of freshwater mass with the heating input. 141
Fig. 5-18: Details of the proposed condenser. 142
Fig. 5-19: Variation of condensation performance with different material. 145

Fig. 5-20: Variation of performance with the number of channels. 146
Fig. 5-21: Variation of condensation performance with convective exchange area of the plate..... 147
Fig. 5-22: Variation of frost properties with different material. 149
Fig. 5-23: Variation of frost properties with the thickness of the material. 150
Fig. 5-24: Variation of frost properties with convective exchange area of the channel. 151
Fig. 5-25: Variation of frost behaviours with convective exchange area of the plate. 152
Fig. 5-26: Variation of condensate with coolant temperature and flow rate. 154
Fig. 5-27: Variation of condensate with moist air temperature and pressure. 156
Fig. 5-28: Variation of condensate with moist air relative humidity. 156
Fig. 5-29: Variation of condensate with a moist air flow rate. 157
Fig. 5-30: Frost thickness and frost accumulation with different air temperature. 160
Fig. 5-31: Effect of air temperature on porosity, frost density and thermal conductivity. 161
Fig. 5-32: Frost surface temperature with time. 161
Fig. 5-33: Frost deposition performance with different velocity of air. 163
Fig. 5-34: Frost thickness and frost accumulation with different coolant temperature. 164
Fig. 5-35: Effect of coolant temperature on porosity, frost density and thermal conductivity..... 165
Fig. 5-36: Frost surface temperature comparison with coolant temperature. 165
Fig. 6-1: Diagram of NG consumption in 48 hours. 168

Fig. 6-2: Schematic diagram of the LNG cold energy recovery system on the case-study ship. 171
Fig. 6-3: LNG cold energy recovery process. 172
Fig. 6-4: Flow chart of genetic algorithm. 179
Fig. 6-5: Flow chart of the multi objective optimisation by the Pareto method. 180
Fig. 6-6: Optimisation performance for single objective with the LNG flow rate of 350kg/h. 184
Fig. 6-7: Optimisation performance for single objective with the LNG flow rate of 2100kg/h..... 185
Fig. 6-8: Optimisation performance for single objective with the LNG flow rate of 3161kg/h..... 185
Fig. 6-9: Exergy efficiency for each optimisation. 188
Fig. 6-10: The multi objective optimisation results in Pareto frontier with the LNG flow rate of 350kg/h. 190
Fig. 6-11: The multi objective optimisation results in Pareto frontier with the LNG flow rate of 2100kg/h 191
Fig. 6-12: The multi objective optimisation results in Pareto frontier with the LNG flow rate of 3161kg/h. 191
Fig. 6-13: The production rate and cost comparison. 194
Fig. 6-14: Optimal performance of FWG system with PTFE coating. 197

LIST OF TABLES

Table 2-1 Detailed information about the desalination technologies. [11] 8

Table 2-2 Summary of the SCD related desalination technologies. 11

Table 2-3 The performance of the FWG from Alfa Laval and Wartsila. 12

Table 2-4 The details of four kinds of vaporizers [40-47]. 16

Table 2-5 Summary of previous desalination utilizing LNG cryogenic energy. 20

Table 2-6 Fabrication methods of hydrophobic and superhydrophobic surfaces.....26

Table 2-7 Influences on frost properties. 31

Table 2-8 Frost density correlations. 37

Table 3-1 Camera specification details. 44

Table 3-2 Instrumentation and propagated uncertainties of the experiment.....46

Table 3-3 Uncertainties of the parameters. 46

Table 3-4 Experiment operation conditions. 49

Table 3-5 Equations for interfacial energy calculations in phase change [122]. 52

Table 4-1 Properties of the text section surface material. 62

Table 4-2 Summarise table of the performance for each case. 76

Table 4-3 C-values fitted to the experimental data in Case 1. 96

Table 4-4 Comparison of the frost properties change trend with the CA. 101

Table 5-1 Nusselt number for fully developed laminar flow in the tubes [67]. 114

Table 5-2 Input parameters of the evaporator chamber for validation [148]. 128

Table 5-3 Input operation parameters of the condenser for validation. [149] 130

Table 5-4 Properties of PVDF.[151]. 132

Table 5-5 The condenser input parameters for validation.[150] 133

Table 5-6 Operation and geometry parameters of the experiment for validation. 137
Table 5-7 Operational parameters of the evaporator. 138
Table 5-8 Operational parameters of the moist air and coolant in the condenser 143
Table 5-9 Geometry parameters of the condenser. 143
Table 5-10 Properties of heat exchanger materials at 20ºC. 144
Table 5-11 Geometry parameters of the condenser 148
Table 5-12 Operational parameters of the condenser in condensation. 153
Table 5-13 Parametric study cases on frosting. 158
Table 5-14 Summarised effect factors on frost properties. 166
Table 6-1 Detailed information about the case-study ship. 169
Table 6-2 Design parameters in the optimisation. 178
Table 6-3 Effect of the operational parameters and geometry parameters on production. 182
Table 6-4 Geometry design of the condenser in the FWG system. 182
Table 6-5 Performance analysis of single-objective optimisation. 186
Table 6-6 Performance values of different multi-objective optimizations. 190
Table 6-7 Performance values of the optimisation with different coatings. 195
Table 6-8 Optimal design operation and geometry parameters of the proposed FWG in the system. 196
Table 6-9 Capital cost of components in the system. 198

NOMENCLATURE

Roman symbols

A	Contact area, m^2
B_c	Boltzmann constant, 1.38 x 10^{-23} J/K
C	Cost
CRF	Capital recovery factor
c_p	Heat capacity at constant pressure, J/(kg · K)
c_v	Heat capacity at constant volume, J/(kg · K)
D_h	Diameter, m
d	Hydraulic diameter, m
e_x	Specific exergy, kJ/kg
E	Relative error
Ex	Exergy, kW
f	Enhancement factor
F_{TP}	Two-phase flow enhancement factor
F_{NB}	Correction factor for nucleate boiling
g	Gravity, m/s^2
ΔG	Gibbs energy
$\Delta\tilde{g}_v$	Specific Gibbs free energy change per unit volume, J/m^3

He	Molar Helmholtz energy
h	Specific enthalpy, J/kg
I_0	Kinetic constant, $m^{-2}s^{-1}$
I_c	Minimum embryo formation rate, $m^{-2}s^{-1}$
Ja	Jacob number
k	Heat transfer coefficient, $W/(m^2 \cdot K)$
k_m	Mass transfer coefficient, $W/ (m^2 \cdot K)$
Le	Lewis number
l	Length, m
L	Latent heat, kJ/kg
M	Mass of per unit area, kg/m^2
M_i	Compounds molar masses, g/mol
MF	Maintenance factor
m	Mass, kg
$\dot{m}$	Mass flow rate, kg/s
Nu	Nusselt number
n	Number of pixels
Pr	Prandtl number
p	Pressure, Pa
PP	Payback period

Q	Heat transfer capacity, kJ
q	Heat transfer rate, W
R_v	Universal gas constant, 8.314 J/K/mol
R	Perfect gas constant, J/ (kg · K)
Ra	Rayleigh number
Re	Reynold number
RH	Relative humidity
rr	Relative roughness
T	Temperature, K
s	entropy, kJ/(kg · K)
t	Time, s
U	Internal energy, kJ
u	Internal energy per unit of mass, kJ/kg
v	Specific volume, m^3/kg
V	Volume, m^3
v_m	Molar volume
W_e	Electricity power
x_i	Compounds molar fractions
x	Vapour fraction

Subscripts

0	Environment temperature
aw	Water vapour in the moist air
b	Brine
c	Critical
cc	Capital cost
ch	Channel
co	Coolant
$coat$	Coating
$cond$	Condensation
cv	Convective boiling
d	Exergy destruction
da	Dry air
e	Experimental
em	Embryo
ex	Exergy
f	Frost layer
$final$	Final
fix	fixed cost
fs	Frost layer surface

fw	Fresh water
gz	Potential energy
ice	Ice layer
in	Inlet
ini	Initial
j	Parent phase
k	New phase
l	Liquid
lam	Laminar flow
lat	Latent heat
lo	Local
lw	Liquid water
ma	Moist air
max	Maximum
mc	Maintenance cost
n	Nucleation
NB	Nucleate boiling
$NB0$	Constant parameter that depends on the fluid used
NE	Net earning
o	Outlet

oc	Operation cost
s	Simulation
s	Seawater
sat	Saturation condition
sen	Sensible heat
$surf$	Surface
t	Theoretical
$trans$	Transition flow
$total$	Total
$turb$	Turbulent flow
use	Useful
v	Vapour
w	Wall
wv	Water vapour

Greek symbols

ζ	Friction coefficient
δ	Thickness, m
φ	Diffusion coefficient
ω	Absolute humidity, $kg/kg_{dry\ air}$
σ	Interfacial energy, J/m^2

χ	Frost porosity
ρ	Density, kg/m^3
μ	Dynamic viscosity, kg/(m · s)
λ	Thermal conductivity, W/(m · K)
η	Efficiency

Abbreviations

AAV	Ambient air vaporizer
AWG	Atmospheric Water Generator
CA	Contact angle
CO	Carbon monoxide
CO_2	Carbon dioxide
DCMD	Direct-contact membrane distillation
DI	Deionized
FD	Freeze Desalination
FEP	Fluorinated Ethylene Propylene
FWG	Freshwater generator
GOR	Gain output ratio
HEX	Heat exchanger
HDH	Humidification-Dehumidification
ICFD	Indirect-contact freeze desalination

IFV	Intermediate fluid vaporizer
IMO	International Maritime Organization
LNG	Liquefied natural gas
MED	Multi-effect Distillation
MSF	Multi-stage Flash Distillation
MTPA	Metric Tonnes Per Annum
MVC	Mechanical Vapour Compression
NG	Natural gas
NO_x	Nitrogen oxides
ORV	Open rack vaporizer
PM	Particulate matter
PR	Performance ratio
PTFE	Polytetrafluoroethylene
RO	Reverse Osmosis
RR	Recovery Rate
SCD	Single-stage Conventional Distillation
SCV	Submerged combustion vaporizer
SD	Solar Distillation
SO_2	Sulphur dioxide
TVC	Thermal Vapour Compression

LIST OF PUBLICATIONS

I. Journal Papers

1. Liu, M., Wu, D., Tsolakis, A. and Gao, W., 2021. A waste cryogenic energy assisted freshwater generator for marine applications. Desalination, 500, p.114898.
2. Liu, M., Singh N., Wu, D., Gao, N., Tsolakis, A. and Gao, W., 2021. An experimental study of frost on hydrophobic surface on chilled temperature surface. (submitted)

II. Conference Papers

1. Liu, M. and Wu, D., 2020, January. Evaluation of LNG cryogenic energy utilization in seawater desalination on LNG fuelled ships. In RINA, Royal Institution of Naval Architects-International Conference on LNG/LPG and Alternative Fuel Ships 2020 (pp. 43-48). Royal Institution of Naval Architects.
2. Liu, M. and Wu, D., 2019. A new fresh water generation system under high vacuum degrees intensified by LNG cryogenic energy. Energy Procedia, 158, pp.726-732.

CHAPTER 1 INTRODUCTION

1.1 Background

1.1.1 Freshwater generator

Although 70% of the earth is covered by water, the vast majority contains saline which is not suitable for direct human direct consumption. [1] As industry demands grow and domestic use increases, the issue of water scarcity has become severe. Desalination technologies, removing the salts and minerals from seawater, provide a solution for producing fresh water in water scarcity regions. Considering the economic and technical factors, a freshwater generator (FWG) is the preferred choice to meet freshwater requirements on most deep-sea vessels, rather than storing fresh water in big tanks.

To address climate change, there is a need to reduce emissions from the use of conventional fuels. The utilization of marine fossil fuel results in increased emissions of SO_X and NO_X, which is responsible for acid rain [2]. Due to the SOx regulations released by international maritime organization in January 2020, liquefied natural gas (LNG) has been introduced as an alternative to heavy oil as a marine fuel, and most of the vessels in service operating around the world are expected to accelerate the shift from heavy fuel oil to LNG or other alternative fuels. Hence, the investigations of the LNG cryogenic energy recovery applications have been accelerated in the last decades driven by the developments of LNG.

Single-stage conventional distillation (SCD) has been used to produce potable water on board, however currently SCD technology suffers from lower water recovery rate with intensive thermal energy. Due to the on-going imbalance between energy supply and demand on board, developing the recovery technology could assist in providing solutions and enhancing the feasibilities of the FWG systems. As a result, the SCD system could recover the waste heat from the exhaust gas to provide heating resource for evaporation. For the condensation process in SCD system, the commonly used coolant for condensation is seawater. On LNG powered ships, about 830 kJ/kg cryogenic energy will be released LNG during the regasification process, which has been unexploited until today. No work has been reported to use this cryogenic energy for cooling effect production with no harmful environment impact.

Significant research has been carried out on the surface treatment to enhance the condensation performance which increases the applications in many industries that have several demands like food chain, power generation and seawater desalination [3]. However, limited work has been investigated to examine the effect of the surface characteristics on the condensation and system performance under chilled and cryogenic conditions, such as the operation temperature of LNG. Consequently, an in-depth investigation is needed to test the improvement of the condensation and system performance, and the adaptability of the system under cryogenic temperature conditions by using hydrophobic surfaces.

Computation modelling, such as Siemens Simcenter Amesim, has become popular in recent years to model and analyse the engineering systems. It is a commercial integrated system simulation platform to allow the simulation engineers to assess and

optimise the system performance. Thus, the simulation could provide detailed surface information about the thermodynamics and fluid mechanisms in the condensation process of the system. Therefore, the numerical study on the system performance prediction is developed by Siemens Simcenter Amesim. Furthermore, the integration of the FWG system and the LNG cryogenic energy recovery system on the LNG powered shown in Fig. 1-1 is developed to predict the freshwater recovery performance in Siemens Simcenter Amesim and optimised using genetic algorithm.

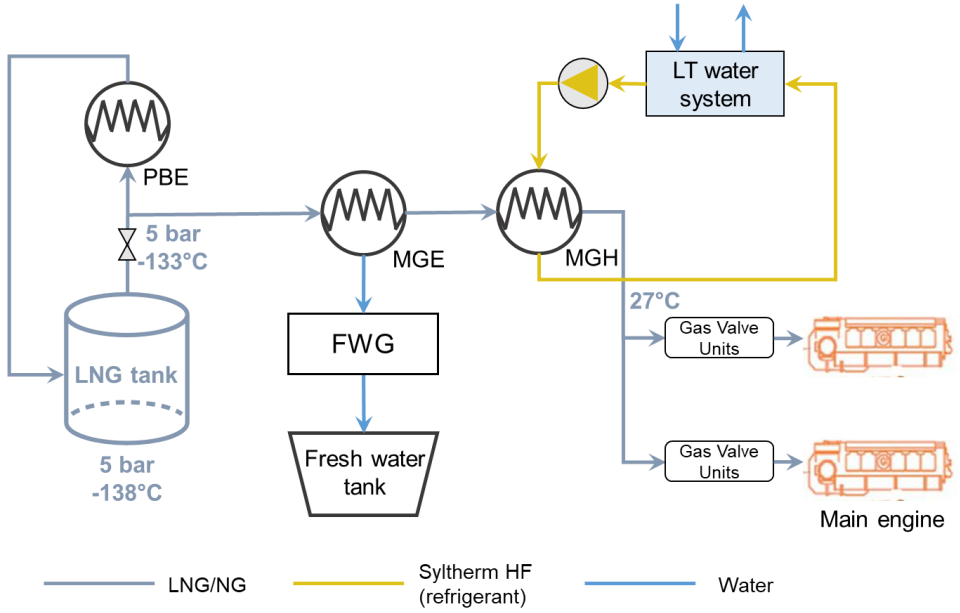


Fig. 1-1: Schematic of the system on the LNG powered ship.

1.2 Research objectives

The purpose of this research is to investigate the potential of FWGs utilising recovered LNG cryogenic energy on LNG-powered ships by experimental and numerical study. The current study could be used as a guideline for the design of heat exchangers operating under frost and condensation conditions. The following specific objectives were pursued:

(1) To investigate the state-of-art LNG cryogenic energy recovery applications, condensation improvements and the surface treatment methods to enable anti-freezing, as shown in the literature review.

(2) To create, build and optimise a test facility to investigate the effects of surface treatments on the condensation and frosting phenomena and evaluate the system's efficiency potential of a cryogenic energy assisted freshwater generator.

(3) To introduce and validate numerical models in Siemens Simcenter Amesim software to predict the effects of the operation parameters and geometry parameters on thermodynamic performances of the evaporation and condensation processes in the freshwater generator system.

(4) To assess the performance of the freshwater generator on an LNG-powered case-study ship using real-life operational data and examine the economic viability of the proposed technology.

1.3 Thesis layout

This thesis will be focused on the optimal design of applying LNG cryogenic energy to an FWG on LNG-powered ships, to obtain high water generation. The chapters of two to seven are organised as follows:

Chapter 2: Literature review

This chapter introduces a comprehensive literature review of condensation improvement methods. The use of LNG cryogenic energy and surface modification is investigated. A thorough study on the background of LNG cryogenic energy and its applicability to desalination is specified. Then the effect of the surface characteristic on

condensation efficiency is discussed. Due to the low operation temperature of LNG, an extensive investigation on the frost deposition phenomenon and thermodynamic performance is explored. Finally, the solutions that alleviate the surface frosting are introduced.

Chapter 3: Experimental Methodology

Chapter three presents the methodology of the experimental study to see how the operation conditions affect the condensation and frosting phenomenon on the cold surface. The experimental test rig is explained with test rig descriptions, measuring devices, materials, measuring methods and calculations.

Chapter 4: Experimental analysis

This chapter primarily analyses the experimental results of the effect of the surface treatment on condensation and frosting. The effect of the air property, surface temperature and surface characteristics are analysed in different mechanism cases.

Chapter 5: Numerical study

The feasibility of recovering LNG cryogenic energy for FWGs is investigated in this chapter. Validated mathematical models of the evaporation and condensation are conducted by Siemens Simcenter Amesim software. The parametric analysis of evaporation and condensation to evaluate the performance of system production and efficiency is carried out.

Chapter 6: Case study

According to the results from the previous chapters, a case study for the freshwater generator and LNG cryogenic energy system is proposed to be employed on an LNG-powered ship. The water production, exergy analysis and economic analysis of the system are analysed and optimised with various LNG flow rates.

Chapter 7: Conclusions

This chapter concludes the major results of the research and makes recommendations for future work.

.

CHAPTER 2 LITERATURE REVIEW

This chapter presents a comprehensive literature review and focuses on four areas: (a) Available LNG cryogenic energy recovery techniques and applications, (b) Condensation fundamental introduction and enhancement methods, and (c) Frosting phenomenon on the chilled and cryogenic temperature surface and (d) Anti-frosting technologies. Certain content is published in the paper: 'A waste cryogenic energy assisted freshwater generator for marine applications' by Liu, et al. [4].

2.1 Fresh water generation

Driven by climate change, population growth, economic development, and expansion of irrigated agriculture, the shortage of freshwater supplies has threatened the sustainable development of human societies [5]. And among the 3% of the freshwater reserve in the natural water reserve, the largest porportion is frozen in ice caps and glaciers (68.7%) [6]. As reported by World Health Organization in 2021, 771 million people lack access to safe water [7]. Desalination facilities could help to reduce the gap between the supply and demand for fresh water.

2.1.1 Desalination techniques

Desalination is defined as a dissolved solids removal process from seawater to obatin fresh water [8]. The techniques can generally be divided into two categories: thermal distillation and membrane. Thermal distillation includes: single-stage conventional distillation (SCD), multi-stage flash distillation (MSF), multi-effect distillation (MED), mechanical vapour compression, thermal vapour compression and solar distillation.

The membrane type includes: reverse osmosis (RO), electrodialysis, and membrane distillation [9]. Apart from these, atmospheric water generation, freeze desalination (FD) and humidification-dehumidification (HDH) are also emerging technologies on a small scale.

2.1.2 Freshwater generator on board

Among the technologies mentioned above, such types of systems are prevalent to be used as FWG: SCD, MSF, MED and RO [10]. Detailed performances of these desalination technologies are shown in Table 2-1.

Table 2-1 Detailed information about the desalination technologies. [11]

Techniques	SCD [12]	MSF	MED	RO
GOR (kg/kg) *	0-1	8-12	10-16	N/A
PR (kg/MJ) **	0.9	3.5-5.25	4.35-6.9	N/A
Thermal energy consumption (MJ/m^3)	214.25	190-282	146-229	N/A
Electricity consumption of pumps and others (kWh/m^3)	-	2.5-5.0	2.0-2.5	3.5-6.0
Water recovery rate	<10%	10%-15%	20%-35%	<55%
Total Dissolved Solids (ppm)	<10	<10	<10	200-500
Water costs ($\$/m^3$)	20 [13]	0.6-1.8	0.5-8.0	0.3-13.0

*GOR (kg/kg): the gain output ratio, the ratio of the mass of distillate (kg) to the mass of the input steam (kg).
**PR (kg/MJ): the performance ratio, the ratio of the mass of distillate (kg) and input heat.

Although RO is used in more than 60% of installed desalination plants around the world, it is easily affected by the quality of the seawater feed; by inherent problems from the relatively high level of total dissolved solids in the produced fresh water; by high energy/chemical consumption; and high operational and maintenance costs. [14] Due to its simple design, lower maintenance costs, improved freshwater quality, potential for waste energy recovery, and small size, SCD is seen to be the ideal option for FWG maritime applications when compared to other complex systems like MSF and MED. [9]

2.1.3 Single-stage conventional distillation

As shown in Fig. 2-1, SCD consists of an evaporator, a condenser, filters, demister, salinometer, ejector, pumps and other accessories. The seawater pump delivers the seawater from the sea chests on the ships to the FWG. Then part of the seawater is sent to the evaporator as feed water for evaporation while the other part is used for the cooling water in the condenser. The jacket heat or the waste heat of the marine engines is operated as the heat source for boiling and evaporation of the seawater to vaporize into the water vapour in the evaporator. At the same time, the FWG plant is maintained at vacuum conditions to make sure the boiling temperature below 100 °C by the vacuum pump. The residual seawater from the evaporation process is drained and ejected as brine. The water vapour passes through the demister to clear the mist, then the vapour enters the condenser to be condensed by the input seawater for fresh water. The distilled water will be taken out by a freshwater pump and then controlled by a salinometer to supervise the salinity level.

Table 2-2 presents the related SCD technologies in recent studies. And several manufacturers, such as Alfa Laval and Wartsila, have directed their attention on how to promote the FWG for marine applications. Detailed information about these models is illustrated in Table 2-3. SCD has a low freshwater recovery rate, of less than 10%. Furthermore, SCD is also hindered by a high input energy consumption, which attracts researchers' interests to focus on energy consumption reduction and freshwater recovery rate promotion. [5]

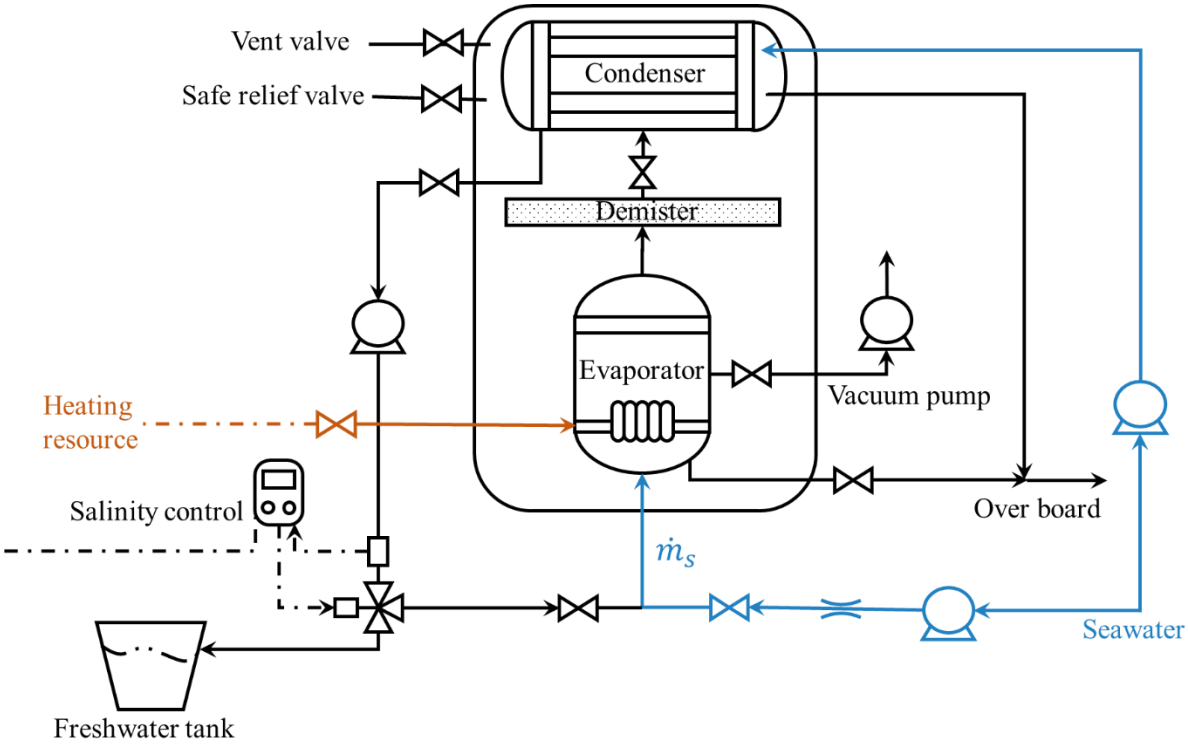


Fig. 2-1: The freshwater generator on board.

Table 2-2 Summary of the SCD related desalination technologies.

Method	Ref.	Description	Maximum freshwater production	RR	GOR
SCD	Kumar, et al. [15]	Possibility of ocean thermal gradient utilisation in SCD, using surface seawater as the feed and deep seawater as the coolant	5 kg/h	-	-
SCD	Chen, et al. [16]	The spray evaporation method is intensified by a 7.6 m^2 solar collector.	30 L/day	0.5%	0.80
SCD-Solar distillation	Mahkamov, et al. [17]	A solar distillation system with a solar collector with an area of 2.250 m^2.	1.6 kg/h	-	-
SCD-FWG	Yuksel, et al. [10]	The freshwater recovery rate of an FWG system was increased by 5.06% through an optimization study utilising the Taguchi method.	1069 kg/h	1.82%	-
	Morsy and Othman [13]	The waste heat recovered from scavenging air provided heat for the evaporator in an FWG is proposed to supply 8 t/day freshwater.	8 t/day	7.78%	-

Table 2-3 The performance of the FWG from Alfa Laval and Wartsila.

Manufacture	Alfa Laval			Wartsila
Model	AQUA series [18]	Dolphin series [19]	Multi-effect plate distiller [20]	Single-stage desalination [21]
Production (m^3/day)	5-60	10-75	200-10000	8-35
Production salinity (ppm)	<2	<2	<6	<2
Thermal power (kWh/t)	-	-	-	740
GOR	1-1.5	1-3	3-6	-

2.1.4 Improvements on SCD

According to the above system introduction, the main process of the SCD (evaporation and condensation) is based on the principle of heat transfer in thermodynamics, so the improvement of SCD is also based on the improvement of heat transfer efficiency. The improvements mainly focused on the following aspects: (1) utilization of the free energy; (2) Evaporation efficiency; (3) Condensation efficiency.

Freshwater generation is an energy intensive process, requiring heat and cold source. It is sustainable if the energy consumption is free and available in abundance, such as solar energy [22], ocean thermal energy [15] and waste heat [23]. Great efforts have been spent towards the development of the evaporation process in driving the SCD process, among the promising techniques is the utilization of the flash evaporation. It

occurs when the water is injected to a depressurized chamber at a pressure lower than the saturation pressure that corresponds to the water temperature [24]. The researchers found that the superheated liquid in the flash evaporation process absorbs the latent heat of the water for vapour generation more efficiently and obtains the higher evaporation rate [25]. Vacuum flash evaporation process is mostly applied to the FWG system due to its enhancement on separation rate [26]. Based on the experimental investigations from Gao's research team [26-29], the enhancement methods on the evaporation process are explored in-depth, including the improvements on vacuum degrees, the heating flux and heat source temperature. Therefore, the current study focuses on the condensation process.

Condensation efficiency is equally important to affect energy consumption and freshwater production rate in the SCD system. Multiple methods on condensation efficiency enhancement have been implemented to improve the system performance. Kumar, et al. [15] has indicated that the condensation efficiency and the freshwater production increase with the decrease of the coolant temperature, due to the reduction in heat removal rate from the condenser. Hence, several research focused on economic, environmental-friendly and abundant low temperature cooling sources, such as liquid hydrogen, LNG cryogenic energy. Apart from the operation conditions, the surface characteristics of the heat exchanger has a significant impact on the condensation performance. Generally, the dropwise condensation offers 5-7 times higher heat transfer coefficients than the filmwise condensation [30]. And this dropwise condensation could be achieved by creating the surface with hydrophobic characteristic.

2.2 LNG cryogenic energy

Cryogenics is the science of production and application of artificial cold, that the working substances in the cryogenic industry (including helium, hydrogen, nitrogen, air and natural gas) operate at very low temperatures below 120 K [31]. Due to the high energy density, the applications of the recovered cryogenic energy have inspired researchers to investigate, which can be categorized into three: (1) process cooling; (2) gas mixture separation and distillation; and (3) liquefaction for transportation and storage [32].

This section introduces the potential cryogenic energy on the LNG powered ships during the regasification process and the developments of recovered LNG cryogenic energy for various desalination technologies.

2.2.1 Liquefied natural gas

Natural gas (NG) is considered as the best substitute for coal and oil to generate electricity and has been used as a transportation fuel in recent years because of its lower emissions of CO_2 compared with other fossil fuels [33]. Instead of transporting NG via the costly and risky long-distance pipelines, the liquid phase is preferred, transporting it by cooling it to -162ºC and reducing its volume by a factor of 600 with non-toxic, non-corrosive and easily stored under atmospheric conditions as a cryogenic liquid [34].

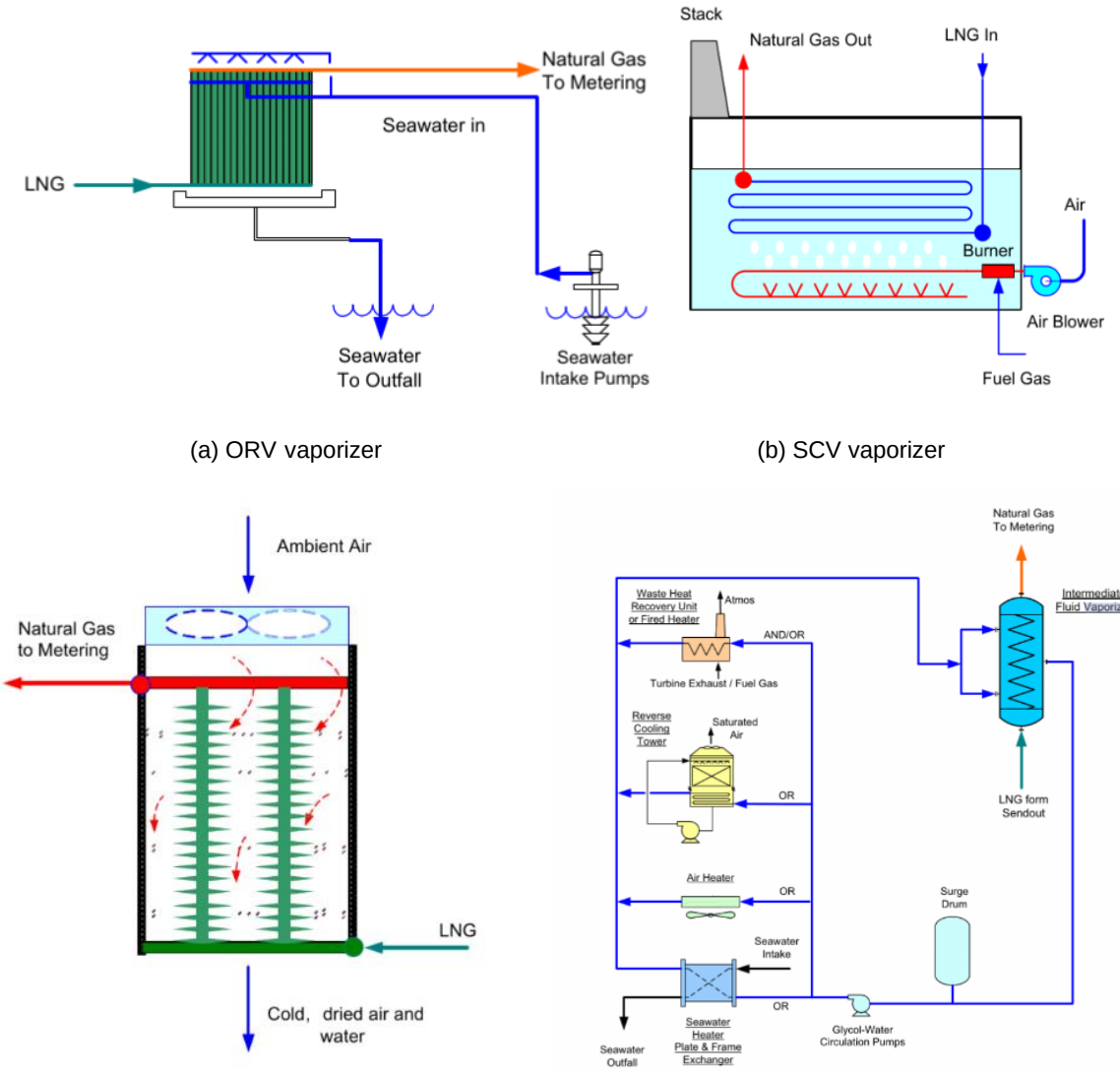
Although COVID-19 has had related impacts on the supply-and-demand side, the total volumes of global LNG trade increased to 372.3 million tonnes in 2021. [35] The increased LNG trade volumes have stimulated the demand for LNG transportation.

The LNG carriers, as the main transportation method to transport LNG between terminals in the current market have reported that there were 641 LNG active tankers available for work until the end of April 2022, a 9.9% advance compared to 2021. [35] As reported by DNV GL, the numer of LNG-ready fuelled ships is expected to increase in 2022, reaching 156, with 251 operating and 266 being on order. [36]

In the LNG regasification stage, LNG absorbs heat and then converts to gas phase in an LNG vaporizer, including Open rack vaporizer (ORV), Submerged combustion vaporizer (SCV), Intermediate fluid vaporizer (IFV) and Ambient air vaporizer (AAV) [37-39]. The vaporizer selection is based on many parameters such as site conditions and energy efficiency. Among these vaporizers, the most common use type is ORV which covers 70% market. The characteristics and the schematics of four types are shown in Table 2-4 and Fig. 2-2.

Table 2-4 The details of four kinds of vaporizers [40-47].

Method	ORV	SCV	IFV	AAV
Heat source	Seawater	NG or BOG	Air heater; reverse cooling tower; seawater heater; waste heat recovery system or fired heater	Ambient air
Shape	Panel shaped tubes	Submerged in a water bath	Shell and tube exchanger	Vertical heat exchanger
Advantage	Low operation costs	Reliable; safety; less stall area; quick launch;	Better adaptability; better energy efficiency; better robustness; no icing	Low costs; energy saving
Disadvantage	Requires clean and high seawater temperature; thermal pollution for sea; ice formation	The emissions of NO_x and CO_2; high running cost	More complex; rely on seawater nearby; require high quality seawater	Low heat transfer coefficient; easily influenced by conditions; ice generation
Major application	Along with terminals	Coupled with ORV or IFV during cold seasons	-	In hot climate equatorial regions
Plot plan	Medium size	Medium-large size	Small size	Large size



(a) ORV vaporizer (b) SCV vaporizer

(c) AAV vaporizer (d) IFV vaporizer

Fig. 2-2: Schematic of four different kinds of vaporizers [42].

2.2.2 LNG cryogenic energy recovery for desalination

Usually, the cryogenic energy around 830 kJ/kg could be recovered from the LNG regasification process for other applications such as separation process, seawater desalination, cold storage systems, waste incinerator, cryogenic CO_2 capture, power generation and so on rather than wasting [38].

Seawater desalination is a potential application for large amount of LNG cold energy reutilization in these years. Its cryogenic energy was widely investigated in several desaliantion techniques such as FD. Research on FD starts from 1977, when Cravalho, et al. [48] proposed a net-zero work system recovering cryogenic energy for desalination. The theoretical maximum freshwater output was 6.75 kg water/kg regasified LNG.

A combined freeze desalination-membrane distillation desalination process utilizing LNG cold energy was proposed by Wang and Chung [49]. The feed seawater was firstly treated by indirect-contact freeze desalination (ICFD) and then the leftover brine was transferred to the direct-contact membrane distillation (DCMD). During this process, the required coolant temperature for crystallizer to pre-cooled solution in the first stage FD and the distillate cooler of the second stage membrane distillation was achieved by LNG cold energy. Concluding from the experimental result, the system has recovered 71.5% drinkable water. And large amount of LNG cold energy has been effectively used to reduce energy consumption. Cao, et al. [50] designed an indirect freeze desalination plant with LNG to lower the temperature of the employed refrigerant R410A. The numerical result shows that 1 kg equivalent LNG cryogenic energy produced 2 kg of ice. Lin, et al. [51] designed a freeze seawater desalination process prototype, with liquid nitrogen as the cold source and R410A as the secondary refrigerant to transfer LNG cold energy to seawater. The study experimented the refrigerant temperature, seawater flowrates and number of spraying nozzles influencing to the system and the prototype performance. The study demonstrated that LNG could help the FD process, however with a 50% salt removal rate. In hybrid desalination systems, FD is also combined with other technologies, such as the hybrid

indirect-contact freeze desalination-direct contact membrane distillation process [49] and RO-freeze process [52]. Xia, et al. [53] has simulated a RO desalination system with trans critical CO_2 Rankine cycle powered by solar energy by using the LNG cold energy. In this system, LNG releases cold energy to condense exhaust CO_2 to liquid form and transfer to NG which works for NG turbine and produces work for RO combined with CO_2 turbine by absorbing heat from CO_2. The commercial and technologies advantages developed the utilization of FD in industry. Researchers have suggested that FD utilizing LNG cryogenic energy is an applicable way to solve the drought problem in Sicily. [54].

Another desalination method, hydrate-based desalination, might potentially use LNG cryogenic energy recovery. The generation of hydrates and crystal separation in this process both need cold energy. According to He, et al. [55], clathrate hydrate-based desalination processes that use LNG cryogenic energy provide greater water recovery rates while using less energy than conventional FD processes. The economic assessment report's decreased water cost with LNG use suggests that the hydrate-based procedure is a feasible way to boost the supply of freshwater in LNG regasification infrastructures [56]. Babu, et al. [57] suggested using the technology for business purposes and the system could achieve the highest salt rejection rate of 87.5%. A table of the previous desalination processes that utilize LNG cryogenic energy is summarized in Table 2-5.

Table 2-5 Summary of previous desalination utilizing LNG cryogenic energy.

Ref.	Method	Description	Fresh water production	Exergy efficiency	RR
Cravalho, et al. [48]	FD	A net-zero work theoretic system utilizing cryogenic energy generated by a heat engine and a heat pump	6.7kg/1kg LNG	-	-
Antonelli-Consultant [58]	FD	A desalting plant based on Secondary refrigerant freezing process	3.2kg/1kg LNG	-	-
Wang and Chung [49]	ICFD-DCMD	A hybrid desalination system integrated ICFD and DCMD intensified by LNG with the feed water of 8 kg, 3.5 wt%.	5.72 kg	-	71.5%
Xia, et al. [53]	RO	A RO desalination system with trans critical CO^2 Rankine cycle powered by solar energy by using the LNG cold energy	2537.33m^3/day	4.90%/day	-
Cao, et al. [50]	FD	An LNG-powered indirect freeze desalination facility to reduce the operating temperature of the refrigerant R410A	2kg/1kg LNG	-	-
Chang, et al. [59]	FD	An indirect contact FD that uses R23 as LNG and ethylene glycol as a coolant to reduce the temperature of the ethylene glycol.	0.52-0.55 kg/h	-	26%

Lin, et al. [51]	FD	An indirect-contact FD method technique using LNG as the cryogenic fluid and R410A as the intermediate fluid	190.9 kg/h	-	42.2%
He, et al. [55]	Hydrate-based	A design of clathrate hydrate-based desalination process by utilizing LNG cold energy	1.3 m^3/h	-	40%
Babu, et al. [57]	Hydrate-based	An innovative HyDesal process utilizing LNG cold energy	-	-	34.85%

2.3 Condensation enhancement – Surface modification

Several strategies have been adopted for condensation enhancement, such as enhancing the heat convection between the vapour and the surface, using the high thermal conductivity material as the heat exchange surface or changing the surface characteristic. In this section, based on the condensation mechanism, the surface modifications and its effect on the condensation performance are introduced.

2.3.1 Condensation

Compared to evaporation, condensation efficiency is equally important to affect energy consumption and freshwater production rate [60]. Enhance the condensation heat transfer efficiency could improve the overall heat transfer efficiency, economize on the system and optimize the size. A diagram showing three phases of water under different pressure and temperature is presented in Fig. 2-3. According to the phase rule [61],

the number of freedom degrees F for a system at thermodynamic equilibrium is given by following:

$$F=C-P+2 \tag{2-1}$$

where C is the number of components in the system and P is the number of phases in the system. For the pure water, pure water vapour or ice, only one phase is thermodynamically stable on its own in certain range of pressures and temperatures presenting in one-component system, then single-phase regime is decided by F=1-1+2=2. When any two phases in the system coexist, F=1-2+2=1, the pressure is not freely variable at a fixed temperature such as freezing and condensation. When three phases are in equilibrium in the system with F=1-3+2=0. Then the system is invariant which has no degrees of freedom. Only the triple point with temperature of 273.16 K at 611.657 Pa in Fig. 2-3 could achieve the equilibrium state. When sufficient energy is supplied to the system, a phase change occurs from one phase to another. Fig. 2-4 summarized the phase change mechanisms between solid, liquid and vapour.

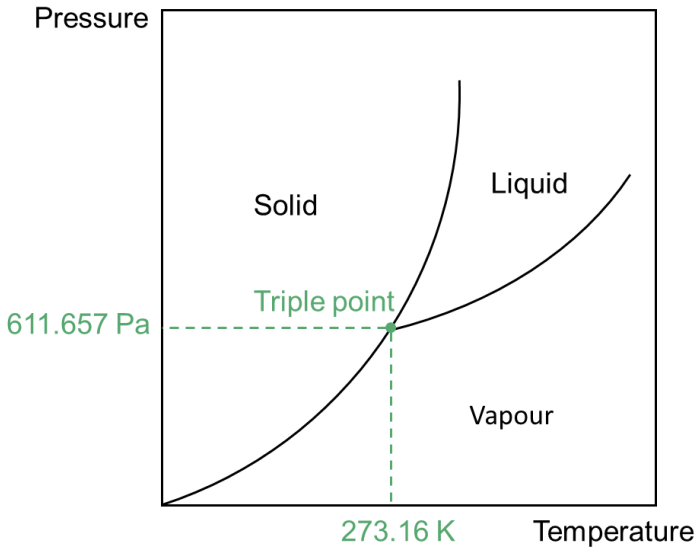


Fig. 2-3: Phase diagram of water in P-T [62].

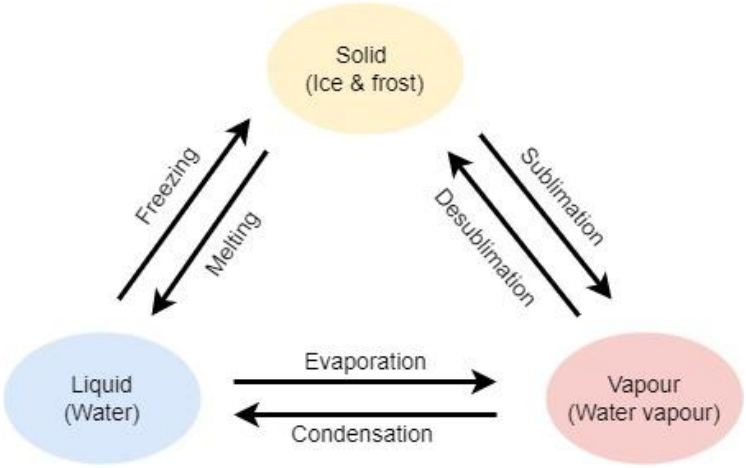


Fig. 2-4: Phase change mechanism between solid, liquid and vapour.

When saturated water vapour contacts with a cold surface, the vapour condenses into liquid phase. Condensation mode requires nucleation which means that thousands of water nucleus form on the substrate. Two types of nucleation modes in nature are applied: heterogenous and homogenous. Homogeneous nucleation rarely occurs only when the vapour under supersaturated condition and without the presence of a foreign phase [63]. Instead, heterogeneous nucleation dominates in any system that impurities and roughness may exist [64]. Therefore, the current study is limited in the case of heterogeneous nucleation. In this mode, a supersaturation degree or subcooling degree is required. The reason is that for the new interface creation between two phases, the energy barrier at the surface requires supersaturation degree as an additional driving force to overcome. From the psychrometric chart for nucleation process in the Fig. 2-5, along the fixed surface temperature, the vapour pressure could increase until the nucleation occurs at a supersaturated pressure $p_{n,w}$. The nucleation process could be expressed by three distinct processes: cool down, supercooling and supersaturation. The water vapour in the humid air is firstly cooled down (A→B), then

cooled beneath the dew point leading to the heat and mass transfer (B→C) and at last proceeds to the supersaturation state to initiate the frost formation (C→D).

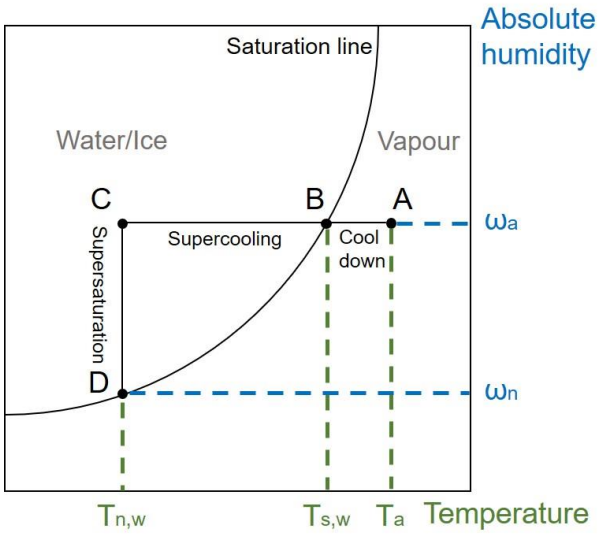


Fig. 2-5: Psychrometric chart for nucleation process [65].

Otherwise, an alternate method is to reduce the surface temperature while maintaining the vapour pressure. Some literatures have proposed new replacements for condenser or seawater to reduce energy consumption and increase the system efficiency comparing to the conventional condensing methods, such as ocean thermal energy. Zhi-jiang Jin et al. [66] introduced the ocean thermal energy to supplement the condenser which refers to the temperature difference between the surface seawater and the deep seawater, and analysed the system exergy. In this process, the surface seawater is utilized for the feed water to evaporation and the lower temperature deep seawater is utilized for condensing. From the experiment and ASPEN simulation results, the entire system exergy efficiency is promoted to 7.81% and the produced freshwater can be up to 100kg/h. Therefore, the utilization of the LNG cryogenic energy provides a potential method for enhancing the condensation efficiency.

The heat transfer performance is also associated with the surface condition. Generally, the condensation occurs in two modes, depending on the characteristic of the surface, film condensation and dropwise condensation [67]. For generally clean and uncontaminated surfaces with high surface energy and high affinity to the water, the entire condensing surface is covered by a liquid film. Conversely, the droplets formed and grow to maintain the dropwise condensation on the substrate coated with the low energy surface. So far, it has been found that the dropwise condensation transfers the heat through the droplets is more than an order of magnitude larger than the film condensation. Therefore, in this study, the wasted LNG cryogenic energy with low temperature could be an alternative to be applied in the system to enhance the condenser heat transfer performance. And modifications on the heat exchange surface to maintain the dropwise condensation is expected to achieve greater heat transfer.

2.3.2 Surface characteristic

Surface characteristics are categorized into four types distinguished by contact angle (CA) range and wetting behaviour: superhydrophilic ($0^{o}<CA<10^{o}$), hydrophilic ($10^{o}<CA<90^{o}$), hydrophobic ($90^{o}<CA<150^{o}$) and superhydrophobic ($150^{o}<CA<180^{o}$) [68]. Superhydrophobic and hydrophobic surfaces have higher water repellence to form dropwise condensation and promote heat transfer. To obtain the hydrophobic characteristic, the surface could be implemented by the methods as the following [69]:

(1) Coating a surface with a water-repellent material, including coating of fin press oil, automobile wax and fluorinated materials.
(2) Etching, such as laser ablation and micro-machining.
(3) Hybrid method, the combination of both above.

Table 2-6 below lists some fabrication methods and their performances on wettability.

Table 2-6 Fabrication methods of hydrophobic and superhydrophobic surfaces.

Type	Reference	Method	Substrate material	Coating material	CA
Super-hydrophobic	Tadanaga, et al. [70]	Sol-gel	Glass	Alumina	165°
	Artus, et al. [71]	Chemical vapor deposition	Aluminium	Silicone (polysiloxane) nanofilaments	168°
	Qu, et al. [72]	Etching + Fluorination	Steel	Nitric acid and hydrogen peroxide as etchant	161°
	Fresnais, et al. [73]	Plasma Treatment	Low density polyethylene	CF_4	170°
Hydrophobic	Hoque, et al. [74]	Fluoride coating	Copper	1H,1H,2H,2H-perfluorodecyltrichlorosilane	125°
	Luo, et al. [75]	Laser ablation	Steel	Amorphous carbon	130°
	Na and Webb [76]	Chemical coating	Aluminium	Silicone wax	95°
	Min and Webb [77]	Chemical coating	Aluminium	Press oil	90°

2.3.3 Effect of the surface characteristic

A few studies were conducted to investigate the effect of the treated surface of the heat exchanger (HEX) on condensation heat transfer performance. Rausch, et al. [78] explored the dropwise condensation experiments on the Al alloys 3003 treated by ion beam implantation technology and concluded that the condensation heat transfer coefficient is enhanced by the higher steam pressure and lower subcooling. Ji, et al. [79] explored the heat transfer performance on a superhydrophobic surface with a CA of 166º fabricated by self-assembled monolayer method and a bare tube with a CA of 83º. The condensation phenomena and the heat transfer coefficient are compared with two variables: coolant Re number and the saturation pressure in the chamber. Based on the different conditions, in the whole process, three condensation types are observed depending on the droplet size: dropwise condensation, flooded condensation and attached condensation. Among these, the overall heat transfer coefficient of the dropwise condensation has been improved the most, at 105%. Gu, et al. [80] investigated how the 3D-finned tube with three different surface treatments affect the condensation heat transfer performance. By comparing the heat transfer coefficient and the heat flux change, the hydrophilic treatment surface presents the best heat transfer performance and then followed with hydrophobic and superhydrophobic surfaces. Compared with the smooth tube, the 3D-finned with a height of 1.5mm structure has promoted the heat transfer coefficient by 94%. The reason is that the 3-D finned tube increases the heat transfer area and broke the flow boundary near the wall. Hu, et al. [81] designed a hydrophilic-superhydrophobic hybrid by self-assembled monolayer coatings of n-octadecyl mercaptan with oxidation and chemical etching on a finned tube with an outside diameter of 14.26mm. This hybrid finned tube intensifies

the condensation heat transfer coefficient by maximum 215% compared to the hydrophilic plain tube and by maximum 98% compared to the hydrophilic finned tube.

2.4 Frosting

The maximum evaporation temperature can be significantly lowered to a low-grade heating temperature level (lower than 70 ºC) as condensation occurs at the cryogenic temperature of the proposed FWG. This increases the variety of low-temperature waste heat sources and lowers the high-grade thermal energy consumption. However, the regasification process of LNG may bring issues, e.g. the frosting/freezing occurring on the air-wall interface, which will influence heat transfer performance and block the vapour flow. In this section, the following are explained: mechanisms of frosting formation, frost properties, effects of the frosting in engineering applications and anti-frosting solutions.

2.4.1 Frosting introduction

Frosting formation on a cold surface is a well-observed phenomenon in nature and industrial applications, such as refrigeration, air-condition and aerospace. Frost generally occurs when humid air contacts a cold surface with its temperature lower than the dew point of air. In some cases, although the surface temperature is beneath the freezing point, the water vapour condenses into the supercooled droplets and then freezes into ice. This two-step process is called condensation frosting. Nath, et al. [82] summarized the condensation frosting process into the following five stages:

a) supercooled condensation
b) onset of freezing

c) frost halos

d) inter-droplet ice bridging and dry zones

e) percolation clusters and frost densification

The first stage of the condensation frosting is supercooled condensation which occurs on the surface temperature beneath the dew point. Once the droplets formed on the cold substrate, these supercooled droplets absorb the water content from the humid air and grow up. The second stage is the droplets freezing process. In general, the onset of liquid freezing is when the temperature of the liquid reaching the freezing point. However, the supercooled droplets are unstable form of liquid that related with several factors, such as subcooling degree, surface characteristic and volume of the droplet. As reported by Koop [83], the supercooled droplets could be frozen until -40ºC. After the ice nucleation, two stages of freezing are followed: recalescence and freeze front propagation. The third stage is defined as frost halos which occurs just after the recalescence process. The droplet grows bridges to freeze the surrounding annular ring of microdroplets and turns to frost halos. In this process, the temperature of the droplet is found to increase from supercooled temperature to 0ºC. As the freezing of the supercooled droplets is a probability function of the abovementioned factors, the supercooled droplets freeze at different time [84]. Therefore, the unfrozen droplets interact with their neighbouring frozen droplets via inter-droplet ice bridging and localized dry zones in the fourth stage. Then this interaction reacts as a chain to percolate all the condensate on the substrate. Once all the liquid droplets transfer to the solid phase completely, the frost densification is the dominant mode through heat and mass transfer.

Several parameters were proved to affect frost formation process, such as air humidity, air temperature, surface temperature, geometry and characteristics. Tahavvor and Yaghoubi [85] investigated the effect of air properties on the frost growth on a horizontal circular cylinder with surface temperature varying from -10ºC to -4ºC with heat transfer by natural convection. The experimental results showed that the greater relative humidity and temperature lead to thicker frost and higher heat flux between the surface and the air. Similar trends were also observed by Amini, et al. [86], Li, et al. [87] and Lai, et al. [88]. Fossa and Tanda [89] found that the lower temperature surface had thicker frost, and frost mass increases linearly with time and is affected by relative humidity in natural convection experiment with a surface temperature in the range of -13ºC to -4ºC.

Compared to the research abovementioned on near ambient low temperature surfaces, frost formation phenomena are different on cryogenic temperature surfaces. An experimental study of frost deposition on a surface of -165ºC under natural convection investigated by Liu, et al. [90] showed an opposite frost growth trend that the frost layer thickness diminished with the decrease of surface temperature. The explanation in the paper was that the phase change of water vapour already occurred in cooled surrounding air before it contacting the cold surface. Li, et al. [87] experimentally studied the influence of air humidity, air temperature and surface temperature on frost deposition on a copper plate with the surface temperature varying from -190ºC to -100ºC under free convection conditions. The study found that the frost thickness grows with the increased relative humidity and temperature of air. The other influence factors on frost properties are presented in Table 2-7 below.

Table 2-7 Influences on frost properties.

Increase affecting factor	Study	Year	Geometry	Surface temperature	Frost thickness	Frost density	Frost thermal conductivity	Frost mass
Air temperature	Hermes, et al. [91]	2009	Flat plate	-30 to 0	↓	↑	-	-
Air relative humidity	[92]	2015	Flat plate	-35 to -4	↑	-	-	-
Air velocity	Hayashi, et al. [93]	1977	Flat plate	-25 to 0	-	↑	↑	↑
Surface temperature	Hayashi, et al. [93]	1977	Flat plate	-25 to 0	-	↑	↑	-
	Şahin [94]	2000	Parallel flat plates	-	↓	No effect	↑	↑
	Lüer and Beer [95]	2000	Parallel flat plates	-16 to -2	↓	-	↑	-
Surface contact angle	Hoke, et al. [96]	2004	Flat plate	-13	↑	Various	↓	↑
	Boyina, et al. [97]	2019	HEX	-10 to -5	-	-	-	↓
	Lee, et al. [98]	2020	fin-tube HEX	-20	↓	-	-	-

2.4.2 Frosting on LNG vaporizers

As introduced in the previous section, four kinds of LNG vaporizers are widely used in the market, ORV, SCV, IFV and AAV. Among these, AAV covers the small and medium scale terminals market due to its low operation cost and high environment sustainability. The general operation method is that the LNG flows inside the tube while the ambient air provides the heat outside to vaporize the LNG to NG. However, the performance of AAV is mainly influenced by the environment conditions and operation conditions, such as the air temperature and air humidity. Therefore, the AAV should be designed by considering the local environment conditions. In addition, the cryogenic temperature that LNG operating may cause the frost formation on the surface which will block the air flow and weaken the heat transfer performance. Several researchers focused on the frost formation mechanism in LNG vaporizer.

Liu, et al. [99] developed a coupled dynamic heat transfer model to investigate the heat transfer performance of AAV using MATLAB considering the frost formation on the cryogenic temperature surface and LNG flow boiling inside the tube at the same time. The numerical calculations found that the influence factors on heat transfer are relative humidity, air temperature and wall temperature. And considering the AAV structure, along the length of the exchanger, the frost layer thickness is smaller while the heat transfer coefficient is greater. Lee, et al. [100] also proposed a heat and mass transfer model to predict the dynamic performance of the AAV including LNG outlet temperature, frost thickness and heat flux. The results showed that the AAV performance is also related to the air velocity. As the air velocity increases, the amount of air flowing increases which enhances the heat transfer coefficient of the HEX. Similar

investigations are also concluded by Liu, et al. [101], Kim, et al. [102] and Liu, et al. [43]. Besides these factors, the flow rate of the coolant is also considered as an important parameter that affecting the frost formation process by Kuang, et al. [103]. Ren, et al. [104] employed the LN_2 as the coolant fluid to provide cryogenic temperature surface to observe the frost morphology and the properties. Based on the experimental data, the correlations for frost density and frost thickness prediction are modified to include the wall temperature as a function.

2.4.3 Solutions

The frosting phenomenon causes many negative effects, especially in heat transfer processes. Frost layer blocks air flow contacting the surface directly, thereby forming an insulation layer to increase the thermal resistance of the surface, consequently causing worse heat transfer performance and system malfunction. Over the years, researchers have been working on how to minimize and prevent these negative effects. One method is to defrost, e.g. evaporation [105] and ultrasonic vibration [106] while another method is to apply specific coatings on surface to delay or totally avoid frost formation. Compared to active approaches removing frost with chemical, mechanical and thermal methods, surface treatment methods are less time and energy consuming. Other than enhancing the condensation performance by maintaining dropwise condensation, the hydrophobic coating could affect the frost formation.

Hydrophobic surface that affects frost formation under near ambient low temperature range was investigated by several researchers. Huang, et al. [107] proved treated hydrophobic surface strongly affects freezing time after comparing five surfaces with contact angles varying from 97.2º to 154.9º experimentally. In this study,

superhydrophobic surfaces were treated by rinsing in 1.0 mol/l NaOH solution and 0.05 mol/l $K_2S_2O_8$ solution, and then modified by immersing into a pre-hydrolysed ethanol–fluoroalkyl silane solution. The water droplet was frozen at a later stage on the surface with a larger contact angle. Liu, et al. [108] found that a superhydrophobic surface of 162º CA pre-treated with a rapid fluorinated process of carbon tetrafluoride plasma, delayed freezing time for 55 minutes compared to a plain surface without coating. Therefore, frost thickness on the superhydrophobic surface was reduced by 52% at the end of the experiment. A similar study reported by Dyer, et al. [109] that frost thickness grows 13% thicker on a coated hydrophilic surface than on a bare surface or hydrophobic surfaces.

Several researchers also focused on how the surface treatment affects the performance of HEXs. Lee, et al. [98] investigated the effect of the surface wettability on frost retardation on the fin-tube HEXs with three different coatings of 72º, 117º and 160º. A new method to evaluate the frost retardation was proposed by comparing the time taken for the air flow rate to decrease when reaching the same ratio. The experimental results show that compared with the bare tube, the hydrophobic surface and superhydrophobic surface has delayed the frost time by 14.4% and 42.0%. And the surfaces with higher hydrophobicity delayed the decrease in heat transfer rate and the increase in the pressure drop. Kim and Lee [110] also proved that under frost conditions, the hydrophobic surface on heat pump louvered-fin HEXs could provide the best heat transfer performance compared with the bare surface and the hydrophilic surface by experiencing the smallest air side pressure drop and the smallest heat transfer rate reduction. Recently, a similar study for investigating the effect of the surface treatment on the louvered-fin HEX was explored by Ye, et al. [111]. The study

found that the hydrophobic surface help to delay the frost time by 12min, and the air pressure drop to the specific pressure by 118min compared to the bare surface. A superhydrophobic crossflow HEX treated by chemical vapour deposition method to deposit the heptadecaflouro-tetrahydrodecyl trimethoxy silane in a 2.5nm thickness on the surface was employed by Boyina, et al. [97] to test how this coating method affect the HEX performance. Through the mass change of the HEX, heat transfer rate and the image captured, the reduction on the heat transfer rate on the superhydrophobic HEX was delayed by around 90min. Defrosting time and defrosting cycle are also an important parameter to evaluate the performance, as in the applications, defrost is an essential cycle for the HEX to remove all the frost and reuse. In this study, the superhydrophobic surface spent the longest defrosting time but retained the least water on the surface which reduces the manual frost removal time afterwards by 50%. Wang, et al. [105] investigated the effect of surface energy on frosting and defrosting behaviour of a fin-tube HEX at -10ºC. Sodium hydroxide solution etching method was employed to obtain the surface super hydrophobicity. The treated surface showed greater anti-freezing performance which achieved a reduction of 17.1% and 28.8% on frost thickness and frost mass respectively compared to bare surface. And the superhydrophobic surface performed the lowest pressure drop and the best heat transfer. Superhydrophobic treatment also helped to reduce defrosting time and energy consumption of the evaporation in the defrost process.

However, some research showed contradictive observations in frost formation. Kim and Lee [112] compared frost and defrost performance on three surfaces in heat pump applications: plain, hydrophilic and hydrophobic surfaces with temperature from -18 to -10ºC. The hydrophobic surface coated with fluorinated resin and nano-protrusions

fabricated led to water droplets formation on the surface. However, the poly-acrylate resin coated as hydrophilic surface created a water film at an early stage, thereby the lowest frost thickness. Hoke, et al. [96] experimentally compared frost formation parameters on flat glass plate (CA<10°) and polytetrafluoroethylene (PTFE) (84°<CA<103°). It was concluded that the plain glass surface generates thicker frost with a lower density than the PTFE surface at the mature frost growth stage, while adverse behaviour was observed at the early frost growth stage.

According to the above investigation research, the surface temperature in the ordinary low temperature range: -30ºC to 0ºC is focused the most. And it has been proved that the cryogenic temperature (below -100ºC) surface presents different frosting phenomena and performance compared with near ambient low temperature surface. However, few papers were found to explore the chilled temperature (-100ºC to -30ºC) range surface. This temperature range is widely used in industrial applications, such as LNG regasification process.

As summarized above, the frost mechanism is complicated as it is related to several factors. The predictions of the frost properties numerically were explored in recent years as an important issue in engineering applications. Hermes, et al. [113] proposed a semi-empirical correlation to predict frost density by combining a theoretical model and experimental data. The proposed correlation was related to thermodynamic conditions of humid air and Jacob number as presented in Table 2-8. Although this correlation has a good agreement with the experimental data presented in the paper, it is only applicable for surface temperature in the range of -15ºC to -5ºC and room-temperature humid air. Considering the effect of surface characteristics, Sommers, et

al. [114] proposed a new correlation (in Table 2-8) based on Hermes, et al. [113]'s work. However, the correlation is restricted for use in the following specific conditions: contact angle of 45°<CA<160°, relative humidity of 40%< φ <80% and surface temperature of -13ºC <T_w< -5ºC under natural convection. The existed correlations for frost density predictions were limited in near ambient surface temperature range and high humidity air environment. To extend the applicable range of the correlations, we aim to propose a new predictive correlation for treated surfaces of chilled temperature in this study.

Table 2-8 Frost density correlations.

Study	Correlation	Conditions
Biguria and Wenzel [115]	$\rho = \frac{\rho_l \int_{x_0}^{x_L} f(x)dx}{L - x_0} = \rho_L(0.612)$	-
Hayashi, et al. [116]	$\rho = 650 \cdot \exp(0.277 \cdot T_{fs})$	-
Hermes, et al. [91]	$\rho = 207 \cdot \exp(0.266 \cdot T_f - 0.0615 \cdot T_w)$	-
Shin, et al. [117]	$\rho_f = (109.53 - 45.54 \cdot \log DCA) \cdot t^{0.0479 \cdot DCA^{0.4357}}$	23º<CA<88º
Hermes, et al. [113]	$\rho_f = 2.2Ja^{-3/2}t^{1/2}$ *	16°<T_a<22°, 50%<φ<80%, -15°< T_w <-5°
Sommers, et al. [114]	$\rho_f = 2.17Ja^{-3/2}t^{1/2}(\frac{4.5}{\ln CA})^{0.95}(\frac{0.80}{\phi})^{0.61}$ *	45°<CA<160°, 40%< φ <80%, -13°< T_w <-5°

* Jacob number: $Ja = \frac{c_p}{L} \cdot \frac{T_{sat,a} - T_w}{\omega_a - \omega_{sat,w}}$

2.5 Research motivation

Due to environmental and economic considerations, sustainable transportation is a growing trend in the marine sector. In this regard, waste heat recovery applications used in ships have increased its importance in recent years. One of the greatest practices of utilizing waste heat is FWG system. Currently, almost all employed FWG systems on board are based on SCD, where extensive energy is used, leading to high energy consumption and low freshwater recovery rate. Therefore, the evaporation and condensation of the SCD process have been continuously developed for the last decades, from the applications of the following techniques, flash evaporation, low temperature coolant and surface modification. However, limited work was found to investigate the utilization of the coolant under cryogenic temperature for condensation in freshwater generation systems. The fast-growing LNG trade market around the world may further create potential FWG applications co-located with vast LNG cryogenic energy source. Therefore, this research makes contribution to propose an integration system of LNG cryogenic energy recovery and FWG system for freshwater generation on LNG powered ships.

With the development of various coating materials, different technologies for surface coating are applied in recent years for anti-frosting which causes from the ultra-low temperature surface. In this study, several types of hydrophobic coatings were prepared to explore their effects on the frosting behaviours through an experimental setup. Various researchers have experimentally investigated the effect of the condensation and frosting performance on subcooled surfaces. The wetting behaviour, distribution and growth of water droplets in the condensation process are influenced

by the surface wettability, which in turn affects the formation, growth and properties of the frost. However, most of the frosting formation studies have been focused on the flat plate with a surface temperature range between -25 to -5ºC. The number of experimental studies that have focused on frosting on the flat surfaces with the surface temperature lower than -35 ºC is very limited [118]. And this temperature range is widely found in industries, such as the LNG outlet temperature of LNG cryogenic energy recovery process for power generation. In order to meet the conditions of natural gas for internal combustion engines, a two-stage regasification-preheating process is normally applied to increase the temperature of LNG which highlights the necessity of the investigation on frosting phenomenon in the transition temperature range. In the novel LNG cryogenic energy harvest systems for power generation proposed in some literatures [119], the outlet temperature of natural gas is around -50ºC. Hence, it is necessary to investigate the phenomenon and performance of the condensation and frosting experimentally around this surface temperature range. One of the novelties of this research is to explore the frosting and condensation formation process on various treated surfaces by extending the surface temperature to the chilled temperature range.

By conducting the numerical study on the integrated FWG system, it helps to understand the water generation process and enables further optimisation using advanced simulations. The evaporation and condensation processes are firstly carried out by Siemens Simcenter Amesim and validated by the experimental studies. The parametric study including the operation conditions and geometry conditions is explored. Then a case LNG powered ship is used to assess the feasibility of this FWG

system that on board. The optimisation analysis based on the thermodynamic and economic requirements was developed on the operation conditions in the FWG.

2.6 Summary

SCD, primarily extracting freshwater from seawater through the evaporation and condensation processes, is now commonly used on board ships as desalination devices. An in-depth literature review was conducted on the main stages ‘evaporation’ and ‘condensation’ processes involved in SCD, while explained and highlighted the advantages and disadvantages. Compared to other techniques, SCD benefits from the less complex design and less maintenance cost. However, there is still potential to improve the comparatively low freshwater recovery rate and the system energy efficiency. Hence, this chapter focuses on the condensation improvement methods to improve the efficiency of FWG system by utilizing recovered LNG cryogenic energy and the surface modifications. LNG cryogenic energy recovery methods were thoroughly explained firstly. Desalinating seawater as one of the important industrial applications that can benefit from cryogenic energy is investigated whilst acknowledging the advantages and disadvantages of these processes. Secondly, an in-depth literature review was conducted on the surface modifications mechanisms and its effect on the condensation performance. During the LNG regasification process, the temperature would be in a wide temperature range including cryogenic temperature, chilled temperature and ordinary temperature which causes different phenomena. It is expected that the hydrophobic surface treatment technologies on the HEX surface provides an enhancement effect on heat transfer and suspends the frosting formation on the cold surface. However, the exploration of the effect of the surface temperature

range in these literatures is limited in the ordinary temperature range of the surface temperature. Therefore, the experimental investigations on the condensation and frosting phenomena under various surface temperature and various surface materials are discussed in ‘Chapter 3 – Experimental methodology’ and ‘Chapter 4 – Experimental results and discussion’. Then the numerical study of the use of the cryogenics for freshwater generation and the optimisation study on an LNG powered ship was investigated and discussed in ‘Chapter 5 – Numerical analysis’ and ‘Chapter 6 – Case study’.

CHAPTER 3 EXPERIMENTAL METHODOLOGY

As discussed in Chapter 2, the utilisation of LNG cryogenic energy and the surface modification are developed for the condensation process to enhance the output of the FWG system. Various researchers have experimentally and numerically explored the formation of the water droplets and the frost layer on subcooled surface in terms of frost growth rate, heat transfer performance and temperature distribution. However, limited work investigated the effect of the surface characteristics when the surface temperature is at the chilled temperature range experimentally.

This chapter describes the test facility that used to investigate the thermodynamic performance and phenomena on the tubes with different surface characteristics under such mechanisms as: condensation, condensation frosting and desublimation. The visualisation method is introduced to detect and monitor the phenomena on the surface and evaluate the system performance at different operating conditions.

3.1 Experiment description

This section introduces the experimental facility setup, preparation, procedures and data analysis methods.

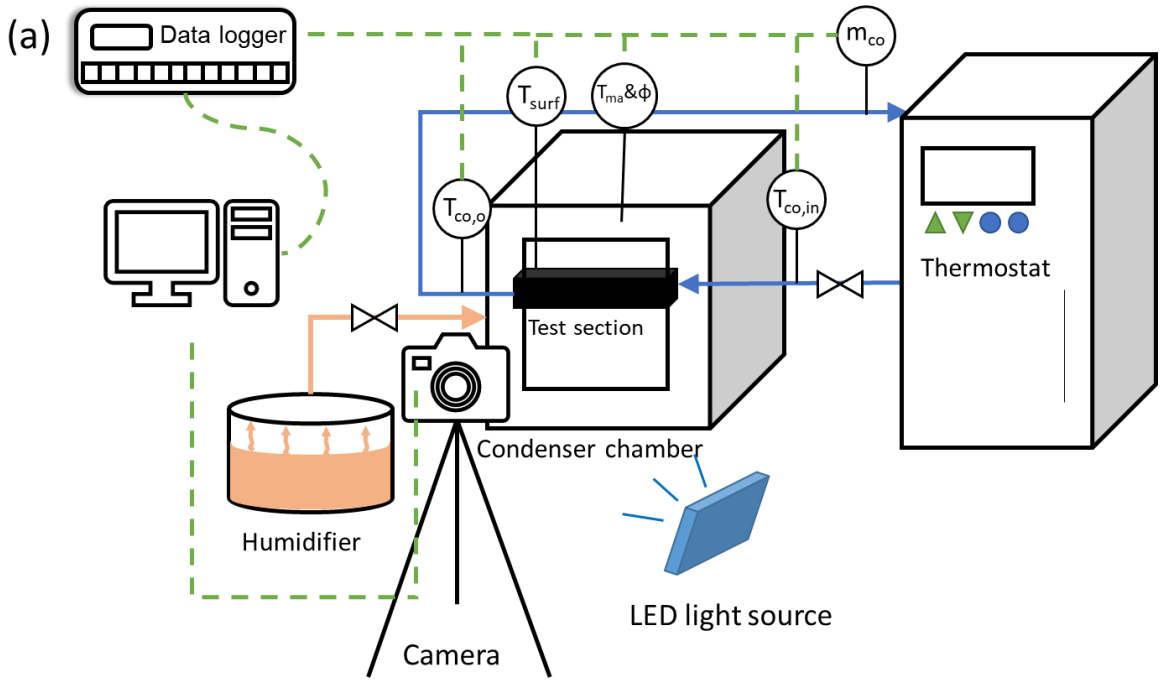
3.1.1 Experimental apparatus

An experimental platform was established as shown in Fig. 3-1. The platform included a condenser chamber, a humidity section, a cooling section and a vision system. The condenser chamber was designed in stainless-steel material in a cube shape, with a size of 300 x 300 x 300 mm. The test section is the part where the frosting experiments

are performed. A few stainless-steel rectangle tubes with a 30 mm width x 30 mm height x 150 mm length and a thickness of 1.5 mm were employed in this study. The humidity section was designed as a humidifier to satisfy the experimental humidity conditions in the test section chamber. The cooling section consisted of several valves, a volumetric flow meter and a thermostat. The coolant pumped from the thermostat flowed through the test section to cool the test surface to the designed temperature. The thermostat has the ability to maintain the coolant temperature in the range of -80 to 10 ºC and to flow the coolant at a maximum flow rate of 10 l/min. An ultrasonic flow meter (UFD5500) scaled from 0.03 to 12 m/s was used to measure the coolant flow rate during the experimental measurements. Visualisation windows made of acrylic were installed on the front and back views of the condenser chamber to observe and record the phenomena that took place on the surface. A high-speed camera, Phantom v710 with an AF Micro Nikkor 105 mm 1:2.8 D lens was used to record from the front of the front view window. The specification details of the camera are presented in Table 3-1. The camera was mounted parallel to the test section surfaces to capture the live process. The connection pipes and the inside walls of the condenser chamber were insulated by polyethylene foam sheets to avoid heat losses.

Table 3-1 Camera specification details.

Parameter	Specifications
Camera	v710
Lens	AF Micro Nikkor 105mm 1:2.8 D
Speed	100 µs
Colour	Monochrome 8 bits or 12 bits
Resolution	1280 x 800



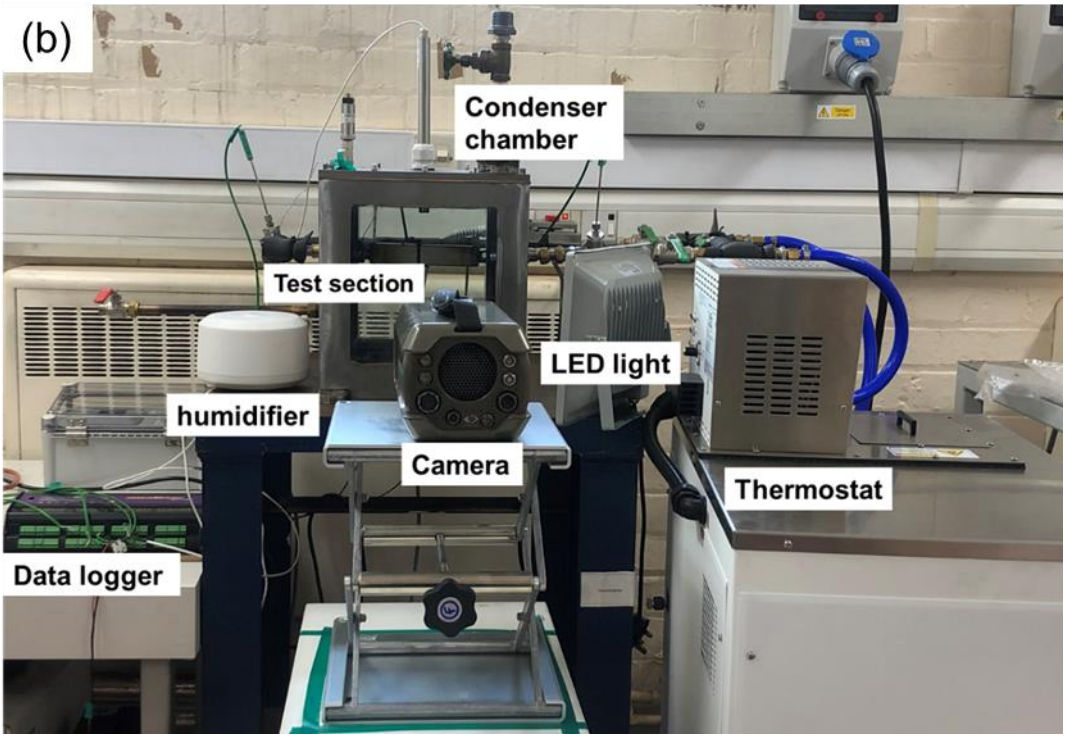


Fig. 3-1: (a) Experiment setup diagram. (b) Photo of the test rig.

The thermocouples measuring the coolant operational temperatures were K type stainless-steel 304 sheathed thermocouples (KMQSS-IM100U-300). The two surface thermocouples used in the test section were K type thermocouples with silicone-based and self-adhesive backing. The humidifier in use was HX94BV1W with a temperature range of 0-100 ºC and relative humidity of 0-100%. The details of the instruments in the experiment are shown in Table 3-2. The data acquisition system 'Data Taker' was employed to record the surface temperature, the temperature in the chamber, inlet and outlet temperature of the coolant and the humidity in the chamber every second for further analysis. The uncertainties and the accuracies of the parameters in the experiment are summarised in Table 3-3.

Table 3-2 Instrumentation and propagated uncertainties of the experiment

Instrument	Manufacture	Range	Accuracy
Temperature/relative humidity transmitter	Omega Engineering	0 to 100%	±3.5% (5 to 20%); ±2.5% (20 to 80%); ±3.5% (80 to 95%)
Temperature/relative humidity transmitter	Omega Engineering	0 to 100ºC	±0.6ºC (0 to 50ºC); ±1.25ºC (50 to 100ºC)
Thermocouple	Omega Engineering	<220ºC	±0.75%
Thermostat	Thermo scientific	-80 to 10ºC	±0.03ºC
Surface thermocouple	Omega Engineering	-73 to 260ºC	

Table 3-3 Uncertainties of the parameters.

	Parameters	Accuracy
Measured	Temperature	0.75%
	Relative humidity	±4% (0 to 5% and 95 to 100%)
		±3.5% (5 to 20%)
		±2.5% (20 to 80%)
		±3.5% (80 to 95%)
	Parameters	Uncertainty
Calculated	Frost thickness	±0.3%
	Frost accumulation	±5.4%
	Frost density	±5.7%

3.1.2 Preparation of the surfaces

Two methods of fabrication were applied on the test tubes to achieve different coatings: plasma polymerisation and spray coating. The stainless-steel sample tubes were firstly cleaned in isopropanol and plasma. Then the plasma polymerisation was applied to form polymers directly to bond on the surface to achieve the hydrophobic coating layer: a fluorine-based coating (manufactured by Diener electronic GmbH + Co. KG). The details and working conditions of plasma system were described in the study of Tur, et al. [120]. For the spray method, the sample tube was firstly degreased and then sandblasted with aluminium oxide powder to remove any surface scale and rust, and to also increase the surface roughness. Two chemical coatings: PTFE and fluorinated ethylene propylene (FEP), were then sprayed with a thickness of 20-50 μm as described in Leivo, et al. [121]. Thereafter, the tubes were cured in an oven for an hour with the peak temperature at 390 °C.

The static, advancing and receding contact angles were measured to demonstrate the surface characteristics. An OCA 15EC contact angle measurement goniometer system was employed using the sessile drop method. Deionised (DI) water as the probe liquid was used for each measurement, to create the drop on the sample surfaces through a syringe. A 5 μL liquid droplet at a dosing rate of 1 μL/s was dropped on the surfaces from a gastight 500 μL precision syringe. The static CA was measured when the droplet was in the equilibrium state. The advancing CA and receding CA were made to advance (or recede) by slowly feeding (or withdrawing) a small amount of water. The goniometer captured a cross-sectional image of the drop on a screen and measured the angles which are presented below in Fig. 3-2. The reported CA values are the

average of five measurements of the CA of droplets at five different locations on each surface. The five measurements for calculating the average contact angle are typically agreed within ±3°.

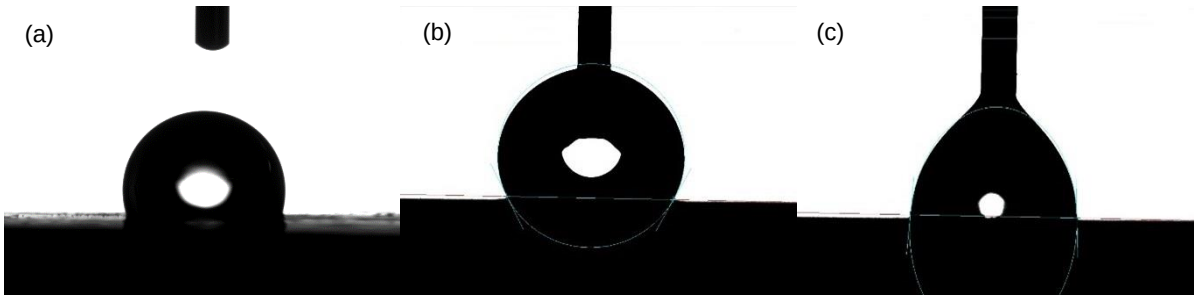


Fig. 3-2: Contact angle measurement shortcut. (a) static CA (b) advancing CA (c) receding CA.

3.1.3 Experimental procedure

Before each experiment case, the test section surfaces were firstly washed thoroughly with ethanol to eliminate oil contamination and then rinsed with deionised water. The camera was adjusted to the correct focus, and then the LED light was turned on and adjusted until the surface could be seen clearly. To initiate the experiment, the thermostat chiller was switched on to allow the coolant to reach the designed temperature. Then the water vapour from the humidifier entered the condenser chamber to reach the designed humidity and turned off all the valves to achieve a closed environment. After the absolute humidity inside the chamber reached 0.019 kg/kg of dry air and was stable for 10 minutes, the coolant was pumped from the thermostat and circulated in the system to start the experiment. The experiment ended at the time when the relative humidity in the condenser chamber did not change for 5 minutes. The experimental data were recorded by the data logger DT85 every second, and the images were captured by the camera in a fixed time period. Each experiment

was repeated more than three times per experimental condition to prevent the unreliability factors affecting the results.

The experimental operation conditions in Table 3-4 are designed to investigate how these different coating materials on the test section surfaces affect the frosting process and heat transfer performance under natural convection. The experiments were divided into four cases considering the different coolant temperatures: Case 1 at -36ºC, Case 2 at -22 ºC, Case 3 at -8 ºC and Case 4 at 6 ºC. Each case was operated with different procedures, the mechanism and a few parameters were evaluated. Apart from the operation mechanism being verified as condensation in Case 4, as the coolant operates at an ordinary temperature, the mechanisms in the other three cases were unsettled. Therefore, the mechanism of each case was firstly analysed. Then, different parameters were measured and analysed based on the specific mechanism for each case.

Table 3-4 Experiment operation conditions.

Experimental conditions	Unit	Value
Air temperature	ºC	25 ± 1
Air absolute humidity	kg/kg	0.019 – 0.020
Pressure	bar	1
Coolant temperature	ºC	6, -8, -22, -36

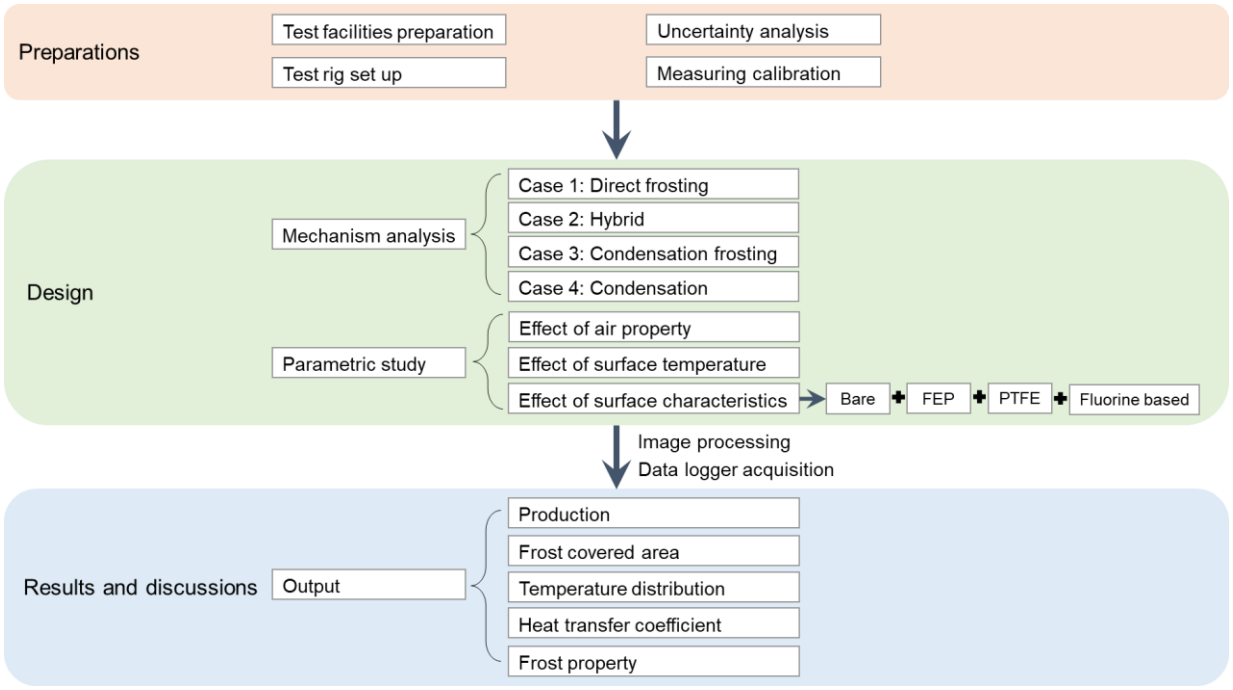


Fig. 3-3: Schematic of the experiment process.

3.2 Mechanism introduction

Generally, the mechanisms are defined as the following:

- Condensation
- Condensation frosting
- Direct freezing

However, the boundaries between each process are related to several factors, such as surface temperature, humidity conditions and surface characteristics. Thus, the performance analysis for each mechanism will be detailed in the following section consisting of the methodology and evaluation parameters. The current chapter describes the experimental methodology to explore the effect of the surface temperature and surface material on condensation and frosting. The mechanisms and

performances are introduced and analysed, including the condensate, frost accumulation, frost properties and heat transfer performance during the actual operation time of the condensation and frosting process. The image analysis method is also introduced to analyse the frost thickness in the frosting cases.

To determine the mechanism, the nucleation mechanism with different surface characteristics is introduced in the current section. The occurrence of the nucleation process requires the vapour embryo to overcome the Gibbs energy barrier. The water vapour has to be in a supersaturated state to achieve nucleation on the cold surface. When the embryo contacts the cold surface, the Gibbs energy changes as follows [122]:

$$\Delta G = V_{em}\Delta\tilde{g}_v + A_{jk}\sigma_{jk} + A_{kw}(\sigma_{kw} - \sigma_{jw}) \quad (3\text{-}1)$$

where A_{jk} and σ_{jk} represent the contact area and interfacial energy, respectively, between the parent phase, j and the new phase, k, which can take the values of ice (i), water (l) and vapour (v) and finally, the subscript w denotes the substrate. It is noted that σ_{jk} is a function of temperature as described in Table 3-5. The V_{em} represents the volume of the new phase, while $\Delta\tilde{g}_v$ is the specific Gibbs free energy change between the phase per unit volume as follows [122]:

$$\Delta\tilde{g}_v = -\frac{R_v T_w}{v_m}\ln\frac{p_{n,w}}{p_{sat,w}} \quad (3\text{-}2)$$

Table 3-5 Equations for interfacial energy calculations in phase change [122].

Phase change	State of i	State of j	Interfacial energy σ_{ij} (J/m^2)
Condensation	Vapour	Water	$\sigma_{v,l} = (75.7 - 0.1775 \cdot (T - 273.15)) \times 10^{-3}$
Desublimation	Vapour	Ice	$\sigma_{v,ice} = (99.5 - 0.075 \cdot (T - 273.15)) \times 10^{-3}$
Freezing	Water	Ice	$\sigma_{l,ice} = (23.8 + 0.1025 \cdot (T - 273.15)) \times 10^{-3}$

According to Eq. (3-1), Gibbs energy change is related to the interfacial energy between the phase and the substrate. The surface energy is an important parameter that affects the nucleation. Assuming that the nucleating embryo is a uniform spherical-cap shape, by differentiating Eq. (3-1), the critical Gibbs free energy change could be calculated by the following:

$$\Delta G_c = \frac{16\pi}{3} \frac{\sigma_{ij}^3}{\Delta \tilde{g}_v^2} \frac{(2+cosCA)(1-cosCA)^2}{4} \tag{3-3}$$

where $cosCA$ is the characteristics of the surface wettability.

$$\cos CA = \frac{\sigma_{js} - \sigma_{is}}{\sigma_{ij}} \tag{3-4}$$

As described above, the water vapour for phase change should overcome the nucleation energy barrier. As shown in Eq. (3-3), the critical Gibbs free energy is related to the interfacial energy, surface wettability and specific Gibbs free energy change. To change the specific Gibbs free energy, two methods are applied: (1) surface temperature lower than saturation temperature at a fixed water vapour pressure; (2) the water vapour pressure should be higher than the saturation pressure at a fixed surface temperature, this is called supersaturation pressure [82]. Therefore,

by combining Eqs.(3-1), (3-2), (3-3) and (3-4), the critical supersaturation for embryo formation could be calculated as below[123]:

$$p_{n,w} = p_{sat,w} \cdot exp\left(\frac{v}{R_v T_w}\sqrt{\frac{4\pi}{3}\cdot\frac{\sigma_{ij}^3}{B_c T_w \ln\left(\frac{I_0}{I_c}\right)}\cdot(2+\cos CA)\cdot(1-\cos CA)^2}\right) \quad (3\text{-}5)$$

where $p_{sat,w}$ represents the saturation vapour pressure of water $p_{sat,l,w}$ and ice $p_{sat,ice,w}$ as a function of surface temperature as follows [124],

$$p_{sat,l,w} = exp\,(54.842763 - \frac{6763.22}{T_w} - 4.210\,ln(T_w) + 0.000367T_w + tanh\big(0.0415(T_w - 218.8)\big) \times \left(53.878 - \frac{1331.22}{T_w}\right) - 9.44523\,ln(T_w) + 0.014025T_w)) \quad (3\text{-}6)$$

$$p_{sat,ice,w} = exp\,(9.550426 - \frac{5723.265}{T_w} + 3.53068\ln T_w - 0.00728332T_w) \quad (3\text{-}7)$$

and I_0 is the kinetic constant at 10^{29} $m^{-2}s^{-1}$ while I_c is the minimum embryo formation rate at 10^4 $m^{-2}s^{-1}$ for both condensation and desublimation modes. B_c represents the Boltzmann constant at 1.38 x 10^{-23} J/K.

According to these definitions of the mechanisms, the critical condition for the embryo formation on the substrate was explored as a function of the surface energy and the surface temperature. The preferred mode of the embryo nucleation with varying operation parameters is defined and investigated experimentally in the following chapter.

3.3 Performance analysis – Condensation

For condensation mechanism cases, the heat transfer performance such as the heat transfer rate and the production rate are evaluated. The total amount of water formed on the substrates during the experiment period was calculated from the absolute humidity difference in the condenser chamber between the start of the experiment and the end of the experiment, which is presented as follows,

$$m = m_{ma}(\omega_{ma,ini} - \omega_{ma,final}) \tag{3-8}$$

The amount of total heat transfer of the tube was calculated based on the temperature difference and mass flow rate of the coolant as the following,

$$Q_{co} = m_{co} c_{p,co}(T_{co,o} - T_{co,in}) \tag{3-9}$$

where m_{co} is the mass flow rate of the coolant; $c_{p,co}$ denotes the specific heat of the coolant, and $T_{co,o}$ and $T_{co,in}$ represent the outlet and inlet temperature, respectively.

Based on the energy conservation law, the heat transfer from the water vapour in the humid air to the surface is equal to the heat conduction through the wall. However, the experiments were performed at an unsteady state at the beginning with a variable temperature. Therefore, the lumped capacitance method was applied to achieve the conductive heat transfer, which is defined as,

$$Q_w = (T_{surf} - T_{co}) \cdot \rho_{co} \cdot c_{p,co} \cdot A \cdot l \cdot \left[1 - \exp\left(-\frac{k_{co} A}{\rho_{co} \cdot c_{p,co} \cdot A \cdot l} \cdot t\right)\right] \tag{3-10}$$

where A is the surface area; l is the length of the tube; and t is the experiment time.

In this process, the heat transfer between the moist air and the surface consists of two parts: sensible heat Q_{sen} [kJ] and latent heat Q_{lat} [kJ]. The energy released by the water vapour condensed on the tube surface is defined as the latent heat transfer rate as the following,

$$Q_{lat} = m_{cond} \cdot L \tag{3-11}$$

As in the experiment, the inner walls of the chamber were covered by the insulation layer to minimise heat loss, and the sensible heat transfer is equal to the subtraction of the conductive heat transfer and the latent heat transfer and the radiation heat transfer as follows:

$$Q_{sen} = Q_w - Q_{lat} \tag{3-12}$$

During the condensation process, the liquid wets the surface as a thin film layer along the tube, which is known as filmwise condensation or as droplets on the surface defined as dropwise condensation. In this study, the condensation heat transfer coefficient was applied as follows [67]:

$$k_{cond} = 0.725[\frac{\rho_l(\rho_l-\rho_v)gL\lambda_l^3}{\mu_l D_h(T_{ma}-T_{surf})}]^{1/4} \tag{3-13}$$

In this equation, ρ_l and ρ_v are defined as liquid density and vapour density, respectively; g is the gravity acceleration, defined as 9.81 m^2/s; μ_l and λ_f are the dynamic viscosity and thermal conductivity of liquid at T_l.

3.4 Performance analysis - Frosting

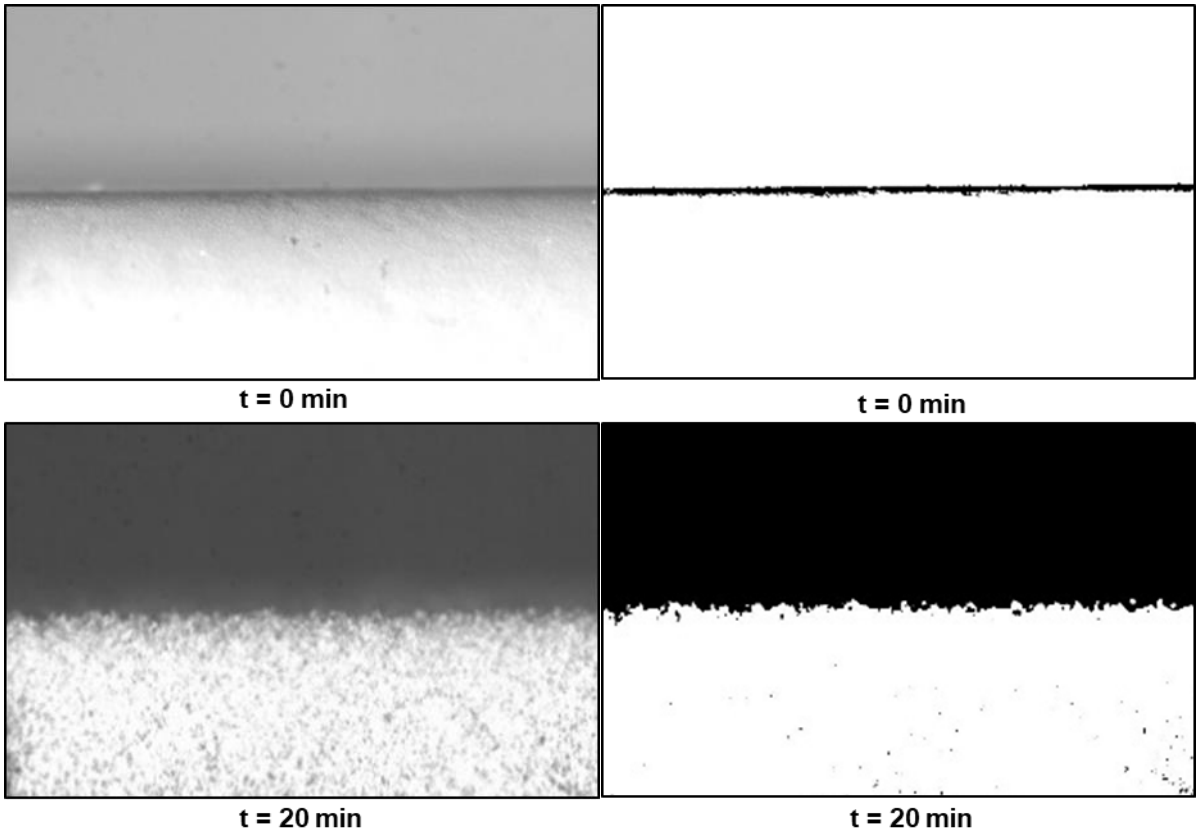
For frosting mechanism cases, the frost properties such as the frost accumulation, frost porosity and frost density were compared by the captured images from high-speed camera firstly. Then the heat transfer performance, such as the heat transfer rate and the production rate were evaluated. The methodologies are detailed in the following sections.

3.4.1 Frost properties

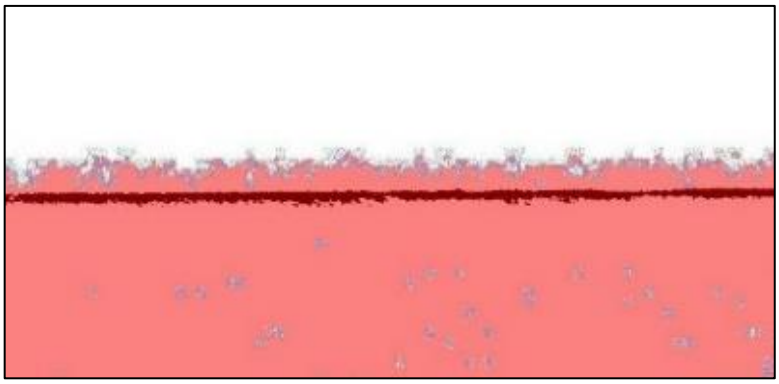
The frost accumulation is expressed in Eq. (3-8). As the distribution of the frost thickness on the surface was uneven, the frost thickness was obtained by averaging the captured section. Two types of frost thickness measurement were explored in the previous literature: direct measurement and indirect measurement. The direct method employs measurement facilities such as the digital micrometre, the scanning probe microscope and a Vernier gauge to measure the frost thickness directly. The indirect method includes the laser displacement gauge, photo analysis from the side-view, and optical signal and neutron radiography conversion measurement. [118] In this study, the image analysis method is employed for the frost thickness measurement. As the frost formation on the surface is uneven, the averaged frost thickness on the surface could present an accurate result. Two averaged measurement methods have been proposed. Wang, et al. [125] defined the frost thickness as the average value of the minimum value and maximum value. Kandula [126] obtained the averaged thickness by averaging the values at five locations on the surface. In the current study, the averaged thickness on the surface was obtained by a new indirect measurement method: image analysis in Image J and MATLAB, as follows.

As shown in Fig. 3-4(a), the front view of the frost layer is captured at t = 0 min and t = 20 min. These captured images are operated threshold in Image J software to decide the boundary of the baseline and the frost layer, as presented in Fig. 3-4(b). Then, the frost layer image overlaid on the baseline image in MATLAB presents the different pixels value in Fig. 3-4(c). The pink area above the baseline is the frost layer deposition on the surface (Appendix A). The average number of the different pixels occupying each point of the baseline is calculated as the averaged frost thickness. Therefore, the frost thickness δ_f was calculated as follows:

$$\delta_f = \frac{n_f}{n_l} \cdot l \tag{3-14}$$



(a) Original image (b) Threshold processed image



(c) Overlay processed image

Fig. 3-4: Illustration of the image processing.

Based on the previously measured frost mass and frost thickness, the frost density is obtained by the following equation:

$$\rho_f = \frac{m_f}{V} = \frac{m_f}{A\delta_f} \tag{3-15}$$

As the frost is assumed as a mixture of humid air and ice, the frost density is calculated based on the porosity and density of each component as follows,

$$\rho_f = \chi \cdot \rho_{ice} + (1-\chi) \cdot \rho_{ma} \tag{3-16}$$

where ρ_{ice} and ρ_{ma} are the densities of ice and humid air, respectively. Similarly, the thermal conductivity of the frost layer is calculated based on the porosity and thermal conductivity of each component:

$$\lambda_f = \chi \cdot \lambda_{ice} + (1-\chi) \cdot \lambda_{ma} \tag{3-17}$$

3.4.2 Heat transfer analysis

As the frost surface temperature is hard to achieve from the thermocouples, the conservation laws of heat and mass transfer are applied to calculate. And a few assumptions are made in the calculation:

1) Heat and mass diffusion within the frost layer is assumed quasi-steady and one-dimensional.
2) The frost layer grows in a direction normal to the cold plate surface with uniform frost thickness along the plate length.
3) The air pressure is uniform in the airstream and within the frost layer.
4) Conduction is the dominant heat transfer mechanism within the frost layer.

The total convective heat transfer from the air to the surface or the frost layer consists of the sensible heat and the latent heat as follows:

$$\frac{Q}{t} = q_{sen} + q_{lat} \tag{3-18}$$

The sensible heat q_{sen} [W] is transferred from the humid air to the cold surfaces while the latent heat q_{lat} [W] is released from the condensation or desublimation process [67].

$$q_{sen} = k \cdot A \cdot (T_{ma} - T_{fs}) \tag{3-19}$$

where T_a is the air temperature, T_{fs} is the frost surface temperature and k_n denotes the heat transfer coefficient.

$$q_{lat} = \frac{m_f L}{t} \tag{3-20}$$

where L is the latent heat of sublimation which is calculated by the following equation:

$$L = 2.88 \times 10^6 - 195 \times T_f \quad (3\text{-}21)$$

Therefore, the energy conservation is described as:

$$\frac{\lambda_f (T_{fs} - T_w)}{\delta_f} = k\left(T_{ma} - T_{fs}\right) + \frac{m_f L}{At} \quad (3\text{-}22)$$

3.5 Summary

This chapter provides a detailed description of the test rig for condensation and frosting by introducing all the test components, measuring devices, the preparation work, and the procedures. The performance of the condensation and frosting has been experimentally explored in terms of the mass transfer and heat transfer. A parametric analysis has been carried out to investigate the effect of the surface characteristics and surface temperature on the production and heat transfer rate. Using the visualisation method and the image processing programming in MATLAB, the morphology results have been recorded, including the frost mechanism and characteristics, e.g., the frost layer growth rate, frost density and thermal conductivity. The detailed experimental results are discussed in 'Chapter 4 – experimental results and discussion'.

CHAPTER 4 EXPERIMENTAL RESULTS AND DISCUSSION

4.1 Introduction

In this chapter, the experimental data of the moist air condensation and frosting on the treated cold surfaces are presented by measuring from the facilities and calculating from the theory. Four cases of the experiments are classified according to the coolant temperature, and each case has a specific mechanism, phenomenon and performance. The experimental results of condensation and frosting vary significantly. Many factors influence heat transfer, such as contact angles, mass fluxes and surface temperature. Therefore, the mechanism for boundary determination is introduced and analysed for each case. Then, to evaluate the effect of the surface temperature and the coating material on the system performance, the droplet distribution, frost properties, heat transfer performance and the production level are compared. In addition, the air properties and the coolant temperature are also investigated to explore the influences on moist air condensation and frosting.

4.2 Mechanism analysis

As introduced in Chapter 2 and Chapter 3, the frosting process could be categorised into two mechanisms: condensation frosting and desublimation. When the surface temperature is below 0ºC, the condensed liquid water droplets freeze into ice. The two-step phase change consisting of the condensation and freezing process is described as condensation frosting. The critical conditions for these two mechanisms are

determined by the phase boundaries, including the melting point and saturation vapour pressure of ice and water. With the measurements of the OCA 15EC contact angle measurement goniometer system, the details about these four different tubes and their properties are presented below in Table 4-1. Fig. 4-1 illustrates the vapour saturation pressure of water and ice and the critical nucleation pressure for desublimation and condensation mode as a continuous function of the surface temperature from -40ºC to 0ºC on four sample tubes. When the water vapour partial pressure is lower than both nucleation pressures, there is no nucleation occurred on the surface. When the water vapour partial pressure is higher than the nucleation pressure for condensation ($p_{n,lw}$), the condensation is the preferred mode. And when the water vapour partial pressure is higher than the nucleation pressure for desublimation ($p_{n,iw}$), the desublimation will happen. It could be seen that among these four tubes, the Fluorine-based sample tube has the highest nucleation pressure. The reason is that at a fixed surface temperature, the surface with higher hydrophobicity has a higher energy barrier to overcome. The corresponding detailed mechanisms and performances for the four temperature cases on each tube are explored in the next section: Case 1 at -36°C, Case 2 at -22°C, Case 3 at -8°C and Case 4 at 6°C.

Table 4-1 Properties of the text section surface material.

Tube	Bare	PTFE	FEP	Fluorine based
Modification method	-	Spray	Spray	Plasma polymerization
Static contact angle (º)	82.00	98.32	99.28	117.65
Contact angle hysteresis (º)	31.06	31.63	27.46	29.74
Food compatibility	No	Food	Food	No

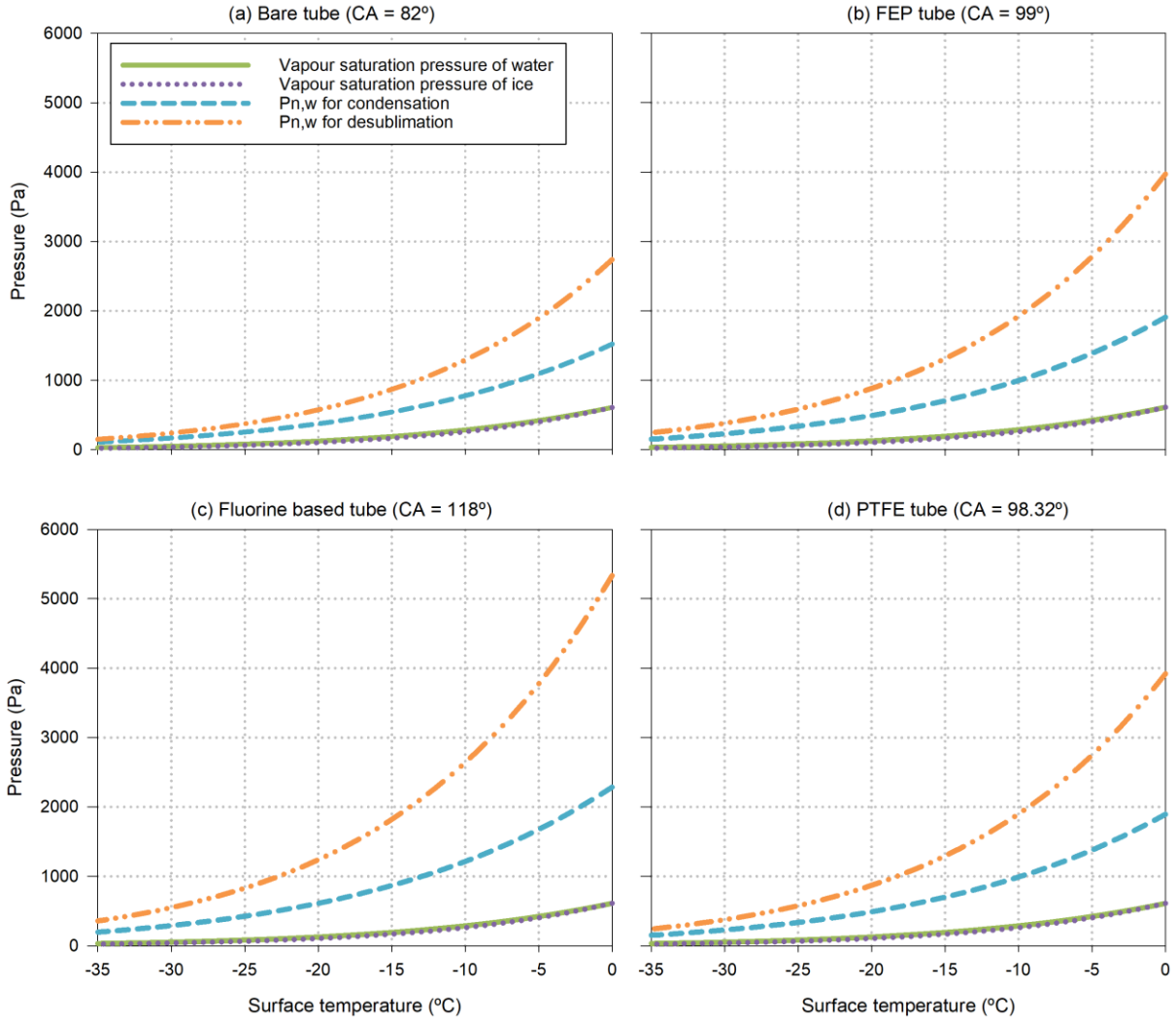


Fig. 4-1: The comparison of theoretical critical supersaturation pressure for condensation and desublimation on each tube (a) bare tube, (b) FEP tube, (c) Fluorine based tube and (d) PTFE tube.

4.2.1 Condensation mechanism analysis

In Case 4, the coolant temperature is fixed at 6°C, and as the experiment processes, the surface temperature decreases from the environment to the designed temperature. Then in this process, the critical nucleation pressure, the saturation pressure and the vapour pressure are compared in Fig. 4-2. It can be seen that at the beginning of the experiment, the water vapour partial pressure (p_{wv}) is lower than both nucleation pressures for all the tubes. Therefore, there is no condensation or desublimation

occurring on the surface at that time. Then when the coolant starts circulating in the pipe as the time goes, the coolant absorbs the heat to cool down the tube surface temperature. when the surface temperature reaches 11.8 ºC, p_{wv} becomes bigger than $p_{n,lw}$ but smaller than $p_{n,iw}$ only on the bare tube, which concludes that the condensation nucleation mode occurs on the surface. Although the water vapour pressure is always beneath the critical nucleation pressure for condensation for the other coated tubes, the condensation still appears on the surface. The reason is that there are impurities such as dust and condensation nuclei in the moist air, which easily promote nucleation on the surface [127]. Therefore, condensation is the dominant mechanism on all the tubes in this case.

The morphology photos on each surface are recorded by the high-speed camera to track the growth of the droplets. As shown in Fig. 4-3, the morphology photos of the whole condensation process on the bare tube are recorded from the beginning to the end. It could be seen that the droplets formed on the surface and grew up by absorbing the water content from the humid air. As the water vapour concentration decreases, the formed droplets' growth stops.

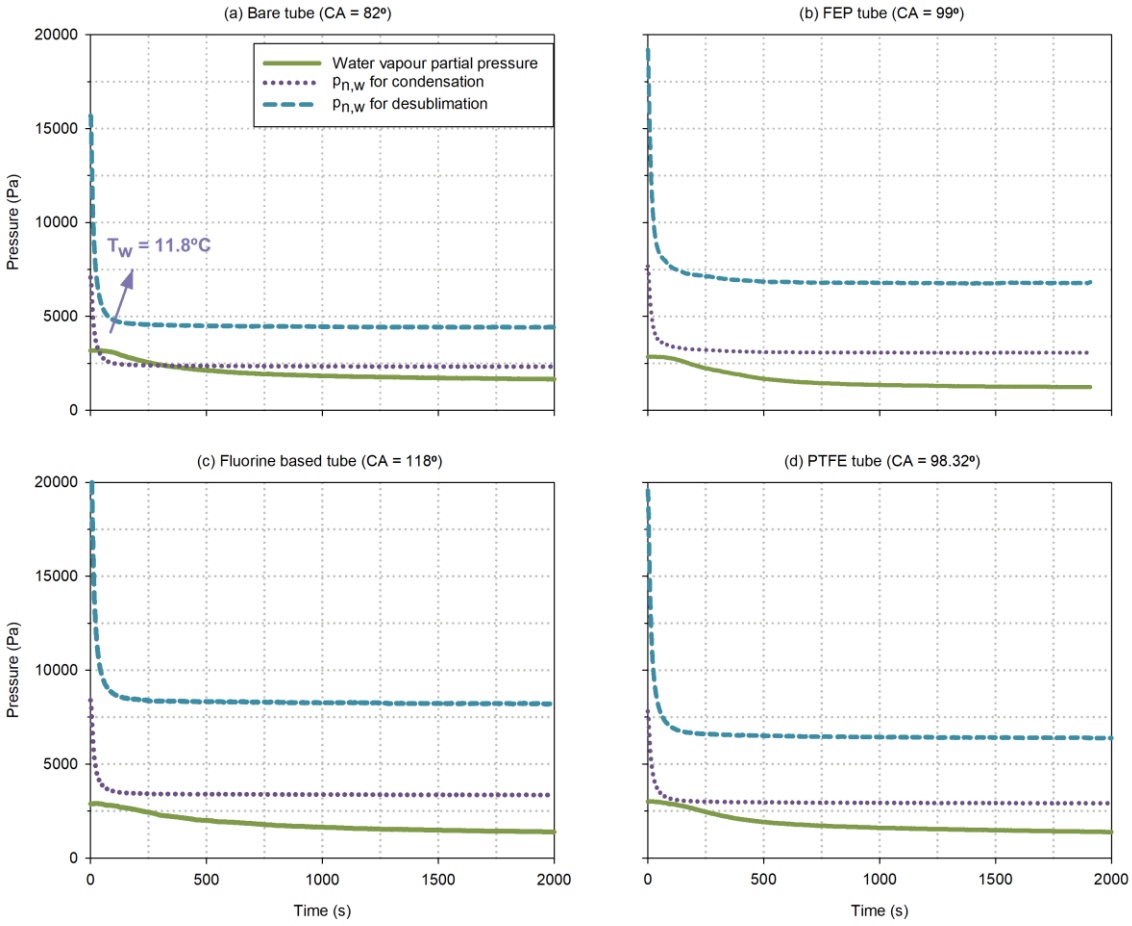


Fig. 4-2: Comparison of water vapour partial pressure and critical supersaturation pressure with the coolant temperature at 6 ºC in Case 4 (a) Bare tube, (b) FEP tube, (c) Fluorine based tube and (d) PTFE tube.

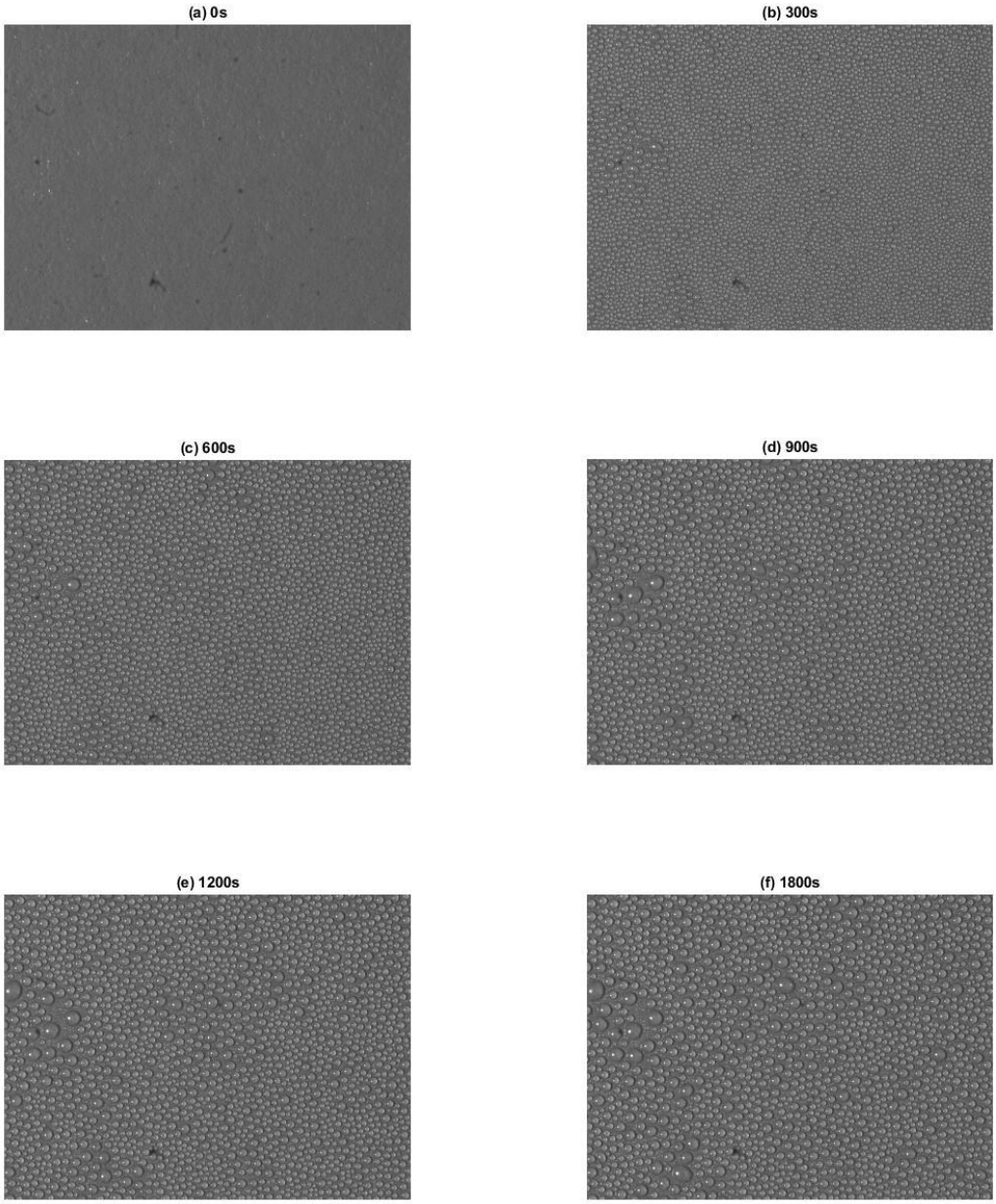


Fig. 4-3: Morphology photos of condensation on the bare tube with a coolant temperature of 6ºC.

4.2.2 Condensation frosting mechanism

The coolant temperature in Case 3 is fixed at -8 ºC. Fig. 4-4 illustrates the water vapour and nucleation pressure comparison. The water vapour pressure and the condensation nucleation pressure on treated surfaces obtained the transition point when the surface temperature reaches 6.81 ºC, 4.54 ºC and 6.74 ºC on the FEP tube, Fluorine based

tube and PTFE tube, respectively. These transition points represent the time when condensation nucleation occurs on the surface. However, two transition points are presented at the bare tube with the surface temperature of 10.1 ºC and 1.27 ºC. This phenomenon describes that when the surface temperature reaches 10.1 ºC, the water vapour partial pressure is greater than the condensation nucleation pressure. Then the condensation mode occurs. When the surface temperature decreases to 1.27 ºC, p_{wv} is greater than the desublimation nucleation pressure, then the desublimation mode is preferred.

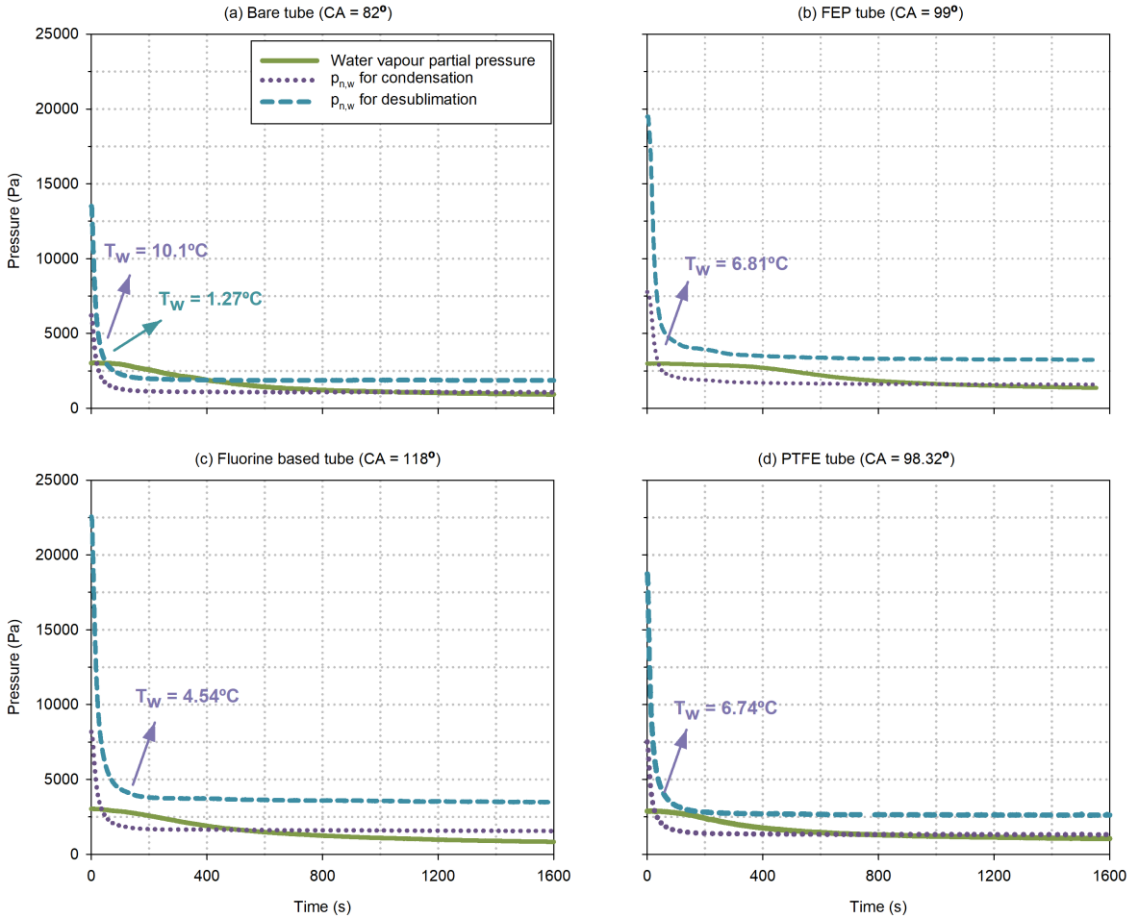


Fig. 4-4: Comparison of water vapour partial pressure and critical supersaturation pressure with a coolant temperature of -8ºC in Case 3 (a) Bare tube, (b) FEP tube, (c) Fluorine based tube and (d) PTFE tube.

However, the morphologies photos show a conflicting result on the FEP tube as shown in Fig. 4-5. Recall from the nucleation analysis in Fig. 4-4, the condensation nucleation occurs at T_w=6.81 °C at t = 40s, and the water condensed on the supercooled surface as droplet shapes. Then as the droplet temperature decreases below the freezing point, the mechanism comes to the onset of the freezing stage. As shown in Fig. 4-5 (c), the droplets start to freeze and then interact with the neighbouring droplets to enlarge the frozen area. This phenomenon presents that the onset of the droplet frosting depends on the droplet temperature, not the comparison between the nucleation pressure and the vapour partial pressure. Therefore, in the current case, the onset point of the droplet freezing is decided by the first frost halo that appears on the surface as recorded by the high-speed camera. Furthermore, different phenomena are observed according to the different surface characteristics in this case. Compared with the bare, FEP and PTFE tubes, the Fluorine tube only has the condensation mechanism on the surface. This phenomenon proves that the higher hydrophobicity surface helps to delay the freezing time at the same condition compared to the high surface energy tube.

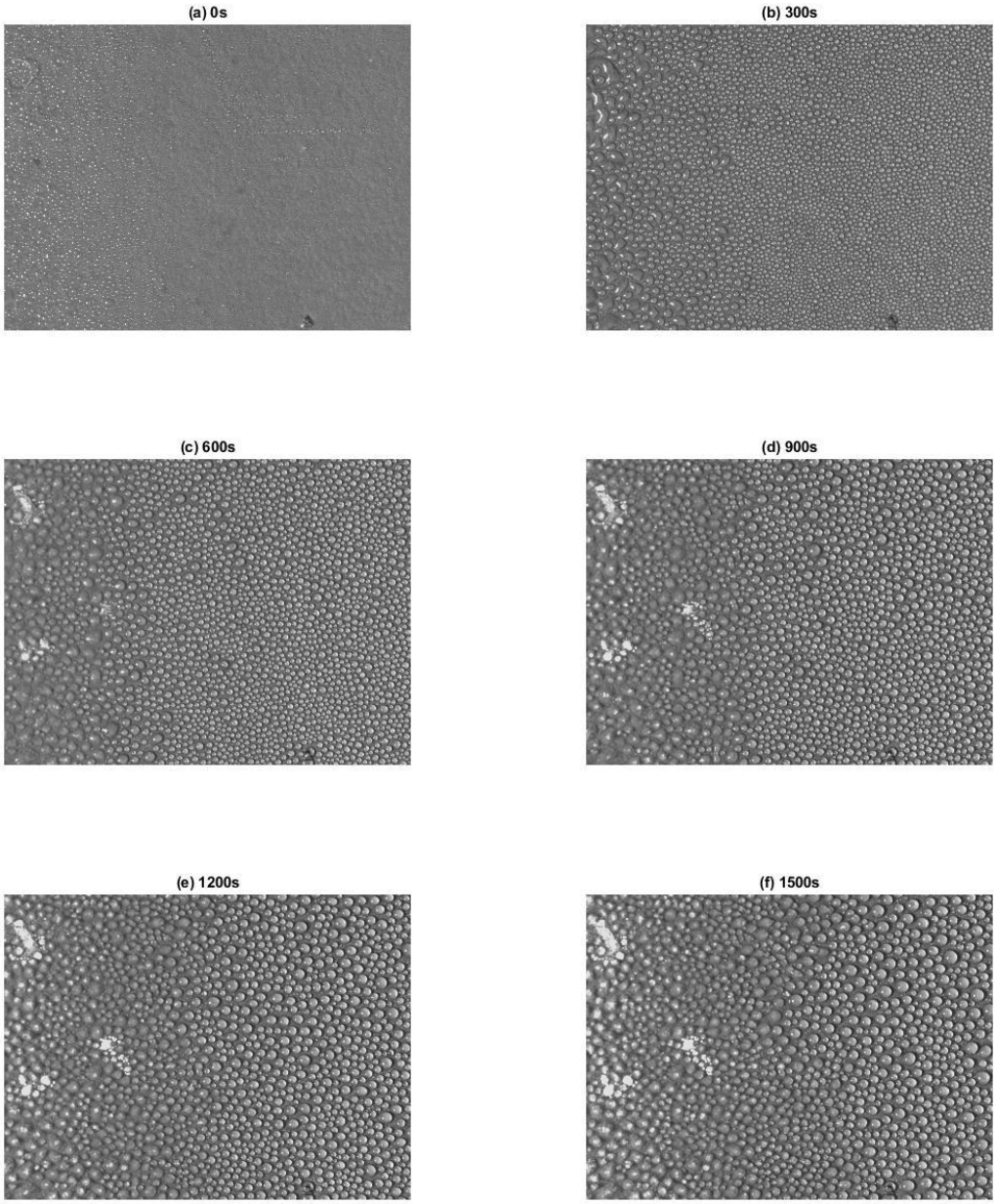


Fig. 4-5: Morphology photos of condensation frosting process on FEP tube with a coolant temperature of -8 ºC.

Fig. 4-6 compares the water vapour partial pressure and critical nucleation pressure in Case 2 with the coolant temperature of -22 ºC. In this case, all of the tubes have two transition points. The corresponding nucleation temperature for condensation and desublimation is the lowest on the Fluorine-based tube due to the lowest surface

energy. Similar morphology performance is presented in Fig. 4-7 during the experiment time from 0s to 1200s. It is clear that at t = 420s, the tube is covered by supercooled and frozen droplets at the same time. Then these frozen droplets start to freeze the surrounding unfrozen droplets as the third phase of condensation frosting. As shown in Fig. 4-7 (c), the frozen area gets bigger than in the previous stage. Until t = 780s, the frozen droplets cover the whole surface of the tube, and then the frost layer grows in densification. Therefore, the mechanisms for all the four tubes are also condensation frosting.

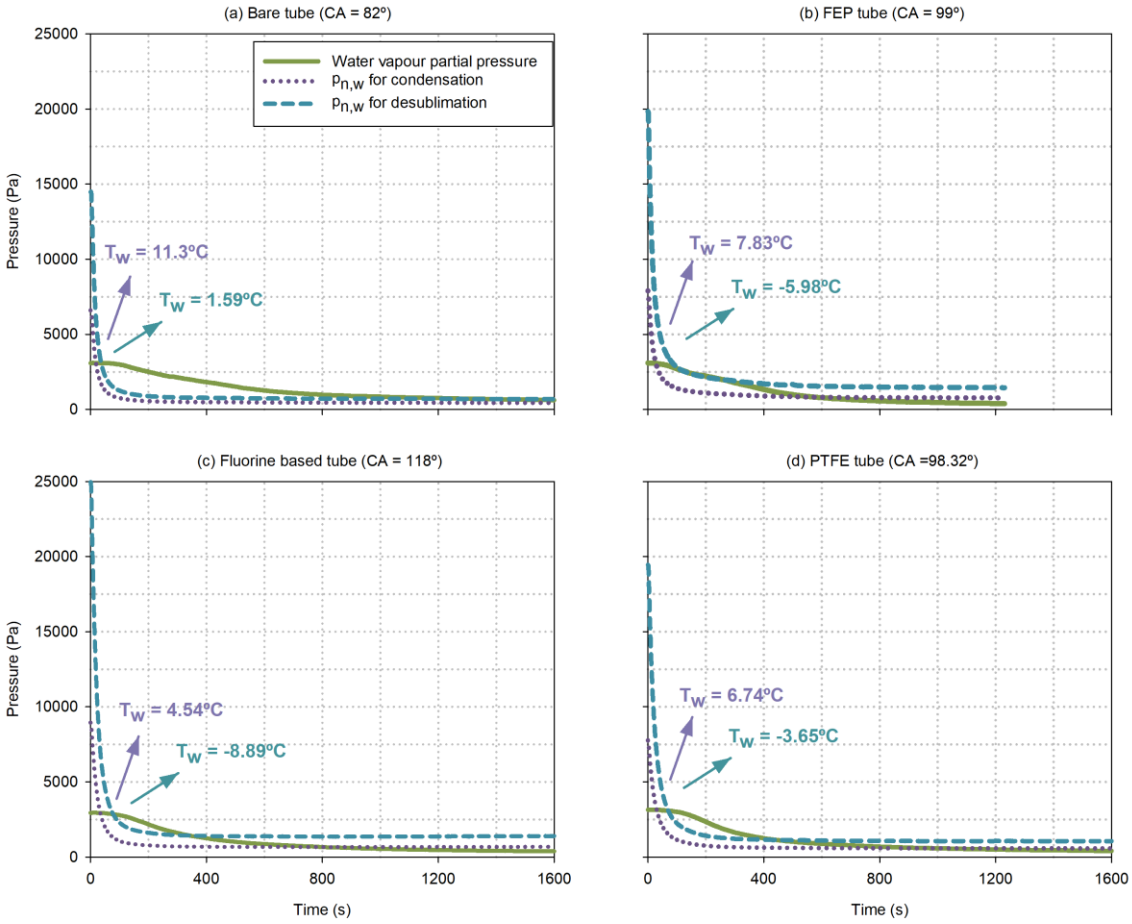


Fig. 4-6: Comparison of water vapour partial pressure and critical supersaturation pressure with a coolant temperature of -22 ºC in Case 2 (a) Bare tube, (b) FEP tube, (c) Fluorine based tube and (d) PTFE tube.

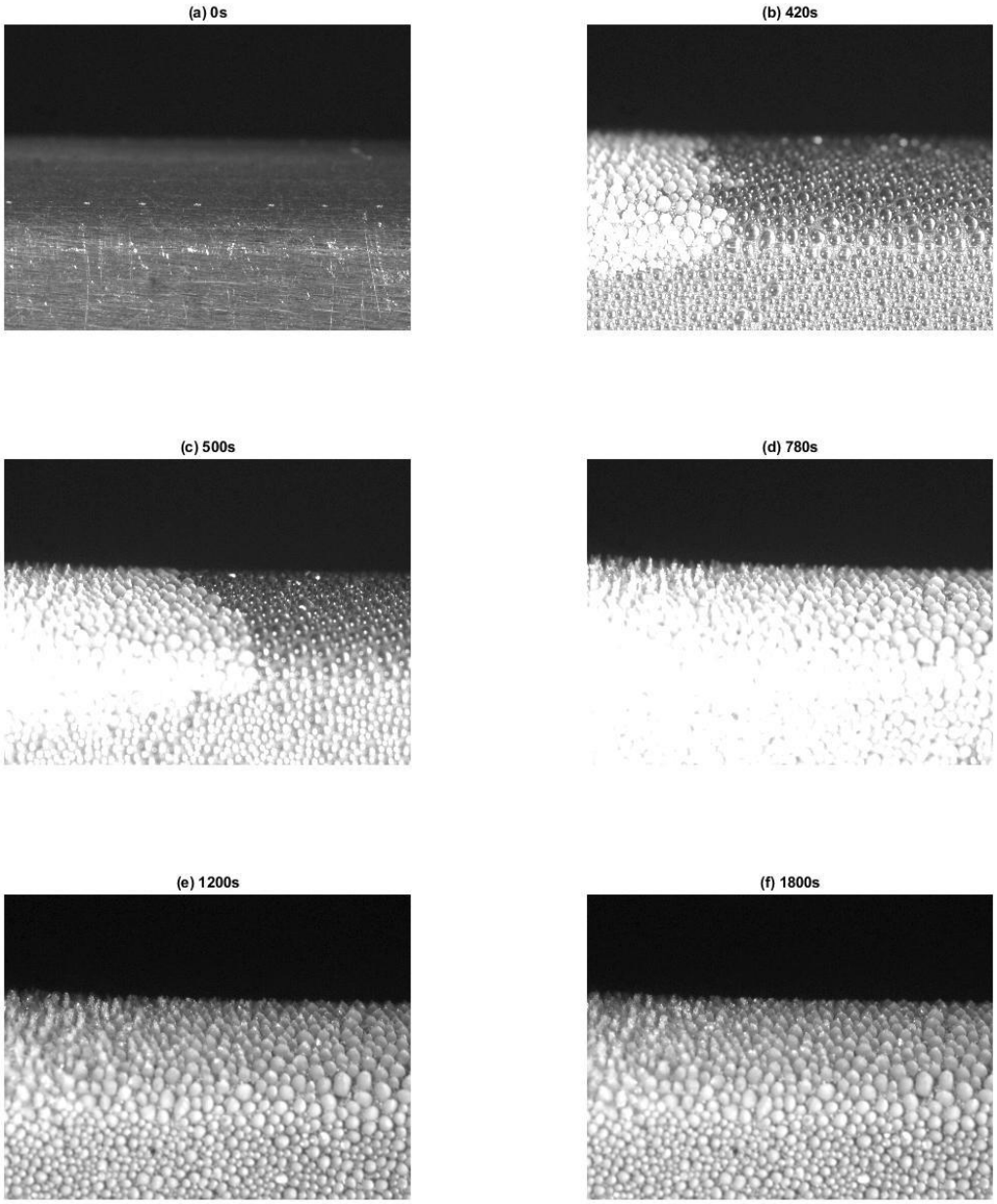


Fig. 4-7: Morphology photos of condensation frosting on Fluorine based tube with a coolant temperature of -22ºC.

Fig. 4-8 compares the partial pressure of water vapour in the chamber with the critical nucleation pressure for condensation and desublimation with the coolant temperature of -36°C in Case 1. At the early stage, supercooled droplets occur on the small section of surface originate from the humid air condensation. Then when the subcooling of the

surface temperature reaches a specific degree, the frost halos are discovered by frozen supercooled droplets, while desublimation initiates on the surface at the same time as p_{wv} is greater than the $p_{n,iw}$. After the frost fully covers the tubes, desublimation drives the frost formation on the pre-existing ice surface. As the surface temperature becomes stable, the frost crystals start to grow. In the final stage, the frost crystals begin to interact with each other. It could also be seen that with the fixed humid air environment, the subcooling degree ($T_w - T_{sat}$) required for nucleation increases as the increased hydrophobicity.

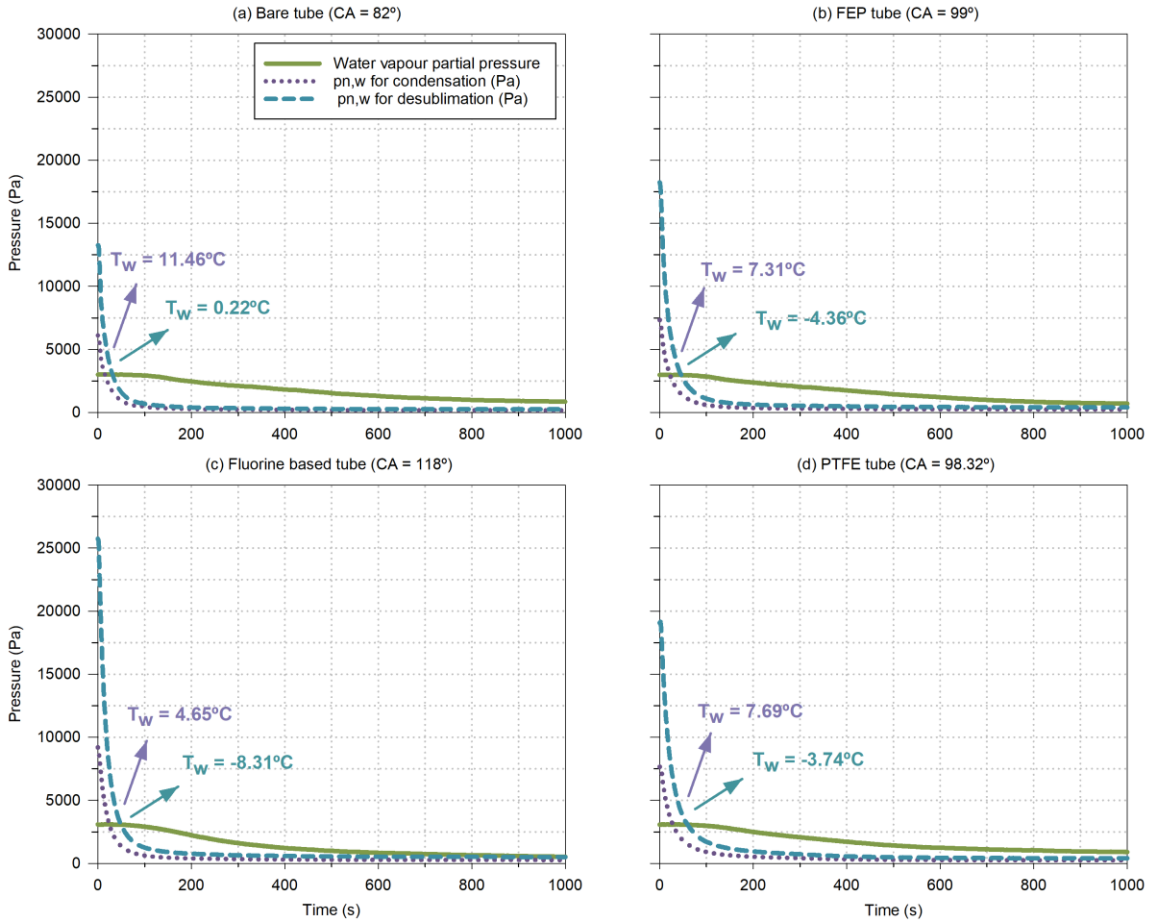


Fig. 4-8: Comparison of water vapour partial pressure and critical supersaturation pressure with a coolant temperature of -36ºC in Case 1 (a) Bare tube, (b) FEP tube, (c) Fluorine based tube and (d) PTFE tube.

The captured phenomena could prove the mechanism of the whole process analysis above. The morphologies of the whole frost formation process are presented in Fig. 4-9. The FEP tube is selected as an example of a typical frost crystal growth process on the hydrophobic coating surface. At the initial stage, as shown in Fig. 4-9 (b), several supercooled droplets are condensed on the surface. Then as shown in Fig. 4-9 (c), these water droplets turn into frost crystals, and the rest are desublimated into frost crystals directly from the water vapour in the humid air. As the surface temperature becomes stable, the frost crystals' growth presents a linear trend while maintaining their feather shapes and covering the whole surface in the image of Fig. 4-9 (d) [128]. At last, as the water vapour in the chamber reduces to a quite low level, the frost crystals interact. The water vapour diffuses inside the existing frost layer, which decreases the porosity and increases the frost density. Therefore, according to the frost formation mechanisms and morphologies, the experiments are defined in four stages: supercooled condensation, water droplet freezing/frost crystals formation, frost crystals growth and frost crystals interaction.

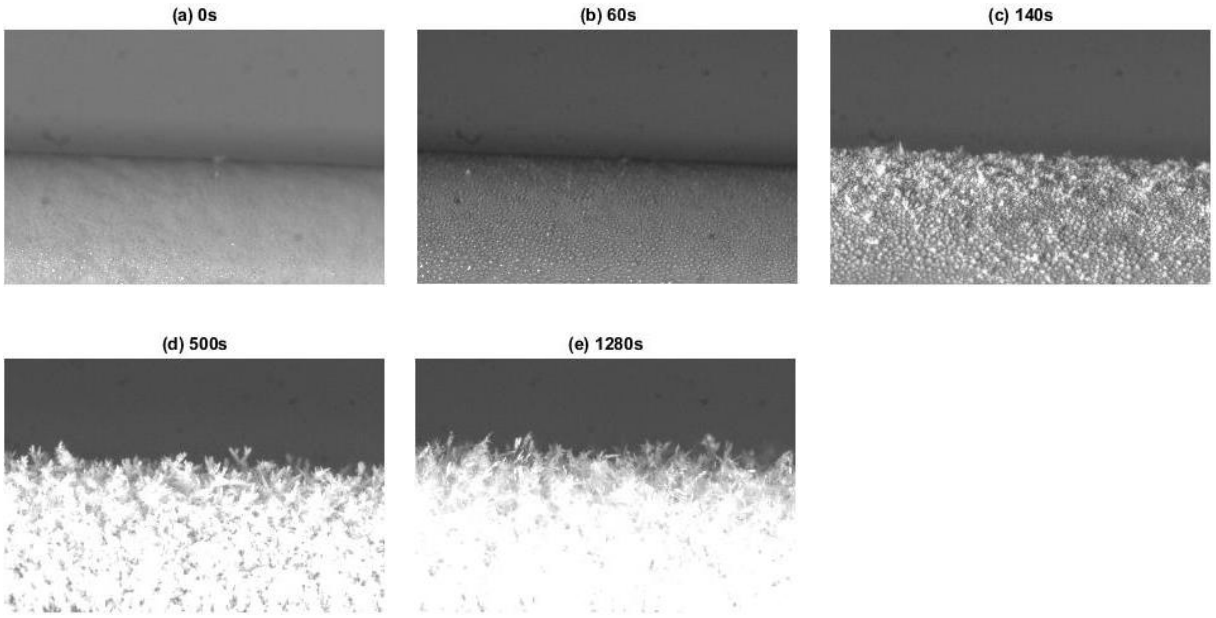


Fig. 4-9: Process of frost formation on the sample section with a coolant temperature of -36ºC.

4.2.3 Nucleation on ice

When the tube is fully covered by the ice droplets and frost layer, the nucleation has a different mechanism as the frosted surface is superhydrophilic at 1º [129]. As shown in Fig. 4-10, the critical nucleation pressure for desublimation is lower than that for condensation at all temperature ranges. Consequently, the favoured nucleation mode on the existing frost layer surface below 0ºC is always desublimation.

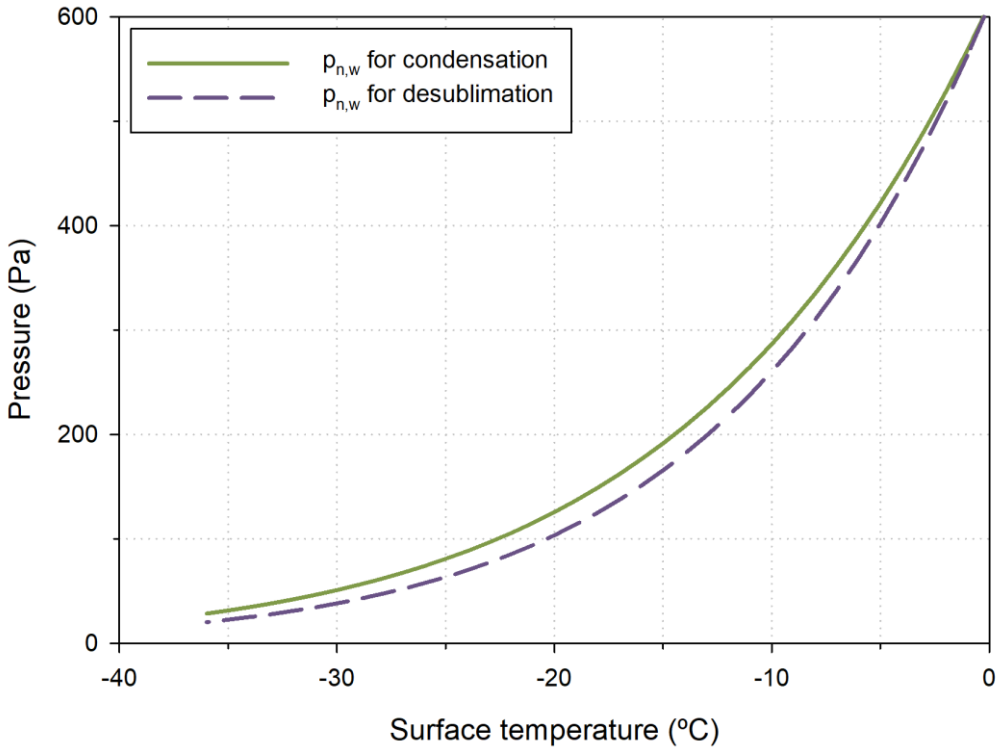


Fig. 4-10: Comparison of theoretical critical supersaturation pressure on the ice surface.

4.3 Parametric study

According to the mechanism discussion above, the preferred mode for each case has been decided, and the corresponding performances are explored as follows in Table 4-2.The parametric study of the condensation and frosting performance is explored in this section, including the effect of the air property, the surface temperature and the surface treatment.

Table 4-2 Summarise table of the performance for each case.

Case	Coolant temperature	Mechanism	Performance
Case 1	-36 ºC	Direct frosting	Frost properties
			Mass transfer performance
			Heat transfer performance
Case 2	-22ºC	Condensation frosting	Delay time
			Frost coverage area ratio
			Mass transfer performance
			Heat transfer performance
Case 3	-8ºC	Condensation frosting & Condensation	Delay time
			Mass transfer performance
			Heat transfer performance
Case 4	6ºC	Condensation	Mass transfer performance
			Heat transfer performance

4.3.1 Effect of air property

The moist air property plays a vital role in investigating the moist air condensation process. In this case, the comparison of the air property on frosting performance on the uncoating tube is explored. The temperature of the coolant is kept constant at 6ºC with a flow rate of 2.6 l/min. The initial environment temperature is controlled at 25ºC and relative humidity of 90%. The performance of the mass growth, the frost thickness formed on the surface and the total heat transfer rate are analysed.

As shown in Fig. 4-11, the frost mass accumulation and frost thickness are compared between two different air temperature environments: 25.9 ºC and 22.9 ºC. The total production decreases with the decreased air temperature. The moist air maintained at the higher temperature in the chamber contains more water vapour at a fixed relative humidity. The water vapour mass concentration is greater at higher air temperature, leading to a more significant difference between the water vapour mass concentration at air and frost temperatures. Then more water will be extracted from the higher temperature moist air than its lower temperature counterpart, resulting in higher frost deposition. The total heat transfer rate as a function of the moist air temperature illustrated in Fig. 4-12 could also prove this phenomenon. With the increase of the moist air temperature, the driving force of the condensation increases, and more water vapour content is available to accumulate on the surface.

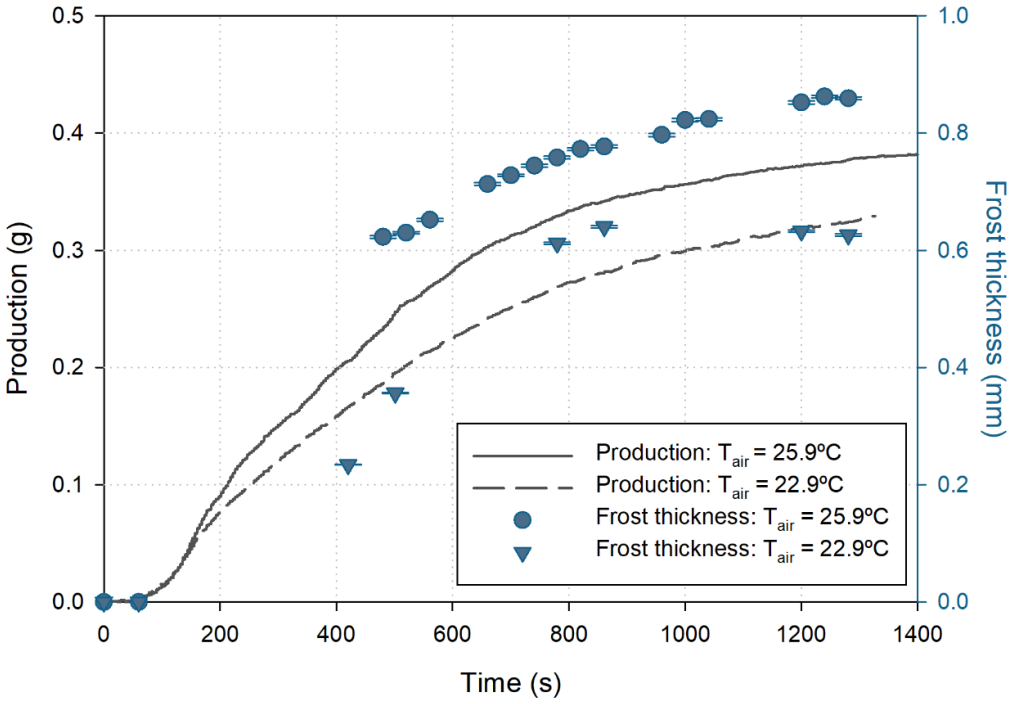


Fig. 4-11: Variation of mass growth rate and thickness of frost on the bare tube with the moist air temperature.

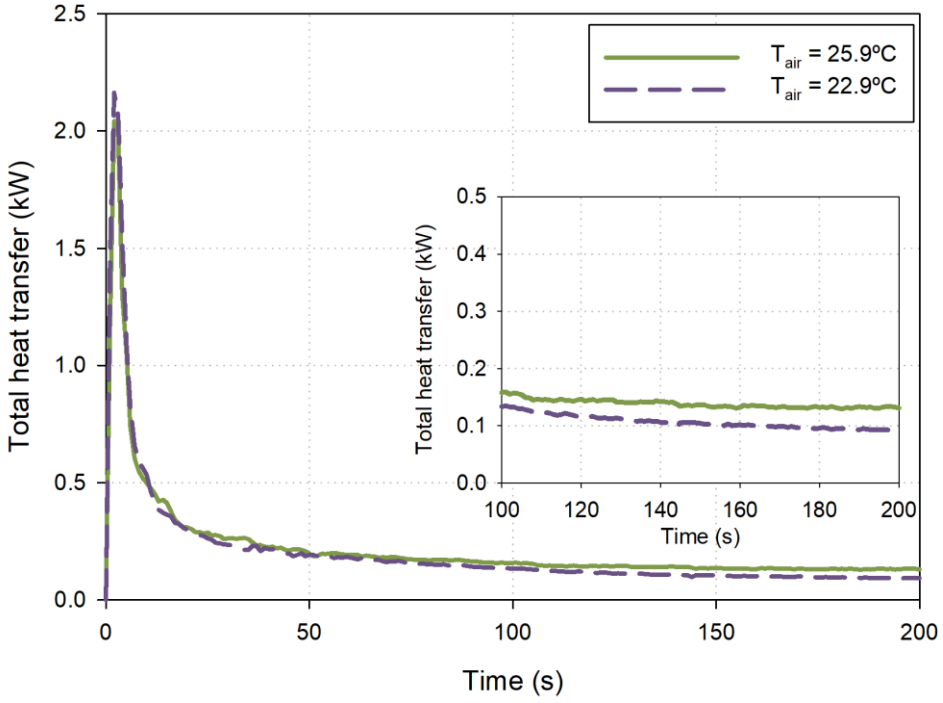


Fig. 4-12: Experimental data of heat transfer comparison with different air temperatures.

4.3.2 Effect of surface temperature

Apart from the air properties, the condensation performance also depends on the surface temperature. This investigation explores four different coolant temperatures: -36 ºC, -22 ºC, -8 ºC and 6 ºC operated on the bare tube to understand its influences on production and heat transfer performance. The coolant flow rate is fixed at 2.6 l/min. And the initial environment temperature remains constant at 25ºC and relative humidity of 90%. The mass transfer and the heat transfer performance on the bare tube are explored.

The total production accumulations with four coolant temperatures from -40 ºC to 6 ºC are shown in Fig. 4-13. The production measured after the experiment increases with the decreased coolant inlet temperature. Supersaturation degree ($p_n - p_{sat}$) was the factor that affected the mass transfer on the surface in the phase change process. As the surface temperature decreases, the increased supersaturation degree leads to the increased production between the water vapour in the humid air and the tube surface. In the first 5 minutes, the coolant provides the cooling capacity to decrease the surface temperature to the designed and set up the supersaturation condition between the environmental air and the surface. After supersaturation is created, water vapour is extracted from the moist air and deposited on the surface in condensation and desublimation modes in the next 10 minutes. Therefore, the productions of ice and water are the greatest. The effect of the surface temperature on the total heat capacity of bare samples in four cases is shown in Fig. 4-14. The heat transfer rate increases with the wall subcooling. With an increase in the wall subcooling, the driving force of the condensation and frosting increased due to the greater temperature difference.

More condensate and frost halos are retained on the tube wall. It is clear that different performances are demonstrated in the different surface subcooling cases. Therefore, the detailed performance and characteristics of these four cases will be introduced and explored separately in the following sections.

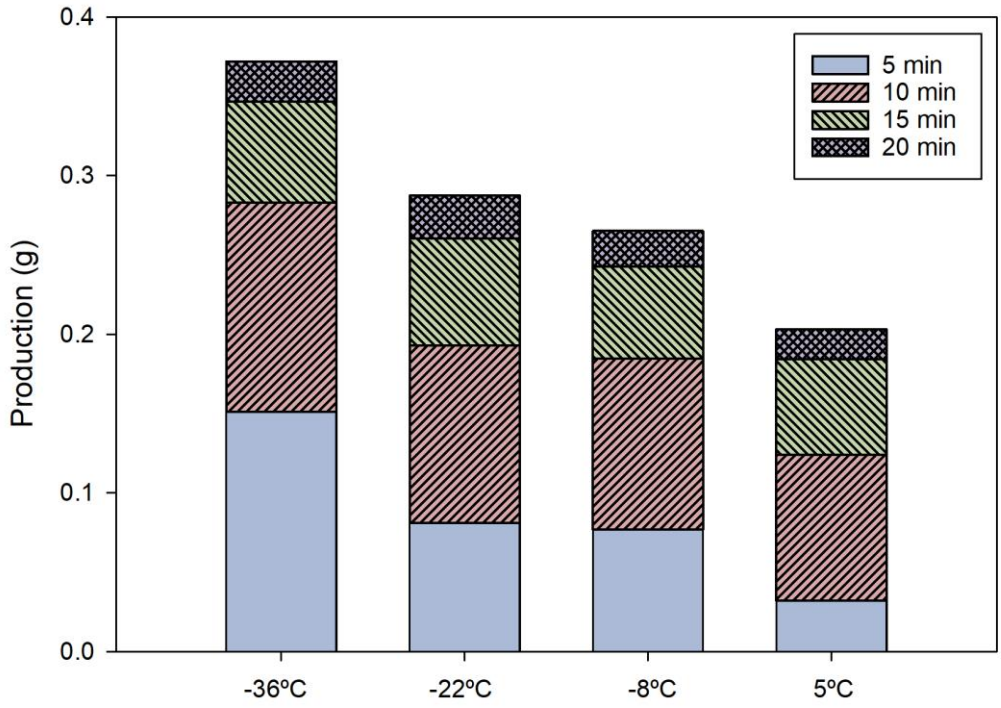


Fig. 4-13: Experimental data of production with different coolant temperature on bare tube.

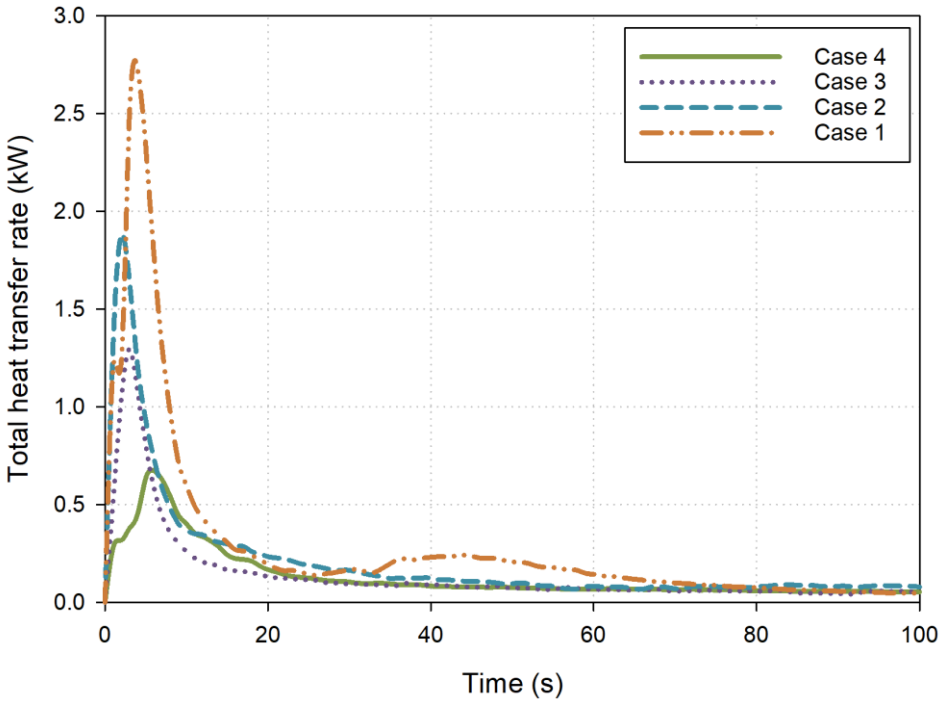


Fig. 4-14: Experimental data of total heat transfer performance in different cases on the bare tube.

4.3.3 Effect of surface characteristics on condensation

In this section, the condensation phenomenon and the performance of all the sample tubes are explored for Case 4. The coolant temperature is fixed at 6ºC with a flow rate of 6.4 l/min. And the initial environment temperature is controlled at 25ºC and relative humidity of 90%. The performance of the mass transfer and heat transfer of the condensation process are compared on different tubes.

Fig. 4-15 presents the water accumulation trend with the wall temperature on four different tubes during the 20-minute experiment time. As the surface temperature decreases, the production increases rapidly and subsequently becomes stable. This makes a small influence of the conductive thermal resistance of the coating thickness. According to the condensation mechanism, higher CA surfaces require higher

supersaturation to nucleate for phase change, the water vapour on the Fluorine based tube condenses at a later stage, leading to the worst production.

Fig. 4-16 compares the specific heat transfer amount of 4 tubes, including the sensible heat transfer and the latent heat transfer between the moist air and the substrate surface during the experiment time. The trend is similar to the production analysis. The sensible heat transfer is related to the heat transfer coefficient and the temperature difference between the moist air and the droplet while the latent heat is related to the droplet formation and growth rate. Therefore, latent heat as a leading role affects the heat transfer performance, which is more efficient than sensible heat transfer leading to lower air temperature conditions. The heat transfer for the FEP is the highest among the four tubes. The reason is that the FEP coating creates dropwise condensation on the surface, leading to the highest heat transfer coefficient. For the hydrophobic surfaces, the condensate droplets form spherical shapes and cover a smaller surface area, thereby leading to more free surfaces contacting with the moist air directly [80]. And the presence of the droplets roughens the condensation surface and changes the temperature gradient near the surface, accelerating the latent heat transfer [130].

The comparison in the averaged condensation heat transfer coefficient on each tube during the experimental period is also analysed, as shown in Fig. 4-17. The condensation heat transfer coefficient illustrates the condensation performance on the uncoated and coated tubes, following the decreased tendency as FEP, PTFE, Bare and Fluorine based, same as the water accumulation results shown in Fig. 4-15. Although the thermal resistance of the condensate increases with condensate amount, the increase in the condensation heat transfer on FEP tube is much larger, which

represents that the thermal resistance of the condensation convection is lower [80]. Therefore, the condensation process is intensified by FEP and PTFE tubes while weakened by the Fluorine based tube. As a result, an effectiveness enhancement factor to express the heat transfer performance for each tube is defined as:

$$f_m = \frac{k}{k_{bare}} \tag{4-1}$$

And based on the measurement, the enhancement factors for the coated tube are defined as: $f_{m,Fl}$= 0.8, $f_{m,FEP}$= 2.1 and $f_{m,PTFE}$ = 1.5.

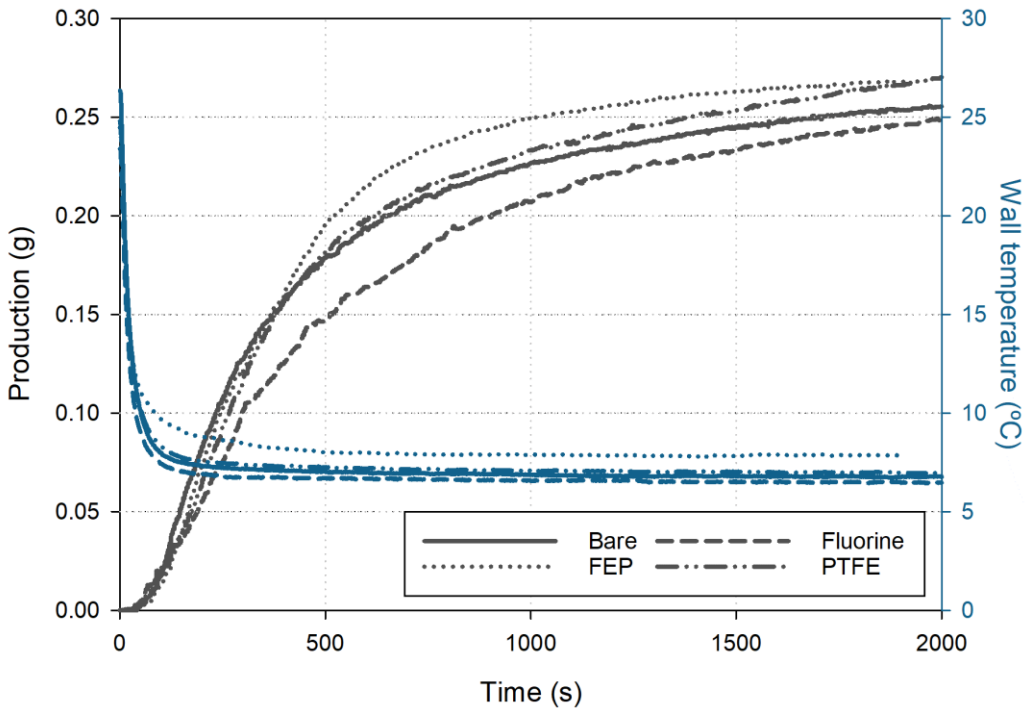


Fig. 4-15: Experimental data of water accumulation and wall temperature with different sample tube.

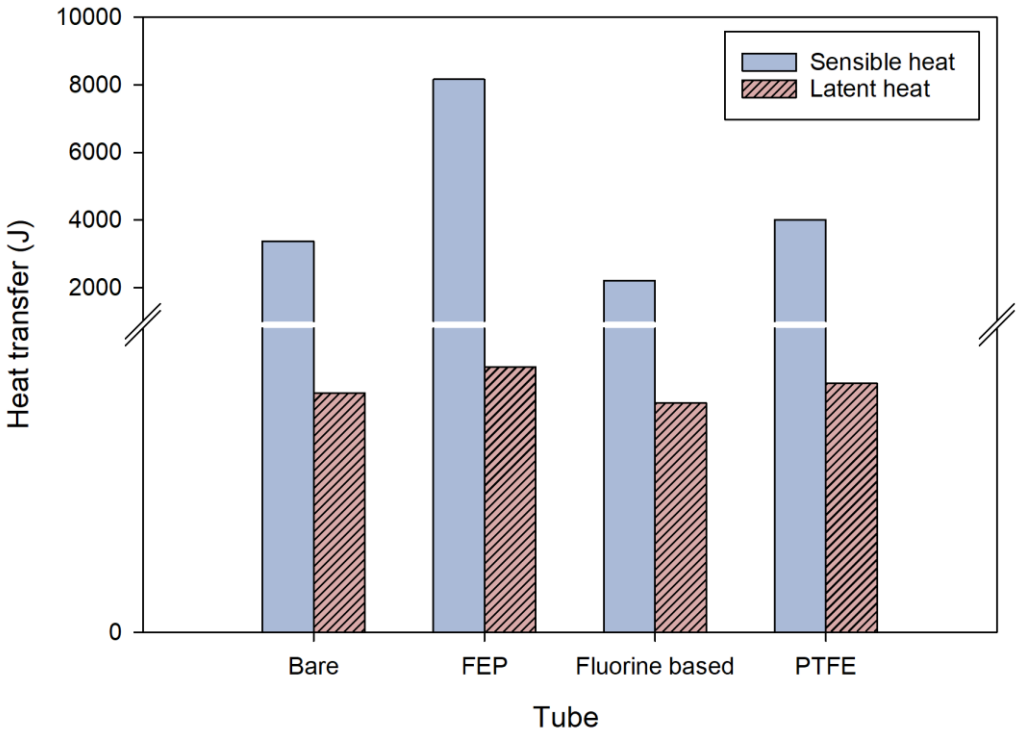


Fig. 4-16: Experimental data of heat transfer performance comparison.

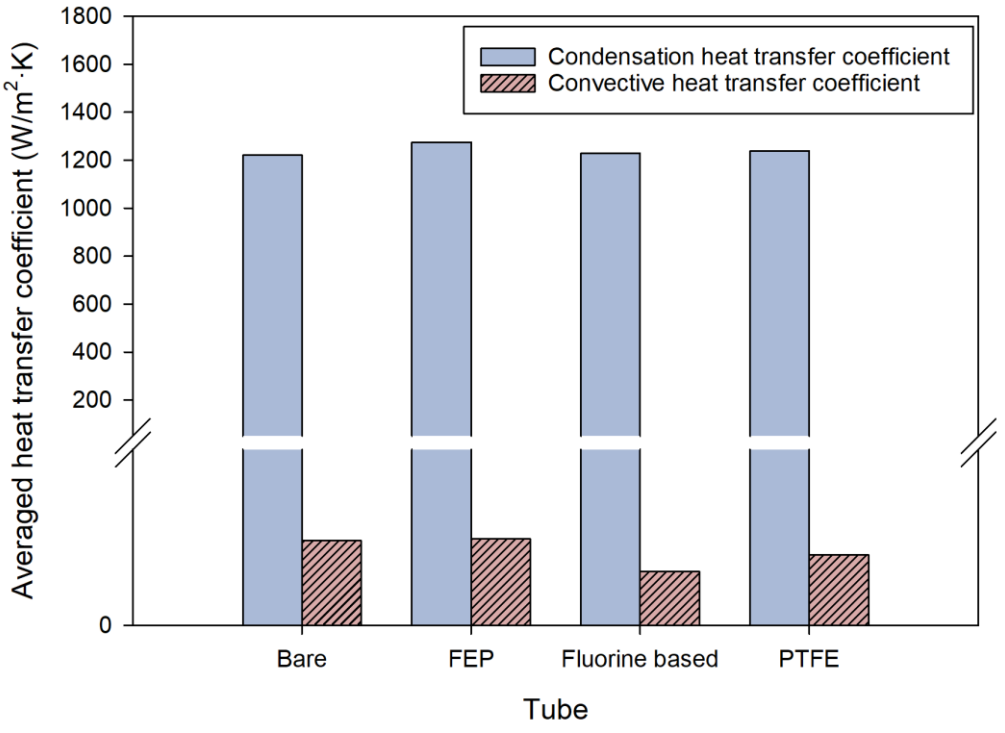


Fig. 4-17: Averaged condensation heat transfer coefficient on different tubes.

4.3.4 Condensation frosting mechanism case

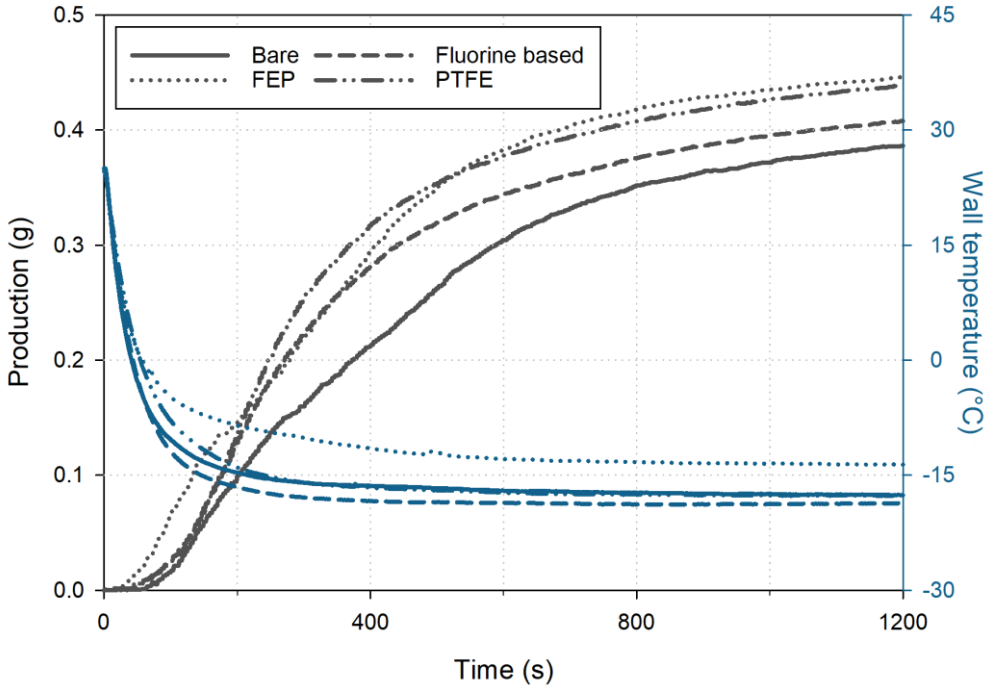
In this case, the condensation frosting phenomenon and the performance on all the sample tubes in Case 2 are explored. The coolant temperature is fixed at -22ºC with a flow rate of 4.2 l/min. And the initial environment is controlled at the temperature of 25ºC and relative humidity of 90%. The performance of the mass transfer and heat transfer of the condensation frosting process are analysed. And based on the specific phenomena on the surface obtained from the captured morphology images, the start time of the freezing and the frost coverage area ratio (the ratio of the frost-covered area to the total surface area) on all the sample substrates are also compared.

The frost accumulation measured after the experiment including the condensate and frost on four tubes is shown in Fig. 4-18. The frost on all the tubes presents the similar deposition trend in the same period. FEP and PTFE show the best production and then the Fluorine based tube. The water/ice extraction trends on these four tubes follow the supersaturation theory as mentioned in Section 3. As the coolant temperature decreases, the increased supersaturation helps to promote the condensation ability on the higher CA surface.

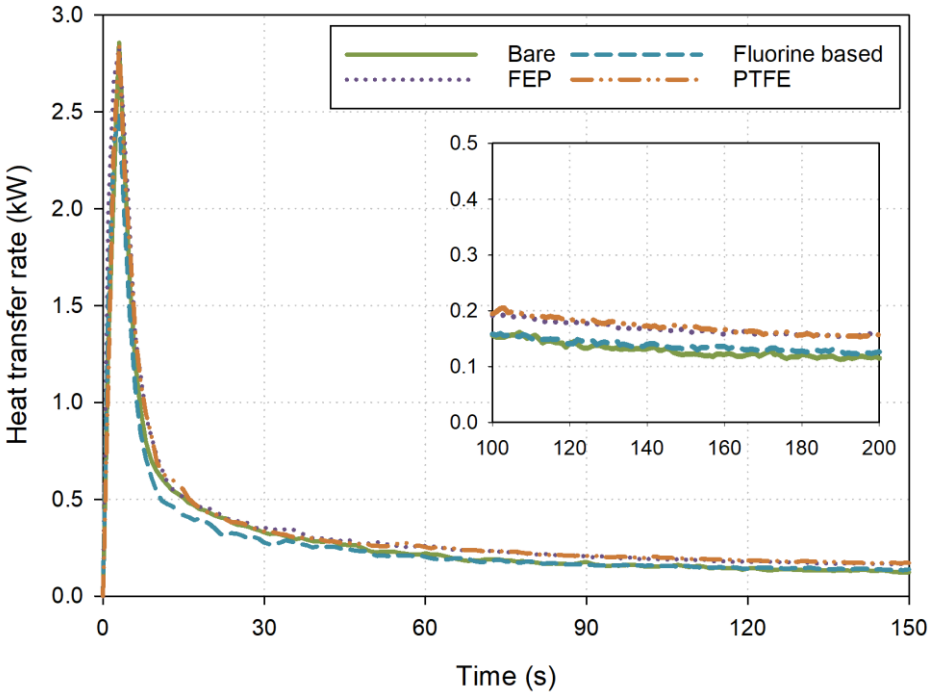
The onset of freezing start time and increasing trend of the frost coverage area can be detected by visualisation results on different surfaces. The ratio of the frost area to the total surface area defined as frost covered percentage of surface on each surface is detected as shown in Fig. 4-19. The freeze delay time is defined as the supercooling period between the freeze start time and freezing point (0ºC) [131]. Fig. 4-20 shows the variations of surface temperature versus time on the bare and the treated surfaces. The plots could be divided into three stages. At the beginning of the experiment, water

vapour first condenses on the substrate to form nanoscale droplets. Continuous vapour condensation then leads to the droplets' growth and coalescence. Preferred heterogeneous ice nucleation occurs at the interface between the droplets and the substrate when the supercooled droplet stays on the sub-zero degree substrate for a long enough period of time. The comparison of the delay time between these tubes proved the anti-freezing characteristic of the hydrophobic surfaces. The diagrams show that the bare tube is the first tube to start to freeze at the time around 43s with the surface temperature at -2.6ºC. As the experiment continues, the frost coverage area increases slowly until fully covered at t = 1800s. Then the first frost halo occurs on the FEP tube from 63s with the surface temperature at -1ºC. At the same time, the PTFE tube starts to freeze at 65s when the surface temperature reaches -1.7ºC. Then the frost area increases as the decrease of the surface temperature due to the ice bridge built between the frost halos and the water halos. From t = 780s, the tube surface is fully covered by the frost. The Fluorine based tube with the highest hydrophobicity is the last one to start freezing on the tube at 94s when the surface temperature reaches -10ºC. In the current case, it is clear that the lower surface energy helps extend the supercool period and then delay the freeze time. Although compared to the bare tube, FEP and PTFE tubes present the characteristic of frosting delay, the freeze happens at higher surface temperatures. On one hand, the surface energy provides an extension of time. On the other hand, according to the mechanism mentioned earlier, freezing only happens when the temperature of the droplets declines below 0ºC [82]. The extra thermal resistances resulting from the coating thickness and the worse thermal conductivity drive less heat transfer between the coolant and the surface. The surface temperature decreases at a slower speed but

generates more water droplets covering the surface. Then these droplets absorb the heat from the surface and motivate the decrease of the inside temperature with a slower speed to 0ºC with the constant heat transfer.



(a) Production variation with different tubes.



(b) Heat transfer performance comparison on different tubes.

Fig. 4-18: Experimental data of production and heat transfer performance with a coolant temperature of -22ºC.

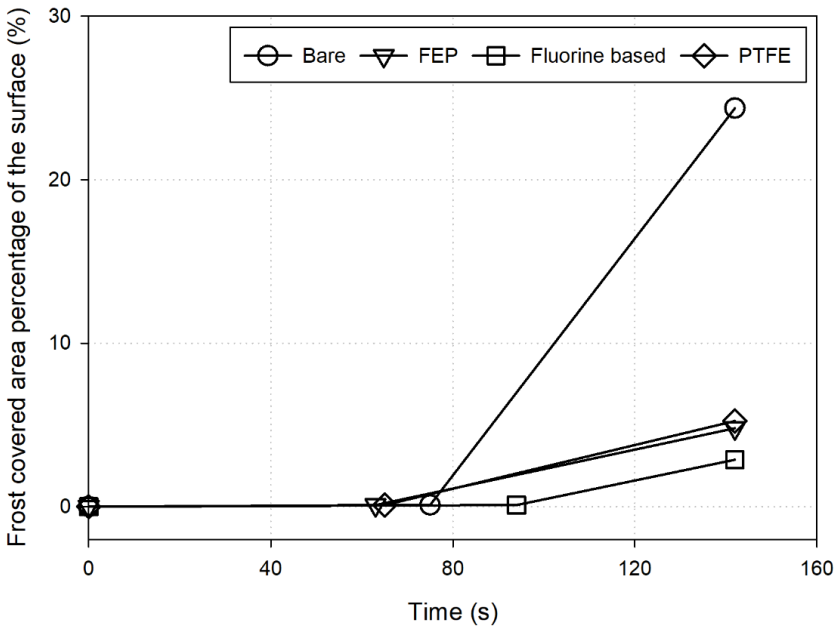


Fig. 4-19: Frost covered area percentage of the surface with a coolant temperature of -22ºC.

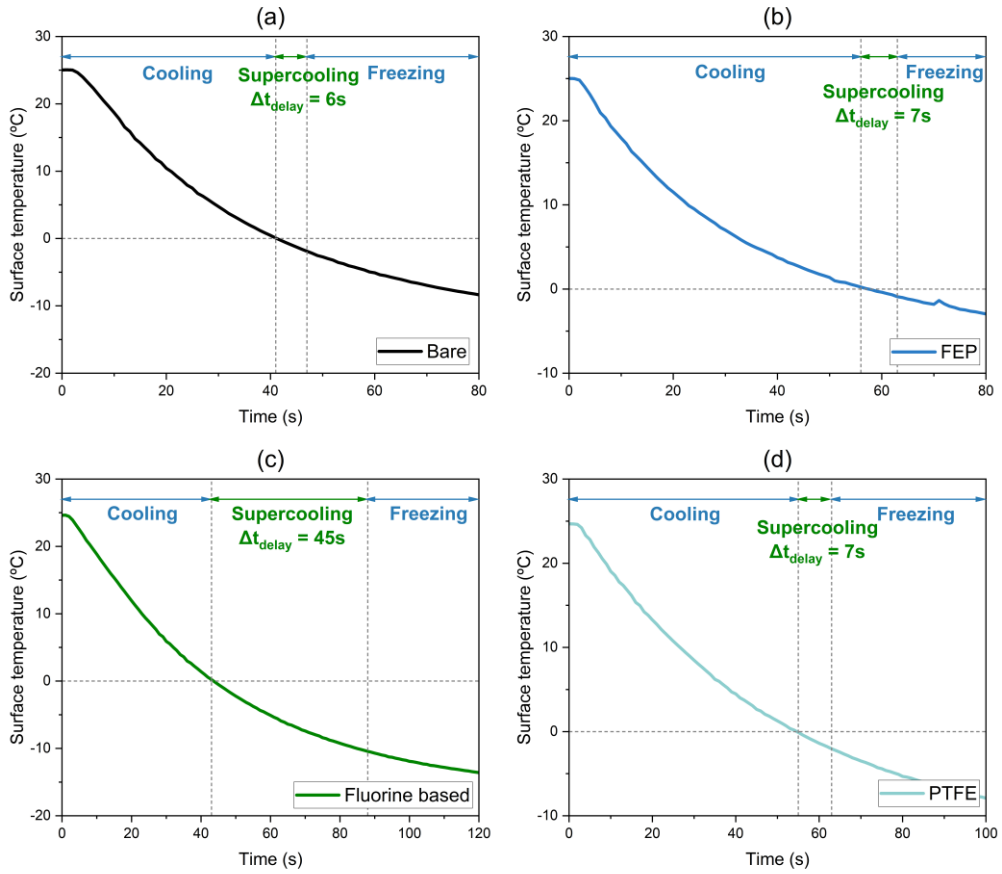


Fig. 4-20: The temperature profile with time on four surfaces with a coolant temperature of -22ºC.

4.3.5 Direct frosting

In this case, the frosting phenomenon and the performance on all the sample tubes in Case 1 are studied. The temperature of the coolant is constantly processed at -36ºC with a flow rate of 2.6 l/min. And the initial environment temperature is controlled at 25ºC and relative humidity of 90%. The performance consisting of frost accumulation, heat transfer and morphology of the frosting process are analysed. And based on the experimental data of the frost properties, the empirical correlation of the frost porosity is proposed.

The production results for these four different coating samples: bare, FEP, PTFE, Fluorine based tubes are shown in Fig. 4-21. The frost accumulation increases with the increase of the static CA. As the surface temperature decreases at the beginning, the Fluorine based tube with higher hydrophobicity required a higher supersaturation degree and extended the condensation period compared with the other three tubes. Water droplets formed on the surface have higher temperatures, leading to extra condensation to increase the embryo sizes. Therefore, more frost is accumulated on the Fluorine based tube. Although the coolant temperature is the same in all the experiments, the surface temperature on FEP and PTFE surfaces is higher than the other two. The reason is the thickness of the FEP and PTFE coating of 20-50μm and the lower thermal conductivity resulting in the extra thermal resistance and worse heat transfer which was introduced in the later section.

Fig. 4-22 compares the frost thickness on the different treatment sample tubes. The frost thickness grows the fastest at the early stage of the experiment because the supersaturation degree is one of the factors affecting the mass transfer on the surface in the phase change process. It is defined as the difference between the water vapour pressure of the humid air ($p_{v,a}$) and the saturation pressure of the surface temperature ($p_{v,s}$). When the experiment starts, the surface temperature drops immediately which lowers the saturation pressure and then increases the supersaturation degree. Then the frost thickness grows slowly from around 13 minutes of the experiment. On one hand, the formed frost layer on the surface increased the thermal resistance and decreased heat transfer [110]. On the other hand, as time goes by, the reduced water vapour content in the chamber leads to less water vapour in the humid air contributing to the frost layer growth but to the frost density. After 16 min, the frost thickness is

reduced due to the frost crystal's interaction. At this stage, the frost density is the highest.

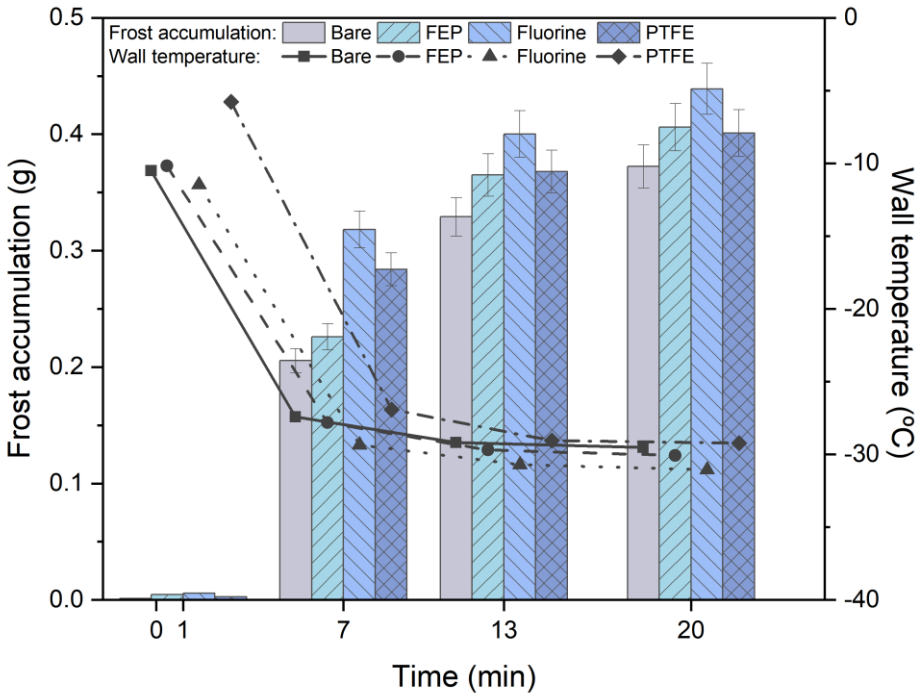


Fig. 4-21: Experimental data of frost accumulation comparison with different coatings with a coolant temperature of -36ºC.

As indicated in the diagram, the thickness of the frost layer is the highest on the bare tube, and then FEP, PTFE, Fluorine based. The reason is that these hydrophobic coatings could retard frost formation. At the early stages of the experiments, the water vapour in the humid air condensed into water droplets on the surface and then solidified. Then after all the surfaces are covered with a frost layer, there is no direct contact between the humid air and the surfaces, the frost growth rate becomes similar. The thermal resistance of the frost related to the frost thickness is lower than the uncoated tube, resulting in a better heat transfer performance. During the total 100 min

experimental study Huang, et al. [107], the frost thickness presents the same trend as the current study.

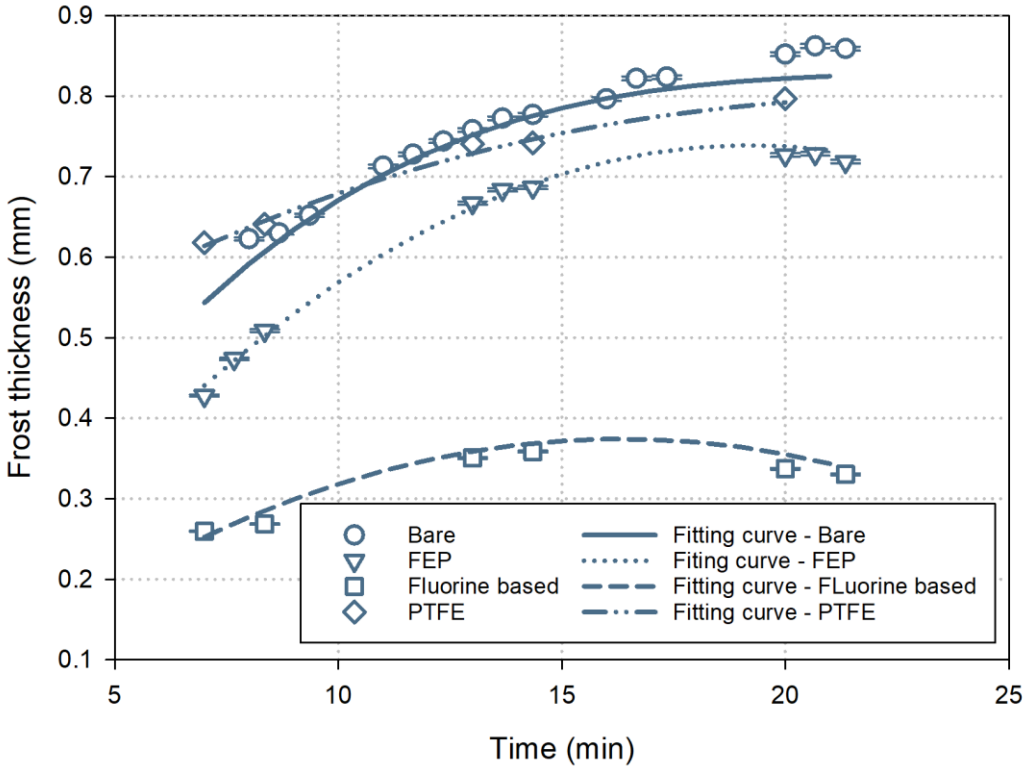


Fig. 4-22: Experimental data of frost thickness comparison with different coatings with a coolant temperature of -36ºC.

The comparison of the averaged frost density at 8.35 min and 20 min is presented in Fig. 4-23. Under the same conditions, the frost density was the highest on the Fluorine based tube and the lowest on the bare tube. As presented earlier, the lowest frost thickness and the highest frost accumulation resulted in the highest frost density on the Fluorine based tube.

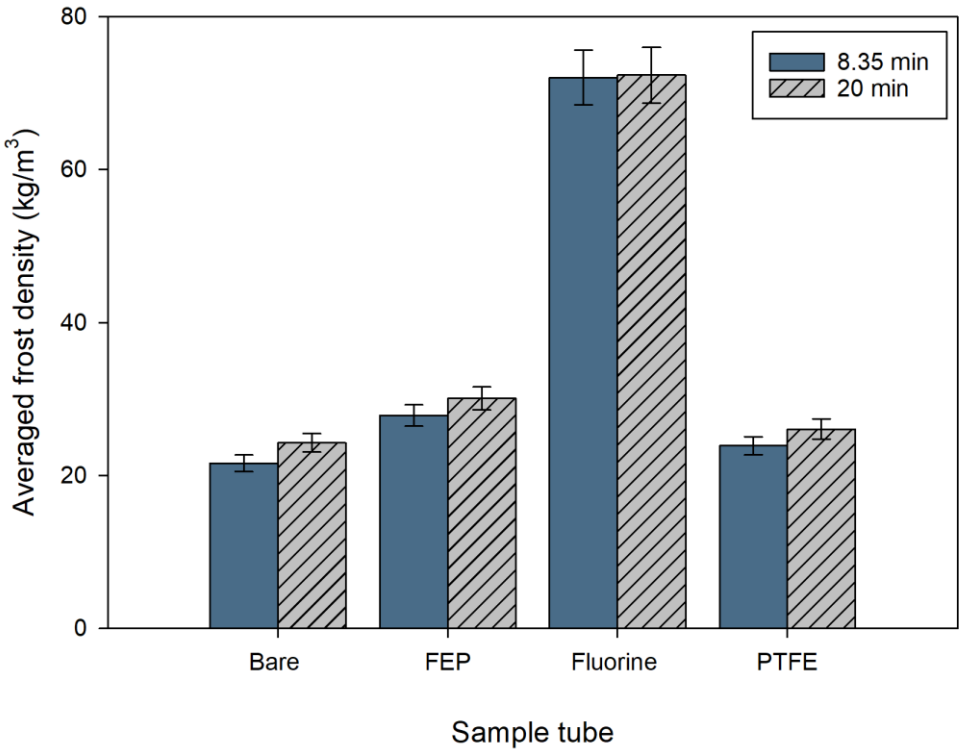


Fig. 4-23: Experimental data of frost density comparison with different coatings with a coolant temperature of -36ºC.

The total heat flux and the frost surface temperature with the different coatings are shown in Fig. 4-24. In general, the trend of the total heat flux to the surface is similar on each coating. The heat flux increased rapidly at the beginning and decreased steadily at the final stage, the same as the frost layer growth trend. Before the frost layer covers the surface, a significant temperature difference between the wall temperature and the humid air helps to increase the heat transfer coefficient. And the formation of the small droplets and crystals, as the fins, enhanced the heat transfer. After the frost layer covers all of the surface, the frost layer, as an extra thermal resistance, weakens the heat transfer ability. The Fluorine based coating presents 16% and 19.5% greater heat transfer performance than the other two coatings. Due to the

worse thermal conductivity and the extra thickness of the FEP and the PTFE coating, the same heat transfer performance with the bare tube is indicated.

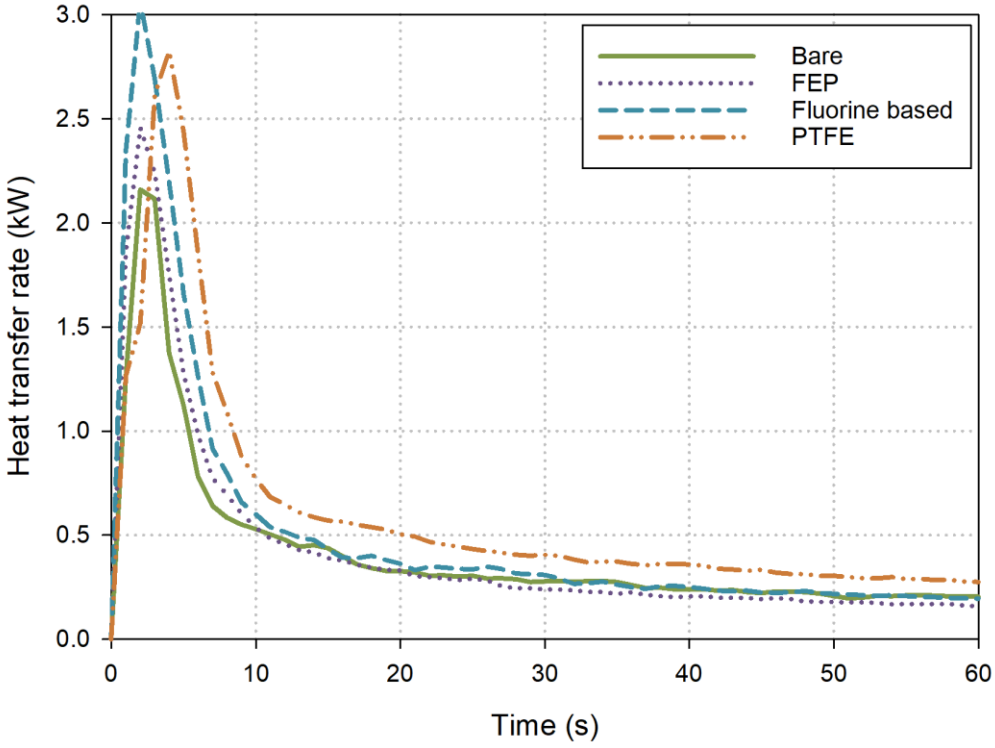


Fig. 4-24: Experimental data of heat transfer rate comparison on different coatings with a coolant temperature of -36ºC.

The theoretical model for predicting the frosting properties mainly relies on two assumptions: (a) the frost is a uniform porous media consisting of column-shaped ice crystals [132, 133]; and (b) the temperature difference between the ice crystal tips and the surface is constant. In the current study, the frost layer is defined as a porous medium comprised of moist air and ice crystals, and the frost density could be calculated from the porosity of the frost as follows:

$$\rho_f = \rho_a \cdot \chi + \rho_{ice}(1-\chi) \tag{4-2}$$

where ρ_a and ρ_{ice} are the densities of the air and ice, respectively. And χ is the frost porosity.

A few theories to predict the frost density were investigated in the modern days. From the theory of Fletcher [122], Şahin [132] and Hermes, et al. [113], the frost could be modelled as an array of ice columns, as shown in Fig. 4-25. As Hermes, et al. [113] defined, the porosity of the frost layer on the surface could be calculated as the following,

$$\chi = 1 - C\sqrt{t} \tag{4-3}$$

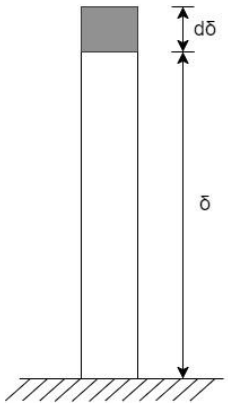


Fig. 4-25: Schematic of the frost column growth.

Experimental data of Case 1 has been summarised in Table 4-3, which are applied to determine the C-coefficient in Eq. (4-3). The dataset of Case 1 on all the sample tubes, which span the relative humidity from 10% to 90%, surface temperature from -30 to -10ºC and air temperature from 24 to 25ºC, was applied to the system. Based on the curve fitting shown in Fig. 4-26, the porosity has fitted the calculation presented in Eq. (4-3). A Jacob number, the sensible-to-latent-heat ratio, defined by Hermes [134], is introduced in Eq. (4-4). As the frost property is related to properties of the air, surface

temperature and surface material, the coefficient C could be expressed as a function of these parameters, as shown in Eq. (4-5). Therefore, the porosity and the frost density are expressed in Eq. (4-6) and Eq. (4-7).

$$Ja = \frac{c_p}{L} \cdot \frac{T_{sat,a} - T_w}{\omega_a - \omega_{sat,w}} \tag{4-4}$$

$$C = 0.009 \cdot Ja^{-0.4} \cdot (\frac{100}{RH})^{0.04} \cdot |cosCA| \tag{4-5}$$

$$\varepsilon = 1 - 0.009 \cdot Ja^{-0.4} \cdot (\frac{100}{RH})^{0.04} \cdot |cosCA| \cdot \sqrt{t} \tag{4-6}$$

$$\rho_f = \rho_{ice} - (1 - 0.009 \cdot Ja^{-0.4} \cdot \left(\frac{100}{RH}\right)^{0.04} \cdot |cosCA| \cdot \sqrt{t}) \cdot (\rho_{ice} - \rho_a) \tag{4-7}$$

Where RH is the relative humidity in the system, ρ_{ice} and ρ_a are the densities of the ice and air, respectively.

Table 4-3 C-values fitted to the experimental data in Case 1.

T_a (ºC)	RH	T_w (ºC)	CA (º)	t (s)	χ
25.0	51.0	-28.0	82	480	0.981
25.0	46.6	-28.3	82	520	0.978
24.9	44.2	-28.5	82	561	0.965
24.9	37.9	-28.9	82	660	0.962
24.8	36.1	-29.0	82	700	0.960
24.9	34.6	-29.1	82	741	0.951
24.7	33.0	-29.2	82	780	0.949
24.7	31.5	-29.2	82	820	0.946
24.7	30.6	-29.3	82	861	0.939

24.7	28.6	-29.4	82	960	0.936
24.6	27.8	-29.4	82	1000	0.934
24.6	27.1	-29.4	82	1041	0.929
24.8	24.5	-29.5	82	1200	0.925
24.5	24.5	-29.5	82	1241	0.924
24.5	23.9	-29.6	82	1281	0.913
24.6	54.4	-27.2	99	420	0.971
24.6	51.1	-27.6	99	460	0.971
24.6	46.9	-27.9	99	501	0.970
24.3	28.8	-29.0	99	780	0.969
24.3	27.1	-29.1	99	820	0.969
24.3	26.1	-29.2	99	861	0.969
24.1	20.0	-29.5	99	1200	0.968
24.1	19.4	-29.5	99	1241	0.968
24.1	19.0	-29.5	99	1281	0.968
25.6	35.8	-29.3	118	420	0.927
25.6	30.3	-29.9	118	501	0.923
25.3	20.7	-30.7	118	780	0.932
25.2	19.0	-30.8	118	820	0.932
25.0	13.5	-31.1	118	1200	0.922
25.0	12.5	-31.0	118	1241	0.917
25.5	50.3	-25.8	98.32	420	0.977
25.5	43. 6	-27.1	98.32	501	0.975

25.3	32.5	-28.8	98.32	780	0.973
25.2	30.5	-28.8	98.32	861	0.972
25.0	26.0	-29.3	98.32	1200	0.972
22.2	57.2	-14.9	82	420	0.958
22.1	51.1	-15.96	82	501	0.9663
21.9	34.3	-17.8	82	780	0.974
21.9	31.6	-18.1	82	861	0.973
21.7	22.7	-18.6	82	1200	0.970
21.7	21.8	-18.6	82	1280	0.968

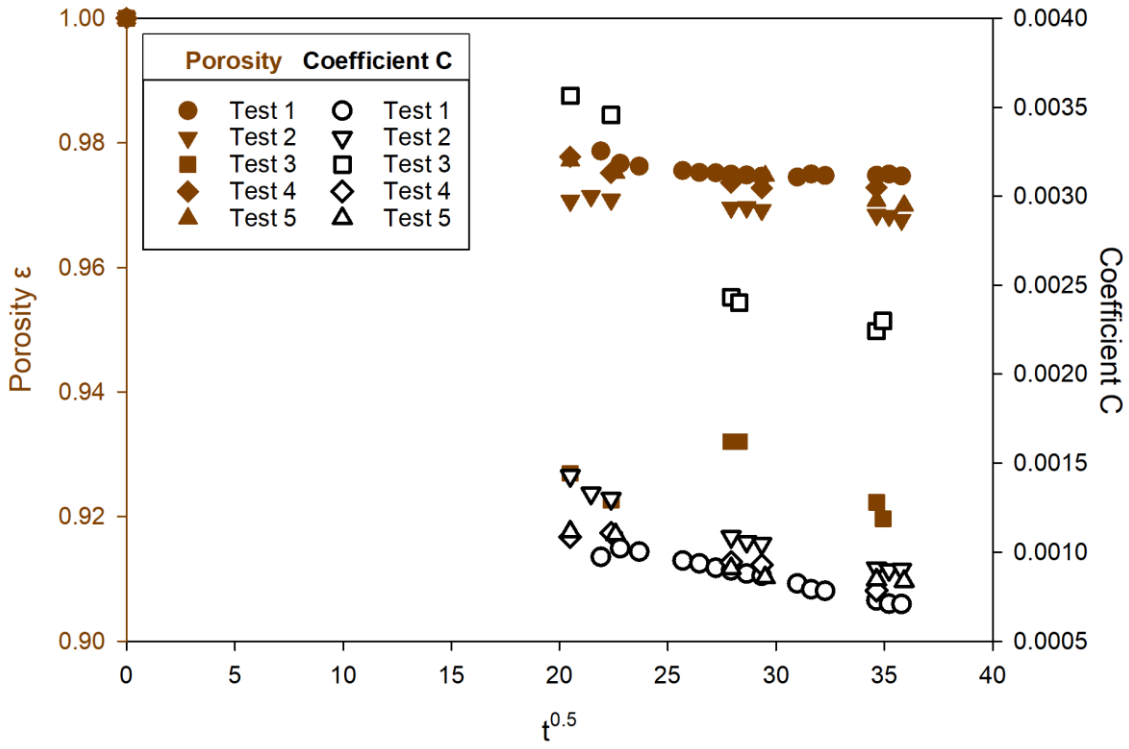


Fig. 4-26: Fitting of experimental data with the porosity and coefficient C.

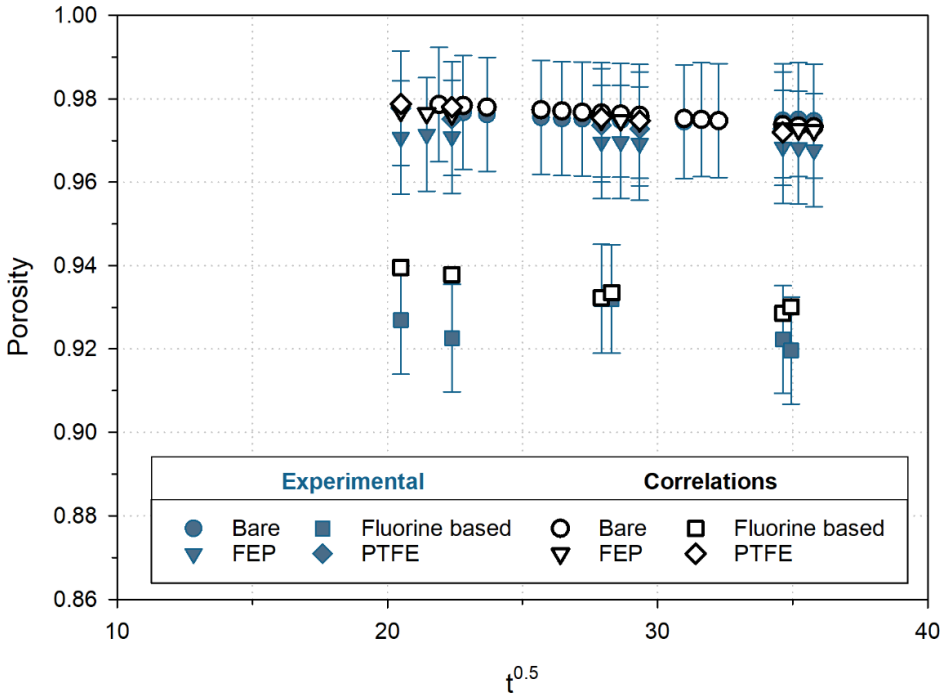
Fig. 4-27 illustrated the validation analysis of the frost porosity and the frost density from the experimental data and the proposed correlation. The new correlation has a good agreement with the experimental data which the error varied from 0.07% to 7% on bare tube, 6.5% to 14.7% on FEP tube, 0.8% to 15.3% on Fluorine based tube and 3.1% to 10.8% on PTFE tube. The Fluorine based coating has the highest error at the beginning time. The reason is that at an early stage, the frost thickness on the surface is uneven, which results in the measurements differences. Similarly, as defined by Hayashi, et al. [116], the thermal conductivity is also related to the porosity, and thermal conductivity of ice and air as follows,

$$\lambda_f = \lambda_a \cdot \chi + \lambda_{ice}(1-\chi) \tag{4-8}$$

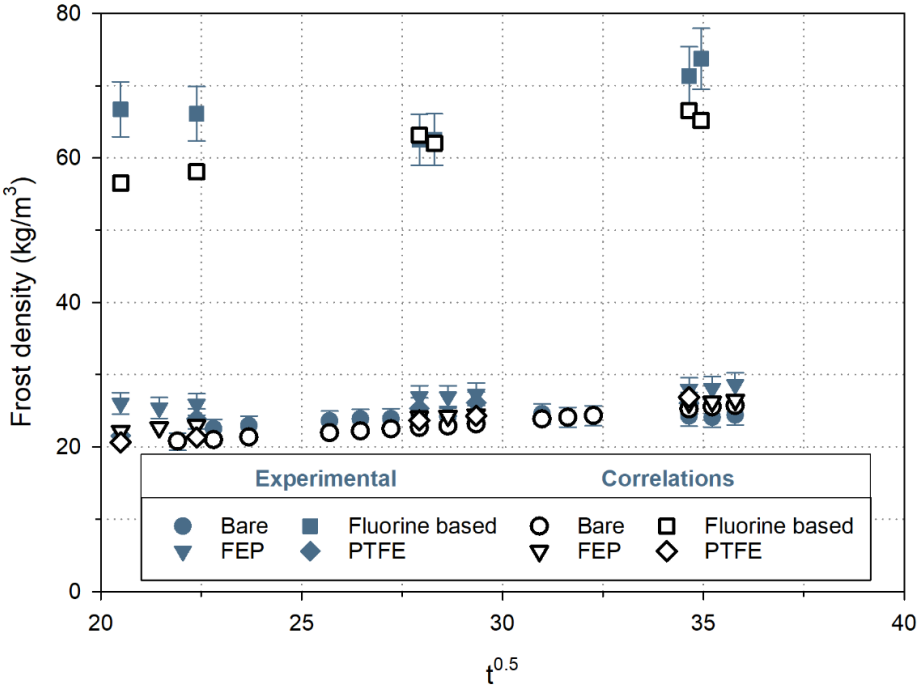
Therefore, recall from Eq. (4-6), the thermal conductivity of the frost could be calculated as follows,

$$\lambda_f = \lambda_{ice} - (\lambda_{ice} - \lambda_{ma}) \cdot (1 - 0.009Ja^{-0.4} \cdot |\cos CA| \cdot \left(\frac{1}{RH}\right)^{0.04} \sqrt{t}) \tag{4-9}$$

The new proposed correlation is intended for use on heat transfer surfaces under natural convection conditions with contact angles between 82° < CA < 120°, relative humidity 0.15 < RH < 0.95, surface temperatures −40 °C < T_w < −20 °C, and air temperatures 20 °C < T_a < 27 °C.



(a) Frost porosity



(b) Frost density

Fig. 4-27: Comparison analysis on frost porosity and density between the experimental and the correlation.

According to the investigations above, the effect of the surface characteristics on frost properties are summarized in Table 4-4. The frost thickness and the heat transfer results exhibit the same trend in most of the studies. As the hydrophobic treatment extends the condensation process, the frost production presents an increasing trend, therefore increasing the frost density.

Table 4-4 Comparison of the frost properties change trend with the CA.

Substrate type	Study	Surface temperature (ºC)	CA	Frost thickness	Frost accumulation	Frost density	Heat transfer
Plate	[108]	-10	↑	↓	-	-	-
	[117]	-22	↑	→	→	↓	-
	[107]	-26 to 0	↑	↑	-	-	-
Heat exchanger	[112]	-18 to -10	↑	↓	-	↓	-
	[105]	-10	↑	↓	↓	-	↑
	[135]	-9 to -4	↑	↓	→	-	-
Tube	Current	-36	↑	↓	↑	↑	↑

↑: increase, ↓: decrease, →: no change detected, -: data not given

4.3.6 Hybrid case

In this case, the temperature of the coolant is fixed at -8 ºC with a flow rate of 4.8 l/min. The initial environment is controlled at the temperature of 25 ºC and relative humidity of 90%. The performance of the mass transfer and the transition point of freezing are analysed. According to the images captured by the high-speed camera, the frozen transition time is recorded and compared as shown in Fig. 4-28. The freezing transition point for bare tube starts from the surface temperature of around -2.6 °C, while FEP

and PTFE tubes start from -3.3 °C and -4 °C. And from the morphology photos comparison on the four tubes, the formed droplets are more spherical on the PTFE and FEP tubes than on the bare tube due to the lower surface energy [111].

Fig. 4-29 compares the water and frost accumulation on four different tubes from the experimental data. As the surface temperature decreases, the production increases rapidly and then becomes stable. According to the condensation mechanism, the embryo nucleation on the surface requires supersaturation. Therefore, the production generated from Fluorine based has been promoted. Different production performance is measured as the surface temperature presents different changing trends due to the different mechanisms.

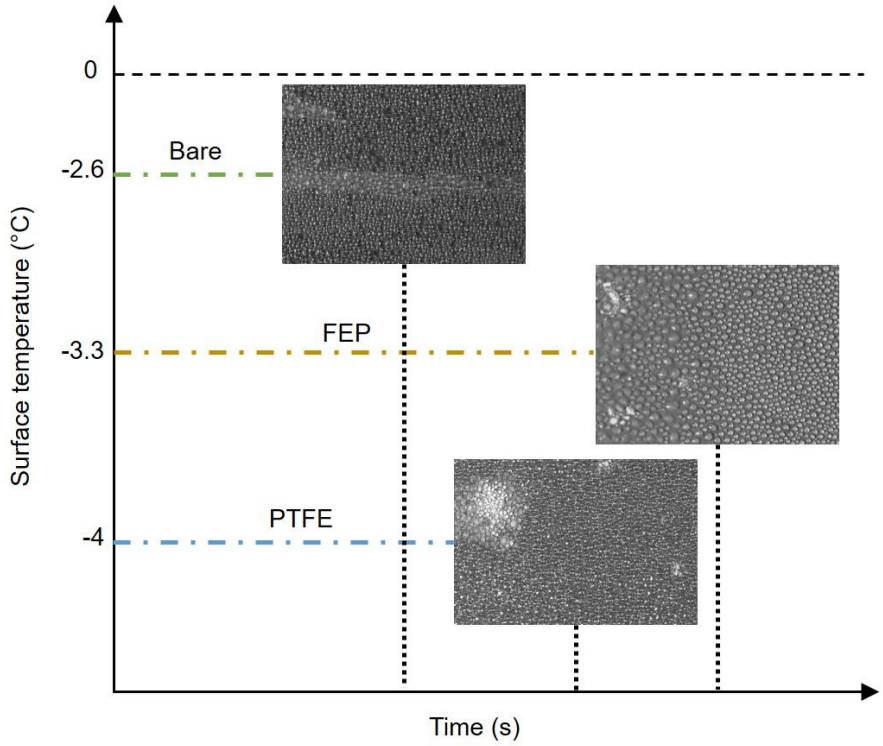


Fig. 4-28: Experimental data of transition point of the sample tubes with a coolant temperature of -8ºC.

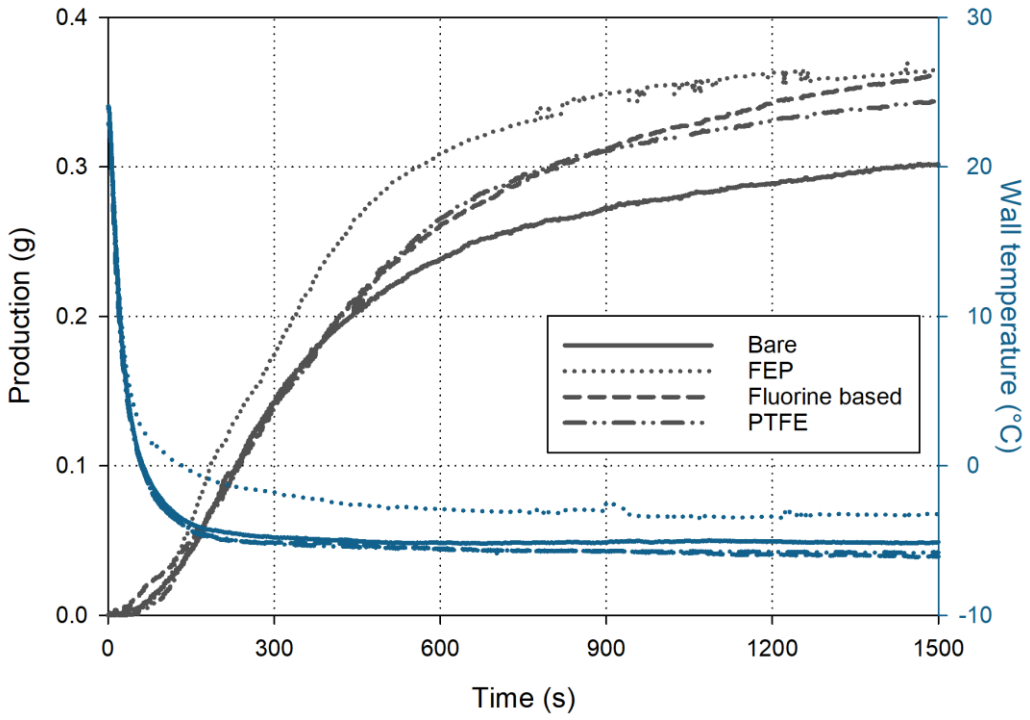


Fig. 4-29: Experimental data of production on four tubes with a coolant temperature of -8ºC.

4.4 Summary

In this chapter, the influence factors of the condensation process in water harvesting from the moist air, including the air property, surface wettability and surface temperature, have been studied experimentally. The experiments are operated on four tubes with different surface characteristics with four cases of different coolant temperatures at -36°C, -22°C, -8°C and 6°C to explore the performance in a wide temperature range. By exploring the mechanism and morphology photos, the characteristics of condensation, condensation frosting and desublimation has been classified by the surface temperature and the surface wettability. Subsequently, the corresponding mass transfer and heat transfer performance and properties are

analysed. The experimental results show that the water production and the heat transfer are promoted by the greater subcooling degree and water vapour content.

The effect of the surface characteristic is investigated by the four different coolant temperatures. For the condensation case, the enhancement factor of the coating material on heat transfer coefficient has been concluded. The hydrophobic coatings have significant effects on the condensation intensification with an enhancement factor of 2.1 times that of untreated. For the condensation frosting case, it is concluded that the FEP and PTFE tube could provide the anti-freezing characteristic in the surface temperature of -4°C to 0°C while the Fluorine based tube extends the temperature range to -8°C. For the frosting case, the Fluorine based tube with the highest CA provides the best anti-freezing characteristic by reducing the frost thickness and a highest freezing delay characteristics for up to 45 seconds compared to plain tubes. Furthermore, a new semi-empirical correlation summarized from the 41 groups of experimental data and obtained from the exhibited frost characteristics on four sample tubes is proposed with an error within ±15%. The correlation provides an alternative method for frost porosity prediction when the experiments are unavailable due to the facilities' limitations. Therefore, the reduced frost deposition conditions resulting from the novel hydrophobic coatings can be leveraged to optimise the geometry of heat exchangers to achieve thermal efficiency that may have been sacrificed from the frost formation.

From the investigations, surface modification provides a potential method for a wide range of applications, including condensation heat exchangers, thermal desalination, food storage and micro fluids. The experimental work in this chapter explored the

performance under all regimes' conditions: condensation, condensation frosting and desublimation. These experimental results with all these regimes could be extended to the full temperature range for industrial applications. Therefore, the work in Chapter 5 focuses on analysing the performance of heat exchangers exposed to a broader range of ambient conditions numerically.

CHAPTER 5 NUMERICAL ANALYSIS

5.1 Introduction

Based on the literature review and experimental results presented in Chapter 2 and Chapter 4, the experimental approach has investigated the performance under various operating conditions in a heat exchanger with all the mechanisms. Therefore, in order to explore the performance under the full temperature range, the numerical study is developed. Firstly, a thorough description and experimental literature validation of the analytical model of the proposed novel FWG are presented. And a further parametric analysis is carried out to maximise the freshwater generation, including the operation parameters of the evaporator and condenser and the geometry design of the condenser. Furthermore, it is necessary to take the frosting and vaporisation of the numerical model of the vaporiser into consideration comprehensively. This chapter proposes a numerical model prediction that accounts for the frosting on the vaporiser surface.

5.2 System description

Fig. 5-1 illustrates an innovative freshwater generator system assisted by LNG cryogenic energy. The system mainly consists of five parts: feed water part, evaporation part, condensation part, freshwater part and accessories. Seawater is injected into a vacuum-pressure evaporator chamber maintained by a vacuum pump. During the evaporation process, the unsalted portion of water is evaporated into the vapour phase, and the rest with a high concentration of salt is drained off from the bottom as brine. Then the pure vapour enters the condenser to be condensed by the

cold energy provided by LNG regasification into freshwater. At the same time, the regasified LNG from the LNG storage tank flows through the condenser pipes and turns into NG that provides fuel for the main engine while supporting the cold energy to the condenser.

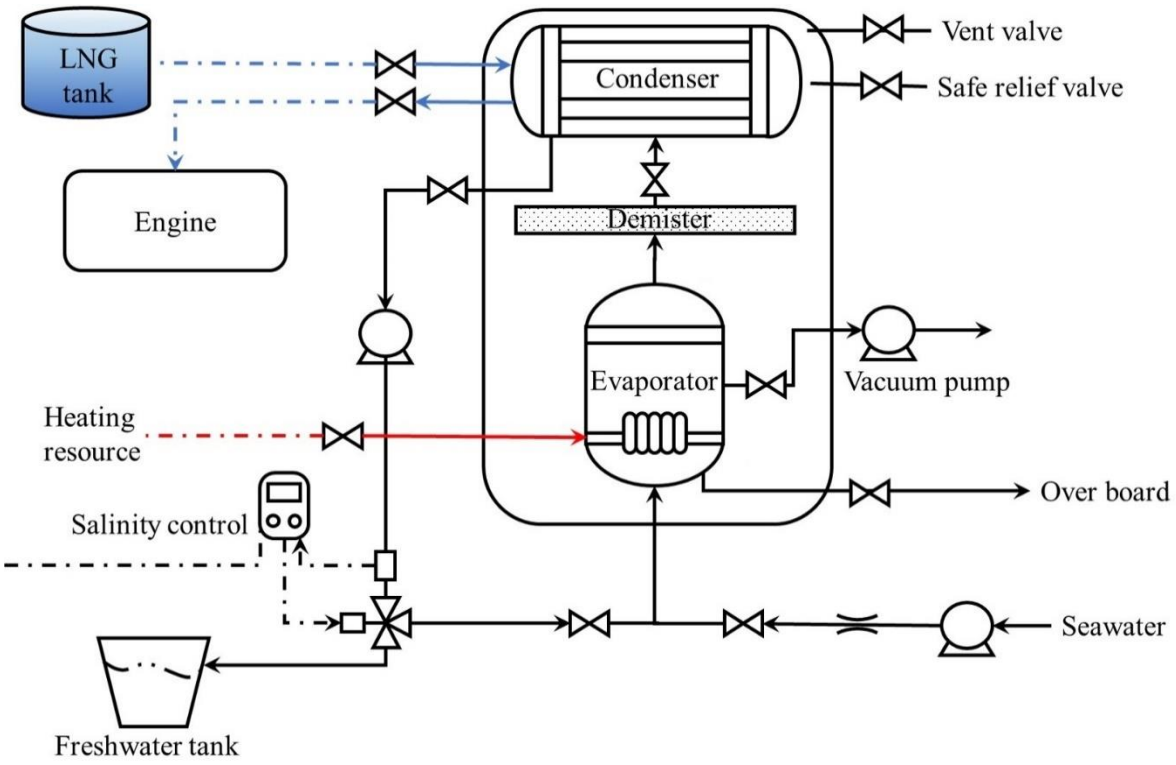


Fig. 5-1: Schematic diagram of the FWG system.

The flash evaporation chamber and the condenser in the system are developed and optimised using numerical method. Two sub-models of the evaporation chamber and the condenser are built in Siemens Simcenter Amesim and validated by the experimental results from the references articles and experimental data in Chapter 4. Both operation and geometry parameters are simulated and analysed. The water production, heat transfer performance and frost effects are evaluated.

5.3 Methodology

In the current study, the model developed in the Siemens Simcenter Amesim focuses on the parametric analysis of each component without surface treatment. As introduced in the earlier section, the surface temperature is the key that determines the mechanism of the condensation and frosting process. The experimental investigations proved that the surface temperature beneath 0ºC on the bare tube only has one mechanism: desublimation. Therefore, the condensation performance is applied and analysed for the cases of the surface temperature above this critical temperature. And for the cases that the surface temperature is beneath the critical temperature, the frosting model is employed.

In general, the heat and mass transfer processes could be obtained by two main methods: numerical study and experimental investigation. Although the experimental measuring method provides the most reliable results, it is limited in extreme conditions. The numerical approach has the advantages of a lower price, variable conditions, complete information throughout the whole domain of analysis and the ability to simulate ideal conditions. However, there are also some restrictions, such as the thorough understanding of requirements and the credibility of the models. Therefore, it is essential to validate the models with the physical data.

The basis of the numerical analysis in this study is designed to fit with the principle of heat and mass transfer. The modelling, analysis and prediction of the system is performed in a commercial simulation software, Simcenter Amesim, which could create models rapidly, virtually assess and optimise designs, boost overall systems

engineering and access application and industry-oriented solutions. It is an integrated system simulation platform using nonlinear time-dependent analytical equations in the advanced 1D simulation environment. Amesim combines multi-physics libraries with application- and industry-oriented solutions supported to create models and perform analysis. To develop a model for a system, a set of libraries is used which contain pre-defined components for different physical domains, e.g., mechanical, electrical, electronic, hydraulic, thermal, control, electric power or process-oriented subcomponents. Based on the Bond graph theory, the component must be connected, and each component contains a variety of inputs and outputs for this purpose. The causality is established by connecting one component's inputs to another component's outputs, (and vice versa). The libraries are written in C language and support Modelica, which is a non-proprietary, object-oriented, equation-based language to model complex physical systems, including thermal management system, electrical system, fluid system, mechanical system, propulsion system, ROM builder and system integration.

The modelling of a flash evaporation chamber and a compact condenser in the proposed FWG is based on the following assumptions:

(1) The evaporator is developed in a controlled volume.
(2) The generated water vapour is salt-free.
(3) The consumption of pump and valves and the heat loss between the evaporator/the condenser and the environment are negligible.
(4) The vacuum condition in the evaporation chamber and the condenser can be maintained throughout.

(5) The mixture of the vapour and minor quantity of air in the system are considered moist air.

5.3.1 Air property

The environmental air properties are modelled as a mixture of dry air (subscript as *da*), which consists of several gases such as nitrogen, oxygen and argon, and water vapour (subscript as wv below). Each component has a partial pressure according to Dalton's Law as follows [136],

$$p_{ma} = p_{da} + p_{wv} \tag{5-1}$$

The perfect gas equation could be applied to achieve the partial pressure of each component as follows,

$$p_{da} = m_{da} \cdot R_v \cdot \frac{T}{V} \tag{5-2}$$

$$p_{wv} = m_{wv} \cdot R_v \cdot \frac{T}{V} \tag{5-3}$$

The absolute humidity is defined as the ratio of the water vapour mass to the dry air mass,

$$\omega = \frac{m_{wv}}{m_{da}} \tag{5-4}$$

Another humidity parameter is relative humidity, defined as the water vapour partial pressure to the saturated vapour pressure,

$$RH = \frac{p_{wv}}{p_{wv,sat}} \times 100\% \tag{5-5}$$

And the specific enthalpy of the moist air is related to the absolute humidity,

$$h_{ma} = \frac{h_{da}+\omega \cdot h_{wv}}{1+\omega} \quad (5\text{-}6)$$

where h_{da} and h_{wv} are the specific enthalpy of the water vapour and dry air, respectively which could be obtained by the follows,

$$h_{da} = \int_{273.15}^{T} c_{p,da} \cdot (p,T) \cdot dT \quad (5\text{-}7)$$

$$h_{wv} = \int_{273.15}^{T} c_{p,wv} \cdot (p,T) \cdot dT + L \quad (5\text{-}8)$$

Similarly, the specific heat at constant pressure could be expressed as follows:

$$c_{p,ma} = \frac{c_{p,da}h_{da}+\omega \cdot c_{p,wv}}{1+\omega} . \quad (5\text{-}9)$$

Both viscosity and thermal conductivity of the moist air are evaluated with the Wilke relation based on kinetic theory as follows [137]:

$$\mu_{ma} = \sum_{i=1}^{2} \left(\frac{x_i \cdot \mu_i}{\sum_{j=1}^{2} x_i \cdot \varphi_{ij}}\right) , \quad (5\text{-}10)$$

$$\lambda_{ma} = \sum_{i=1}^{2} \left(\frac{x_i \cdot \lambda_i}{\sum_{j=1}^{2} x_i \cdot \varphi_{ij}}\right) . \quad (5\text{-}11)$$

where φ_{ij} is the diffusion coefficient calculated from the following,

$$\varphi_{ij} = \frac{[1+(\frac{\mu_i}{\mu_j})^{1/2} \cdot (\frac{M_j}{M_i})^{1/4}]^2}{2\sqrt{2} \cdot [1+(\frac{M_i}{M_j})]^{1/2}} \quad (5\text{-}12)$$

5.3.2 Coolant property calculations

In the current simulation, pure methane (CH_4), as the main component of natural gas is applied. The properties of calculating the properties of methane follow the Helmholtz

free energy theory, which is a function of the density and the temperature as follows [138],

$$\frac{He}{R_v T} = \alpha(\tau, \delta) = f(\rho, T) \tag{5-13}$$

where He is the molar Helmholtz energy. The pressure could be calculated as:

$$p = -(\frac{\delta \alpha}{\delta v})_T \tag{5-14}$$

Then based on the theory in Eq. (5-13), the specific enthalpy could be expressed by,

$$h(\rho, T) = \frac{P - \rho r T}{\rho} + \int_0^p \left\{ p - T(\frac{\partial P}{\partial T})_\rho \right\} \frac{\partial \rho}{\rho^2} + \int_{T_a}^T c_p^0 dT \tag{5-15}$$

where T_a is an arbitrary temperature. As the transport characteristic of the coolant properties, the viscosity and the thermal conductivity are modelled using the residual concept as follows,

$$\nu = \nu_0(T) + \rho \nu_l(T) + (\nu_c + \nu_r) \cdot (\rho, T) \tag{5-16}$$

$$\lambda(\rho, T) = \lambda_0(T) + \rho \lambda_l(T) + (\lambda_c + \lambda_r) \cdot (\rho, T) \tag{5-17}$$

where λ_0 is a dilute gas term function of temperature, λ_l accounts for the behaviour at low densities, λ_c is the critical contribution and λ_r represents the residual term for the behaviour at higher densities, including liquid densities.

5.3.3 Coolant flow boiling in the tube

As the wall temperature is greater than the coolant temperature inside the sample tube, convective boiling is the primary heat transfer mechanism inside the tube. Several correlations were proposed previously to predict the heat transfer coefficient [139],

such as Chen [140], Zou, et al. [141] and Steiner and Taborek [142]. Considering the phase condition of the coolant, two types of boiling correlation are studied: single phase and two phase.

(a) single phase

In the case of the turbulent single phase flow, the heat transfer coefficient could be expressed from Gnielinski correlation in the following [143],

$$k_{turb} = \frac{(\frac{\zeta}{8})\cdot(Re-1000)\cdot Pr}{1+12.7\sqrt{\frac{\zeta}{8}}\cdot(Pr^{\frac{2}{3}}-1)} \cdot \frac{\lambda}{D_h} \tag{5-18}$$

where ζ is the friction coefficient which is computed from the Churchill expression as follows [144],

$$\zeta = 8 \cdot \left[(\frac{8}{Re})^{12} + (\left[2.457 \cdot \ln\left(\frac{1}{\left(\frac{7}{Re}\right)^{0.9} + 0.27 \cdot rr} \right) \right]^{16} + \left[\frac{37530}{Re} \right]^{16})^{-3/2} \right]^{1/12} \tag{5-19}$$

where Re is the Reynolds number of the fluid inside the tube, and rr is the relative roughness of the tube material.

In the case of the laminar regime, the laminar convective exchange coefficient could be used in the following:

$$k_{lam} = Nu_{lam} \cdot \frac{\lambda}{D_h} \tag{5-20}$$

The laminar Nusselt number is defined as constant and related to the geometry of the exchanger, as shown in Table 5-1.

Table 5-1 Nusselt number for fully developed laminar flow in the tubes [67].

Cross section	b/a (length and width)	Nu number	
		Uniform heat flux	Uniform surface temperature
Circular	-	4.36	3.66
Square	1.0	3.61	2.98
	1.43	3.73	3.08
	2.0	4.12	3.39
Rectangular	3.0	4.79	3.96
	4.0	5.33	4.44
	8.0	6.49	5.60

Between the laminar regime and turbulent regime, there is a transition condition for the Nusselt number, which is defined as,

$$Nu_{trans} = Nu_{lam} \cdot \left[1 + \ln\left(1 + \exp\left(10 \cdot \ln(2) \cdot \frac{Nu_{turb} - Nu_{lam}}{Nu_{lam}}\right)\right) \cdot \frac{1}{10 \cdot \ln(2)}\right] \quad (5\text{-}21)$$

And then, the heat transfer coefficient could be defined as,

$$k_{trans} = Nu_{trans} \cdot \frac{\lambda}{D_h} \quad (5\text{-}22)$$

(b) Two phase

The correlation of heat transfer coefficient on a horizontal tube proposed by Steiner and Taborek [142] is expressed by the following,

$$k_{co} = \sqrt[3]{k_{cv}^3 + k_{NB}^3} \quad (5\text{-}23)$$

where k_{cv} corresponds to the convective boiling in Eq. (5-24) while k_{NB} corresponds to the nucleate boiling in Eq. (5-28). For the convective boiling mechanism, the heat transfer coefficient could be expressed by the following,

$$k_{cv} = k_{lo} \cdot F_{TP} \tag{5-24}$$

Where k_{lo} refers to the local heat transfer coefficient as defined in Eq.(5-18) and F_{TP} is the two-phase flow enhancement factor which is derived as a function of the vapour fraction x and the density ratio as the following,

$$F_{TP} = \frac{1}{(C_1+C_2)^{0.5}} \tag{5-25}$$

$$C_1 = (1-x)^{0.01} \cdot ((1-x) + 1.2x^{0.4}(\frac{\rho_l}{\rho_g})^{0.37})^{-2.2} \tag{5-26}$$

$$C_2 = x^{0.01} \cdot \left[\frac{h_{vo}}{h_{lo}}(1 + 8 \cdot (1-x)^{0.7} \cdot (\frac{\rho_l}{\rho_g})^{0.67})\right]^{-2} \tag{5-27}$$

The nucleate boiling mechanism in this process is corrected by the correction factor F_{NB} as follows,

$$k_{NB} = k_{NB0} \cdot F_{NB} \tag{5-28}$$

Where k_{NB0} is a constant parameter that depends on the fluid.

5.3.4 Evaporator modelled in Siemens Simcenter Amesim software

In the evaporator model, the evaporated water vapour amount is the evaluation of the system performance, which is related to these parameters: pressure, seawater flow velocity, flow cross-section area, seawater inlet temperature and the heating resource.

According to the above assumptions, the mass balance and the energy balance in the evaporator are expressed as:

$$\dot{m}_s = \dot{m}_b + \dot{m}_v \tag{5-29}$$

$$\dot{m}_b h_b + \dot{m}_v h_v = \dot{m}_s h_s + \dot{Q} \tag{5-30}$$

The time derivative of the density of the feed-in seawater is given by the mass conservation law in the evaporator as follows:

$$\frac{d\rho}{dt} = \frac{1}{V} \cdot \sum \dot{m} \tag{5-31}$$

The internal energy based on the first law of thermodynamics is expressed as [145]:

$$\frac{dU}{dt} = \sum \dot{m} \cdot h + \dot{Q} \tag{5-32}$$

After simplification of Eq. (5-31) and Eq. (5-32), the feed-in seawater temperature is expressed as the following:

$$\frac{dT}{dt} = \frac{1}{m \cdot c_v} \cdot \left(\sum \dot{m} \cdot h + \dot{Q} - h \cdot \sum \dot{m} - m \cdot \left(P + \frac{\partial u}{\partial v}\Big|_T\right) \cdot \frac{dv}{dt}\right) \tag{5-33}$$

where P is the evaporator pressure, the value is determined using the Maxwell relation [145]:

$$\frac{dP}{dt} = \frac{\partial P}{\partial v}\Big|_T \cdot \frac{dv}{dt} + \frac{\partial P}{\partial T}\Big|_v \cdot \frac{dT}{dt} \tag{5-34}$$

The numerical process in the evaporator is presented as shown in Fig. 5-2.

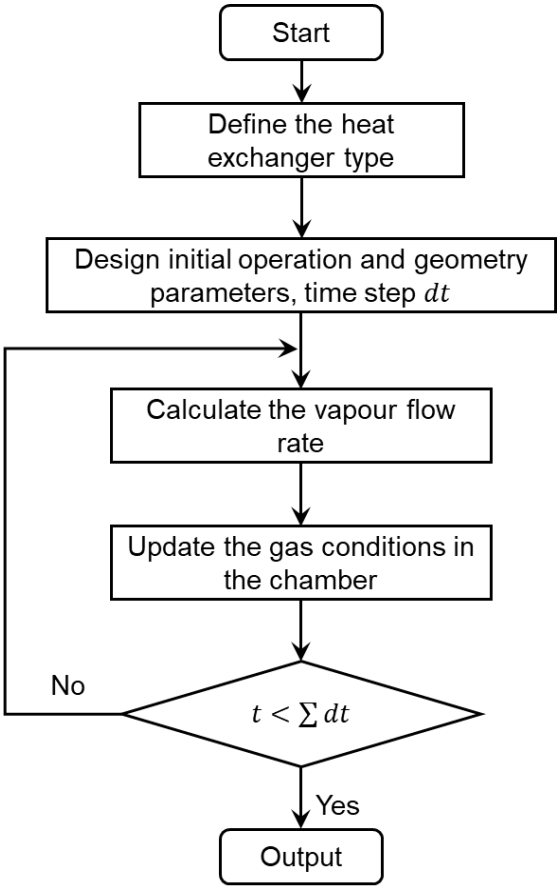


Fig. 5-2: Flow chart of the modelling in the evaporator.

5.3.5 Condenser modelled in Siemens Simcenter Amesim software

In the condensation process, the condensate is the key indicator to evaluate the performance of the system through the varied operational and geometry parameters. Operational variables consist of the air properties, initial pressure in the condenser, coolant temperature and coolant flow rate operating in the condensation process. And different geometry parameters such as the exchange area and the material are also considered in the parametric analysis in the following section to identify the maximum freshwater production. In this numerical modelling procedure, the direct-contact vaporiser is considered. For this type of vaporiser, the ambient air surrounds the vaporiser and transfers heat directly to the flowing coolant in the tubes. To perform the numerical analysis, all the bends and junctions are not considered. To simplify the NG

components in the model, methane is employed as the working fluid. The coolant receives heat through two mechanisms: sensible heat from the ambient air and latent heat from the vaporisation of water vapour through the wall. Both single- and two-phase convection heat transfers occur during this process. The condensation process is simulated in three sections: (a) coolant convection in the tube, (b) heat convection between the outer surface and the vapour, and (c) heat conduction between the inner surface and outer surface.

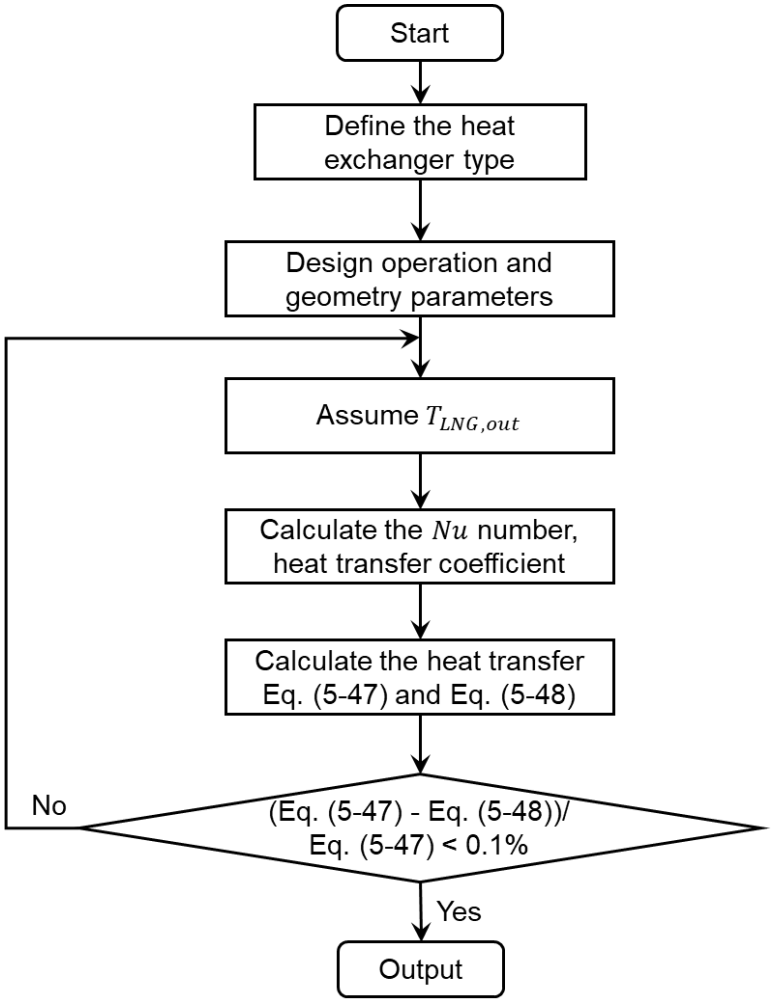


Fig. 5-3: Flow chart of the condenser model.

According to the assumptions, the mass balance and the energy balance in the compact condenser are given as follows:

$$\dot{m}_{ma} = \dot{m}_v + \dot{m}_{da} + \dot{m}_{aw} \tag{5-35}$$

$$\dot{m}_{fw} = \dot{m}_v + \dot{m}_{aw} \tag{5-36}$$

$$\dot{m}_v h_{v(sat)} + \dot{m}_{LNG,in} h_{LNG,in} = \dot{m}_{fw} h_{fw(sat)} + \dot{m}_{LNG,o} h_{LNG,o} \tag{5-37}$$

For the ordinary coolant temperature, only condensation occurs in the system. The heat transfer between the air and the surface consists of the latent heat of phase change and the sensible heat of temperature reduction, which is given as:

$$q = k_{ma} \cdot A \cdot \left(T_{ma,in} - T_w\right) + \dot{m}_{fw} \cdot L \tag{5-38}$$

where $T_{ma,i}$ is the air temperature, and k_{ma} is the convective heat transfer coefficient of the moist air side, which is determined by the Nusselt Number (Nu), the thermal conductivity of the air and the characteristic length of the heat exchanger as follows:

$$k_{ma} = \frac{\lambda \cdot Nu}{l} \tag{5-39}$$

The quantity of Nu depends on the type of moist air flow [67]:

$$Nu = Constant; \text{ (Laminar flow)} \tag{5-40}$$

$$Nu = 0.023 Re^{0.8} Pr^{0.4}; \text{ (Turbulent flow; } Re \geqslant 10{,}000, 0.7 \leqslant Pr \leqslant 160) \tag{5-41}$$

$$Nu = Nu_{lam} \cdot \left(1 + \frac{1}{10 \cdot ln(2)} \cdot ln\left(1 + exp\left(10 \cdot ln(2) \cdot \frac{Nu_{turb} - Nu_{lam}}{Nu_{lam}}\right)\right)\right); \tag{5-42}$$

(Transition flow)

The condensate generated in the condenser during this process is gauged based on the inlet and outlet absolute humidity:

$$\dot{m}_{fw} = \dot{m}_{da} \cdot (\omega_{in} - \omega_o) \tag{5-43}$$

The outlet temperature of the moist air after condensation is determined by the inlet moist air conditions and the heat transfer between the moist air and the surface:

$$T_{ma,o} = T_{ma,in} + \frac{q}{q_{max}} (T_w - T_{ma,in}) \tag{5-44}$$

Similar to the outlet temperature of the moist air, the outlet absolute humidity after condensation is expressed as:

$$\omega_o = \omega_{in} + \frac{q}{q_{max}} (\omega_w - \omega_{in}) \tag{5-45}$$

where q_{max} is the maximum heat transfer between the wall and the moist air. It is expressed as:

$$q_{max} = \frac{\dot{m}_{ma}}{1+\omega_{in}} \cdot ((1 + \omega_{sat}) \cdot \left(h_{ma,in} - h_{ma,w,sat}\right) + (\omega_{ma,in} - \omega_{w,sat}) \cdot (h_{ma,in} - h_{lw,w,sat})) \tag{5-46}$$

where $h_{ma,w,sat}$ is the moist air specific enthalpy at wall saturation conditions and $h_{lw,w,sat}$ is the liquid water specific enthalpy at wall saturation conditions.

With the coolant entering the tubes, the convective heat exchange occurs between the inside surface and the coolant. The heat transfer between the coolant and the inside surface is expressed as:

$$q = k_{co} \cdot A \cdot (T_{co} - T_{w,co}) \tag{5-47}$$

where k_{co} is the convective heat transfer coefficient between the coolant and the wall, $T_{w,co}$ is the temperature of the internal tube.

In addition, the heat transfer rate by conduction between the internal and external surface should be taken into consideration due to the temperature difference between both sides and the material. Therefore, the heat transfer rate of conduction is referred as:

$$q = \frac{\lambda_w A_w}{\delta}(T_{w,ma} - T_{w,\mathrm{co}}) \tag{5-48}$$

where δ is the thickness of the wall and λ_w is the thermal conductivity of the tube material.

5.3.6 Frosting phenomena modelled in Siemens Simcenter Amesim software

The mathematical model of the frost formation on the chilled and cryogenic surface is based on the conservation laws of mass and energy. As shown in Fig. 5-4, the frosting process could be expressed as the freezing of water vapour into crystals which moving from the ambient air into the frost layer by convective mass transfer through diffusion and desublimation. The following assumptions are proposed to simplify the model:

(1) The thermodynamic parameters of the frost layer are uniform.

(2) The frost growth is one-dimensional.

(3) The temperature of the surface and the atmospheric conditions are constant.

(4) The melting of the frost layer is neglected.

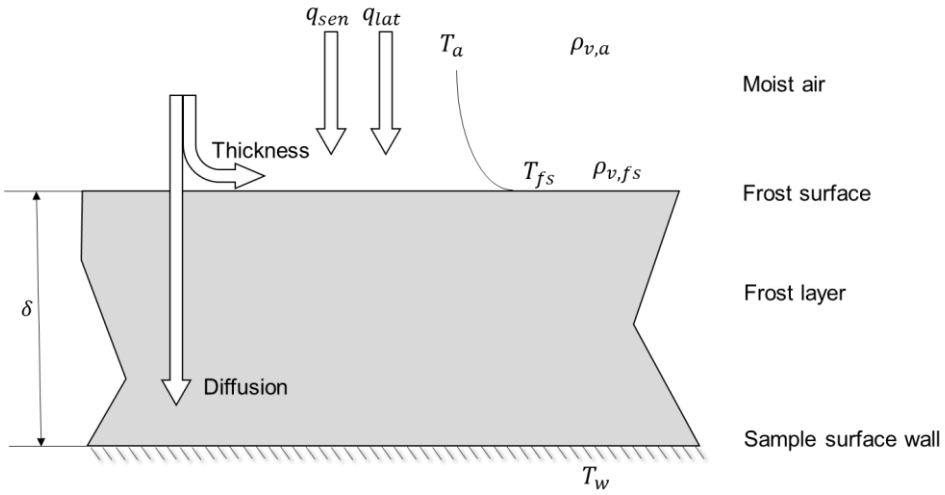


Fig. 5-4: Heat and mass transfer during frosting.

The total heat transfer rate from the moist air to the surface (including the frost surface) q could be expressed as the sum of the convection, phase change and radiation.

$$q = k_{ma}(T_{ma} - T_{fs}) + m_f L + \varepsilon\sigma(T_{ma}^4 - T_{fs}^4) \tag{5-49}$$

where k_{ma} is the convective heat transfer coefficient, T_{fs} is the frost surface temperature and m_f represents the mass of the frost on the surface from the convective heat transfer. The entry of the water molecules into the frost layer from the moist air through the gas-solid interface, leads to an increase in both thickness and density of the frost layer. The mass growth rate of the frost layer equals to the convective mass transfer rate of the water vapour, which is related to the mass transfer coefficient k_m as follows,

$$m_f = \frac{dM_f}{dt} = k_m(\rho_{v,ma} - \rho_{v,f}) \tag{5-50}$$

where $\rho_{v,ma}$ and $\rho_{v,f}$ represent the concentration of water vapour of the ambient air and frost surface, respectively, which are expressed as

$$\rho_{v,ma} = \frac{RH \cdot p_{sat,ma}}{R_v T_{ma}} \quad (5\text{-}51)$$

$$\rho_{v,f} = \frac{p_{sat,f}}{R_v T_f} \quad (5\text{-}52)$$

$p_{sat,f}$ and $p_{sat,ma}$ denote the saturation pressure of water vapour on frost surface and air, respectively. Based on the Chilton-Colburn analogy, the mass transfer coefficient k_m could be obtained as follows [146],

$$k_m = \frac{k_{ma}}{\rho_{ma} c_{p,ma} Le^{2/3}} \quad (5\text{-}53)$$

where Le is the Lewis number, the ratio of the thermal diffusivity and mass diffusivity of the moist air. When the moist air on the frost surface is natural convection, the air natural convective heat transfer coefficient could be calculated by the following equations:

$$Nu = 0.27 \cdot Ra^{0.25} \text{ (for top surface)} \quad (5\text{-}54)$$

$$Nu = 0.54 \cdot Ra^{0.25} \text{ (for bottom surface)} \quad (5\text{-}55)$$

$$Nu = \left(0.825 + \frac{0.387 \cdot Ra^{1/6}}{\left(1+\left(\frac{0.492}{Pr}\right)^{9/16}\right)^{8/27}}\right)^2 \text{ (for sides surfaces)} \quad (5\text{-}56)$$

$$k_{ma} = f_1 f_m Nu \cdot \frac{\lambda}{l} \quad (5\text{-}57)$$

Where f_1 is the empirical enhanced factor from 1.20 to 1.25 as Yavnel' [147] proposed, as the frost layer surface is a rough surface that strengthens the heat transfer. And f_m is the enhancement factor for the surface material obtained by experimental data from the previous chapter. When the moist air flows above the surface by forced convection, the air convective heat transfer coefficient could be given by [67]:

$$Nu = 0.023 \cdot Re^{0.8} \cdot Pr^{0.4}$$ (Turbulent flow; Re≥10,000,0.7≤Pr≤160) (5-58)

$$Nu = Nu_{lam} \cdot \left(1 + \frac{1}{10 \cdot ln(2)} \cdot ln\left(1 + exp\left(10 \cdot ln(2) \cdot \frac{Nu_{turb} - Nu_{lam}}{Nu_{lam}}\right)\right)\right)$$ (transition flow) (5-59)

$Nu =$ Constant; (laminar flow with constant surface temperature or heat flow) (5-60)

The latent heat of desublimation is described as the following,

$$L = 1000 * (2834.1 - 0.29 * (273.15 + T_a) - 0.004 * (273.15 + T_a) * (273.15 + T_a))$$ (5-61)

The total heat transfer rate could also be expressed as the thermal conduction between the wall and the frosted surface as the following,

$$q = \frac{\lambda_f}{\delta_f} \cdot (T_{fs} - T_w)$$ (5-62)

Heat is transferred to the wall through the frost layer during the vaporisation process, which includes sensible heat from air free convection and forced convection outside the vaporiser, as well as latent heat from vapour desublimation. The heat in all forms is subsequently then transferred to the cryogenic coolant in the tube. As illustrated in Fig. 5-5, the air convection, frost conduction, wall conduction and cryogenic coolant convection are considered in the model.

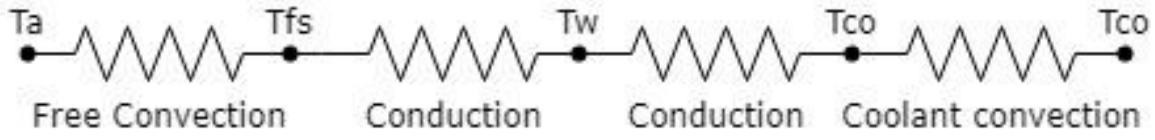


Fig. 5-5: Thermal resistance schematic of the vaporiser.

The frost formation model for cryogenic application is complicated and the frost surface temperature is an unknown parameter, so the iteration method is required. As illustrated in Fig. 5-6, the flowchart of the numerical calculation is applied in Siemens Simcenter software to process the frost properties and heat transfer performance. After assuming the frost surface temperature, the frost properties are calculated from semi-empirical correlations and the heat transfer coefficient is derived using an Eq.(5-57). Then the overall heat transfer rate between the surface and moist air was calculated through a series of calculation processes described in Eq. (5-49) and Eq. (5-62). Then the iteration stops until the error between these two heat transfer rates is less than 0.1%, and frost surface temperature is obtained.

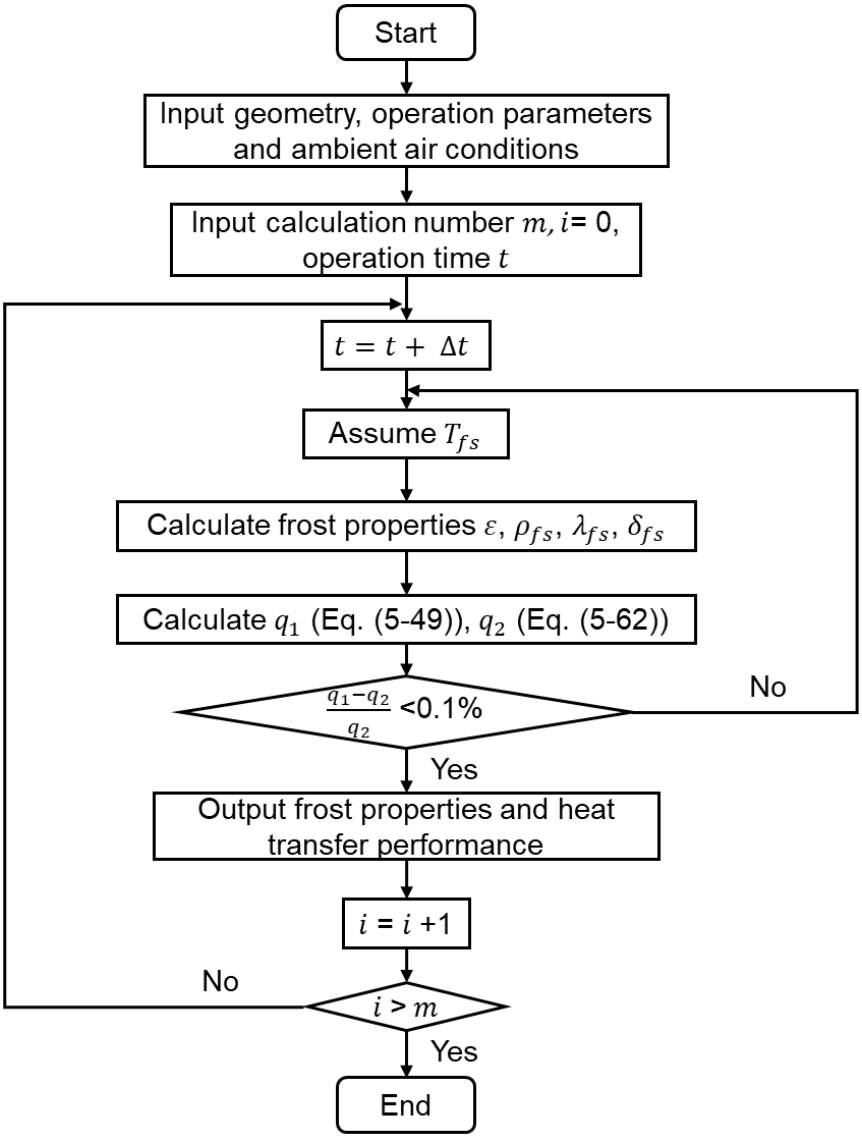


Fig. 5-6: Flowchart of calculation program for the frost formation.

5.4 Validation

The experimental data from the literature [148] and the experimental data in Chapter 4 are used to validate the accuracy of the evaporator model and the condenser model developed in Siemens Simcenter Amesim, respectively. The relative error between the experimental value and simulation value is used to evaluate the operation performance by follows:

$$E = \frac{Value_e - Value_s}{Value_s} \times 100\% \quad (5\text{-}63)$$

5.4.1 Evaporator

Rahman, et al. [148] proposed a submerged vertical tube heat exchanger as the evaporation part of the single-effect desalination unit, as shown in Fig. 5-7. Seawater flows upwards from the feedwater tank through a vertical tube while being heated by the hot water outside the tubes. A series of experiments are designed to investigate the effect of the temperature, pressure, and flow rates of both feed-in and hot water on the evaporation process, e.g. in the evaporator chamber. The output vapour production rate at the upper outlet is the key indicator of the evaporator performance.

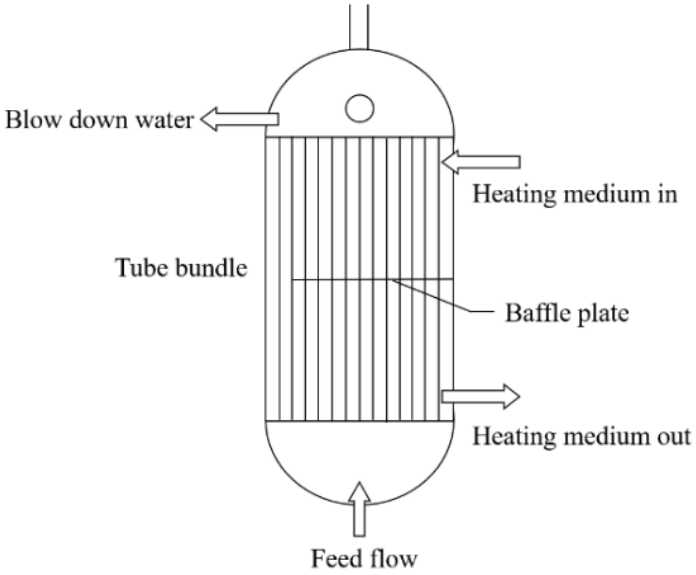


Fig. 5-7: The evaporator diagram in Rahman, et al. [148].

The operation parameters of the evaporator are presented in Table 5-2. Fig. 5-8 compares the simulated and experimental results for the freshwater vapour production rate in the evaporator at four different superheat degrees. The simulated production trends are in good agreement with the experimental data.

Table 5-2 Input parameters of the evaporator chamber for validation [148].

Parameter	Unit	Quantity
Volume of the chamber	L	31.416
Height of the chamber	mm	500
Initial percentage of liquid volume	-	0%
Temperature of inlet feed-in seawater	ºC	41.5, 46.5, 56.5, 61.5
Mass flow rate of feed-in seawater	kg/s	0.0694
External heating medium capacity	W	12156
Initial pressure of the chamber	bar	0.08

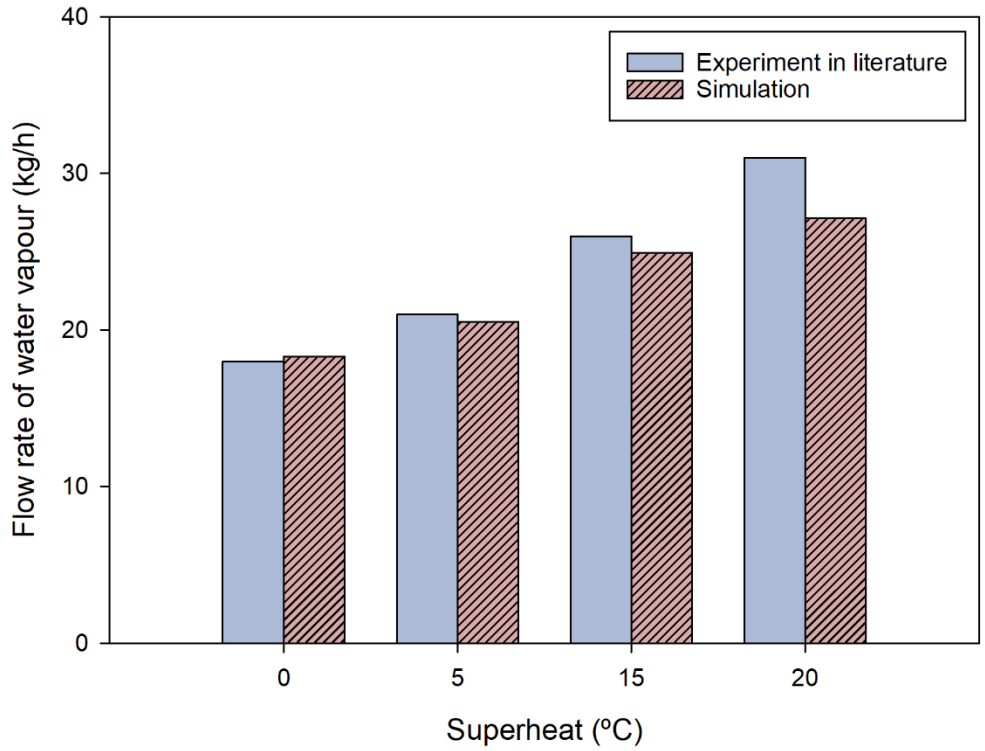


Fig. 5-8: Comparison between the measured and predicted in the evaporator model.

5.4.2 Condenser

By analysing several indications in four different scenarios, the validation for the condenser model is produced. The developed condenser model in the Siemens Simcenter Amesim was firstly compared with the experimental data conducted by Wu and Vierow [149] and Cheng and Geld [150] for validation. Wu and Vierow [149] investigated at the heat transfer performance of the condensation process on horizontal tubes. The experiment was conducted using a double pipe heat exchanger manufactured of SS304 with a length of 3.0 m and an outer pipe diameter of 31.7 mm as illustrated in Fig. 5-9. While the coolant flowed outward in the opposite direction, the steam was flowing within the inner tube. The input parameters for validation presented in Table 5-3 are applied as two conditions, Condition 1 and Condition 2. The simulated steam temperature was compared in Fig. 5-10 at four different locations of tube: 0m, 0.5, 1.5m and 3m. The numerical data shows a good agreement with the experimental data with the error within 7%.

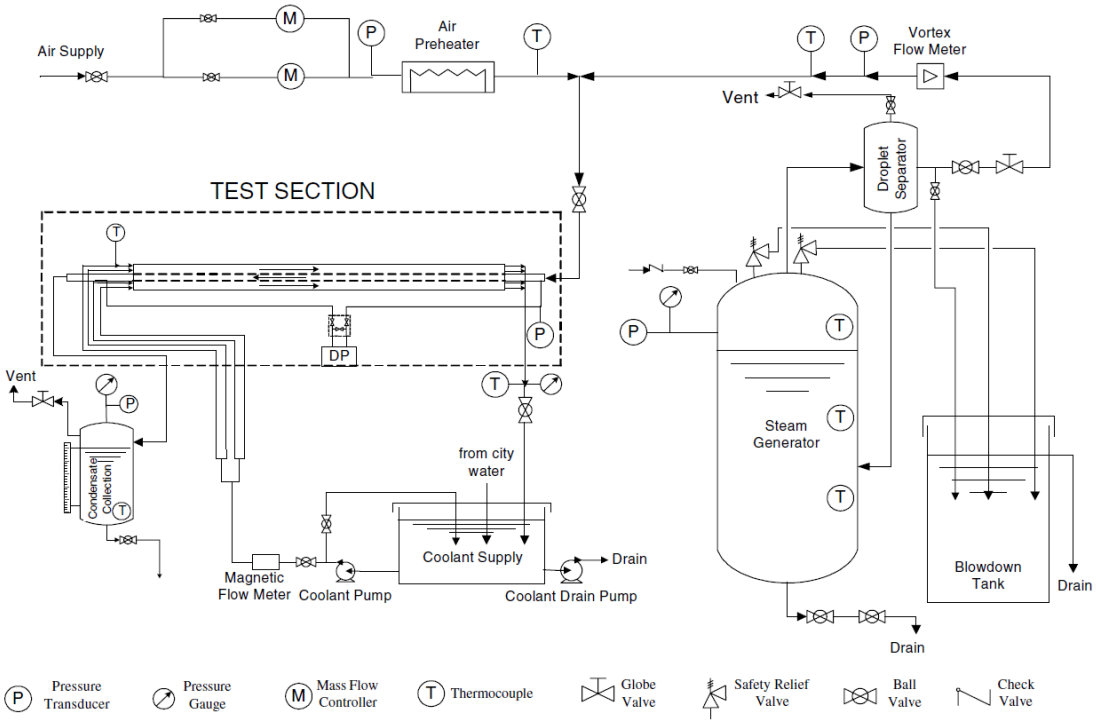


Fig. 5-9: Schematic of the test facility. [149]

Table 5-3 Input operation parameters of the condenser for validation. [149]

Parameter	Unit	Condition 1	Condition 2
Inlet temperature of air steam	ºC	99	118
Air mass fraction	-	15%	15%
Absolute humidity	g/kg	5667	5667
Inlet steam flow rate	kg/s	0.007	0.012
Inlet temperature of the cooling water	ºC	45	45
Flow rate of cooling water	kg/s	1.48	1.48
Pressure	Bar	1	2

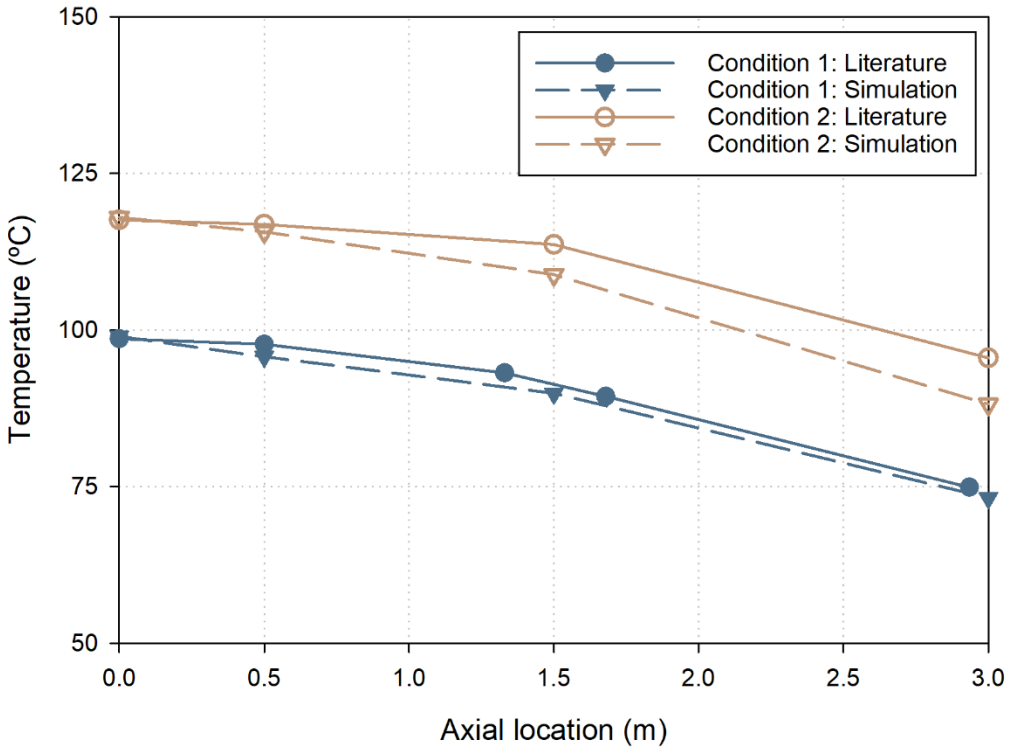


Fig. 5-10 Comparison between the measured and predicted in the condenser model.

The quantity of condensate from the secondary condenser model is tested to see if it matches with the experimental findings in the study of Cheng and Geld [150]. A compact polymer heat exchanger made of Poly-Vinyli-Dene-Fluoride (PVDF) for air steam-to-water heat exchange was conducted. The heat exchanger, as shown in Fig. 5-11, is made up of 48 parallel plates with 42 small cooling water channels in each plate. The mixture of water steam and the air are introduced into the condenser. The properties of PVDF are presented in Table 5-4The input parameters are introduced in Table 5-5.

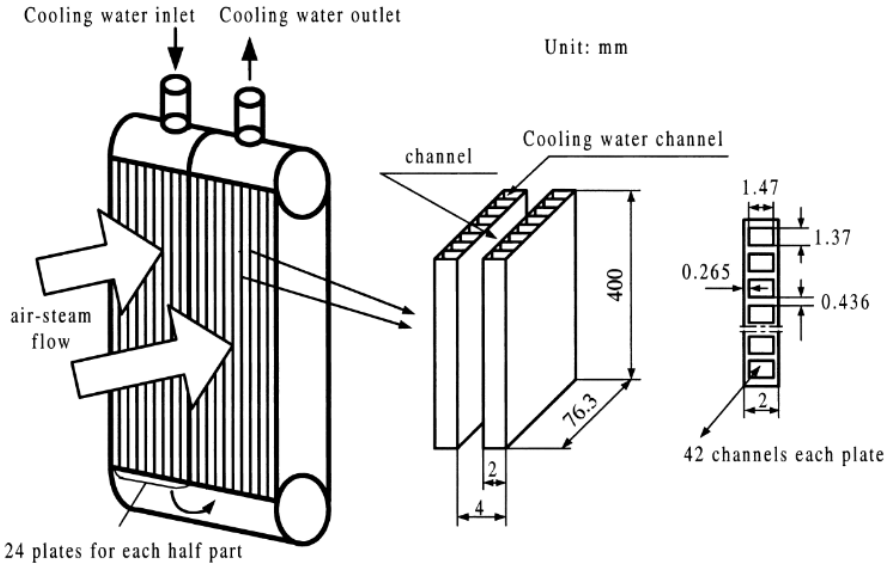


Fig. 5-11 Schematic of the polymer compact heat exchanger [150].

Table 5-4 Properties of PVDF.[151].

Parameter	Unit	Quantity
Density	kg/m^3	1780
Minimum temperature	ºC	-62
Maximum temperature	ºC	149
Specific heat	J/(kg·K)	1400
Thermal conductivity	W/(m·K)	0.2

Table 5-5 The condenser input parameters for validation.[150]

Parameter	Unit	Quantity
Inlet temperature of air steam	ºC	80, 90
Mass flow rate of air stream	kg/s	0.25 – 0.38
Relative humidity of air steam	-	20%, 24%, 32%, 40%
Inlet temperature of the cooling water	ºC	25
Flow rate of cooling water	m^3/h	1.5, 2.5
Heat exchange area	m^2	1.4
Cross-sectional area of air stream side	mm^2	37600
Cross-sectional area of cooling water side	mm^2	2030
Pressure	bar	1
Duration time	s	1800

As shown in Fig. 5-12, the predictions of the model agreed with the experimental data within -17.3% to +10%. However, when the condensate mass flow rate exceeds 0.009 kg/s, the computed condensate exhibits a progressively growing discrepancy. One of the reasons mentioned in the literature [150] was that it was challenging to set the actual testing parameters exactly the same as those in the test plan, leading to inaccuracy. The freshwater produced in the same duration in the experiments also required time to collect in total. The assumptions might overlook several elements that affect trial outcomes, such as the presence of non-condensable gases in the condenser, the inadequacy of the sealed testing system, heat loss, etc.

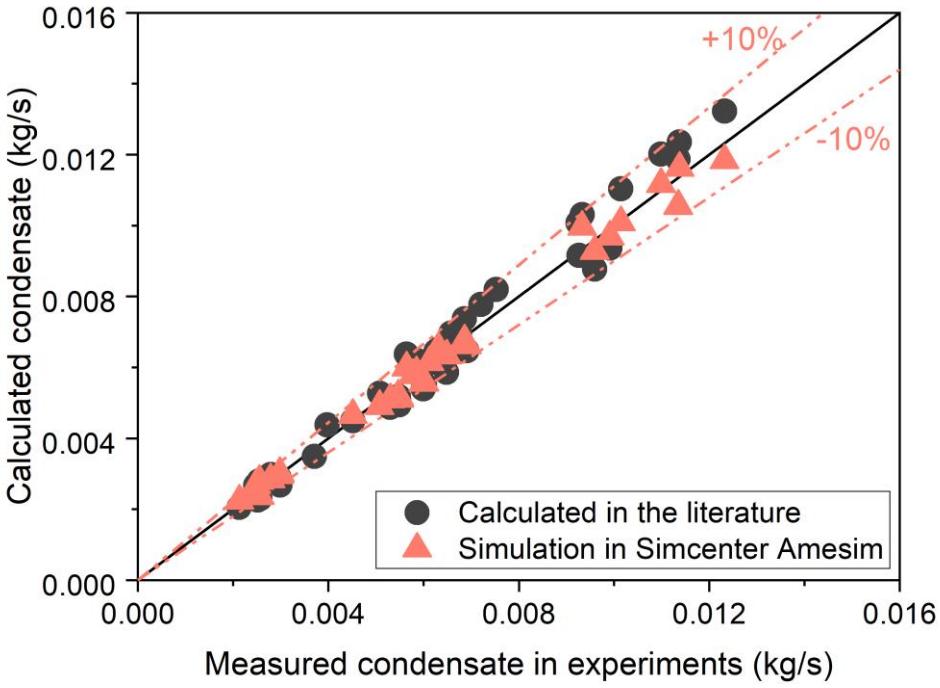


Fig. 5-12 Comparison between the measured and predicted in the condenser model.

The third condenser model is validated by the same parameters operated in the Case 4 of the experimental investigation with the surface temperature of 6 °C. As shown in Fig. 5-13, the error between the production measured in the experiments and the numerical study is -2.3% on bare tube, -1.9% on FEP tube, -1.8% on Fluorine based tube and 2.6% for PTFE tube.

Similarly, for frosting phenomenon cases, the production rate is also the indicator to evaluate the simulation results. The experimental data on sample tubes with the operation parameters in Case 1 with the surface temperature of -36 °C are used to validate the numerical method as shown in Fig. 5-14. The correlation errors for the production, frost thickness, density and the porosity show good agreement with the experimental data at -9.3% to 2.2%, -8.1% to 3%, -7% to 7.3% and -0.25% to 0.25%.

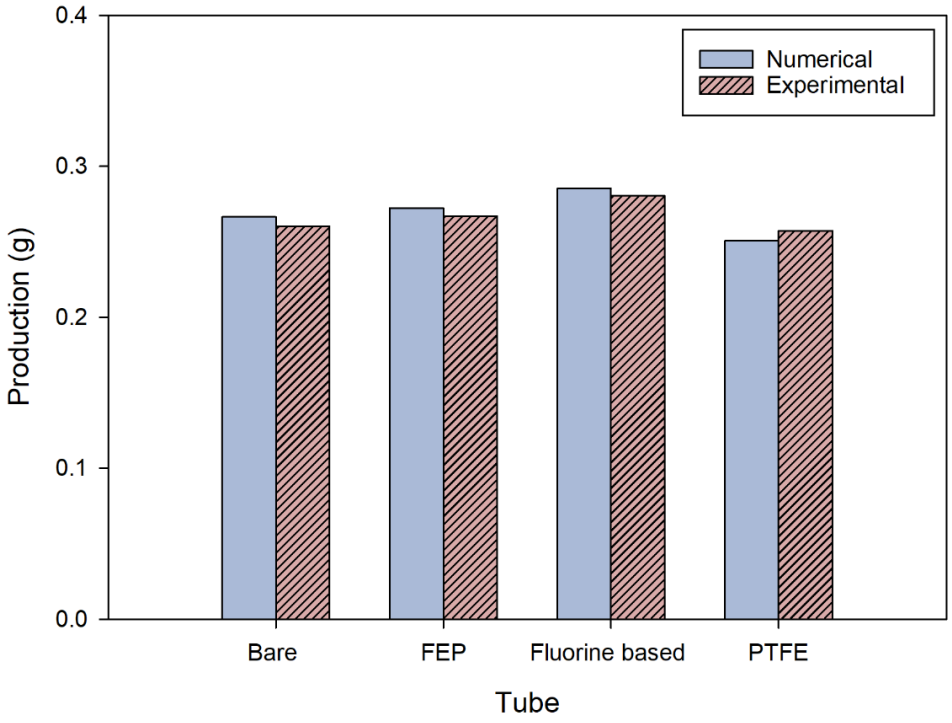


Fig. 5-13: Comparison between the measured and predicted for condensation cases.

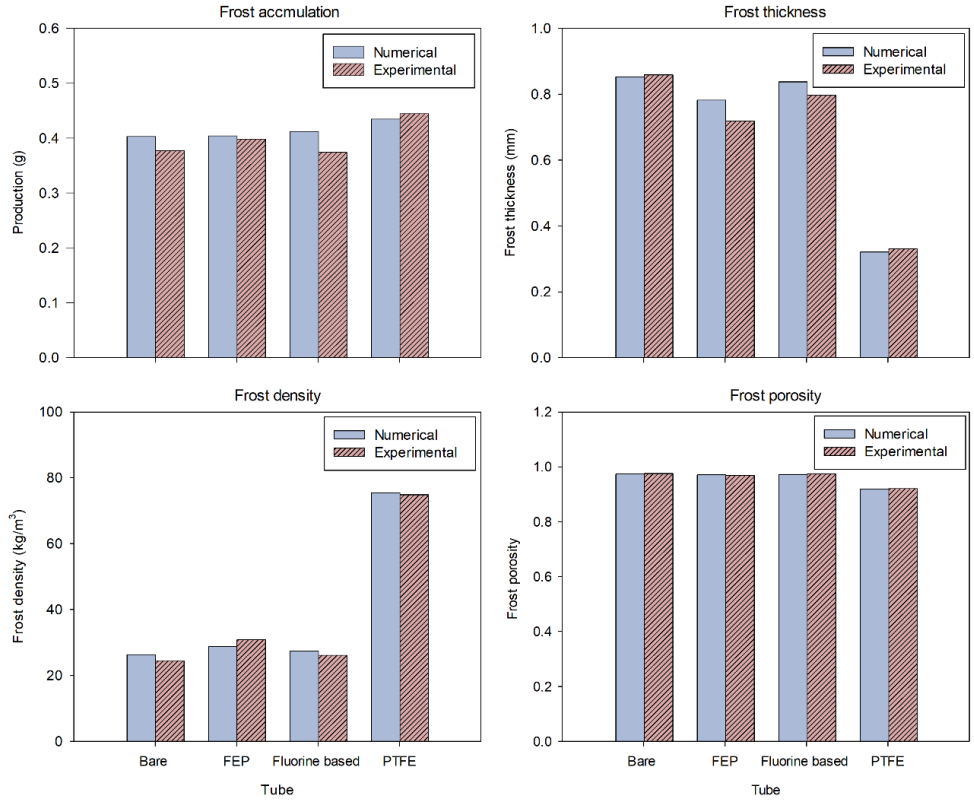


Fig. 5-14: Validation result by the Nusselt theory of frosting conditions.

The fourth condenser model is developed to validate the model application to a cryogenic temperature surface with the operational conditions and geometrical parameters following the data in the related literature [152]. As shown in Fig. 5-15, the ambient air is cooled by the LN_2 flowing from the bottom in a finned tube in the natural convection method. The operation and geometry parameters of the experiment for validation is presented in Table 5-6. Fig. 5-16 displays the comparison results of the frost thickness between the experimental and the simulation data. It can be seen that the simulation results follow the same trend as the experimental results in the literature with the difference within 15%. As a result, the developed model could be used as an effective tool for the frosting analysis on the cryogenic surface.

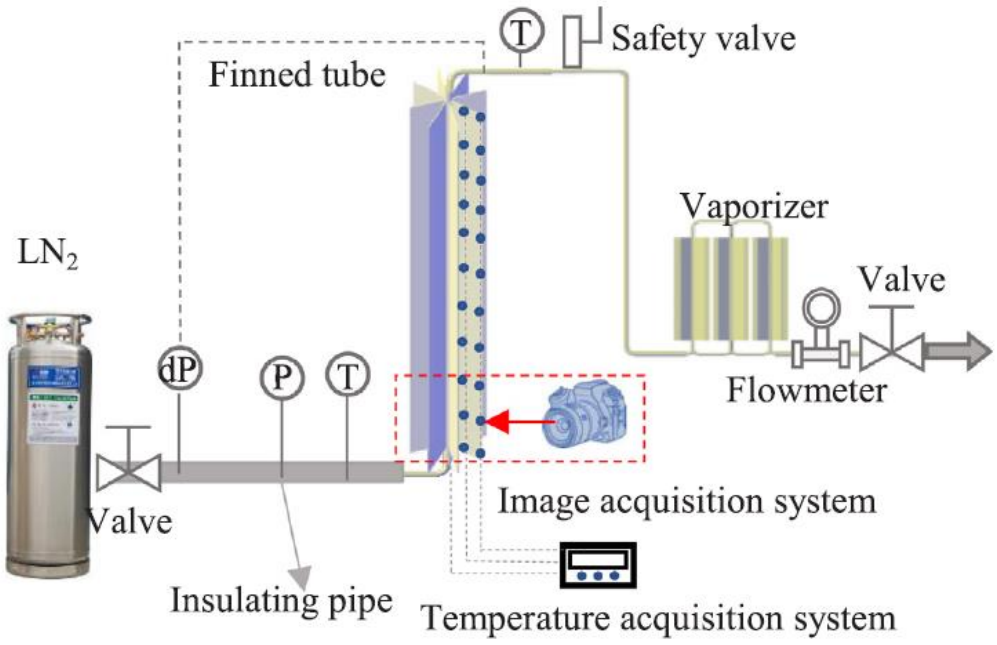


Fig. 5-15: Schematic of the experimental apparatus [152].

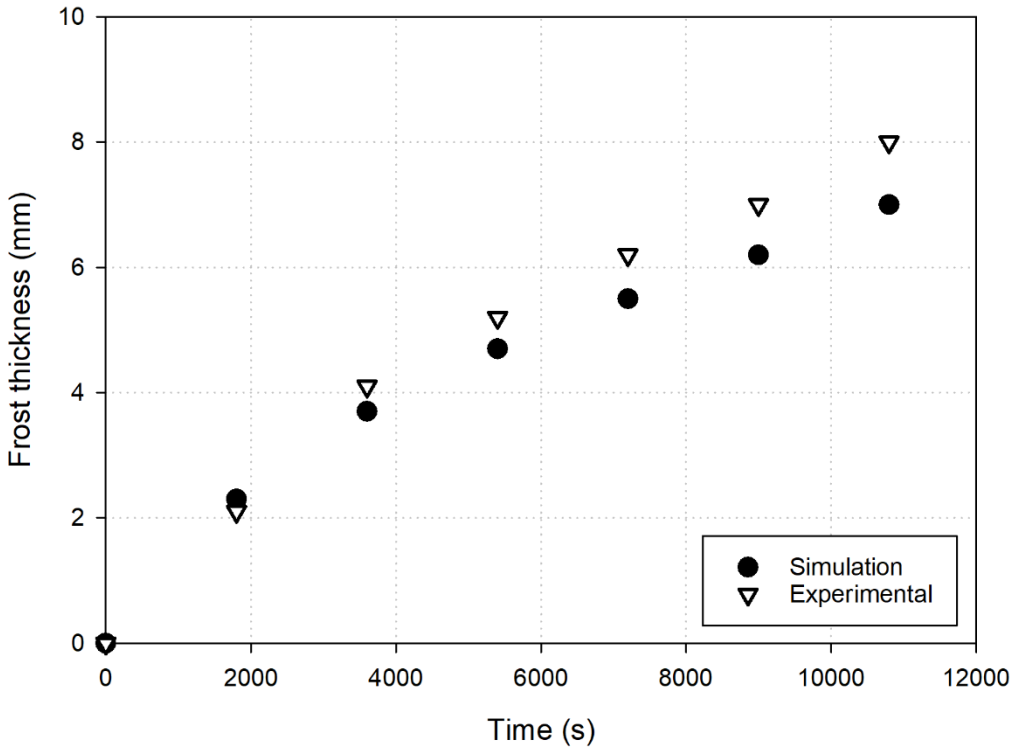


Fig. 5-16: Comparison of frost thickness between the experiment and simulation.

Table 5-6 Operation and geometry parameters of the experiment for validation.

Parameter	Unit	Quantity
Inlet temperature of air	ºC	25
Relative humidity	%	62
Inlet temperature of the nitrogen	ºC	-196
Flow rate of cooling water	kg/h	17.5
Pressure	bar	2
Inner diameter of the tube	mm	24
No of fins	-	8
Height of fin	mm	80
Thickness of fin	mm	2

5.5 Parametric study – Evaporator

The superheat and inlet seawater temperature have an obvious impact on the evaporated mass, as was stated in the previous validation section. Additionally, the effects of additional parameters such as heating input, temperature, initial chamber pressure, and inlet seawater mass flow rate are investigated. The parameters used to simulate are presented in Table 5-7.

Table 5-7 Operational parameters of the evaporator.

No	Pressure (bar)	Heating input (W)	Temperature of feed-in seawater (°C)	Mass flow rate of feed-in seawater (kg/s)
1	0.08	12156	31.5, 41.5, 51.5, 61.5	0 - 0.16
2	0 - 0.20	0, 4052, 8104, 12156, 16208	61.5	0.0694

Fig. 5-17 presents the effect of the inlet seawater temperature on the mass of the water vapour with different mass flow rates and seawater inlet temperature. The initial pressure in the chamber and heating input from the waste heat are fixed at 0.08 bar and 12156 W. Table 5-7 indicates the detailed operating inlet temperature and mass flow rate conditions. It can be noticed that the water vapour generation rate increases with the increase of the inlet seawater temperature, which implies that the flash evaporation is enhanced due to the higher superheat degrees. According to the previous section, the superheat degree is related to the temperature difference between the inlet seawater temperature and the saturation temperature at the same chamber pressure. With higher superheat degrees, the liquid remaining in the chamber

absorbs more heat of vaporisation, which leads to a faster evaporation rate and lower its own temperature to the saturation temperature.

When the inlet seawater temperature is pre-heated above 41.5°C (saturation temperature at 0.08 bar), the water vapour generation rate tends to increase. A greater mass flow rate of feed-in seawater corresponds to a greater flow velocity through the fixed size of the inlet section, which results in a larger evaporative mass with the same heating input. The water vapour generation remains constant over all inlet seawater flow rates when the inlet seawater temperature is pre-heated to 41.5°C. The reason for this is that the heating capacity of the flash evaporation roughly balances the required latent heat for feed evaporation in the chamber at the saturation conditions. Although the feed seawater remains sufficient when the feed seawater is increased, there is no more waste heat available for the remaining seawater evaporation to promote the production. And when the input seawater temperature is below the vapour saturation temperature, the water vapour production rate is reduced because most of the input heating is used to increase the subcooled seawater temperature to the saturation temperature. The temperature level of the inlet seawater is determined based on the presence of a residual heat temperature grade. Therefore, adjusting the initial evaporator chamber pressure accordingly helps to increase the inlet seawater temperature until it is greater than the saturation temperature at the chamber pressure.

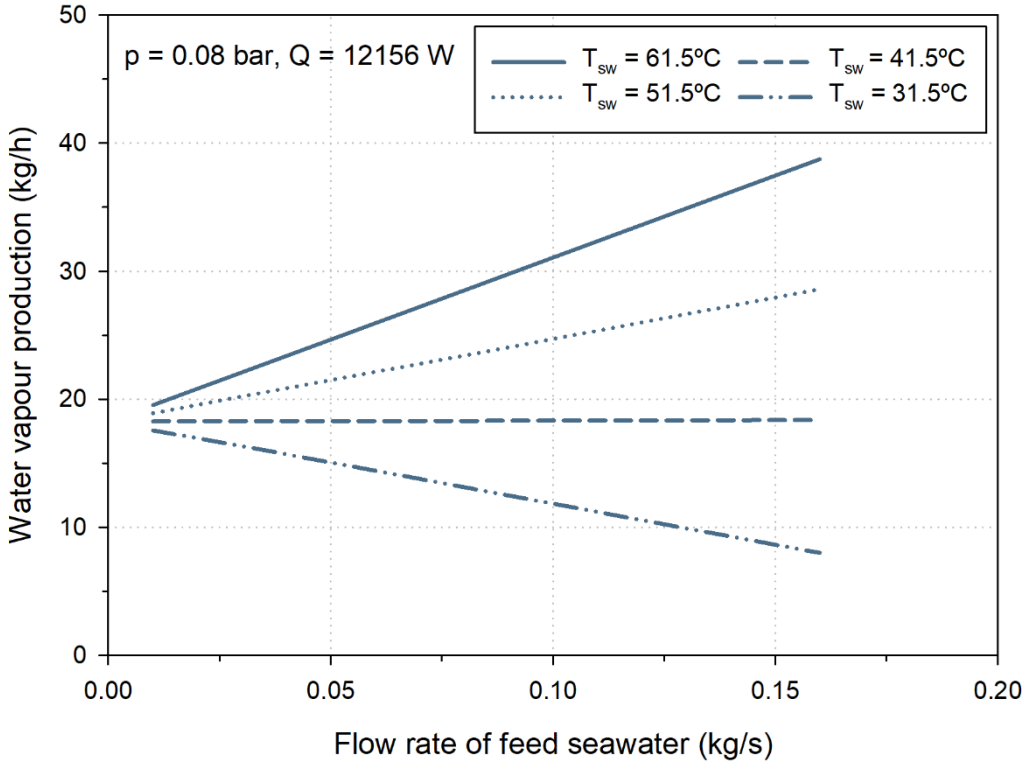


Fig. 5-17: Variation of water vapour mass with different feed-in seawater temperature.

Fig. 5-18 presents the generated water vapour production rate versus five different heating inputs of 0 W, 4052 W, 8104 W, 12156 W and 16208 W. The operation parameters are depicted in Table 5-7. It is clear that the water vapour production rate increases with increasing heating input. The heating capacity drives the flash evaporation of the feed seawater and increases the evaporation rate. It is also clear to conclude from Fig. 5-18 that the water vapour tends to decrease as the initial pressure in the evaporation chamber increases. Lower pressure conditions are associated with lower vapour saturation temperature which augments temperature difference with the inlet seawater temperature. Consequently, there is excess thermal energy for generating more vapour in the flashing evaporation.

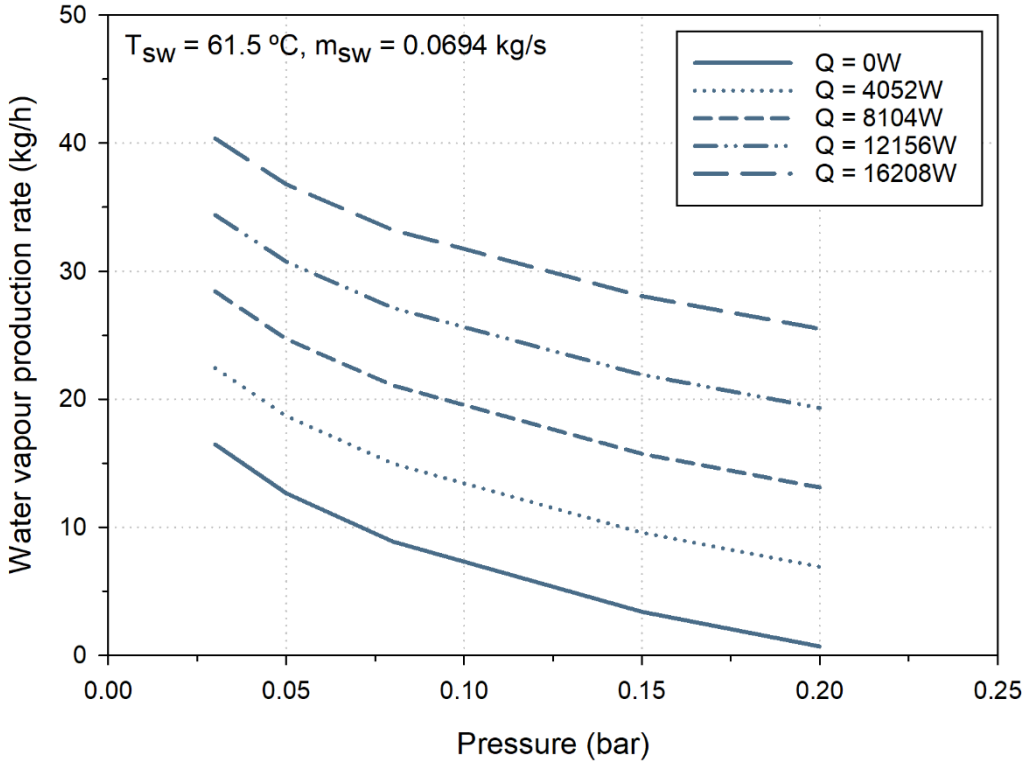


Fig. 5-18: Variation of freshwater mass with the heating input.

5.6 Parametric study – condenser geometry parameters

The condensation performance and the cost are related to the heat exchanger structure and configuration. Therefore, it is of crucial importance to investigate the effect of the geometry parameters of the condenser on condensate production and heat transfer which are the essential indicators for heat exchanger selection. In current section, the main focus is to optimise the geometrical parameters for maximum condensate production and heat transfer. The condenser, which consists of arrays of plates with flat tubes in three passes, utilizes the compact heat exchanger to obtain a large heat transfer surface area. From the first pass until the third pass, moist air flows across the plates and exchanges heat with the coolant CH_4. The schematic of the

condenser is shown in Fig. 5-19. In this section, the moist air is simulated at the pressure of 1 bar, temperature of 41.5ºC, relative humidity of 90%, and the coolant provides the cooling capacity at the temperature of 5ºC as shown in Table 5-8.

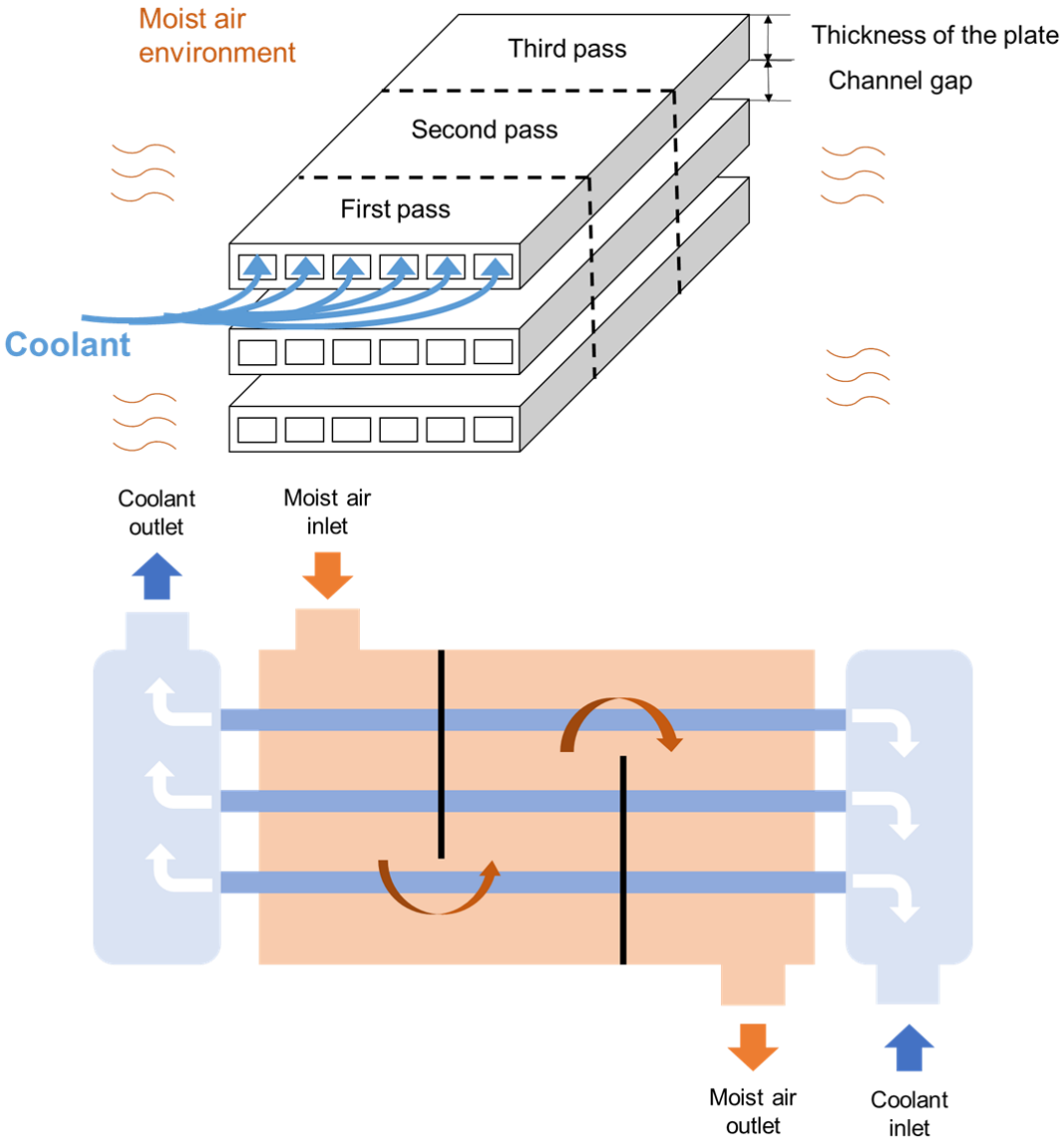


Fig. 5-19: Details of the proposed condenser.

Table 5-8 Operational parameters of the moist air and coolant in the condenser

Parameter	Unit	Quantity
Pressure of the condenser	bar	0.08
Temperature of the moist air	ºC	41.5
Relative humidity of the moist air	%	90
Pressure of coolant	bar	1
Temperature of coolant	ºC	5
Mass flow rate of coolant	kg/s	0.875

5.6.1 Condensation

The most influential geometry parameters are analysed to evaluate their impact on the performance of the proposed system in three cases as defined in Table 5-9.

Table 5-9 Geometry parameters of the condenser.

No	Heat exchange area of the plate (m^2)	Material of the condenser	Number of the channels
1	1.4	Aluminium Alloy 3003-H14, Stainless Steel AISI316, PTFE	42
2	1.4	Aluminium Alloy 3003-H14	10 - 50
3	0 - 1.84	Aluminium Alloy 3003-H14	10

As described in Eq. (5-48), the conduction heat transfer is related to the thickness of heat exchanger material and its thermal conductivity. Fig. 5-20 shows the condensate

production, heat transfer performance and pressure loss affected by different materials: i.e., PTFE, Stainless Steel AISI304 and Aluminium Alloy 3003-H14 at the same operational conditions. The properties of these three materials are presented in Table 5-10. It is clear to see that the performances on Stainless steel 316 with thermal conductivity of 16.2 W/ (m · K) and Al alloy 3003-H14 with thermal conductivity of 159 W/ (m · K) are almost the same, while the PTFE has the worst. When the thermal conductivity of the material is lower, the heat transfer flux over the same time is lower, resulting in less cooling capacity entering the condenser from the coolant. And the heat exchange area is sufficient for Stainless Steel AISI316 to transfer the applicable cooling capacity for condensation although its lower thermal conductivity. Therefore, due to the better performance and inexpensive cost, Aluminium Alloy 3003-H14 is considered as the best material of the condenser for this application, among the materials considered.

Table 5-10 Properties of heat exchanger materials at 20ºC.

Properties	Unit	PTFE [153]	Aluminium Alloy 3003-H14 [154-156]	Stainless Steel AISI316 [154-156]
Density	kg/m^3	2130	2730	8000
Thermal conductivity	W/ (m · K)	0.25	159	16.3
Specific heat capacity	J/ (kg · K)	1000	8930	500
Coefficient of thermal expansion	K^{-1}	$2.7\text{-}5.4\times10^{-4}$	2.3×10^{-5}	1.73×10^{-5}
Maximum temperature	ºC	260	654	1370
Minimum temperature	ºC	-200	-	-
Price	$/kg	15.0	31.2	69.1

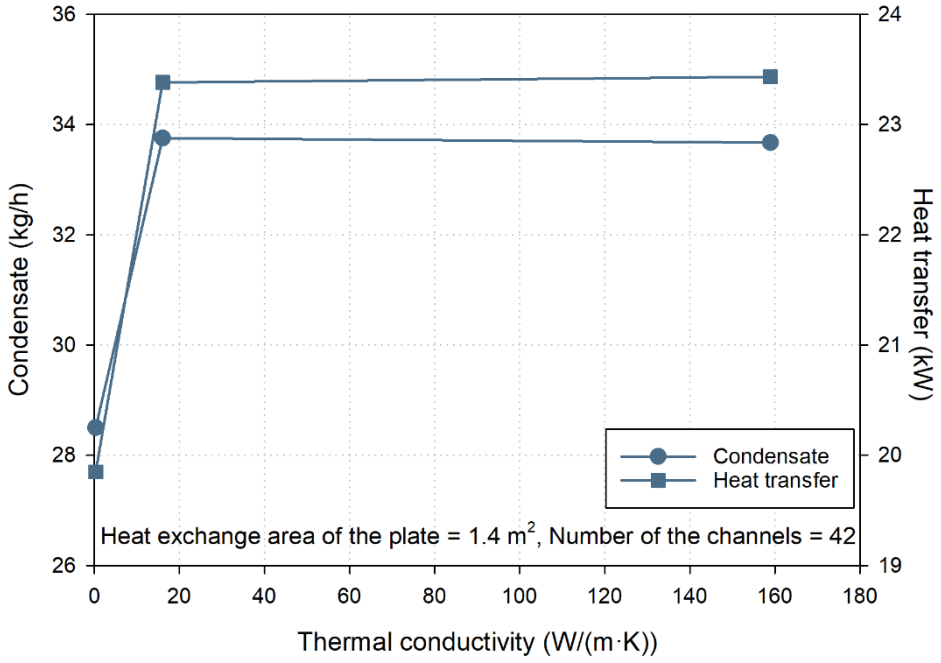


Fig. 5-20: Variation of condensation performance with different material.

Fig. 5-21 depicts the condensation characteristics with varying number of the channels in each plate. The number of channels in each plate is decreased from 50 to 10, which changes the convective heat exchange area of the channel. Based on steady-state data obtained after the simulation has run for 30 minutes, the results shown in Fig. 5-21 are presented. Under the same circumstances, when the number of channels grows, the heat transfer rate shows a rising trend. With the same volume of condenser, the increasing heat exchange area of the channels provides a more efficient area for heat transfer. Additionally, in order to improve the generation of condensate, more coolant is further transported and consumed between the coolant and the surface.

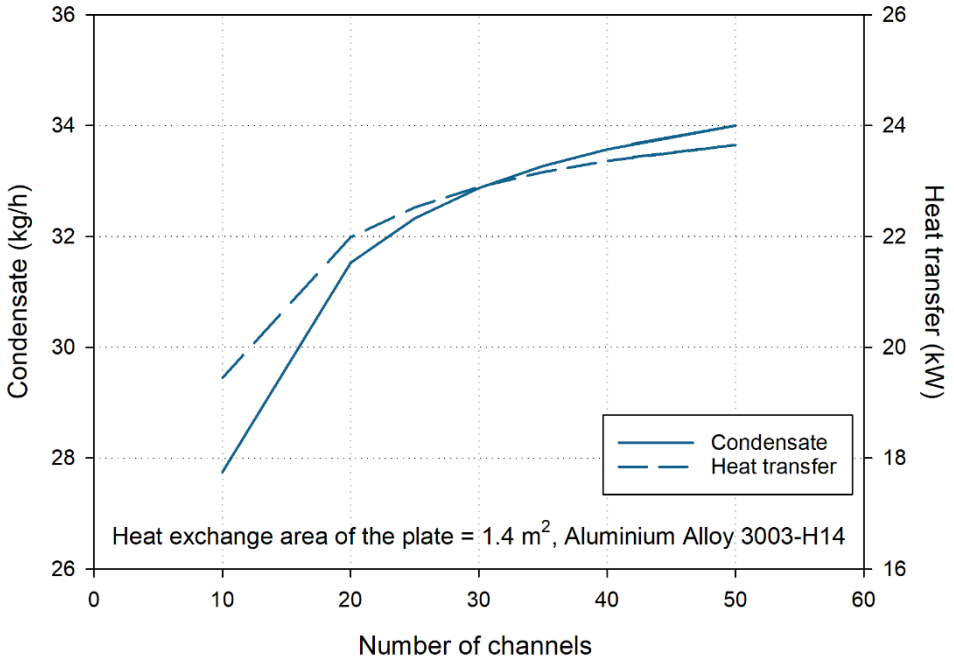


Fig. 5-21: Variation of performance with the number of channels.

Fig. 5-22 shows the impact of the plate heat exchange area on the condensation performance. The width of the condenser varies from 20 mm to 100 mm which results in the plate heat exchange area varying from 0.368 m^2 to 1.84 m^2. The other parameters are fixed. The condensate presents an increase trend with an increasing plate heat exchange area at the beginning and then decreases. The reason is that with an increasing plate heat exchange area, the heat transfer between the outer surface and the moist air is enhanced by the transfer of more cooling capacity. However, as the width of the condenser increases, part of the moist air has already been condensed by the coolant in the first few passes and the temperature drops. This lower temperature moist air will be condensed by the coolant of the same temperature in the latter pass, which is less efficient and thus reduces the condensation rate.

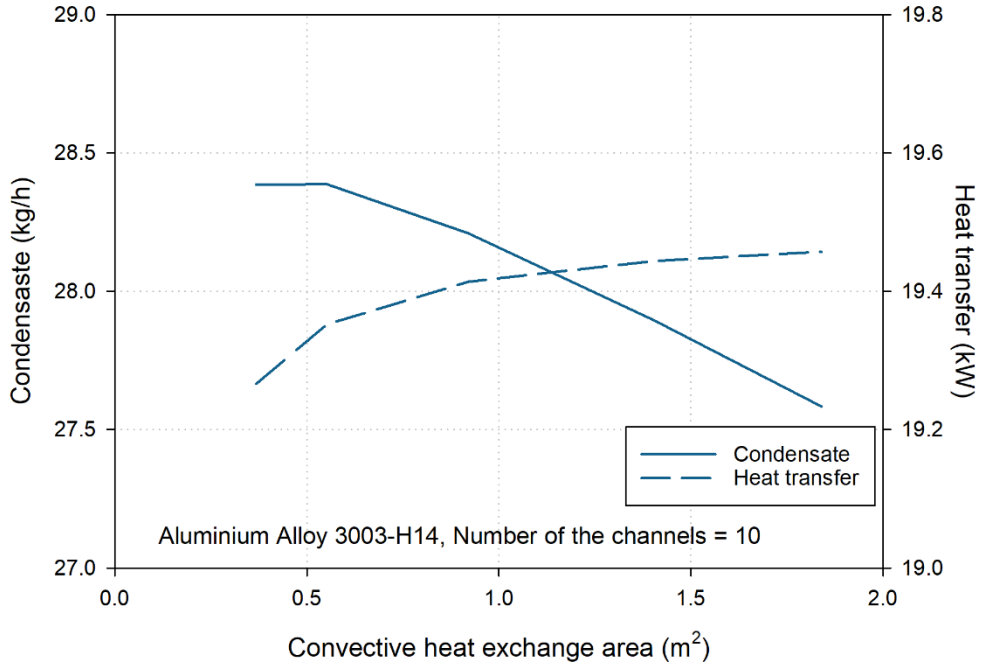


Fig. 5-22: Variation of condensation performance with convective exchange area of the plate.

5.6.2 Frosting

The geometry parameters affect the heat transfer process in the condenser, resultant frost properties when the surface temperature is beneath a certain limit. The wall thickness, configuration of the channel and the plate of the condenser are discussed. As a result, in this section, the impacts of the geometry parameters on the frosting performance are analysed as shown in Table 5-11. The moist air is simulated at the pressure of 1 bar, temperature of 25ºC, relative humidity of 90%. The coolant CH_4 is examined at -60ºC of 1 bar. The frost properties including frost thickness and frost accumulation are the main indicators of the system performance.

Table 5-11 Geometry parameters of the condenser

No	Parameters	Unit	Quantity
1	Material of the condenser	-	Aluminium Alloy 3003-H14; PTFE; AISI316
2	Thickness of the plate	mm	0 - 0.45
3	Heat exchange area of the channel	m^2	1 - 5.5
4	Heat exchange area of plate	m^2	0 - 1.84

As described in the previous chapter, the conduction heat transfer is related to the thickness of heat exchanger material and its thermal conductivity. Fig. 5-23 shows the frost thickness and frost accumulation affected by different materials: i.e., PTFE, Stainless Steel AISI316 and Aluminium Alloy 3003-H14 at the same operational conditions. It is clear to see that the performances are almost the same with all the three materials. The reason for this is that with the same duration time and the same condenser configuration, the thermal conductivity only affects the starting wall temperature. When the sample substrate is covered by the frost and the enough size of the heat exchange area, the wall temperature has limit effect on the frosting performance.

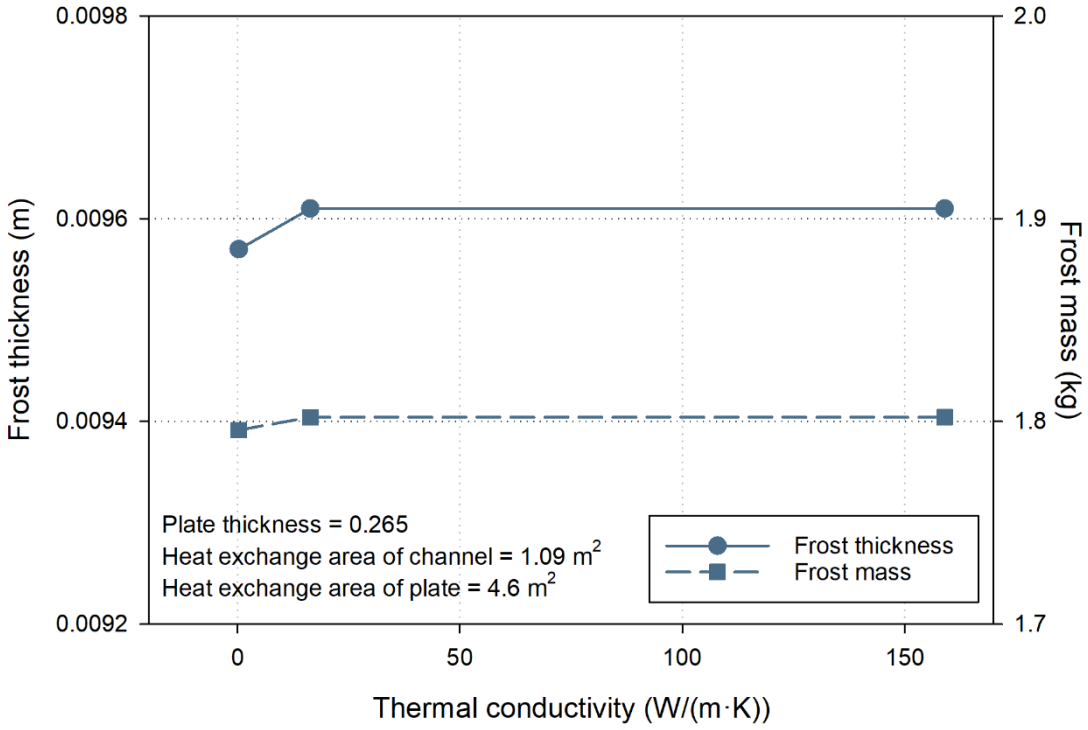


Fig. 5-23: Variation of frost properties with different material.

Fig. 5-24 shows the influence of the wall thickness of a AISI 316 substrate on the frost deposition with frost accumulation and frost thickness. It is observed that the wall thickness varying from 0.265mm to 0.515mm has little influence due to the good performance of AISI316 which reduces the influence of the wall thickness on the heat conduction process over the same duration time. Fig. 5-25 depicts the frost thickness and frost accumulation with varying convective exchange areas of the channels inside the plate. By raising the A and B of the channel from 483 mm^2 to 2416 mm^2 and reducing the number of channels in each plate from 50 to 10, the convective heat exchange area of the channel is changed. After the simulation has run for 30 minutes, the findings are based on the steady-state data. The frost characteristics exhibit a rising trend under the same circumstances as the heat exchange area of channels rises. The larger heat exchange area of the channels creates a more effective area for heat

transfer with the same volume of condenser. Additionally, significantly more capacity of coolant is transferred and consumed between the cooling medium and the surface to increase the frost accumulation.

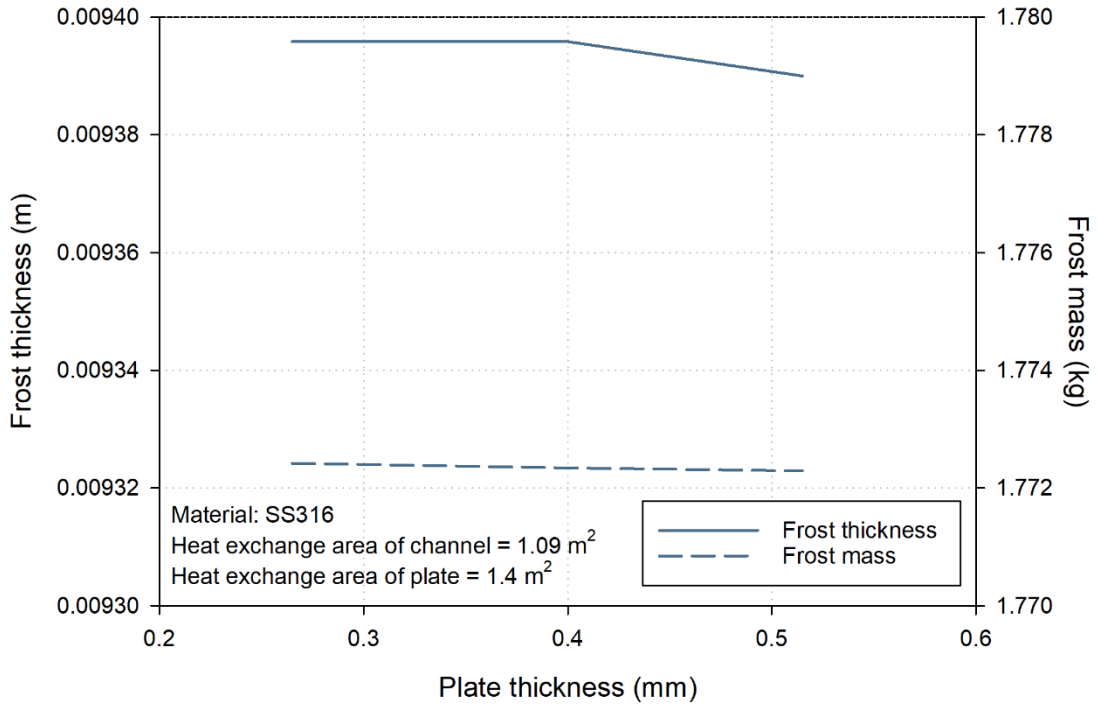


Fig. 5-24: Variation of frost properties with the thickness of the material.

Fig. 5-26 shows the impact of the plate heat exchange area on the frost characteristics. The plate heat exchange area varies from 0.368 m^2 to 1.84 m^2 depending on the condenser's width, which ranges from 20 mm to 100 mm. The other parameters are fixed. With a growing plate heat exchange area, the frost mass shows an upward trend. Because as the surface area of the plate increases, more cooling capacity is transferred, improving the heat transfer between the outside surface and the moist air. However, the frost thickness gets smaller. The reason is that the frost is uniformly

distributed on the whole substrate. Consequently, the optimal heat exchange area of the plate is the precondition of the higher efficiency and lower cost.

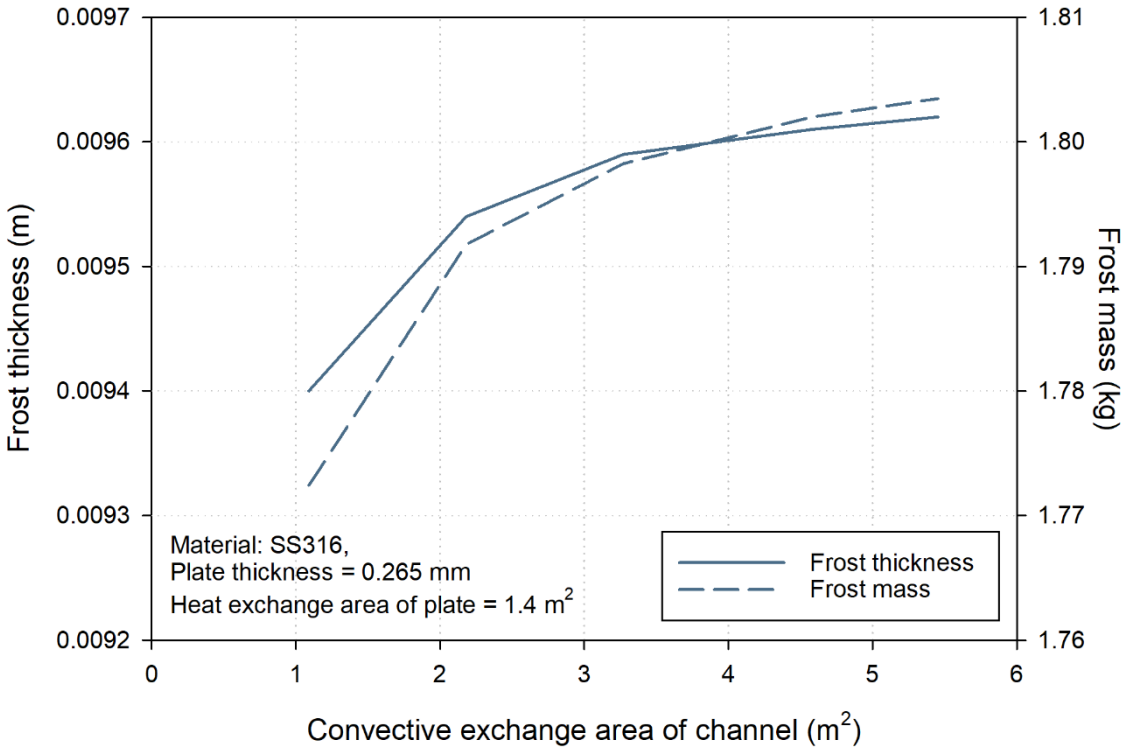


Fig. 5-25: Variation of frost properties with convective exchange area of the channel.

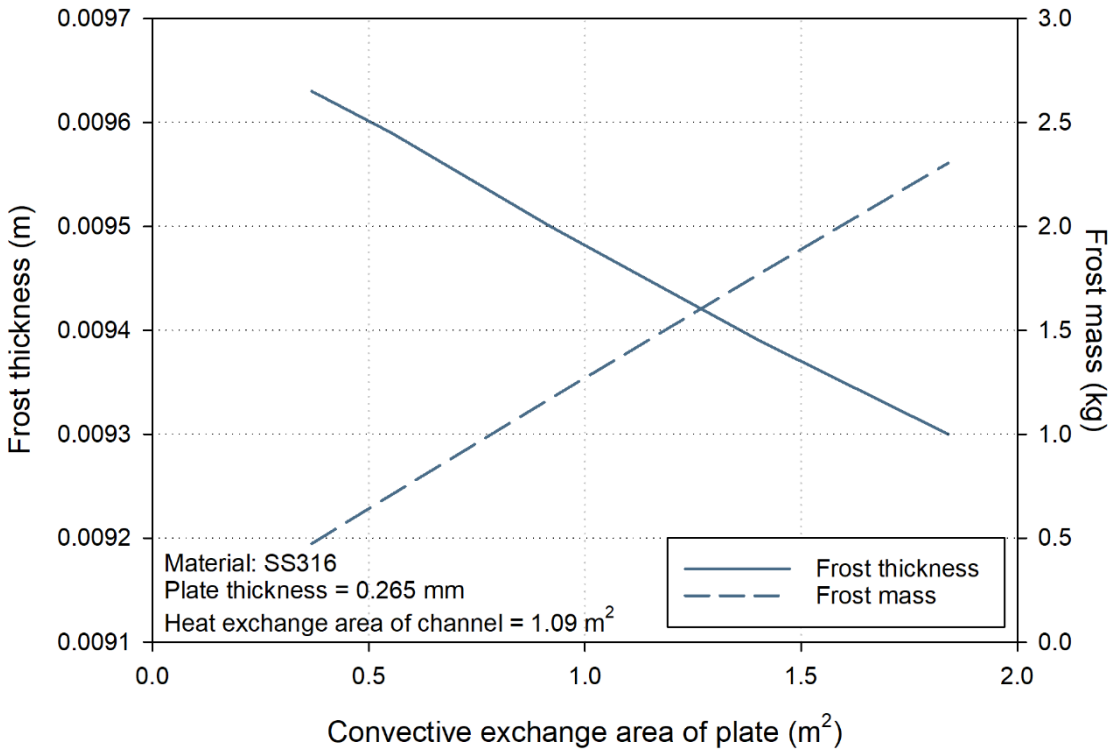


Fig. 5-26: Variation of frost behaviours with convective exchange area of the plate.

5.7 Parametric study - condensation

In this section, a parametric study was carried out to investigate how air properties and the coolant properties affect the condensation performance in the condenser. The operational parameters with a varied coolant temperature from 0ºC to 25ºC are described in Table 5-12. Condensate is the evaluation parameter to evaluate the condensation performance.

Table 5-12 Operational parameters of the condenser in condensation.

No	Air				Coolant	
	Pressure (bar)	Temperature (ºC)	Relative humidity	Mass flow rate (kg/s)	Temperature (ºC)	Mass flow rate (kg/s)
1	1	90	40%	0.25	0, 5, 15, 25	0 - 1.3
2	0.05 - 0.20	30, 40, 50	40%	0.25	5	0.694
3	0.05 - 0.20	40	20%, 30%, 40%, 50%, 60%	0.25	5	0.694
4	0.05, 0.08, 0.15, 0.20	30	40%	0 - 1.3	5	0.694

Fig. 5-27 depicts the condensate produced by varied flow rate of coolant at different temperatures: 0 ºC, 5 ºC, 15 ºC, 25 ºC with other parameters fixed in **Error! Reference source not found.**. The condensate first rises with the rising coolant flow rate at a given coolant temperature and eventually moves closer to its maximum value. Beyond a certain point of the coolant flow rate, the increasing trend reaches its limit. The explanation is that a higher coolant flow rate coolant flow rate offers more condensation cooling capacity, enhancing condenser efficiency. However, a constant moist air flow rate is not sufficient to allow a higher coolant flow rate with additional cooling capacity to be condensed, which directly impacts the heat recovery from condensation. It is also noteworthy that greater amount of condensate is generated with a lower coolant temperature. There is a tremendous potential to lower the moisture content in wet air with a given relative humidity by using a lower coolant temperature as the lower dew point of the condensation process. Consequently, the optimal coolant operating

conditions can be selected according to the economic flow rate and a practically achievable low temperature. Furthermore, this phenomenon also applies to the future section where the imported LNG temperature is cryogenic.

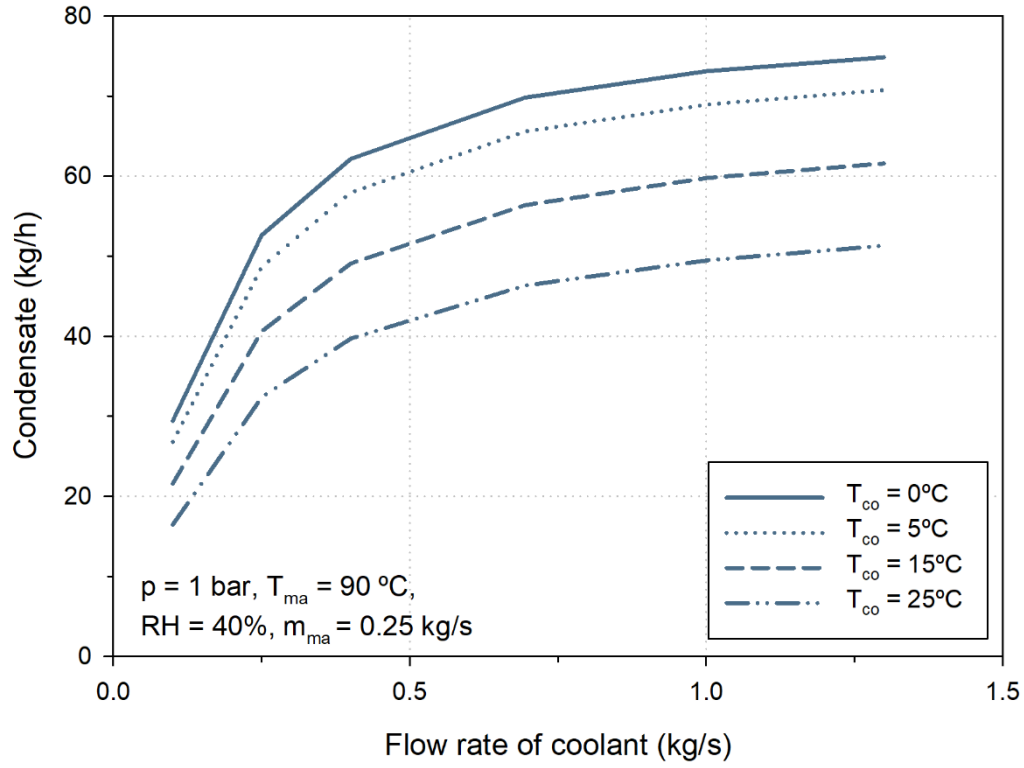


Fig. 5-27: Variation of condensate with coolant temperature and flow rate.

In Fig. 5-28, the moist air with a relative humidity of 40% and the mass flow rate of 0.25 kg/s is condensed by the cooling water of 0.694 kg/s under 5ºC. And Fig. 5-29 shows the cooling water with the same conditions providing the cooling capacity to the air under a temperature of 40 ºC and the mass flow rate of 0.25 kg/s. It can be observed that the production increases with an increase of the temperature and the humidity of moist air which has a higher water vapour partial pressure. The condensate increases by 73% from the 10.8 kg/h generated by 30 ºC, 40% moist air to the 39.6 kg/h created by 50 ºC, 40% moist air in Fig. 5-28 when the pressure in the condenser chamber is

fixed at 0.05 bar. The condensate produced by 40 ºC, 60% moist air increases by 87% from 5.11 kg/h when 40 ºC, 20% moist air is used to 5.11 kg/h when 40 ºC, 20% moist air is used. As a result, condensate begins to be generated at a significantly higher condensing temperature, which increases the pace at which condensate is produced.

In Fig. 5-28 and Fig. 5-29, it is also observed that the condensate drops by around 50% when the pressure increases from 0.05 bar to 0.20 bar at the temperature of 30 ºC and the lower relative humidity level of moist air. Because of this, dew point, saturation temperature, and water vapour partial pressure all decrease as pressure decreases. The geometry of the condenser remains same for the sake of this comparative analysis. Therefore, a lower dew point will result in a lower moisture content after condensation. As a result, with reduced pressure in the chamber, moisture loss, or in other words, condensate generation, is higher.

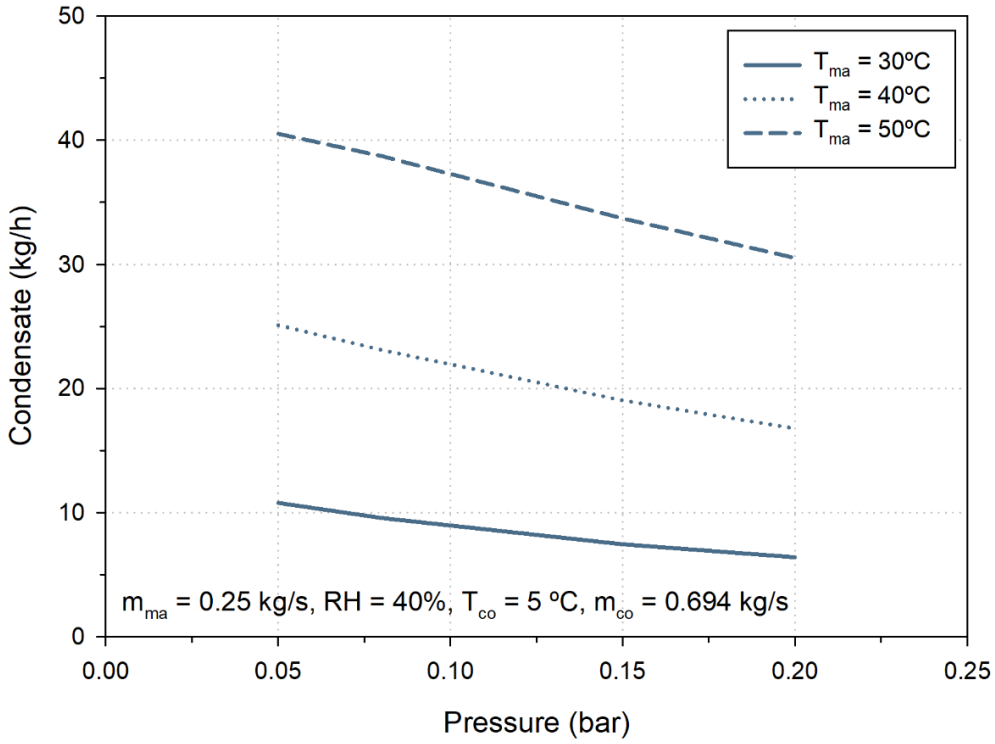


Fig. 5-28: Variation of condensate with moist air temperature and pressure.

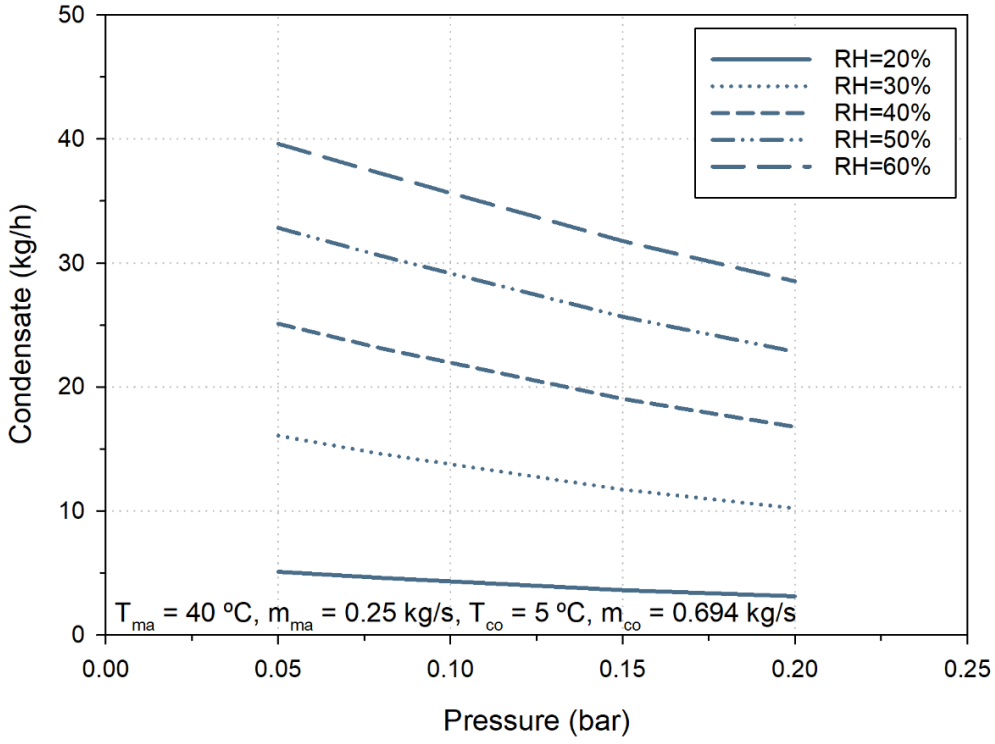


Fig. 5-29: Variation of condensate with moist air relative humidity.

Fig. 5-30 shows the condensate under a varying mass flow rate of moist air and pressure with the operational parameters shown in **Error! Reference source not found.**. Condensate production rate increases with greater moist air flow rate under a given pressure until it hits its limit, at which point it gradually drops. It is obvious that increased moist air flow rates result in higher condensation moisture content and require more cooling power to counteract condensation heat. Furthermore, an excessively high mass flow rate of moist air might negatively impact the condenser's heat exchanger's efficiency and the direct transfer of cooling energy, which is necessary for the condensation process. When determining the ideal moist air flow rate, conflicting impacts should be taken into account.

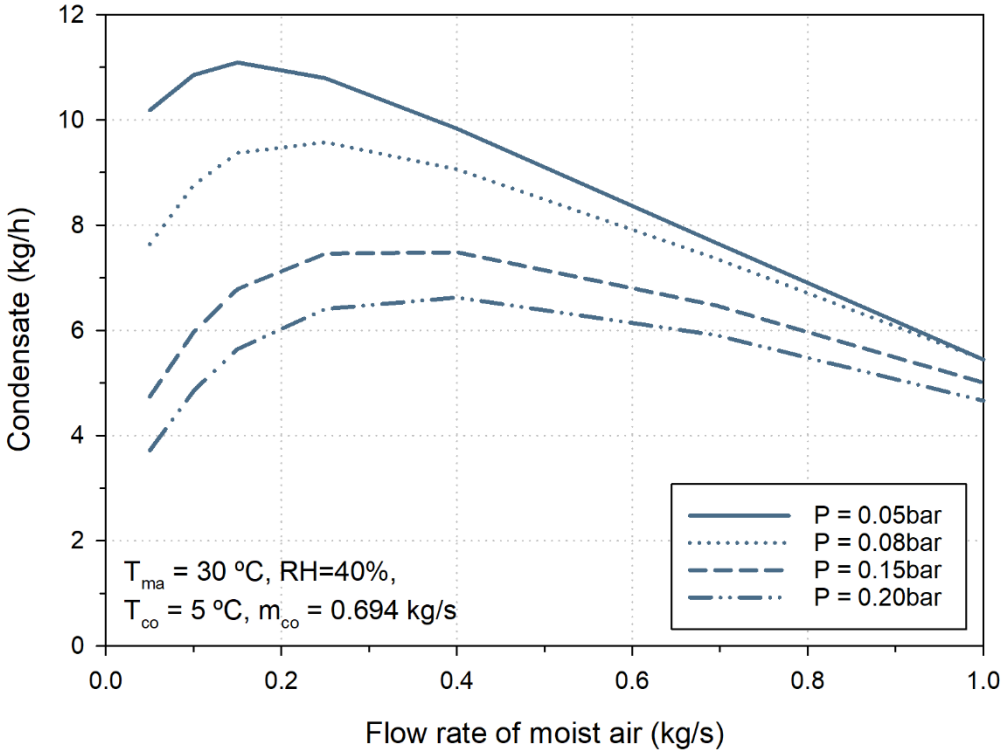


Fig. 5-30: Variation of condensate with a moist air flow rate.

5.8 Parametric study – frosting

Numerical calculations of the parametric study on the cryogenic coolant temperature cases were carried out to investigate the change of the frost properties and the heat transfer performance. The varied operational parameters are described in Table 5-13.

Table 5-13 Parametric study cases on frosting.

No	Air				Coolant	
	Pressure (bar)	Temperature (ºC)	Relative humidity	Velocity	Temperature (ºC)	Mass flow rate (kg/s)
1	1	15, 20, 25, 30	90%	0	-100	0.2
2	1	25	90%	0, 0.1, 0.2	-100	0.2
3	1	25	90%	0	-100, -130, -160	0.2

5.8.1 Effect of air properties – air temperature

Fig. 5-31 shows the relationship between frost thickness and frost accumulation at various environment air temperatures of 15ºC, 20ºC, 25ºC and 30ºC. The frost accumulation increases with the increased air temperature. At constant relative humidity, the humid air contains more water vapour at higher air temperatures, resulting in a higher water vapour mass concentration. This phenomenon could be demonstrated by the results shown in Fig. 5-32. Since the frost accumulation is related to the difference between the water vapour mass concentration in the air and the frost,

the increase in the air temperature drives an increase in the mass concentration difference and the frost accumulation.

The effect of the air temperature on the porosity is shown in Fig. 5-32. The frost density and the frost thermal conductivity is dependent on the porosity and the air properties. As the time goes, the frost grows in two directions: horizontal for densification and vertical for thickness. Part of the vapor is deposited directly onto the frost surface, thickening the frost layer. The remaining vapor diffuses into the frost layer, causing a difference in concentration and leading to a phase change. This ultimately results ina an increase in both the thickness and density of the frost layer. In addition, with the fixed coolant temperature, the temperature difference between the air and the surface becomes greater with the higher air temperature, which enlarges the air side heat transfer coefficient. The total heat transfer between the air and the frost consists of two parts: sensible heat that contributes to the temperature decreasing and latent heat which contributes to the frost growth.

As the time goes, the frost deposits and grows on the surface leading to an extra thermal resistance as shown in Fig. 5-33. Initially, during the early stages of frost formation, the thermal resistance experiences a rapid increase within 25min due to the simultaneous increase in the frost thickness and the decrease in surface temperature. Then the growth of the thermal resistance slow down as the time goes due to the reduction of the porosity, leading to the increase in the frost thermal conductivity. Eventually, the thermal resistance of the frost layer becomes stable over time due to the balance between the back-melting and the regrowth. This phenomenon indicates

that after the specific period, the densification is the main mechanism in the frost deposition process.

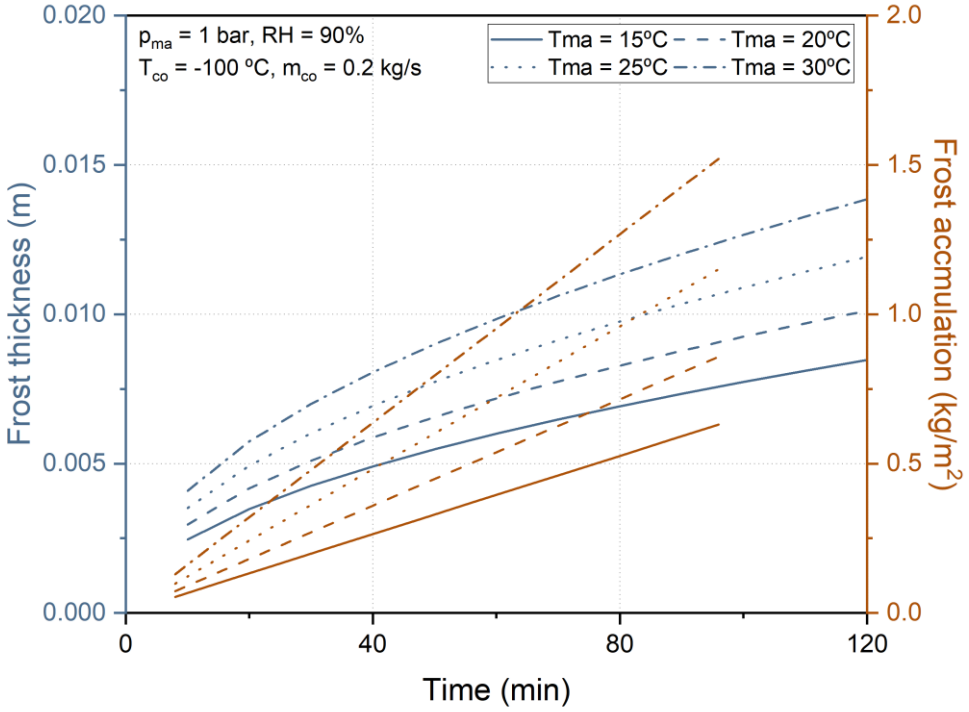


Fig. 5-31: Frost thickness and frost accumulation with different air temperature.

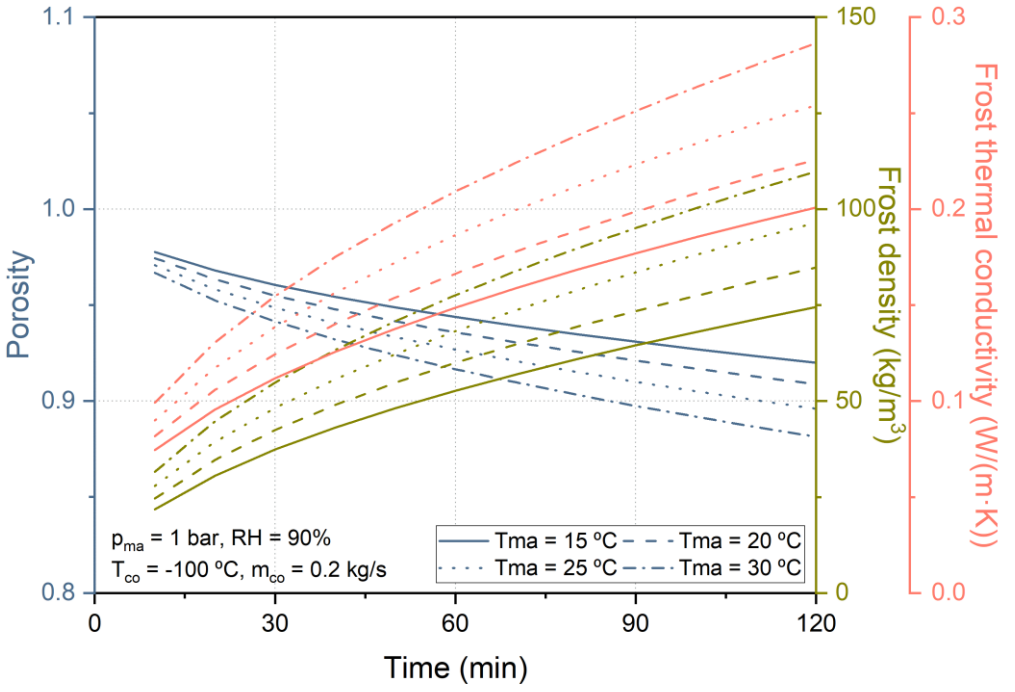


Fig. 5-32: Effect of air temperature on porosity, frost density and thermal conductivity.

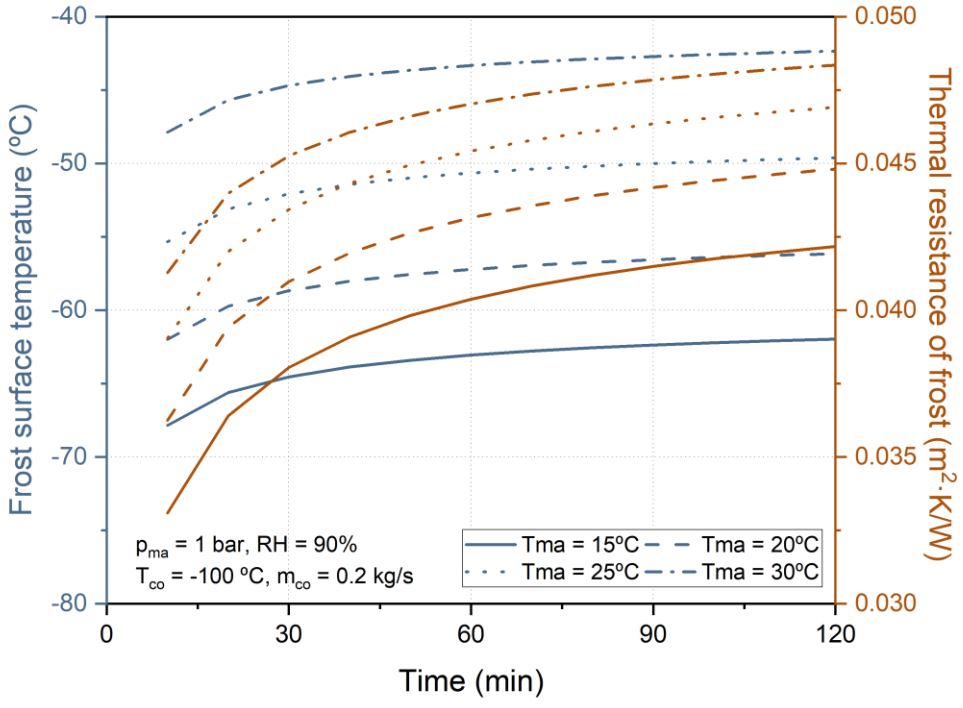


Fig. 5-33: Frost surface temperature with time.

5.8.2 Effect of air properties – air velocity

The third influence factor is the air velocity. As indicated in Table 5-13, the velocity is decided as 0m/s, 1m/s and 2m/s. The air property is fixed at 25ºC with a relative humidity of 90%, while the coolant flows at 0.2kg/s with a temperature of -100ºC. In current case, the air flows above the surface, the mechanism turns to forced convection with a mixed heat transfer between the air and the outer surface. Therefore, the Nu number in this case is defined as the mixture of the free convection and forced convection. Similarly, the frost accumulation on the surface is compared with varied velocity as shown in Fig. 5-34. It could be seen that the air with higher velocity has more frost deposition with higher concentration on the surface. And the heat between the surface and the air transfers more with the velocity. The reason is that the air flow enhances the heat transfer coefficient through the extra forced convection which results in a greater heat transfer ability.

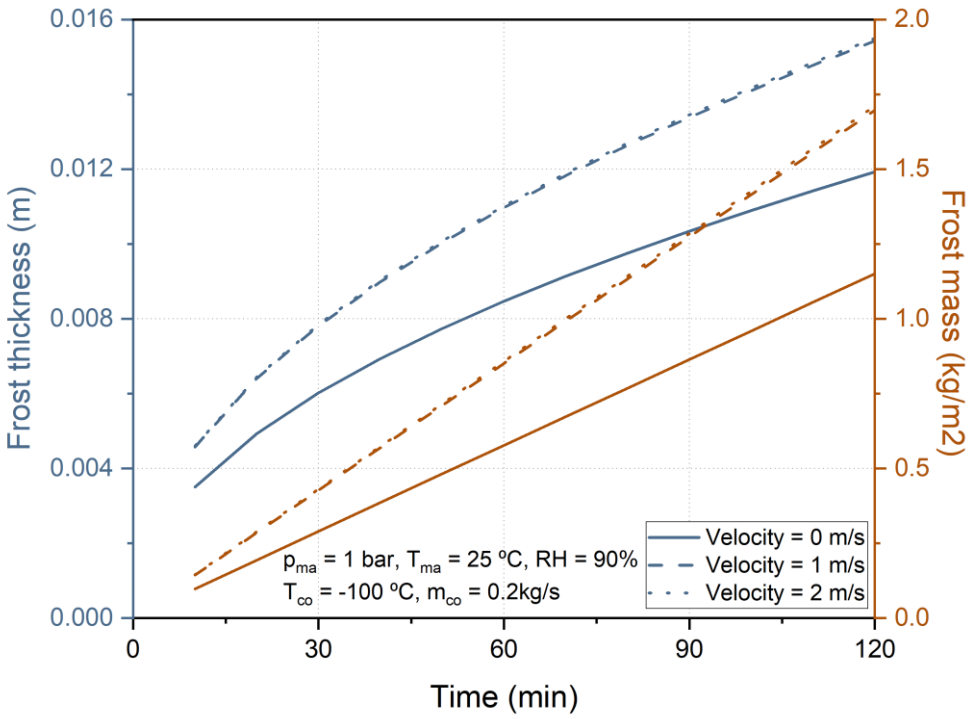


Fig. 5-34: Frost deposition performance with different velocity of air.

5.8.3 Effect of coolant temperature

Different coolant inlet temperature provides different surface temperature which is the main influence factor as proved by the experiments mentioned earlier in the previous chapter because the subcooling affects the heat and mass transfer performance. Fig. 5-35 and Fig. 5-36 show the frost properties changes with the coolant temperature of -100ºC, -130ºC and -160ºC. It could be seen that on the colder surface, the frost accumulated the most only in growth. Fig. 5-36 presents that with lower surface temperature, the porosity is higher. The reason is that with the colder inlet temperature of the coolant, the tube surface has a lower temperature which leads to a colder frost surface as shown in Fig. 5-37. On the colder frost surface, the water vapour nucleates quickly as small nucleus and then the new nucleus deposit on the existing ones that

increase the thickness of the frost. However, the interaction between the nucleus presents a slower speed than the new nuclei formation. Therefore, the frost layer is full of pores which results in a higher porosity and smaller density.

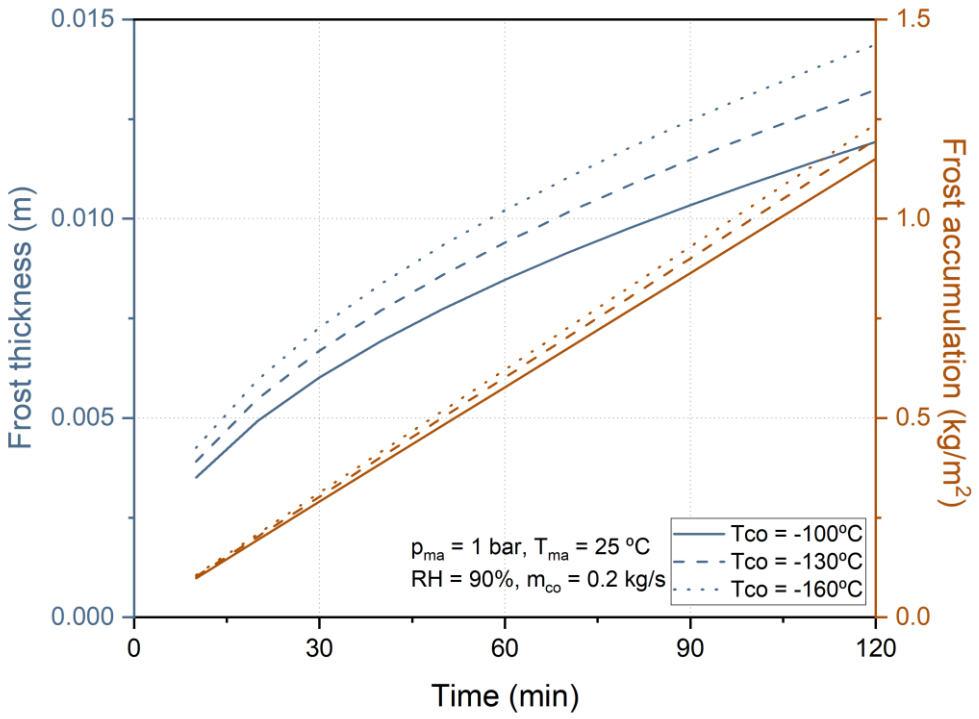


Fig. 5-35: Frost thickness and frost accumulation with different coolant temperature.

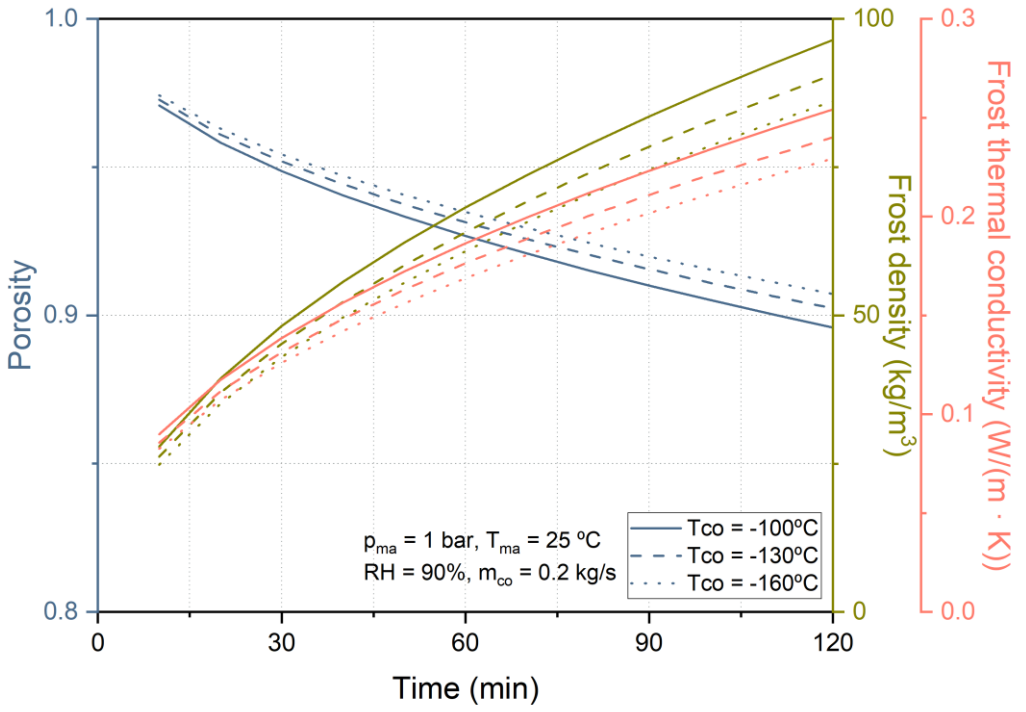


Fig. 5-36: Effect of coolant temperature on porosity, frost density and thermal conductivity.

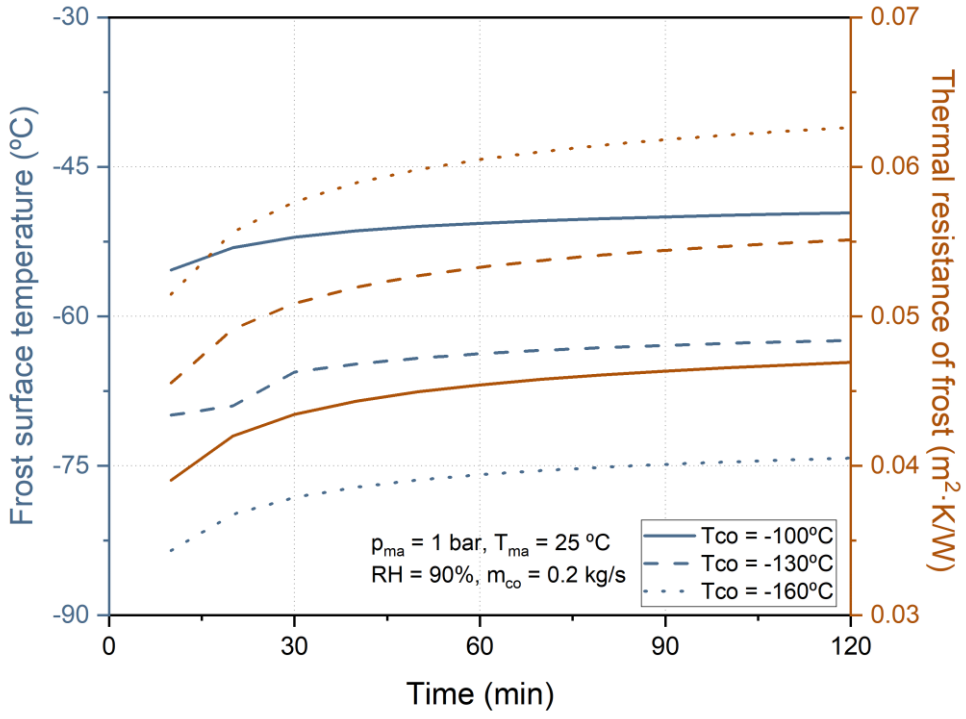


Fig. 5-37: Frost surface temperature comparison with coolant temperature.

In summary of the above results, the effect of these operation parameters on the frosting properties could be summarised in Table 5-14 below:

Table 5-14 Summarised effect factors on frost properties.

Increase of parameter	Thickness	Accumulation	Density	Porosity	Thermal conductivity	Frost surface temperature
Air temperature	↑	↑	↑	↓	↑	↑
Air velocity	↑	↑	↑	↓	↑	↑
Coolant temperature	↓	↓	↑	↓	↑	↑

↑: increase trend, ↓: decrease trend

5.9 Summary

In this chapter, the numerical study on each component of the FWG system has been investigated. The parametric study of the evaporator shows that the pressure of the chamber, the superheat of the feed water and the heating input determine the performance of the water vapour production. For the condenser, under both mechanisms (condensation and frosting), the production (water & ice) is related with the water vapour content and coolant temperature and flow rate. In addition, the geometry design of the heat exchanger also affects the system performance, such as convective heat exchanger area and the material. Therefore, these parameters are primary to optimise in the case ship study in the next chapter.

CHAPTER 6 CASE STUDY

6.1 Introduction

In Chapter 4 and Chapter 5, the experimental and numerical studies were carried out and predicted in detail the evaporation, condensation and frosting behaviours under varying operation conditions. However, the varying LNG flow rate during the voyage on the ship performs differently. Furthermore, the space limitation is not considered. In fact, a ship's engine room is constrained by limited space, which makes it challenging to implement the system. Thus, the primary objectives of the current chapter are summarised as:

(1) To propose a novel LNG cryogenic energy recovery system for freshwater generation and LNG production

(2) To design the operation parameters for the FWG system's optimisation

(3) To analyse the proposed system from the thermodynamics and economics fields.

Therefore, this chapter introduces the detailed freshwater generator arrangement of the design system and optimises it through simulation analysis in Siemens Simcenter Amesim. A genetic algorithm was used to optimise the parameters of the optimised plan. It is expected to provide an innovative technology path for the novel FWG to construct an efficient and compact comprehensive utilisation system of LNG vaporisation and cold energy on LNG powered ships.

6.2 Case-study ship introduction

In this section, the proposed optimised system is employed on an LNG powered cruise ferry utilising a DF-Electric power plant. This ferry operates a 48-hour route from Stockholm to Finland (including five hours harbour time), including a two-way voyage and one intermediate stop. The detailed information about this case-study ship is presented in Table 6-1. The LNG on this ferry is stored in the tank at a temperature of -138 ºC and 5 bar pressures. During the 48 hours, the NG consumption varies from 350 kg/h to 3161 kg/h. The feed-in seawater enters the vacuum evaporator of the FWG, the evaporated water vapour is condensed by the LNG cryogenic energy released from the LNG vaporisation. Based on the voyage records, the NG consumption for 48 hours is presented in Fig. 6-1.

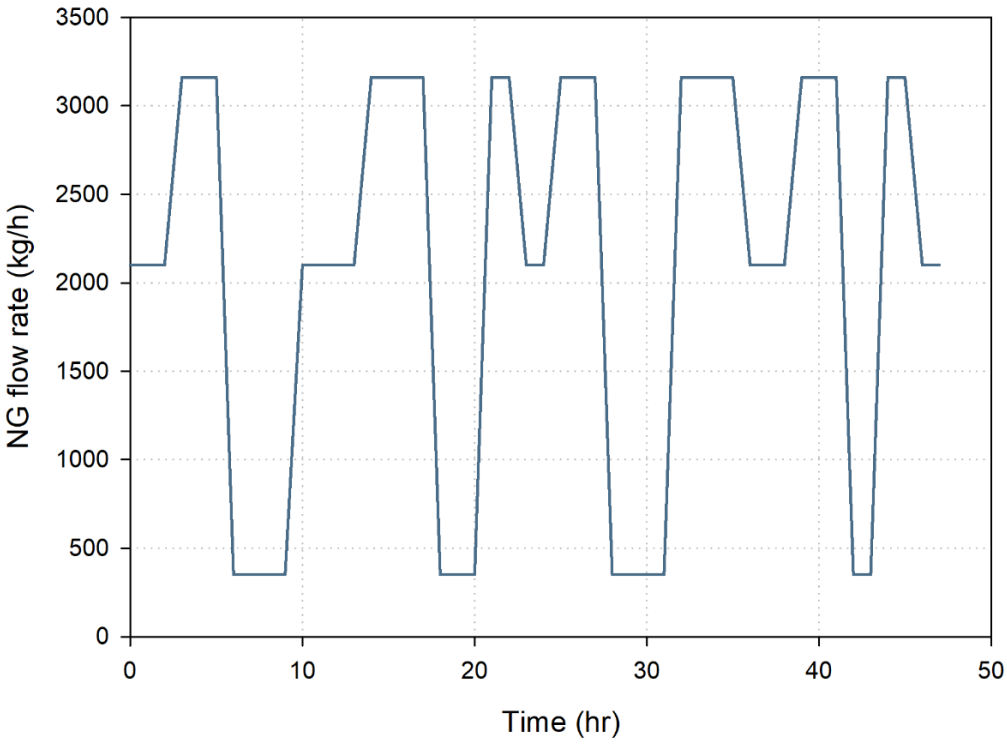


Fig. 6-1: Diagram of NG consumption in 48 hours.

Table 6-1 Detailed information about the case-study ship.

Parameters	Quantity
Ship type	Passenger ship
Built year	2013
Length	218m
Beam	32m
Draught	6.8m
Gross ton	57.565 GT
Net ton	47.600 GT
Speed	22.0 knots
Capacity	2,800 passengers;
Crew	200
Main engines	4 x Wartsila 8L50DF, 7600 kW per unit
LNG fuel tanks	2 x Type C cylindrical cryogenic tanks, 2 x 200 m^3
Boiler	2 dual fuel boilers from SAACKE
Propulsion motor	2 x electrical propulsion motors ABBAMZ1600, 10500kW per unit
Thruster	2 bow thrusters of 2300 kW and one stern thruster if 1200 kW

6.3 System description

Considering the existing design of the LNG regasification system on the case-study ship, the novel LNG cryogenic energy recovery system with the FWG system is designed as indicated in Fig. 6-2, consisting of three parts: LNG tank, dual fuel engines and LNG cryogenic energy recovery system. The recovery system integrates the three vaporisers and two applications:

- Vaporisers: pressure built-up evaporator (PBE), main gas evaporator (MGE) and main gas heater (MGH);
- Applications: FWG system and low temperature (LT) water system.

LNG is stored in the tank at -138 ºC and 5 bar pressure. Since the pressure and temperature are closely correlated in the tank, each change in temperature level also results in a change in pressure. As a result, the PBE builds up and maintains an operational pressure of 5 bars in the tank. The MGE and MGH are designed to increase the temperature of regasified NG up to 27 °C, which is the NG operational temperature to enter the gas valve unit (to maintain the NG inlet pressure to the engines at 3 bars and provides a prompt and reliable gas supply shutdown). During the regasification process, MGE recovers the LNG cryogenic energy in the FWG for freshwater generation; while MGH recovers the remaining cryogenic energy in the LT water system for cooling the low-temperature water to supply the main engine generators, the auxiliary coolers, and other auxiliary systems. The schematic of energy recovery is presented in Fig. 6-3.

It is noticed that the inlet temperature of the LNG in the MGE starts at -133 ºC. At this temperature, the LNG has already been vaporised, which means that the existing recovery system only recovers the sensible heat of the LNG. The cold energy between -138 ºC and -133 ºC is dissipated through the pipes directly after the storage tank, before the MGE. Therefore, the latent heat of the vaporisation of the LNG is wasted through the pipes to the ambience. The amount of the enthalpy change during this process is 470 kJ/kg, resulting in more than 50% losses in the current LNG cold-energy recovery process.

The FWG system consists of five components: the evaporator, solenoid valve, steam accumulator, condenser (MGE) and freshwater tank. It is efficient in creating a lower pressure in the evaporator chamber for flash evaporation by a vacuum pump. [157] The steam generated from the evaporator is stored in the steam accumulator. The flow controlled by the electromagnetic valve enters the MGE and is condensed by LNG cryogenic energy into freshwater. The system consumes the waste heat from the engine as the heat source and the LNG cold energy as the heat sink. To minimise the heat loss to the environment, the insulation layers are placed on the outside of all the components and connection pipes.

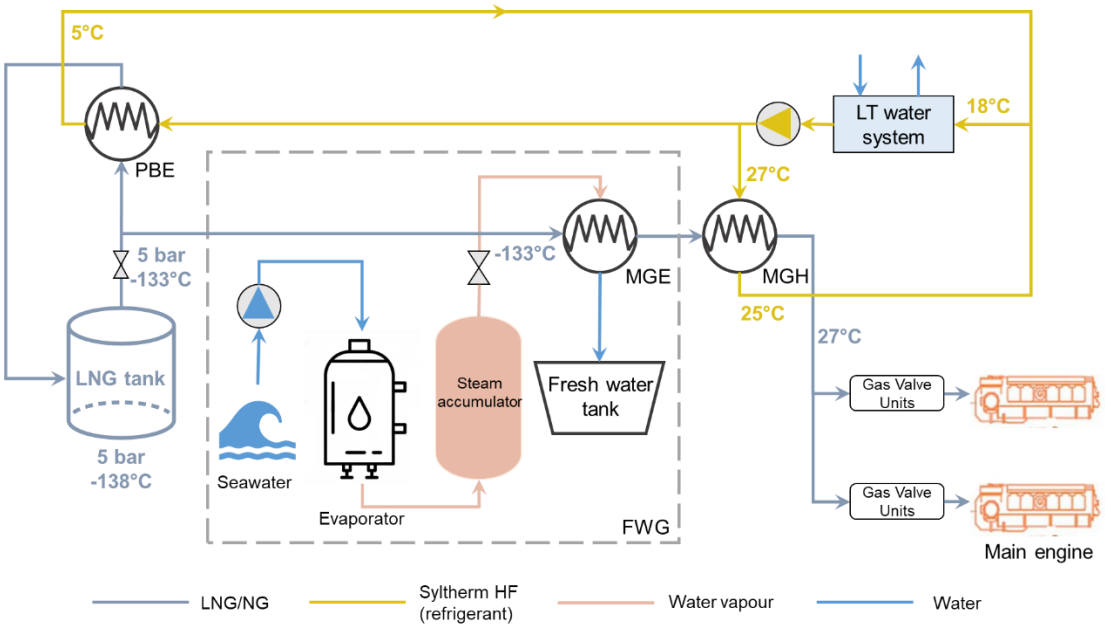


Fig. 6-2: Schematic diagram of the LNG cold energy recovery system on the case-study ship.

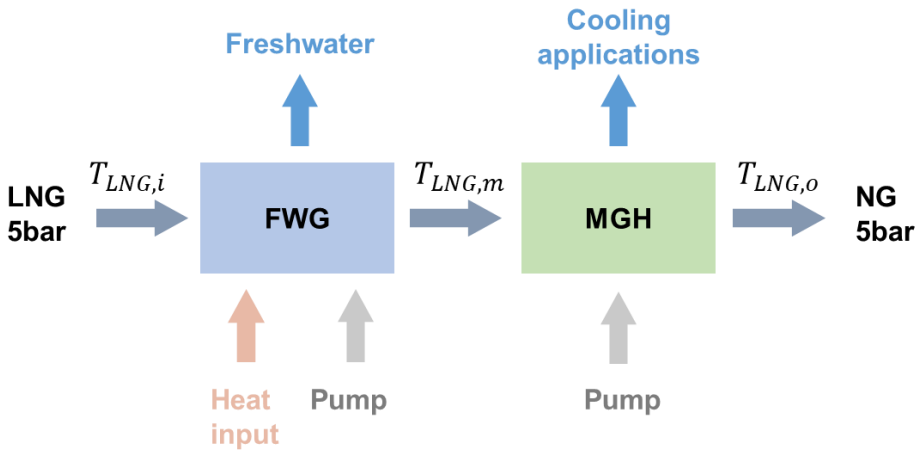


Fig. 6-3: LNG cold energy recovery process.

6.4 Methodology

In this section, the proposed novel recovery system is modelled by Siemens Simcenter Amesim software based on the numerical thermodynamics study in Chapter 5 and the economic viewpoints. The analysis starts by presenting the mathematical models for energy and exergy analysis, considering the thermodynamic assumptions. Following this, both single objective and multi objective optimisations are implemented to enhance the performance of the FWG system under various operation conditions on the case-study ship. Eventually, the overall performance criteria for the proposed FWG system are developed from an economics viewpoint.

6.4.1 Energy and exergy analysis

Both energy and exergy analysis are the key indicators in the thermodynamics optimisation with the following assumptions:

(1) All system components are assumed to be static and isothermal.

(2) Pressure losses in the piping are considered to be negligible.

(3) The temperature losses in the pipe between the components are negligible.

The first and second laws of thermodynamics are utilised to evaluate the energy and exergy efficiencies of the LNG cryogenic energy recovery system. The general energy balance equation is written as follows,

$$\sum \dot{m}_i = \sum \dot{m}_o \tag{6-1}$$

$$\sum \dot{m}_i \dot{h}_i - \sum \dot{m}_o \dot{h}_o + \dot{Q} - \dot{W} = 0 \tag{6-2}$$

where $\dot{Q}$ and $\dot{W}$ represent the heat capacity input and work to the surroundings, respectively.

One of the key indicators to evaluate the system, LNG cold energy recovery efficiency of the condenser, could be calculated as follows,

$$\eta_{LNG} = \frac{q_{LNG,use}}{q_{LNG,total}} \tag{6-3}$$

The useful LNG heat transfer rate $q_{LNG,use}$ could be calculated by the enthalpy difference between the inlet and the outlet LNG as follows:

$$q_{LNG,use} = \dot{m_{LNG}}(h_{LNG,i} - h_{LNG,o}) \tag{6-4}$$

Exergy, defined as the maximum obtainable work that a system is able to achieve, is essential to improve the energy efficiency of the system. The specific exergy of a unit mass basis is given by [145]:

$$e = (h - h_0) - T_0(s - s_0) + \frac{v^2}{2} + gz \tag{6-5}$$

Then the specific exergy changes of the unit from state 1 to state 2 without the kinetic and potential energy are [145],

$$\Delta e = (h_1 - h_2) - T_0(s_1 - s_2) \quad (6\text{-}6)$$

To meet the design principles, the amount of the maximum usable work stored in LNG during the FWG process could be calculated as follows,

$$\Delta W_{max} = \Delta q - \Delta h = T_0 ds - dh \quad (6\text{-}7)$$

In the current case, LNG is stored in the tank at -138°C with 5bar and is vaporised into 27°C before entering the engine cell.

State 1: Enthalpy of CH_4 at -133°C, 5bar is: h_1 = 555.06 kJ/kg, s_1 = 4.15425 kJ/(kg · K);

State 2: Enthalpy of CH_4 at 27°C, 5bar is: h_2 = 910.146 kJ/kg, s_2 = 5.8504 kJ/(kg · K);

The exergy released at states 1-2 per kg of LNG is:

$e_x = e_{x1} - e_{x2} = [(h_1-h_0)+T_0(s_0-s_1)]- [(h_2-h_0)+T_0(s_0-s_2)]$ = 133.4052 kJ/kg

Then the cold energy of 1kg of LNG is

Δh = 910.146-555.06 = 355.086 kJ/kg

Equivalent power output per ton of LNG is: (355.086×1000)/3600 = 98.635 kWh

Exergy output per ton of LNG is: (133.4052×1000)/3600 = 37.057 kWh

The exergy equation for the system is expressed as:

$$\sum_i Ex_i = \sum_i Ex_o + W_e + Ex_d \quad (6\text{-}8)$$

Where Ex_d is the exergy destruction rate, W_e is the electricity power.

The performance of the proposed FWG-LNG system is evaluated by the parameters including water recovery rate (RR), gained output ratio (GOR) and exergy efficiency. The water RR represents the recovery ability of the desalination unit, which is the ratio of the recovery of freshwater to the inlet seawater [1], as shown below:

$$RR = \frac{\dot{m}_f}{\dot{m}_{sw}} \times 100\% \quad (6\text{-}9)$$

The Gained output ratio (GOR) indicates ratio of the equivalent evaporative energy of the distillate to the external heating input to the evaporator chamber as follows [158]:

$$GOR = \frac{m_f Hv}{Q} \quad (6\text{-}10)$$

The exergy efficiency could be achieved by,

$$\eta_{ex} = 1 - \frac{Ex_d}{\sum_i Ex_i} \quad (6\text{-}11)$$

6.4.2 Economic analysis

To determine the financial viability of the optimised energy systems, an economic study of the proposed system is also required, in addition to the energy savings perspective. In the current study, the capital, maintenance and operational costs are calculated for the numerical model. The total cost of this system is calculated by the following [159],

$$C_{total} = C_{fix} + C_{mc} + C_{oc} \quad (6\text{-}12)$$

Where C_{fix} is the fixed cost, C_{mc} is the total maintenance costs and C_{oc} represents the operational costs in total. The detailed calculation methods are shown in the following section. The total fixed cost of the system is obtained by [159],

$$C_{fix} = CRF \times \sum C_i \quad (6\text{-}13)$$

Where C_i is the capital cost for each component in the system, and CRF is the capital recovery factor defined as the followings [159],

$$CRF = \frac{i(1+i)^n}{(1+i)^n - 1} \quad (6\text{-}14)$$

In this equation, i is the interest rate, and n is the lifetime of the system.

The total maintenance and operational costs are then defined as,

$$C_{mc} + C_{oc} = MF * C_{cc} \quad (6\text{-}15)$$

Where MF is the maintenance factor and C_{cc} is the capital cost.

The payback period (PP) is defined as the ratio of the total cost (C_{total}) to the net earnings (C_{NE}). [160] The net earning is calculated as the cost of the produced water (C_f) minus the cost of maintenance, operation, taxes and interest. [161]

$$PP = \frac{C_{total}}{C_f - C_{oc} - C_{mc}} \quad (6\text{-}16)$$

6.4.3 Optimisation process

The primary objective of the current optimisation work is to minimise three performance indicators, namely, (1) the reciprocal of the water recovery rate (RR); (2) the system's exergy loss (Ex_d); and (3) the reciprocal of the recovery LNG cryogenic energy

efficiency (η_{LNG}). The proposed model compares and analyses the single-objective optimisation by the genetic algorithm method under different optimisation cases, including RR maximisation, LNG cryogenic energy recovery efficiency maximisation and exergy efficiency maximisation. The multi-objective optimisation is also compared and analysed by the Pareto optimal method. These design principles are followed:

(1) The design should meet the cooling load requirements of the ship's functional systems. On this basis, the LNG cryogenic energy should be recovered as far as possible.
(2) In order to meet the temperature requirements of the NG combustion in the engine, the outlet temperature of the NG from the FWG system should be maintained lower than 27 ºC.
(3) To minimise the maintenance cost and the negative effects on board, frosting issues should be avoided.

In this study, the design parameter for the genetic algorithm optimisation is shown in Table 6-2, and objective functions are presented in Eq.(6-3), Eq. (6-9) and Eq. (6-11) to obtain the optimum design parameters of the system. The genetic algorithm optimisation was applied for a maximum of 20 generations, using a search for 100 population size, and mutation probability of 10%.

Table 6-2 Design parameters in the optimisation.

Design parameter	Unit	Lower bound	Upper bound
Moist air flow rate $\dot{m_{ma}}$	kg/h	0	0.8
Pressure p	bar	0.08	1
Moist air temperature T_{ma}	K	293	373
LNG outlet temperature $T_{LNG,o}$	K	268	300

(a) Genetic algorithm optimisation

The genetic algorithm is an optimisation technique that is inspired by natural evolution. The algorithm starts from a population of randomly generated individuals, which accordingly become the parent individuals. In each generation, each individual is evaluated by calculating their fitness function. Then the fit individuals are selected and modified through the process of selection, crossover and mutation to create the new generation, called child individuals. Then the algorithm process continues until the satisfactory fitness level has been reached, which represents the best solution for the problem [124, 162, 163]. Fig. 6-4 shows the flow chart of the genetic algorithm process optimised in Siemens Simcenter Amesim software.

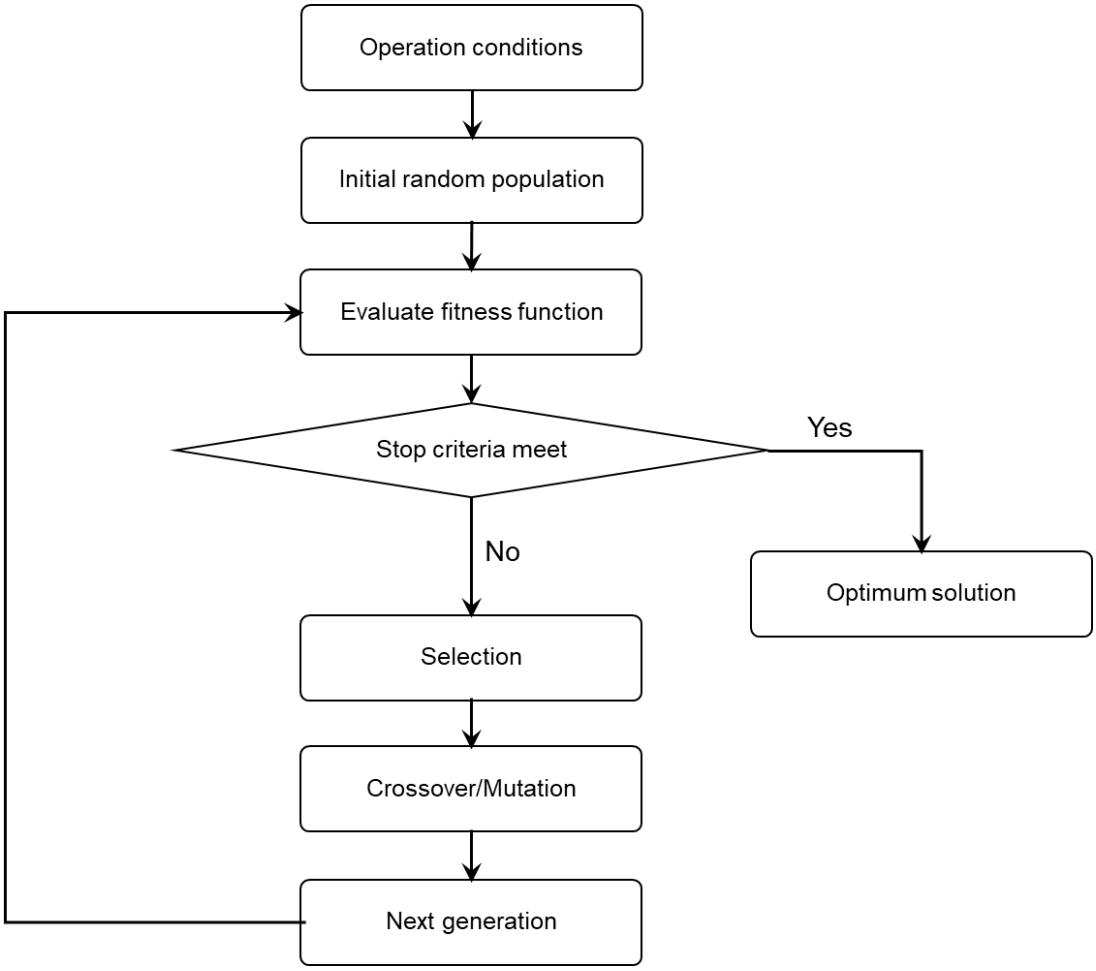


Fig. 6-4: Flow chart of genetic algorithm.

(b) Pareto optimisation

The Pareto optimal method is a commonly used optimisation method dealing with multiple, conflicting, objective functions and design criteria in engineering design. [164] Pareto optimality, which originated with Italian economists, is defined as the absence of any other design that can improve the value of its objective criteria without deteriorating at least one other criterion. In mathematical terms, the multi-objective optimisation concerned with the minimisation of a vector of objectives $f(x)$ could be expressed as [165]:

$$\min_{x \in X}(f_1(x), f_2(x), f_3(x), \ldots, f_k(x)) \tag{6-17}$$

The objective functions $f(x)$ is defined by a number of constraints or bounds.

The Pareto frontier image, as the preferred technique for the Pareto front visualization in multi objective optimisation, could present all the Pareto optimal solutions. The optimisation procedure employed for the system is shown in Fig. 6-5. In this study, the multi objective optimisation is implemented in MATLAB.

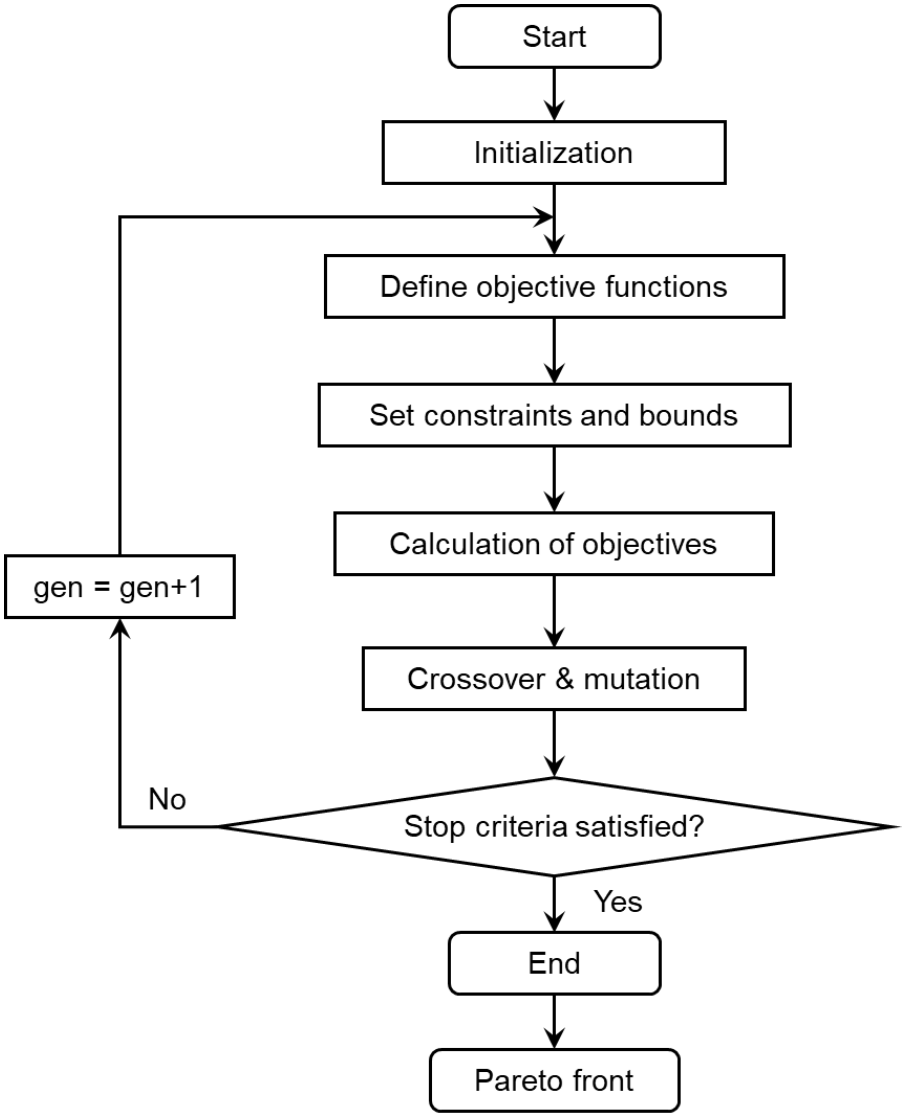


Fig. 6-5: Flow chart of the multi objective optimisation by the Pareto method.

As shown in Fig. 6-1, the LNG flow rate enters at 350 kg/h, 2100 kg/h and 3161 kg/h. The system is optimised by single-objective and multi-objective methods to optimise the water recovery rate (RR), the LNG cryogenic energy recovery efficiency and the exergy efficiency. The mathematical term for multi objective optimisation is written as:

$$min\begin{cases} 1/RR \\ Ex_d \\ 1/\eta_{LNG} \end{cases} \tag{6-18}$$

with the constraints including the moist air flow rate between 0 to 2880kg/h, RR and η_{LNG} at the range between 0 to 100% and the LNG outlet temperature above 0ºC.

As discussed in Chapter 5, the water production rate is mainly related to the operational parameters and geometry parameters. The effects of these parameters on the production rate are shown below in Table 6-3. As a result, to improve the system efficiency, the operation parameters should follow these rules: increase the vacuum degree, temperature, humidity and flow rate of the moist air, increase the coolant flow rate, reduce the coolant temperature, enhance the thermal conductivity and convective exchanger area to enhance the heat transfer. And the geometry parameters of the condenser are designed as shown in Table 6-4.

Table 6-3 Effect of the operational parameters and geometry parameters on production.

Operational parameters	Moist air				Coolant	
	Pressure	Temperature	Humidity	Flow rate	Flow rate	Temperature
Production	↓	↑	↑	↑	↑	↓
Geometry parameters	Thickness		Convective area		Thermal conductivity	
Production	↓		↑		↑	

↑: increase, ↓: decrease

Table 6-4 Geometry design of the condenser in the FWG system.

Parameter	Quantity	Parameter	Quantity
Width (m)	0.6	Height (m)	0.8
Length (m)	0.8	Thickness (m)	0.002
Number of plates	51	Number of channels	5
Material	Al alloy 3003 H-14	Number of passes	3
Convective exchange area (m^2)	47	Volume of the condenser (m^3)	0.12

6.5 Results and discussion

In this section, the numerical study for the operation parameters optimisation of the condenser by single objective optimisation and multi objective optimisation are introduced firstly. Secondly, based on the optimisation results, the effect of the surface treatment on the system performance is explored. The preferred surface coating has been selected as the condenser surface to enhance the condensation process in the

system. Eventually, the economics performance of the proposed FWG-LNG system is evaluated with the employment of the optimised design of the condenser.

6.5.1 Single-objective optimisation

The system is firstly optimised by genetic algorithm for single objective: RR maximisation, LNG cryogenic energy recovery efficiency (η_{LNG}) maximisation and exergy destruction (Ex_d) minimisation. Fig. 6-6 illustrates the single objective optimisation results for the LNG flow rate of 350kg/h. The figure shows that the optimum moist air flow rate for RR maximisation, LNG cryogenic energy recovery efficiency maximisation and exergy destruction minimisation is 50.4kg/h, 360kg/h and 50.4kg/h, respectively. In Fig. 6-7, the single objective optimisation results for the LNG flow rate of 2100kg/h are presented. A similar trend is shown, where the optimum $\dot{m_{ma}}$ for RR maximisation and exergy destruction is 301.3 kg/h, which provides the highest recovery rate at 83.7% and lowest exergy destruction at 99 kW. The optimum flow rate for maximising LNG cryogenic energy recovery efficiency at 62.77% is 1800 kg/h. For the LNG flow rate operating at 3161 kg/h conditions that is presented in Fig. 6-8, the freshwater RR and the exergy destruction is optimised at 83.96% and 141.7 kW with the $\dot{m_{ma}}$ of 439.2 kg/h. The highest LNG cryogenic energy recovery efficiency at 61.95% provided from the moist air flow at 2880 kg/h would be the optimal condition for the system.

As demonstrated in these three diagrams, the exergy destruction of the system increases with the increase of the moist air flow rate while the RR and η_{LNG} present different phenomena. When the moist air flow rate increases, the increment of the velocity makes a thinner boundary layer of the wall and improves the heat transfer.

Consequently, more water vapour is condensed on the surface. However, as the velocity increases to a certain level, the improvement stops. The reason is that for the fixed heat exchanger design, the effective area is insufficient to provide a contact area for the moist air condensation. For the part of moist air away from the surface, the dew point is hard to reach in order to be condensed, which also results in the decreasing trend of the water recovery rate. It could be seen that the efficiency of the LNG cryogenic energy recovery process remains nearly constant for the moist air flow rates above 0.02kg/s. This appears to be due to the higher LNG outlet temperature which lowers the temperature difference between the LNG and the moist air. Table 6-5 presents the performance results for each optimisation.

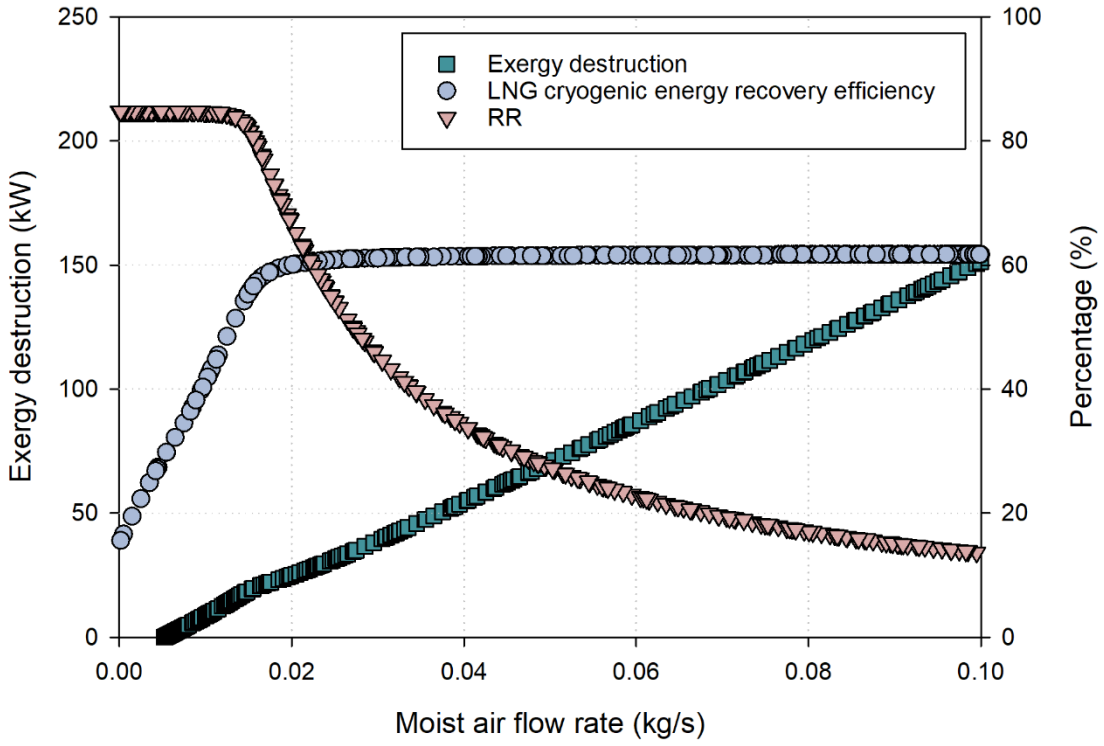


Fig. 6-6: Optimisation performance for single objective with the LNG flow rate of 350kg/h.

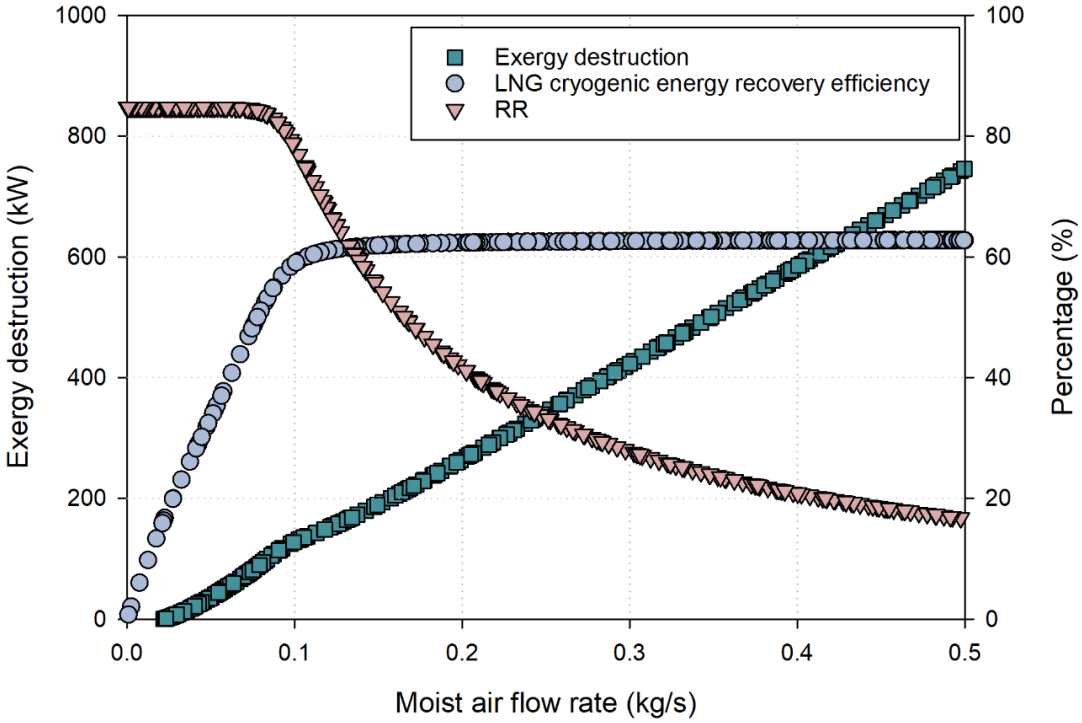


Fig. 6-7: Optimisation performance for single objective with the LNG flow rate of 2100kg/h.

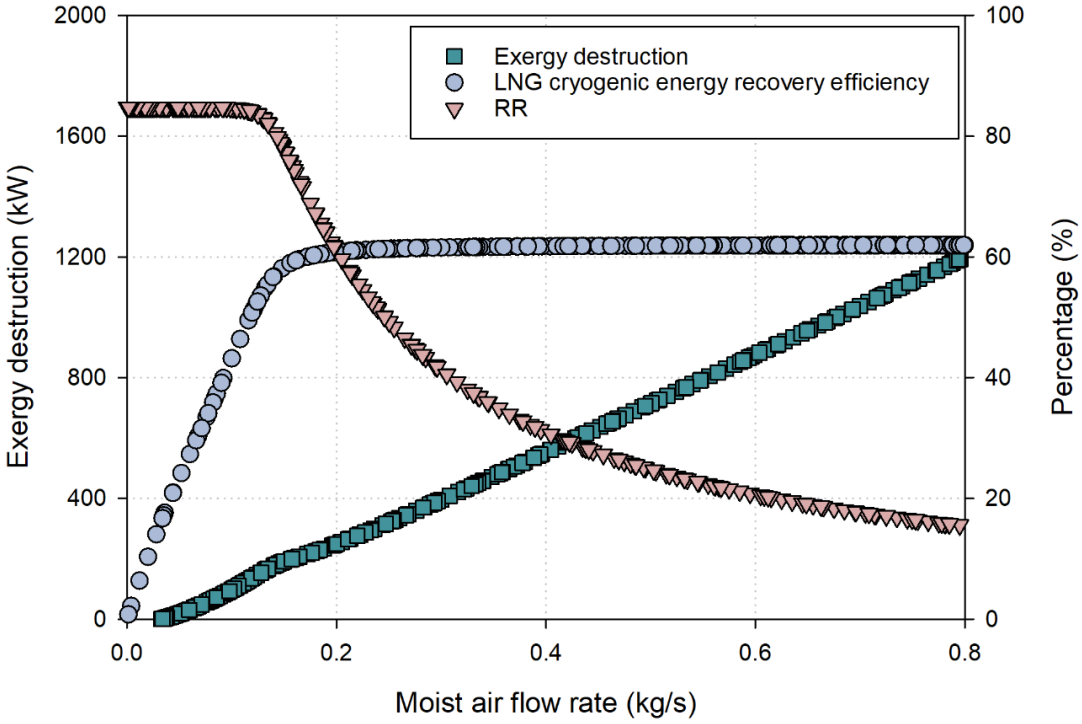


Fig. 6-8: Optimisation performance for single objective with the LNG flow rate of 3161kg/h.

Table 6-5 Performance analysis of single-objective optimisation.

Single-objective optimisation	LNG flow rate (kg/h)	Design parameters	RR	Ex_d (kW)	η_{LNG}
Maximise the water recovery rate	350	$\dot{m}_{ma}$ = 50.4kg/h T_{ma} = 314.6K p = 0.08bar φ_{ma} = 90%,	83.47%	16.9	83.1%
	2100	$\dot{m}_{ma}$ = 301.3kg/h T_{ma} = 314.6K p = 0.08bar φ_{ma} = 90%,	83.7%	99.7	53.1%
	3161	$\dot{m}_{ma}$ = 439.2kg/h T_{ma} = 314.6K p = 0.08bar φ_{ma} = 90%,	83.96%	141.7	51.67%
Maximise LNG cryogenic energy recovery efficiency	350	$\dot{m}_{ma}$ = 360kg/h T_{ma} = 314.6K p = 0.08bar φ_{ma} = 90%,	13.65%	151.4	61.7%
	2100	$\dot{m}_{ma}$ = 1800kg/h T_{ma} = 314.6K p = 0.08bar φ_{ma} = 90%,	16.70%	746.4	62.85%
	3161	$\dot{m}_{ma}$ = 2880kg/h T_{ma} = 314.6K p = 0.08bar φ_{ma} = 90%,	15.49%	1200.1	61.95%
Minimise Exergy destruction	350	$\dot{m}_{ma}$ = 50.4kg/h T_{ma} = 314.6K p = 0.08bar	83.47%	16.7	52.9%

		φ_{ma} = 90%,			
	2100	$\dot{m_{ma}}$ = 301.3kg/h	83.7%	99.7	53.1%
		T_{ma} = 314.6K			
		p = 0.08bar			
		φ_{ma} = 90%,			
	3161	$\dot{m_{ma}}$ = 439.2kg/h	83.96%	141.7	51.67%
		T_{ma} = 314.6K			
		p = 0.08bar			
		φ_{ma} = 90%,			

Fig. 6-9 illustrates the exergy efficiencies of each single-objective optimisation in all three LNG-flow-rate conditions. The freshwater recovery performance and the exergy destruction are optimised well. However, the exergy efficiency is not ideal in the optimisation study of the LNG cryogenic energy recovery efficiency compared with the other two optimisations. The exergy losses in the condenser could take place through the walls' conduction, the heat exchange area limitation and the operation parameters. Furthermore, it is proportional to the moist air flow rate but constrained by RR and η_{LNG}. Therefore, it is noteworthy that single-objective optimisation is still inadequate in optimising the condenser. It is necessary to employ the multi-objective optimisation method to determine the optimal design parameters.

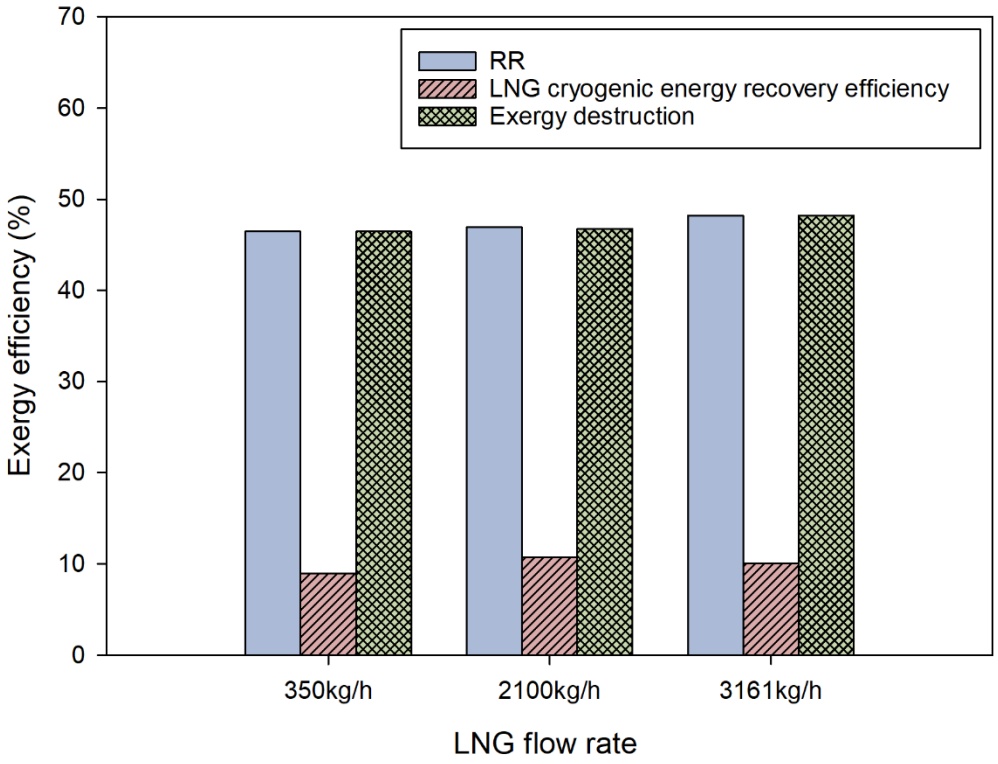


Fig. 6-9: Exergy efficiency for each optimisation.

6.5.2 Multi objective optimisation

Due to the limitations of the single-objective optimisation, the multi-objective optimisation is applied to improve the system's performance for multiple demands. The Pareto optimisation method is employed to derive the optimal design for the system under all the LNG flow rate conditions.

The Pareto frontier results with the three objective functions are shown in Fig. 6-10, Fig. 6-11 and Fig. 6-12 with the LNG flow rates of 350 kg/h, 2100 kg/h and 3161 kg/h, respectively. Each point on the curve shows the potential ideal performance values would satisfy the objectives' requirements at a level that was acceptable and would not be overpowered by other points. As shown in the figures, the base point is the design

that leads to the highest RR and η_{LNG} while incurring the minimum exergy destruction. Among the designs, the final optimal design point in the Pareto frontier is the one leading to shortest distance between the base point and optimal point. Therefore, the optimal moist air flow rate of 66.6 kg/h is selected for the case of the LNG flow rate at 350 kg/h. Then when the LNG flows at the rate of 2100 kg/h and 3161 kg/h, the ideal moist air flow rates are 369 kg/h and 576 kg/h, respectively. The detailed performance of the multi-objective optimisation is presented in Table 6-6.

The significant improvement on exergy efficiency has been made compared to other research on the LNG cold energy recovery system in the literature. Ghaebi, et al. [166] proposed a novel ammonia-water combined cooling and power cycle using LNG cold energy, which achieved an exergy efficiency of 22.51%. The optimisation study of a trans-critical CO_2 power cycle driven by geothermal energy with LNG as its heat sink proposed by [167] had the highest exergy efficiency of 12% with the Fuzzy optimisation method. The industrial study of Matsumoto, et al. [168] introduced a brine chilling system in Senboku, Japan and achieved a 10.3% exergy efficiency.

Table 6-6 Performance values of different multi-objective optimizations.

LNG flow rate	Design parameter	Performance variables
350kg/h	$\dot{m_{ma}}$ = 66.6kg/h	RR = 71.3%
	T_{ma} = 314.6K	η_{LNG} = 59.5%
	p = 0.08bar	Ex_d = 23.15 kW
	φ_{ma} = 90%	
2100kg/h	$\dot{m_{ma}}$ = 369kg/h	RR = 77.0%
	T_{ma} = 314.6K	η_{LNG} = 56.7%
	p = 0.08bar	Ex_d = 131.5kW
	φ_{ma} = 90%	
3500kg/h	$\dot{m_{ma}}$ = 576kg/h	RR = 74.0 %
	T_{ma} = 314.6K	η_{LNG} = 59.4%
	p = 0.08bar	Ex_d = 202.2kW
	φ_{ma} = 90%	

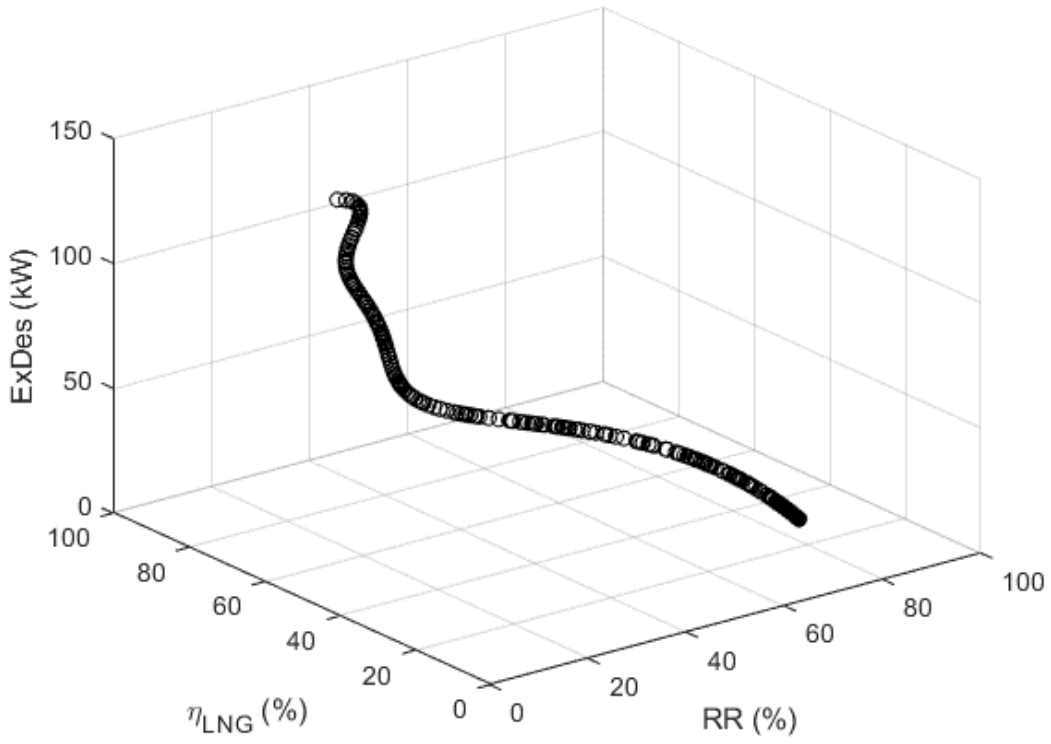


Fig. 6-10: The multi objective optimisation results in Pareto frontier with the LNG flow rate of 350kg/h.

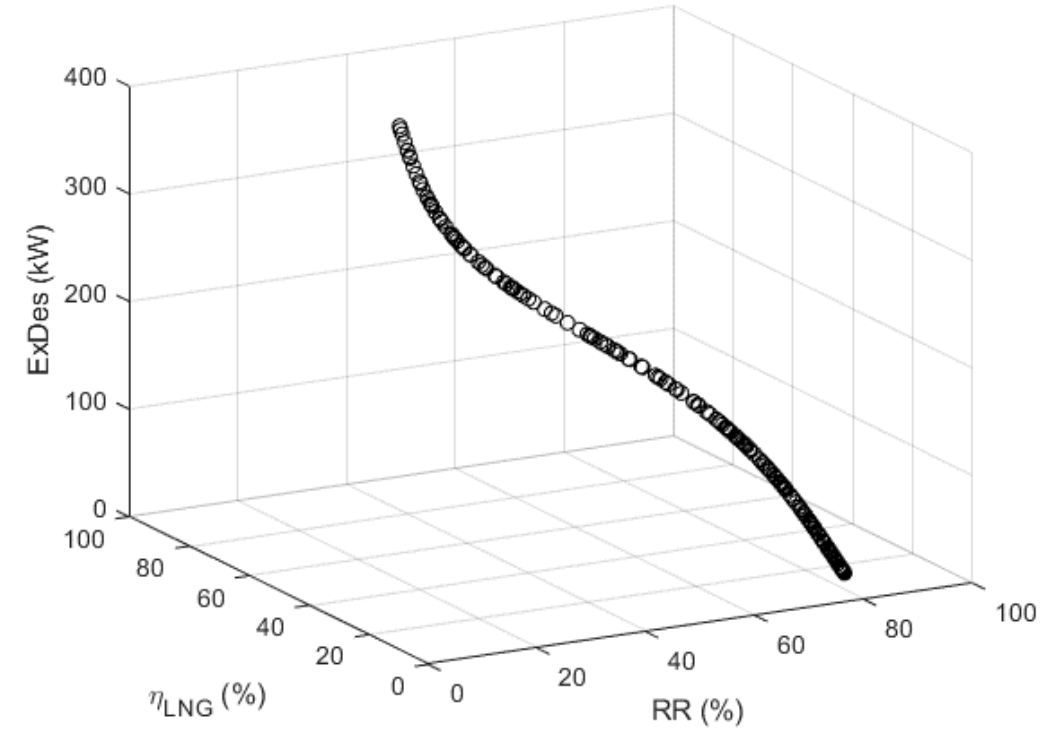


Fig. 6-11: The multi objective optimisation results in Pareto frontier with the LNG flow rate of 2100kg/h

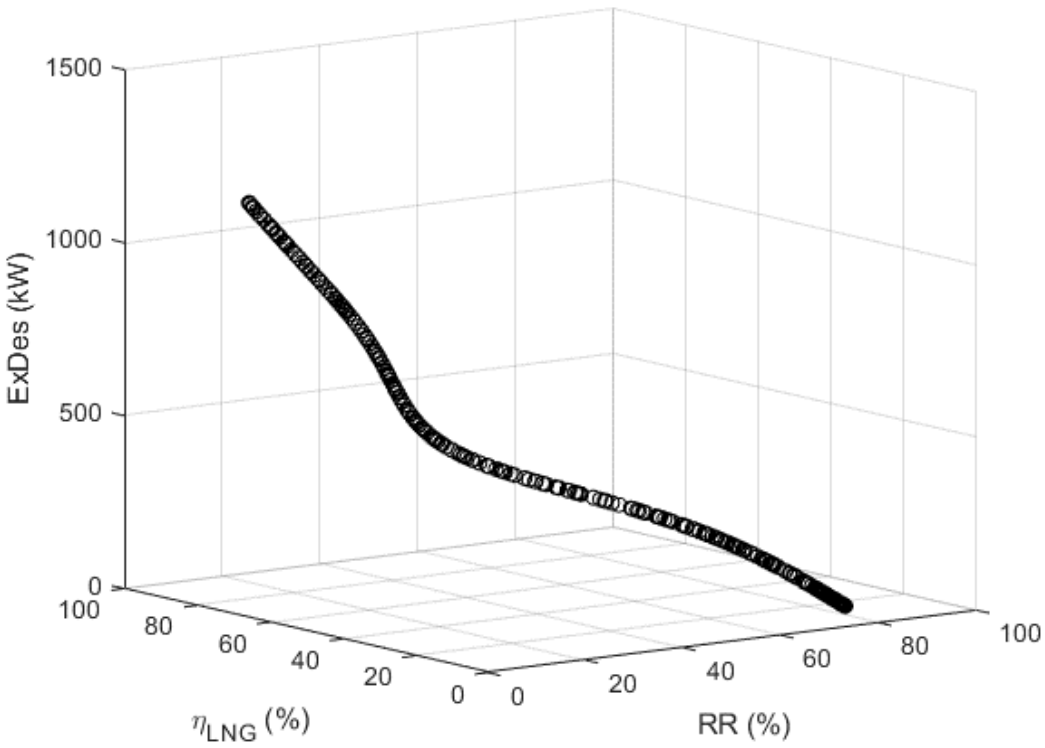


Fig. 6-12: The multi objective optimisation results in Pareto frontier with the LNG flow rate of 3161kg/h.

6.5.3 Optimisation analysis on surface treatments

So far, the surface modification method promotes the heat transfer performance by creating the dropwise condensation mechanism and suspending the frost formation and accumulation on the surface, which could be widely used in many industrial fields, such as aerospace, railway and refrigeration systems. Besides the production, the profitability of the implementation of the coating should also be considered, including the durability, frost thickness influence, capital costs of coating and the application field. Therefore, a fundamental economic estimation of the capital cost of the coating and the frost thickness are compared among four sample tubes as shown in Fig. 6-13.

These treated surfaces should be durable to retain their anti-freezing abilities to minimise application exploitation and maintenance costs. The exploration of the coating durability is performed by measuring the CA of all of the tubes after the experiments. The CA equal with those before the experiments indicated that each coating could last for at least 240 days. In the study of Erb and Thelen [169], they found that the vapour-deposited ultrathin polymer coating costs \$0.01/m^2 to \$0.02/m^2, while the electrodeposited noble metals costs \$0.07/m^2 to \$0.20/m^2 with a higher durability. Preston, et al. [170] employed the chemical vapour deposited method with graphene coatings to enhance the dropwise condensation by both low pressure and atmospheric pressure. The costs for these two conditions were increased to \$11.98/m^2 and \$57.95/m^2, respectively. The capital cost for a heat exchanger treated by superhydrophobic coating in a chemical vapour deposition study by Boyina, et al. [97] was \$158/m^2. In the desalination field, condensation is an essential process in the thermal distillation method to obtain fresh water. Lukic, et al. [171] applied ion

implantation on mechanical vapour compression desalination unit surfaces to achieve dropwise condensation for higher heat transfer performance. The ion-implantation treatment was assumed to be €165/m^2 (equals to about \$193/m^2). In comparison with the classical process, the treated unit reduced the water production cost up to 35.4%. The capital cost was calculated in three parts: (a) the costs of the materials used during the preparation process and coating process, (b) the one-time cost of coating, including principal cost, and (c) operation expenses and the labour charges. The Fluorine treated sample tube costs the most among these three treated tubes; while PTFE has the lowest price due to the cheap material and simple technique.

Considering the various demands in the market, these three sample tubes could be applied to different application fields. For the food industry, such as food storage, desalination and ice generation, the food compatible coatings of PTFE with a high production rate but the lowest price would be the best choice. For the refrigeration systems, aerospace and railway industrial markets, the thinnest frost layer generated from the fluorine-based coating surface would be preferred.

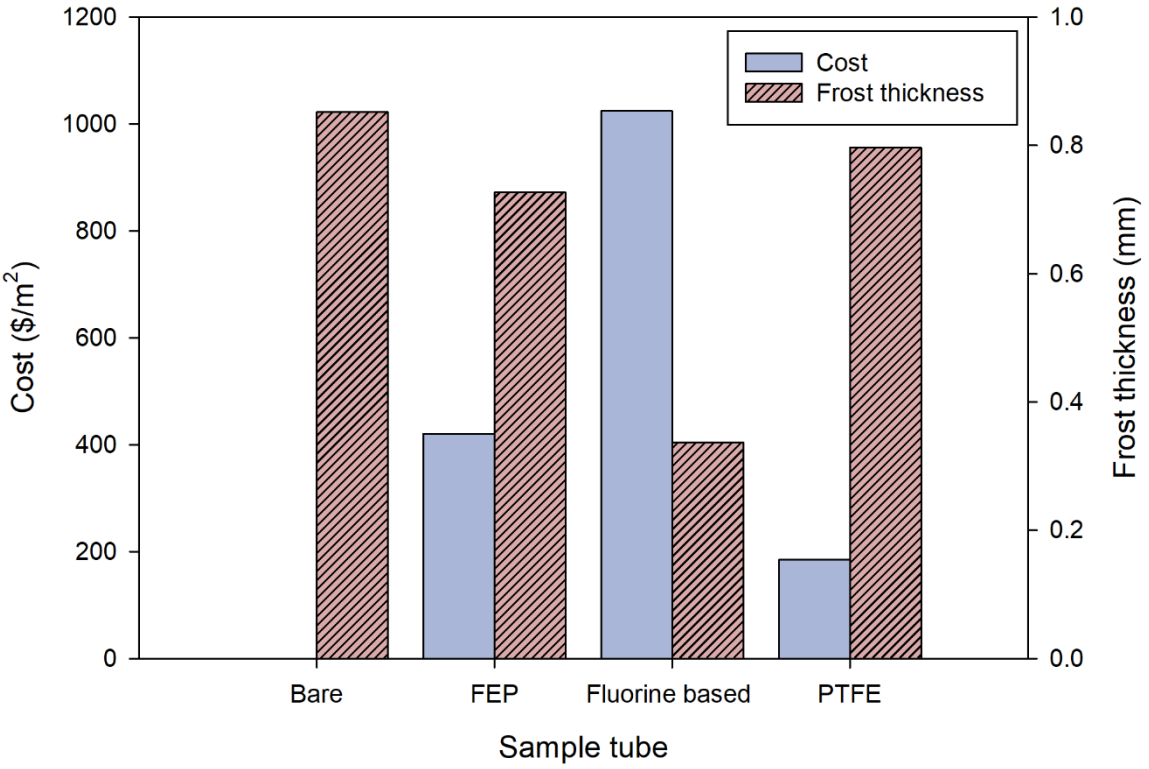


Fig. 6-13: The production rate and cost comparison.

According to the experimental results in Chapter 4 and the coating evaluation report, the optimisation study on different tube coatings is introduced in this section. The optimisation of the system performances of the three scenarios on three treated tubes are shown in Table 6-7. For the condensation mechanism process, Fluorine based coating presents a worse performance than the FEP and PTFE coating due to the surface characteristic. The FEP and PTFE gave similar results as the surface energies are similar. However, the capital cost of PTFE is less than FEP, and so is selected as the preferred coating material to optimise the system. In summary, considering the applications for the drinking water requirements on board, PTFE is the preferred material for the current case.

Table 6-7 Performance values of the optimisation with different coatings.

$\dot{m}_{LNG}$ (kg/h)	Design variables	FEP Performance	PTFE Performance	Fluorine Performance
350	$\dot{m}_{ma}$ = 66.6 kg/h, p_{ma} = 0.08 bar, $T_{ma,i}$ = 41.5 °C, φ_{ma} = 90%,	RR =76.3%, Ex_d = 24.7 kW η_{LNG} = 63.8%	RR = 75.6%, Ex_d = 24.5 kW η_{LNG} = 63.2%	RR = 73.5%, Ex_d = 23.8 kW η_{LNG} = 61.3478%
2100	$\dot{m}_{ma}$ = 369 kg/h, p_{ma} = 0.08 bar, $T_{ma,i}$ = 41.5 °C, φ_{ma} = 90%,	RR = 80.0%, Ex_d = 136.6 kW η_{LNG} = 61.9%	RR = 79.5%, Ex_d = 136.1 kW η_{LNG} = 61.5%	RR = 78.3%, Ex_d = 134.1 kW η_{LNG} = 60.5%
3161	$\dot{m}_{ma}$ = 576 kg/h, p_{ma} = 0.08 bar, $T_{ma,i}$ = 41.5 °C, φ_{ma} = 90%,	RR = 78.3%, Ex_d = 134.0 kW η_{LNG} = 62.8%	RR = 77.7%, Ex_d = 133.0 kW η_{LNG} = 62.3%	RR = 76.1%, Ex_d =130.0 kW η_{LNG} = 60.8%

6.5.3 System evaluation

Based on the optimisation analysis above, the FWG system promotion mainly lies on the feed-in water condition, coolant condition and condenser configuration. The feed-in seawater is expected to be close to the saturation temperature under a specific vacuum pressure and with an optimal flow rate. The LNG is ideal to flow with an optimal flow rate, bringing a high production rate and exergy efficiency without frosting deposition on the surface. In addition, the economical coating promotes the water

quality to a drinkable standard and the efficiency is expected. The optimal design parameters for the system are presented in Table 6-8. And the corresponding performance is shown in Fig. 6-14. In total, 14461 kg of water is produced in the 48 hours of the voyage, and 7037 kW of cryogenic energy is recovered from the FWG system. The production recovery rate RR of 67.7% and the GOR at 1.06 are obtained from the system.

Table 6-8 Optimal design operation and geometry parameters of the proposed FWG in the system.

Operation parameter	Quantity	Geometry parameter	Quantity
Feed seawater temperature (°C)	61.5	Evaporator volume (m^3)	0.3
Feed seawater flow rate (kg/h)	80 to 670	Accumulator volume (m^3)	1.5
Pressure in the evaporator (bar)	0.08	Condenser exchange area (m^2)	47
Coolant temperature (°C)	-133	Water tank volume (m^3)	0.215
Coolant flow rate (kg/h)	350 to 3161	Condenser material	Al alloy 3003
Pressure of LNG (bar)	5	Coating material	PTFE

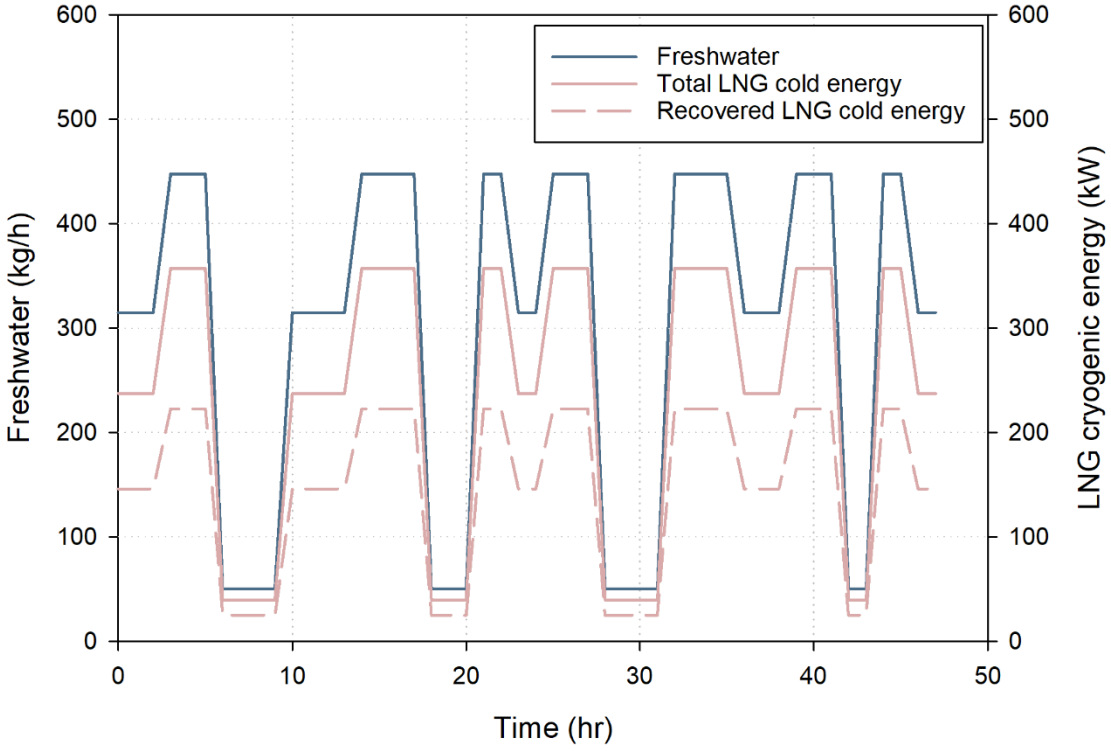


Fig. 6-14: Optimal performance of FWG system with PTFE coating.

6.5.4 Economic analysis

One of the most important indicators of the suitability of the design in the desalination systems is the economic analysis of the system. For the desalination unit, the major annual costs are the capital cost of the components, maintenance and operation costs. The capital cost in the designed system includes the structure cost of the evaporator, steam accumulator, condenser piping, insulation layers, tanks and coating fabrication. According to the UK market, the capital cost of each component is presented in Table 6-9. Thus, the total capital cost for the system is $37,970. The system is expected to operate with a life cycle of 20 years and the interest rate per year is assumed as 5%. Then the CRF is calculated by Eq. (6-14) as 0.08. The fixed cost of the system C_{fix} is given as 0.08 x $37,970 = $3038. The annual maintenance and operating costs are

considered as 4% of the total capital cost [172]. The total cost for the system per year is 0.48 x $37,970 = $18,226. The annual value for the freshwater production is $3,947 when the price of desalinated water is $1.5/$m^3$. Then calculated by Eq. (6-17), the payback period is 16 years. It is also noted that when the price of the desalinated water is greater than $1.2/$m^3$, the FWG system will be paid back in 20 years.

Table 6-9 Capital cost of components in the system.

Component	Cost ($)	Component	Cost ($)
Evaporator chamber	592	Steam accumulator	2,650
Condenser	24,567	Pipes	443
Silicone rubber	10	Insulation layers	220
Al alloy 3003-H14 surface	680	PTFE coating	8,676
Freshwater tank	150		

6.6 Summary

Consequently, the proposed optimal FWG system is feasible on the LNG powered case-ship. The design of the operation parameters is varied with the varied LNG flow rates. The employment of the single-objective optimisation and the multi-objective optimisation methods help to improve the system's efficiency. Additionally, the utilisation of the PTFE coating helps to promote the production rate and the water quality for drinking. For the proposed system on the case-study ship, the production recovery rate of 67.7% and the GOR at 1.06 are obtained from the optimisation process. The computed maximum energy efficiency of the LNG cryogenic energy is

approaching 57%. The extra cryogenic energy could be recovered for a low-temperature water cooling system.

Furthermore, this single-stage FWG system also has the potential to be utilised with an LNG terminal on land. The increased amount of LNG cryogenic energy in the LNG terminal can be expected to produce much more fresh water for land-based industrial and domestic use. The performance results from the current work will be of great benefit to the industries looking to minimise energy loss and maximise cold energy recovery from LNG regasification.

CHAPTER 7 Conclusions

7.1 Conclusions

This PhD thesis focused on developing a marine FWG assisted with waste LNG cryogenic energy from evaporation process of LNG powered ships. This was done through a series of fundamental experiments and theoretical modelling, as presented in the previous chapters, to answer development questions in different aspects. The LNG cryogenic energy has the potential to assist the FWG system in improving the production, system efficiency and economy. And the utilization of the hydrophobic coating treatment to the surface of condenser could effectively alleviate the surface frosting issues, which have negative effects on the freshwater generator. Overall, the integration of FWG and LNG cryogenic energy recovery was supported with the research work from three aspects: the experimental study on the effect of the surface characteristics and surface temperature, a numerical study on parametric analysis of the FWG components, and a case-study for an LNG powered cruise ferry. The main conclusions from each research aspect are summarised as follows.

Experimental study

An experimental investigation was conducted in this thesis to evaluate the effect of operating conditions on condensation performance, frost properties, delay time and coefficient. The mechanisms of condensation, condensation frosting and desublimation have been classified by the surface temperature at -36 °C, -22°C, -8 °C and 6 °C, and the surface wettability with the CA at 82°, 98°, 99° and 117°.

- For the condensation case, the FEP coating presents the highest enhancement factor of 2.1 on the condensation performance, while the Fluorine based coating with the greatest CA has the minor enhancement factor at 0.8.
- The results of the condensation frosting cases indicated that the hydrophobicity characteristics could delay the frost formation by extending the supercooling period. The Fluorine based coating presents the best anti-freezing performance with the smallest frost coverage area ratio on the surface of 4% and the longest supercooling period of 45s.
- For the frosting case, a high-speed camera's measurements of frost accumulation and frost thickness were introduced to calculate the frost properties, such as frost porosity, frost density and frost thermal conductivity. Compared with the bare tube, the treated tubes with hydrophobic characteristics have better anti-frosting performance. Among the three coating tubes, the Fluorine based surface with the lowest surface energy (CA of 118°) generated the most production of 0.44 g and had the smallest frost thickness in a full experimental cycle of 20 minutes. And the Fluorine based surface has the best total heat transfer in the frosting process which is 16% and 19.5% greater than the FEP and PTFE at a surface temperature of -36°C. A semi-empirical correlation for frost porosity prediction is proposed by summarizing 41 groups of experimental data. The correlation is fitted for the natural convection conditions with contact angles between 82° < CA < 120°, relative humidity 0.15 < RH < 0.95, surface temperatures −40 °C < T_w < −20 °C, and air temperatures 20 °C < T_a < 27 °C.

Numerical parametric analysis

The theoretical FWG models were developed and validated by the experimental study and literature.

- The evaporator model was validated by an experimental study in literature with a maximum relative error within ±14%. The condenser model was validated by the experimental results and the literature. The maximum relative error is within ±7%.
- The validated models were then used to investigate the parametric analysis study of the evaporator and condenser, including operation parameters and geometry parameters. The numerical results showed that the heating capacity, pressure, coolant temperature, flow rate, surface area and surface material significantly affect the amount of frost/freshwater and thermodynamic performance. The model could be applied to different types of air-to-air/steam heat exchangers to estimate the frosting performance.

Case-study on LNG powered ships

The integrated FWG and LNG cryogenic energy system was performed in the case-study. According to the parametric analysis results for each component in the numerical study, the optimal component sizing of an FWG operated on an LNG powered ship, aiming to improve the energy efficiency and cost-effectiveness is presented.

- The single-objective optimisation and multi objective optimisation is explored to fit the operating conditions during the voyage, in which the water recovery rate,

exergy efficiency and LNG cryogenic energy recovery efficiency are selected as evaluation indicators. The coating is also considered to be employed in the system to improve the condensation efficiency and prevent frosting issues. The optimization results suggest that the PTFE coating is preferred in terms of performance and economy.

- With the optimal design of the system, 14461 kg of water is produced in the 48 hours of the voyage, and 7037 kW of cryogenic energy is recovered from the FWG system. The production RR and GOR could reach 67.7% and 1.06, respectively. Lastly, an economic evaluation analysis about this FWG is explored. With the total annual cost for the system of $18,226, the FWG system will be paid back in 16 years.

7.2 Future work recommendations

FWG, as one of the most essential facilities on board, remains to be a complex process consisting of low efficiency and high capital cost. The optimizations on both evaporation and condensation processes play important roles in the food industry as well as in other industrial units. Overall, further research could be performed to achieve greater efficiency through reducing cryogenic energy consumption and taking advantage of even lower cryogenic temperature (< -36 °C). Accordingly, the use of LNG cryogenic energy proves to be an encouraging technique to intensify freshwater harvest in the FWG. In this final section, to increase the effectiveness of the process, further research could be conducted as recommended below:

Further experiments on the effect of the surface characteristics on condensation and frosting:

1) The surface modifications of the sample tubes could extend the surface characteristics to superhydrophilic, hydrophilic and superhydrophobic, and observe the phenomena and performance.
2) The effect of the salinity in the feed water on the production and efficiency could be carried out in future developments.
3) The use of liquid nitrogen instead of coolant fluid could be investigated to explore the surface performance under even lower cryogenic temperature conditions.

A fundamental theoretic study on frost property predictions:

1) Improve the frost porosity correlations summarized in Chapter 4, including all the surface characteristics and temperature range.
2) Simulate the effect of the surface characteristics on the droplet movements in advanced analytic models.

Broad LNG cryogenic energy assisted applications:

1) The designed FWG-LNG technology could also be employed with LNG terminals and offshore/floating terminals and provide freshwater resources for domestic and industrial uses.
2) The investigations on the surface modifications effect on the anti-frosting have potential uses in other LNG cryogenic energy related applications to prevent the negative effects on the surface.

Techniques	GOR (kg/kg)	PR (kg/MJ)	Thermal energy consumption (MJ/m^3)	Electricity consumption of pumps or others (kWh/m^3)	Water recovery rate	Total Dissolved Solids (ppm)	Typical plant size (m^3/day)	Water costs ($/$m^3$)
Humidification-dehumidification [173]	-	1.1	-	-	2%	<500	-	19
Freeze desalination	N/A	N/A	N/A	-	<53%	<500	-	0.34
Reverse osmosis	N/A	N/A	N/A	3.5-6.0	<55%	200-500	<128,000	0.3-13.0
Solar distillation	~0.5	-	0 (Solar passive)	-	20-46%	<10	<100	1.3-6.5
Thermal vapour compression	12	4.4	174	1.6-1.8	40%	<10	10,000-30,000	0.9-2.6
Mechanical vapour compression	N/A	N/A	N/A	7.0-12.0	40%	<10	100-3,000	0.9-2.6
Multi-effect distillation	10-16	4.35-6.9	146-229	2.0-2.5	20%-35%	<10	5,000 - 15,000	0.5-8.0
Multi-stage flash distillation	8-12	3.5-5.25	190-282	2.5-5.0	10%-15%	<10	50,000 - 70,000	0.6-1.8
Single-stage conventional distillation [12]	0-1	0.9	214.25	-	<10%	<10	-	20 [13]

Appendix B – MATLAB code for frost layer thickness detection

I = imread(‘Frost.jpg') % import the frost image from the PC

I = rgb2gray(I) % Convert the original RGB image to grayscale format

J = imread('base1.jpg') % import the bare tube image from the PC

J = rgb2gray(J) % Convert the original RGB image to grayscale format to find the base line

K = labeloverlay(I,J); %Overlay the frost image on the base line;

h = imshow(K) % present the new overlay image;

KK = imcrop(K); % crop the new overlay image to the fit size that focused on the frost layer;

h0 = imshow(KK) % present the cropped image;

h1 = impixelregion(h0); %show the pixel values of images

Hfrost = KK(:,:,1) > 232 & KK(:,:,2) > 232 & KK(:,:,3) > 232; % define the colour boundaries of the frost layer area;

numHfrost = sum(Hfrost(:)); % count the pixels of the frost layer;

Reference

[1] R. Tariq, N.A. Sheikh, J. Xamán, A. Bassam, An innovative air saturator for humidification-dehumidification desalination application, Applied Energy, 228 (2018) 789-807.
[2] J. Herdzik, Consequences of using LNG as a marine fuel, Journal of KONES, 20 (2013) 159--166.
[3] M. Ahlers, A. Buck-Emden, H.-J. Bart, Is dropwise condensation feasible? A review on surface modifications for continuous dropwise condensation and a profitability analysis, Journal of advanced research, 16 (2019) 1-13.
[4] M. Liu, D. Wu, A. Tsolakis, W. Gao, A waste cryogenic energy assisted freshwater generator for marine applications, Desalination, 500 (2021) 114898.
[5] X. Chen, B. Zhao, C. Shuai, S. Qu, M. Xu, Global spread of water scarcity risk through trade, Resources, Conservation and Recycling, 187 (2022) 106643.
[6] I.A. Shiklomanov, The world's water resources, in: Proceedings of the international symposium to commemorate, 1991, pp. 93-126.
[7] W.H. Organization, Progress on household drinking water, sanitation and hygiene 2000-2020: five years into the SDGs, (2021).
[8] J. Kucera, Desalination: water from water, John Wiley & Sons, 2019.
[9] A.D. Khawaji, I.K. Kutubkhanah, J.-M. Wie, Advances in seawater desalination technologies, Desalination, 221 (2008) 47-69.
[10] O. Yuksel, Y. Gulmez, O. Konur, S.A. Korkmaz, A. Erdogan, C.O. Colpan, Performance assessment of a marine freshwater generator through exergetic optimization, Journal of Cleaner Production, 219 (2019) 326-335.
[11] A. Al-Karaghouli, L.L. Kazmerski, Energy consumption and water production cost of conventional and renewable-energy-powered desalination processes, Renewable and Sustainable Energy Reviews, 24 (2013) 343-356.
[12] P. Tewari, R. Verma, B. Misra, H. Sadhulkan, Fresh water generators onboard a floating platform, in, 1997.
[13] M. Morsy, H.H. Othman, Improving Green Fresh Water Supply in Passengers Ships Using Waste Energy Recovery, Journal of King Abdulaziz University: Marine Sciences, 21 (2010).
[14] S.S. Shenvi, A.M. Isloor, A. Ismail, A review on RO membrane technology: Developments and challenges, Desalination, 368 (2015) 10-26.
[15] R.S. Kumar, A. Mani, S. Kumaraswamy, Experimental studies on desalination system for ocean thermal energy utilisation, Desalination, 207 (2007) 1-8.
[16] Q. Chen, M.K. Ja, Y. Li, K. Chua, Evaluation of a solar-powered spray-assisted low-temperature desalination technology, Applied energy, 211 (2018) 997-1008.
[17] K. Mahkamov, E. Orda, B. Belgasim, I. Makhkamova, A novel small dynamic solar thermal desalination plant with a fluid piston converter, Applied Energy, 156 (2015) 715-726.
[18] A. Laval, AQUA Blue [Brochure], in, Alfa Laval, Sweden, 2016.
[19] A. Laval, Dolphin series [Brochure], in, Alfa Laval Sweden, 2016.
[20] A. Laval, Multi-effect plate distiller [Brochure], in, Alfa Laval, Sweden 2016.
[21] Wartsila, Wärtsilä's Single Stage Desalination [Brochure], in, Wartsila, Finland, 2018.
[22] M. Alsehli, J.-K. Choi, M. Aljuhan, A novel design for a solar powered multistage flash desalination, Solar Energy, 153 (2017) 348-359.
[23] H. Shih, T. Shih, Utilization of waste heat in the desalination process, Desalination, 204 (2007) 464-470.
[24] D. Saury, S. Harmand, M. Siroux, Experimental study of flash evaporation of a water film, International Journal of Heat and Mass Transfer, 45 (2002) 3447-3457.
[25] Y. Junjie, Z. Dan, C. Daotong, W. Guifang, L. Luning, Experimental study on static/circulatory flash evaporation, International Journal of Heat and Mass Transfer, 53 (2010) 5528-5535.

[26] W. Gao, W. Sun, K. Anderson, Y. Cheng, A. Li, Investigation on temperature distribution of flash evaporation of LiCl droplets released into vacuum, International Journal of Heat and Mass Transfer, 74 (2014) 414-420.
[27] W. Gao, J. Qi, J. Zhang, G. Chen, D. Wu, An experimental study on explosive boiling of superheated droplets in vacuum spray flash evaporation, International Journal of Heat and Mass Transfer, 144 (2019) 118552.
[28] W. Gao, J. Qi, X. Yang, J. Zhang, D. Wu, Experimental investigation on bubble departure diameter in pool boiling under sub-atmospheric pressure, International Journal of Heat and Mass Transfer, 134 (2019) 933-947.
[29] W. Gao, C. Li, C. Xu, D. Wang, Experimental study on water separation process in a novel spray flash vacuum evaporator with heat-pipe, Desalination, 386 (2016) 39-47.
[30] E. Schmidt, W. Schurig, W. Sellschopp, Versuche über die Kondensation von Wasserdampf in Film-und Tropfenform, Technische Mechanik und Thermodynamik, 1 (1930) 53-63.
[31] D. Popov, K. Fikiin, B. Stankov, G. Alvarez, M. Youbi-Idrissi, A. Damas, J. Evans, T. Brown, Cryogenic heat exchangers for process cooling and renewable energy storage: A review, Applied Thermal Engineering, 153 (2019) 275-290.
[32] K. Fikiin, B. Stankov, J. Evans, G. Maidment, A. Foster, T. Brown, J. Radcliffe, M. Youbi-Idrissi, A. Alford, L. Varga, Refrigerated warehouses as intelligent hubs to integrate renewable energy in industrial food refrigeration and to enhance power grid sustainability, Trends in Food Science & Technology, 60 (2017) 96-103.
[33] J.G. Speight, Natural gas: a basic handbook, Gulf Professional Publishing, 2018.
[34] S. Kumar, H.-T. Kwon, K.-H. Choi, W. Lim, J.H. Cho, K. Tak, I. Moon, LNG: An eco-friendly cryogenic fuel for sustainable development, Applied energy, 88 (2011) 4264-4273.
[35] IGU, World LNG report 2022, in, 2022.
[36] D. GL, Decision and design support for future fuel options, in, DNV GL, 2022.
[37] E.S. Jeong, Optimization of power generating thermoelectric modules utilizing LNG cold energy, Cryogenics, 88 (2017) 29-35.
[38] B.B. Kanbur, L. Xiang, S. Dubey, F.H. Choo, F. Duan, Cold utilization systems of LNG: A review, Renewable and Sustainable Energy Reviews, 79 (2017) 1171-1188.
[39] W. Sun, P. Hu, Z. Chen, L. Jia, Performance of cryogenic thermoelectric generators in LNG cold energy utilization, Energy Conversion and Management, 46 (2005) 789-796.
[40] H. Han, Y. Yan, S. Wang, Y.-X. Li, Thermal design optimization analysis of an intermediate fluid vaporizer for liquefied natural gas, Applied Thermal Engineering, 129 (2018) 329-337.
[41] J. Pan, R. Li, T. Lv, G. Wu, Z. Deng, Thermal performance calculation and analysis of heat transfer tube in super open rack vaporizer, Applied Thermal Engineering, 93 (2016) 27-35.
[42] D. Patel, J. Mak, D. Rivera, J. Angtuaco, LNG vaporizer selection based on site ambient conditions, Proceedings of the LNG, 17 (2013) 16-19.
[43] S. Liu, W. Jiao, H. Wang, Three-dimensional numerical analysis of the coupled heat transfer performance of LNG ambient air vaporizer, Renewable Energy, 87 (2016) 1105-1112.
[44] L. Pu, Z. Qu, Y. Bai, D. Qi, K. Song, P. Yi, Thermal performance analysis of intermediate fluid vaporizer for liquefied natural gas, Applied thermal engineering, 65 (2014) 564-574.
[45] S. Xu, Q. Cheng, L. Zhuang, B. Tang, Q. Ren, X. Zhang, LNG vaporizers using various refrigerants as intermediate fluid: Comparison of the required heat transfer area, Journal of Natural Gas Science and Engineering, 25 (2015) 1-9.
[46] S. Egashira, LNG Vaporizer for LNG Re-gasification Terminal, Kobelco Technol Rev, 32 (2013) 64-69.
[47] C. Qi, W. Wang, B. Wang, Y. Kuang, J. Xu, Performance analysis of submerged combustion vaporizer, Journal of Natural Gas Science and Engineering, 31 (2016) 313-319.
[48] E.G. Cravalho, J.J. McGrath, W.M. Toscano, Thermodynamic analysis of the regasification of LNG for the desalination of sea water, Cryogenics, 17 (1977) 135-139.

[49] P. Wang, T.-S. Chung, A conceptual demonstration of freeze desalination–membrane distillation (FD–MD) hybrid desalination process utilizing liquefied natural gas (LNG) cold energy, Water research, 46 (2012) 4037-4052.
[50] W. Cao, C. Beggs, I.M. Mujtaba, Theoretical approach of freeze seawater desalination on flake ice maker utilizing LNG cold energy, Desalination, 355 (2015) 22-32.
[51] W. Lin, M. Huang, A. Gu, A seawater freeze desalination prototype system utilizing LNG cold energy, International Journal of Hydrogen Energy, (2017).
[52] M. Ahmad, D.L. Oatley-Radcliffe, P.M. Williams, Can a hybrid RO-Freeze process lead to sustainable water supplies?, Desalination, 431 (2018) 140-150.
[53] G. Xia, Q. Sun, X. Cao, J. Wang, Y. Yu, L. Wang, Thermodynamic analysis and optimization of a solar-powered transcritical CO 2 (carbon dioxide) power cycle for reverse osmosis desalination based on the recovery of cryogenic energy of LNG (liquefied natural gas), Energy, 66 (2014) 643-653.
[54] A. Messineo, D. Panno, Potential applications using LNG cold energy in Sicily, International Journal of Energy Research, 32 (2008) 1058-1064.
[55] T. He, S.K. Nair, P. Babu, P. Linga, I.A. Karimi, A novel conceptual design of hydrate based desalination (HyDesal) process by utilizing LNG cold energy, Applied energy, 222 (2018) 13-24.
[56] Z.R. Chong, T. He, P. Babu, J.-n. Zheng, P. Linga, Economic evaluation of energy efficient hydrate based desalination utilizing cold energy from liquefied natural gas (LNG), Desalination, 463 (2019) 69-80.
[57] P. Babu, A. Nambiar, Z.R. Chong, N. Daraboina, M. Albeirutty, O.A. Bamaga, P. Linga, Hydrate-based desalination (HyDesal) process employing a novel prototype design, Chemical Engineering Science, 218 (2020) 115563.
[58] A. Antonelli-Consultant, Desalinated water production at LNG-terminals, Desalination, 45 (1983) 383-390.
[59] J. Chang, J. Zuo, K.-J. Lu, T.-S. Chung, Freeze desalination of seawater using LNG cold energy, Water research, 102 (2016) 282-293.
[60] D.W. Meixi Liu, A new fresh water generation system under high vacuum degrees intensified by LNG cryogenic energy, in: 10th International Conference on Applied Energy Hong Kong, 2018.
[61] P. Peter Atkins, J. De Paula, Atkins' physical chemistry, OUP Oxford, 2014.
[62] X.-F. Pang, Water: molecular structure and properties, World Scientific, 2014.
[63] H.Y. Sohn, Process modeling in non-ferrous metallurgy, in: Treatise on Process Metallurgy, Elsevier, 2014, pp. 701-838.
[64] G. Wypych, Handbook of nucleating agents, Elsevier, 2021.
[65] C.J. Hermes, J. Boeng, D.L. da Silva, F.T. Knabben, A.D. Sommers, Evaporator Frosting in Refrigerating Appliances: Fundamentals and Applications, Energies, 14 (2021) 5991.
[66] Z.-j. Jin, H. Ye, H. Wang, H. Li, J.-y. Qian, Thermodynamic analysis of siphon flash evaporation desalination system using ocean thermal energy, Energy Conversion and Management, 136 (2017) 66-77.
[67] T.L. Bergman, F.P. Incropera, D.P. DeWitt, A.S. Lavine, Fundamentals of heat and mass transfer, John Wiley & Sons, 2011.
[68] J. Jeevahan, M. Chandrasekaran, G.B. Joseph, R. Durairaj, G. Mageshwaran, Superhydrophobic surfaces: a review on fundamentals, applications, and challenges, Journal of Coatings Technology and Research, 15 (2018) 231-250.
[69] M.-H. Kim, H. Kim, K.-S. Lee, D.R. Kim, Frosting characteristics on hydrophobic and superhydrophobic surfaces: A review, Energy Conversion and Management, 138 (2017) 1-11.
[70] K. Tadanaga, N. Katata, T. Minami, Super‐water‐repellent Al2O3 coating films with high transparency, Journal of the American ceramic society, 80 (1997) 1040-1042.

[71] G.R. Artus, S. Jung, J. Zimmermann, H.P. Gautschi, K. Marquardt, S. Seeger, Silicone nanofilaments and their application as superhydrophobic coatings, Advanced Materials, 18 (2006) 2758-2762.
[72] M. Qu, B. Zhang, S. Song, L. Chen, J. Zhang, X. Cao, Fabrication of superhydrophobic surfaces on engineering materials by a solution-immersion process, Advanced Functional Materials, 17 (2007) 593-596.
[73] J. Fresnais, J. Chapel, F. Poncin-Epaillard, Synthesis of transparent superhydrophobic polyethylene surfaces, Surface and Coatings Technology, 200 (2006) 5296-5305.
[74] E. Hoque, J. DeRose, P. Hoffmann, H. Mathieu, Robust perfluorosilanized copper surfaces, Surface and Interface Analysis: An International Journal devoted to the development and application of techniques for the analysis of surfaces, interfaces and thin films, 38 (2006) 62-68.
[75] B. Luo, P.W. Shum, Z. Zhou, K. Li, Preparation of hydrophobic surface on steel by patterning using laser ablation process, Surface and Coatings Technology, 204 (2010) 1180-1185.
[76] B. Na, R.L. Webb, A fundamental understanding of factors affecting frost nucleation, International Journal of Heat and Mass Transfer, 46 (2003) 3797-3808.
[77] J. Min, R.L. Webb, Condensate formation and drainage on typical fin materials, Experimental Thermal and Fluid Science, 25 (2001) 101-111.
[78] M. Rausch, A. Fröba, A. Leipertz, Dropwise condensation heat transfer on ion implanted aluminum surfaces, International Journal of heat and Mass transfer, 51 (2008) 1061-1070.
[79] D.-Y. Ji, J.-W. Lee, W. Hwang, K.-Y. Lee, Experimental study of condensation heat transfer on a horizontal aluminum tube with superhydrophobic characteristic, International Journal of Heat and Mass Transfer, 134 (2019) 286-295.
[80] Y. Gu, Y. Ding, Q. Liao, Q. Fu, X. Zhu, H. Wang, Condensation heat transfer characteristics of moist air outside 3-D finned tubes with different wettability, Energy, 207 (2020) 118202.
[81] H. Hu, G. Tang, D. Niu, Experimental investigation of condensation heat transfer on hybrid wettability finned tube with large amount of noncondensable gas, International Journal of Heat and Mass Transfer, 85 (2015) 513-523.
[82] S. Nath, S.F. Ahmadi, J.B. Boreyko, A review of condensation frosting, Nanoscale and Microscale Thermophysical Engineering, 21 (2017) 81-101.
[83] T. Koop, Homogeneous ice nucleation in water and aqueous solutions, Oldenbourg Wissenschaftsverlag, 2015.
[84] E. Moallem, Experimental and theoretical investigation of effect of fin geometry on frost formation on microchannel heat exchangers, Oklahoma State University, 2012.
[85] A.R. Tahavvor, M. Yaghoubi, Experimental and numerical study of frost formation by natural convection over a cold horizontal circular cylinder, International journal of refrigeration, 33 (2010) 1444-1458.
[86] M. Amini, A.R. Pishevar, M. Yaghoubi, Experimental study of frost formation on a fin-and-tube heat exchanger by natural convection, International Journal of Refrigeration, 46 (2014) 37-49.
[87] L. Li, Z. Liu, Y. Li, Y. Dong, Frost deposition on a horizontal cryogenic surface in free convection, International Journal of Heat and Mass Transfer, 113 (2017) 166-175.
[88] T. Lai, P. Ding, X. Dong, B. Zhang, X. Chen, Y. Hou, Experimental study on the frosting characteristics of round tube in confined circular flow path at low temperature, Applied Thermal Engineering, 171 (2020) 115075.
[89] M. Fossa, G. Tanda, Study of free convection frost formation on a vertical plate, Experimental Thermal and Fluid Science, 26 (2002) 661-668.
[90] Z. Liu, Y. Dong, Y. Li, An experimental study of frost formation on cryogenic surfaces under natural convection conditions, International Journal of Heat and Mass Transfer, 97 (2016) 569-577.

[91] C.J. Hermes, R.O. Piucco, J.R. Barbosa Jr, C. Melo, A study of frost growth and densification on flat surfaces, Experimental Thermal and Fluid Science, 33 (2009) 371-379.
[92] D. Kim, C. Kim, K.-S. Lee, Frosting model for predicting macroscopic and local frost behaviors on a cold plate, International Journal of Heat and Mass Transfer, 82 (2015) 135-142.
[93] Y. Hayashi, A. Aoki, S. Adachi, K. Hori, Study of frost properties correlating with frost formation types, (1977).
[94] A.Z. Şahin, Effective thermal conductivity of frost during the crystal growth period, International Journal of Heat and Mass Transfer, 43 (2000) 539-553.
[95] A. Lüer, H. Beer, Frost deposition in a parallel plate channel under laminar flow conditions, International journal of thermal sciences, 39 (2000) 85-95.
[96] J. Hoke, J. Georgiadis, A. Jacobi, Effect of substrate wettability on frost properties, Journal of thermophysics and heat transfer, 18 (2004) 228-235.
[97] K.S. Boyina, A.J. Mahvi, S. Chavan, D. Park, K. Kumar, M. Lira, Y. Yu, A.A. Gunay, X. Wang, N. Miljkovic, Condensation frosting on meter-scale superhydrophobic and superhydrophilic heat exchangers, International Journal of Heat and Mass Transfer, 145 (2019) 118694.
[98] W.-J. Lee, K.J. Bae, O.K. Kwon, Effect of hydrophobic surfaces on frost retardation in fin-tube heat exchangers with various fin pitches, Applied Thermal Engineering, 176 (2020) 115424.
[99] S. Liu, W. Jiao, L. Ren, H. Wang, P. Zhang, Dynamic heat transfer analysis of liquefied natural gas ambient air vaporizer under frost conditions, Applied Thermal Engineering, 110 (2017) 999-1006.
[100] Y. Lee, J. Park, C. Han, Modeling and analysis of frost growth in pilot-scale ambient air vaporizer, Industrial & Engineering Chemistry Research, 57 (2017) 5933-5943.
[101] S. Liu, W. Jiao, L. Ren, X. Tian, Thermal resistance analysis of cryogenic frosting and its effect on performance of LNG ambient air vaporizer, Renewable Energy, 149 (2020) 917-927.
[102] K.-H. Kim, H.-J. Ko, K. Kim, Y.-W. Kim, K.-J. Cho, Analysis of heat transfer and frost layer formation on a cryogenic tank wall exposed to the humid atmospheric air, Applied Thermal Engineering, 29 (2009) 2072-2079.
[103] Y. Kuang, C. Yi, W. Wang, Numerical simulation of frosting behavior and its effect on a direct-contact ambient air vaporizer, Journal of Natural Gas Science and Engineering, 27 (2015) 55-63.
[104] L. Ren, W. Jiao, G. Tian, X. Tian, S. Liu, Frosting characteristics and prediction of thickness of frost layer on a finned tube in regasification process of cryogenic liquids, International Journal of Refrigeration, (2021).
[105] F. Wang, C. Liang, M. Yang, C. Fan, X. Zhang, Effects of surface characteristic on frosting and defrosting behaviors of fin-tube heat exchangers, Applied Thermal Engineering, 75 (2015) 1126-1132.
[106] M. Amer, C.-C. Wang, Experimental investigation on defrosting of a cold flat plate via ultrasonic vibration under natural convection, Applied Thermal Engineering, 179 (2020) 115729.
[107] L. Huang, Z. Liu, Y. Liu, Y. Gou, L. Wang, Effect of contact angle on water droplet freezing process on a cold flat surface, Experimental thermal and fluid science, 40 (2012) 74-80.
[108] Z. Liu, Y. Gou, J. Wang, S. Cheng, Frost formation on a super-hydrophobic surface under natural convection conditions, International Journal of Heat and Mass Transfer, 51 (2008) 5975-5982.
[109] J.M. Dyer, B.D. Storey, J.L. Hoke, A.M. Jacobi, J.G. Georgiadis, An experimental investigation of the effect of hydrophobicity on the rate of frost growth in laminar channel flows, in, Univ. of Illinois, Urbana-Champaign, IL (US), 2000.
[110] K. Kim, K.-S. Lee, Characteristics and performance evaluation of surface-treated louvered-fin heat exchangers under frosting and wet conditions, International Journal of Heat and Mass Transfer, 55 (2012) 6676-6681.

[111] Z. Ye, J. Shi, J. Chen, Frosting behavior of louvered-fin and tube heat exchanger after surface treatment: Experimental analysis, Applied Thermal Engineering, 194 (2021) 117066.
[112] K. Kim, K.-S. Lee, Frosting and defrosting characteristics of a fin according to surface contact angle, International Journal of Heat and Mass Transfer, 54 (2011) 2758-2764.
[113] C.J. Hermes, F.R. Loyola, V.S. Nascimento Jr, A semi-empirical correlation for the frost density, International journal of refrigeration, 46 (2014) 100-104.
[114] A.D. Sommers, A.C. Napora, N.L. Truster, E.J. Caraballo, C.J. Hermes, A semi-empirical correlation for predicting the frost density on hydrophilic and hydrophobic substrates, International Journal of Refrigeration, 74 (2017) 313-323.
[115] G. Biguria, L.A. Wenzel, Measurement and correlation of water frost thermal conductivity and density, Industrial & Engineering Chemistry Fundamentals, 9 (1970) 129-138.
[116] Y. Hayashi, A. Aoki, S. Adachi, K. Hori, Study of frost properties correlating with frost formation types, Journal of heat transfer, 99 (1977) 239-245.
[117] J. Shin, A.V. Tikhonov, C. Kim, Experimental study on frost structure on surfaces with different hydrophilicity: density and thermal conductivity, J. Heat Transfer, 125 (2003) 84-94.
[118] M. Song, C. Dang, Review on the measurement and calculation of frost characteristics, International Journal of Heat and Mass Transfer, 124 (2018) 586-614.
[119] C. Li, J. Liu, S. Zheng, X. Chen, J. Li, Z. Zeng, Performance analysis of an improved power generation system utilizing the cold energy of LNG and solar energy, Applied Thermal Engineering, 159 (2019) 113937.
[120] E. Tur, B. Onal‐Ulusoy, E. Akdogan, M. Mutlu, Surface modification of polyethersulfone membrane to improve its hydrophobic characteristics for waste frying oil filtration: radio frequency plasma treatment, Journal of applied polymer science, 123 (2012) 3402-3411.
[121] E. Leivo, T. Wilenius, T. Kinos, P. Vuoristo, T. Mäntylä, Properties of thermally sprayed fluoropolymer PVDF, ECTFE, PFA and FEP coatings, Progress in Organic Coatings, 49 (2004) 69-73.
[122] N.H. Fletcher, The Chemical Physics of Ice, Cambridge: Cambridge University Press, 1970.
[123] S. Nath, J.B. Boreyko, On localized vapor pressure gradients governing condensation and frost phenomena, Langmuir, 32 (2016) 8350-8365.
[124] D.M. Murphy, T. Koop, Review of the vapour pressures of ice and supercooled water for atmospheric applications, Quarterly Journal of the Royal Meteorological Society: A journal of the atmospheric sciences, applied meteorology and physical oceanography, 131 (2005) 1539-1565.
[125] W. Wang, Q. Guo, W. Lu, Y. Feng, W. Na, A generalized simple model for predicting frost growth on cold flat plate, international journal of refrigeration, 35 (2012) 475-486.
[126] M. Kandula, Frost growth and densification on a flat surface in laminar flow with variable humidity, International communications in heat and mass transfer, 39 (2012) 1030-1034.
[127] H.R. Pruppacher, J.D. Klett, P.K. Wang, Microphysics of clouds and precipitation, in, Taylor & Francis, 1998.
[128] H. Lee, J. Shin, S. Ha, B. Choi, J. Lee, Frost formation on a plate with different surface hydrophilicity, International Journal of Heat and Mass Transfer, 47 (2004) 4881-4893.
[129] N.H. Fletcher, Structural aspects of the ice-water system, Reports on Progress in Physics, 34 (1971) 913.
[130] K.-S. Yang, K.-H. Lin, C.-W. Tu, Y.-Z. He, C.-C. Wang, Experimental investigation of moist air condensation on hydrophilic, hydrophobic, superhydrophilic, and hybrid hydrophobic-hydrophilic surfaces, International Journal of Heat and Mass Transfer, 115 (2017) 1032-1041.
[131] M.-H. Kim, D.R. Kim, K.-S. Lee, Stochastic approach to the anti-freezing behaviors of superhydrophobic surfaces, International Journal of Heat and Mass Transfer, 106 (2017) 841-846.
[132] A. Şahin, An analytical study of frost nucleation and growth during the crystal growth period, Heat and Mass Transfer, 30 (1995) 321-330.

[133] H. Schneider, Equation of the growth rate of frost forming on cooled surfaces, International Journal of Heat and Mass Transfer, 21 (1978) 1019-1024.
[134] C.J. Hermes, An analytical solution to the problem of frost growth and densification on flat surfaces, International Journal of Heat and Mass Transfer, 55 (2012) 7346-7351.
[135] E. Moallem, L. Cremaschi, D.E. Fisher, S. Padhmanabhan, Experimental measurements of the surface coating and water retention effects on frosting performance of microchannel heat exchangers for heat pump systems, Experimental Thermal and Fluid Science, 39 (2012) 176-188.
[136] R. Legg, Air conditioning system design, Butterworth-Heinemann, 2017.
[137] C. Wilke, A viscosity equation for gas mixtures, The journal of chemical physics, 18 (1950) 517-519.
[138] E.W. Lemmon, R. Tillner-Roth, A Helmholtz energy equation of state for calculating the thermodynamic properties of fluid mixtures, Fluid phase equilibria, 165 (1999) 1-21.
[139] D.-S. Jung, M. McLinden, R. Radermacher, D. Didion, A study of flow boiling heat transfer with refrigerant mixtures, International Journal of Heat and Mass Transfer, 32 (1989) 1751-1764.
[140] J.C. Chen, Correlation for boiling heat transfer to saturated fluids in convective flow, Industrial & engineering chemistry process design and development, 5 (1966) 322-329.
[141] X. Zou, M. Gong, G. Chen, Z. Sun, Y. Zhang, J. Wu, Experimental study on saturated flow boiling heat transfer of R170/R290 mixtures in a horizontal tube, International Journal of Refrigeration, 33 (2010) 371-380.
[142] D. Steiner, J. Taborek, Flow boiling heat transfer in vertical tubes correlated by an asymptotic model, Heat transfer engineering, 13 (1992) 43-69.
[143] V.H. Atlas, VDI-Verlag GmbH, in, Düsseldorf, 1993.
[144] S.W. Churchill, C. SW, Friction-factor equation spans all fluid-flow regimes, (1977).
[145] M.J. Moran, H.N. Shapiro, D.D. Boettner, M.B. Bailey, Fundamentals of engineering thermodynamics, John Wiley & Sons, 2010.
[146] T.H. Chilton, A.P. Colburn, Mass transfer (absorption) coefficients prediction from data on heat transfer and fluid friction, Industrial & engineering chemistry, 26 (1934) 1183-1187.
[147] B. Yavnel', The effect of frost on the heat transfer and on the aerodynamic resistance of air coolers, Kholodil'naya Tekh., (1970) 25-29.
[148] H. Rahman, M.N.A. Hawlader, A. Malek, An experiment with a single-effect submerged vertical tube evaporator in multi-effect desalination, Desalination, 156 (2003) 91-100.
[149] T. Wu, K. Vierow, Local heat transfer measurements of steam/air mixtures in horizontal condenser tubes, International journal of heat and mass transfer, 49 (2006) 2491-2501.
[150] L. Cheng, C.W.V.D. Geld, Experimental study of heat transfer and pressure drop characteristics of air/water and air-steam/water heat exchange in a polymer compact heat exchanger, Heat transfer engineering, 26 (2005) 18-27.
[151] HOLSCOT, PVDF, in, https://holscot.com/glossary/pvdf/ [accessed 14 Jan 2019].
[152] L. Ren, W. Jiao, X. Tian, T. Liu, Effect of frost layer on heat transfer of cryogenic fluid in a finned tube, Cryogenics, 109 (2020) 103115.
[153] Matmatch, Polytetrafluoroethylene (PTFE): Properties, Processing, and Applications, in, 2022.
[154] M.H. ASM, Vol. 1: Properties and Selection: Irons, Steels and High-Performance Alloys, American Society for Metals (ASM), (1990) 194.
[155] P.D. Harvey, Engineering Properties of Steels, American Society for Metals, Metals Park, (1982).
[156] T. Lyman, H.E. Boyer, P.M. Unterweiser, Metals handbook, American Society for Metals Cleveland, Ohio, 1948.
[157] M. Liu, D. Wu, A new fresh water generation system under high vacuum degrees intensified by LNG cryogenic energy, Energy Procedia, 158 (2019) 726-732.

[158] E. Deniz, S. Çınar, Energy, exergy, economic and environmental (4E) analysis of a solar desalination system with humidification-dehumidification, Energy Conversion and Management, 126 (2016) 12-19.
[159] A. Kabeel, T. Abou Elmaaty, E.M. El-Said, Economic analysis of a small-scale hybrid air HDH–SSF (humidification and dehumidification–water flashing evaporation) desalination plant, Energy, 53 (2013) 306-311.
[160] K. Zhani, H.B. Bacha, Experimental investigation of a new solar desalination prototype using the humidification dehumidification principle, Renewable energy, 35 (2010) 2610-2617.
[161] K.G. Nayar, Brackish water desalination for greenhouse agriculture: comparing the costs of RO, CCRO, EDR, and monovalent-selective EDR, Desalination, 475 (2020) 114188.
[162] S. Deepa, Introduction to genetic algorithms, Berlin: Springer, 2008.
[163] D.E. Golberg, Genetic algorithms in search, optimization, and machine learning, Addion wesley, 1989 (1989) 36.
[164] I.Y. Kim, O.L. De Weck, Adaptive weighted-sum method for bi-objective optimization: Pareto front generation, Structural and multidisciplinary optimization, 29 (2005) 149-158.
[165] N. Vakhania, F. Werner, Multicriteria Optimization: Pareto-Optimality and Threshold-Optimality, BoD–Books on Demand, 2020.
[166] H. Ghaebi, T. Parikhani, H. Rostamzadeh, Energy, exergy and thermoeconomic analysis of a novel combined cooling and power system using low-temperature heat source and LNG cold energy recovery, Energy conversion and management, 150 (2017) 678-692.
[167] M.H. Ahmadi, M. Mehrpooya, F. Pourfayaz, Thermodynamic and exergy analysis and optimization of a transcritical CO2 power cycle driven by geothermal energy with liquefied natural gas as its heat sink, Applied Thermal Engineering, 109 (2016) 640-652.
[168] M. Matsumoto, Y. Umeda, K. Masui, S. Fukushige, Design for innovative value towards a sustainable society, in: Proceedings of EcoDesign, 2012, pp. 7th.
[169] R. Erb, E. Thelen, Dropwise condensation characteristics of permanent hydrophobic systems, (1966).
[170] D.J. Preston, D.L. Mafra, N. Miljkovic, J. Kong, E.N. Wang, Scalable graphene coatings for enhanced condensation heat transfer, Nano letters, 15 (2015) 2902-2909.
[171] N. Lukic, L. Diezel, A.P. Fröba, A. Leipertz, Economical aspects of the improvement of a mechanical vapour compression desalination plant by dropwise condensation, Desalination, 264 (2010) 173-178.
[172] A.G. Ibrahim, I. Dincer, A solar desalination system: Exergetic performance assessment, Energy conversion and Management, 101 (2015) 379-392.
[173] M. Faegh, M.B. Shafii, Thermal performance assessment of an evaporative condenser-based combined heat pump and humidification-dehumidification desalination system, Desalination, 496 (2020) 114733.